



**THE DEVELOPMENT OF PALLADIUM NANOPARTICLES FOR RADIOPHARMACEUTICAL  
APPLICATION**

by

Sendibitiyosi Gandidzanwa

Submitted in fulfilment of the requirements for the degree of

**Master of Science: Chemistry (MSc Chemistry)**

in the

FACULTY OF SCIENCE

at the

NELSON MANDELA UNIVERSITY

Supervisor: Prof. Zenixole R. Tshentu

Co-supervisors: Prof. Carminita L. Frost and Prof. Michael E. Lee


February 2019

**DEDICATION**

*To my late dad, grandma, and sister...*

**DECLARATION**

I, Sendibitiyosi Gandidzanwa (211175897), hereby declare that the dissertation for student qualification to be awarded is my own work and that it has not previously been submitted for assessment or completion of any postgraduate qualification in another University or for another qualification.

  
\_\_\_\_\_

Sendibitiyosi Gandidzanwa.

## ABSTRACT

The dissertation describes an in-depth synthesis and optimisation of palladium(0) nanoparticles of three distinct size ranges, respective capping agents, and cellular uptake studies using a non-toxic concentration (10  $\mu$ M), laying a foundation for the design of palladium-based folate receptor-targeted theranostic nanoradiopharmaceutical.

In the preliminary selection to determine the optimal diamines for the study, ethylenediamine, hexamethylenediamine, 1,10-diaminododecane, 1,12-diaminododecane, 1,4-diaminobenzene, 4,4'-ethylenedianiline, 1,2-diphenyl-1,2-diaminoethane, and tetraaminophthalocyanine were employed. The characterisation of the nanoparticles obtained from the *in situ* reduction of palladium(II) salt at room temperature by either 1,2,3-trihydroxybenzene (pyrogallol), citric acid, sodium metabisulphite, sodium borohydride, hydrazine hydrate, or formaldehyde was performed. Ethylenediamine and sodium borohydride were found to be the best diamine capping and reducing agent, respectively. Systematic investigations determined that the nanoparticle synthesis was dependent on various reaction parameters: such as reaction temperature, time, reductant reducing power, and capping agents. The parameters effects on the nanoparticle size, morphology, shape, stability, crystallinity, and surface charge were investigated. The optical properties, elemental composition, functional group, concentration and molecular weight for the synthesised nanoparticles or conjugates were determined. These properties were analysed using Ultraviolet-visible spectroscopy (UV-Vis), high resolution transmission electron microscopy (HRTEM) coupled with selective area electron diffraction (SAED) and energy dispersive X-ray spectroscopy (EDS), X-ray powder diffraction (XRD), zeta potential (ZP), dynamic light scattering (DLS), elemental analysis (EA),  $^1\text{H}$  and  $^{13}\text{C}$ -nuclear magnetic resonance ( $^1\text{H}$ - and  $^{13}\text{C}$ -NMR), Fourier-transform infrared spectroscopy (FTIR), inductively coupled plasma-optical emission spectroscopy (ICP-OES), and liquid chromatography-mass spectroscopy (LC-MS).

The *in vitro* cytotoxicity, cell uptake, and internalisation studies of palladium nanoparticles (10  $\mu$ M) ranging in size and different types of capping agent were performed using three breast cancer cell lines: MDA-MB-468, MCF-7 and MDA-MB-231, and a non-tumorigenic MCF-10A breast cell line. The cell uptake and internalisation were investigated using ICP-OES and TEM.

A high dependence between reduction rate and concentration of palladium precursor was observed for the room temperature synthesis of palladium nanoparticles, and the employed synthesis procedure will be applied to the hot palladium isotope ( $^{109}\text{Pd}$ ). A facile, green,



aqueous synthesis route for palladium nanoparticles at room temperature was developed, and the synthesised nanoparticles indicated narrow size distributions. A concentration dependence between cytotoxicity and palladium nanoparticles was observed, with lower concentrations (10  $\mu\text{M}$ ) exhibiting minimal cytotoxicity relative to higher concentrations (100  $\mu\text{M}$ ). The cellular uptake of palladium nanoparticles was found to be concentration, folate-receptor, capping agent, and cell line proliferation-dependent. Well-defined, monodispersed, and negatively charged folate-ethylenediamine and folate-phthalocyanine capped palladium nanoparticles were taken up by cells, with higher nanoparticle internalisation in folate receptor positive tumorigenic cells relative to folate receptor negative non-tumorigenic cells.

It can be concluded that palladium(0) nanoparticles can be synthesised from the reduction of palladium(II) by sodium borohydride at room temperature. The folate-conjugated palladium nanoparticles are non-cytotoxic at 10  $\mu\text{M}$  and were successfully optimised and selectively delivered to folate receptor-positive breast cancer cells (MDA-MB-231 and MCF-7) relative to non-tumorigenic breast cells (MCF-10A) and folate receptor negative cancer cells (MDA-MB-468).

**Keywords:** Palladium nanoparticles, folate receptor, breast cell lines, cytotoxicity, transmission electron microscopy.

**CONFERENCES AND PUBLICATIONS**

This work was presented at the following conferences;

S. Gandidzanwa, M.E. Lee, C.L. Frost, and Z.R. Tshentu. The development of palladium nanoradiopharmaceuticals. 1<sup>st</sup> Three-minute thesis competition, Nelson Mandela University, October 2017. Port Elizabeth (South Africa). Oral presentation finalist.

S. Gandidzanwa, S. Joseph, L. Cairncross, N. Beukes, S. Roux, C.L. Frost, M.E. Lee, and Z.R. Tshentu. The development of palladium nanoparticles for radiopharmaceutical application. 7<sup>th</sup> International Conference on Nanoscience and Nanotechnology in Africa (NanoAfrica2018), April 2018. Durban (South Africa). Oral presentation.

The following manuscripts are under preparation;

S. Gandidzanwa, S. Joseph, C. Blom, N. Beukes, A. Janse van Vuuren, C.L. Frost, M.E. Lee, and Z.R. Tshentu. Synthesis and characterisation of amine-capped palladium nanoparticles; In preparation for Beilstein Journal of Nanotechnology.

S. Gandidzanwa, S. Joseph, L. Cairncross, S. Roux, S. Pinchuck, A. Janse van Vuuren, N. Beukes, M.E. Lee, C.L. Frost and Z.R. Tshentu. Cytotoxicity and uptake of folate-conjugated palladium nanoparticles by folate receptor positive and negative cell lines; In preparation for Journal of Nanomedicine: Nanotechnology, Biology and Medicine.

## ACKNOWLEDGEMENTS

Little achievements often require long, tortuous effort, sweet and bitter experiences, including some sacrifices. I want to express my deepest thanks and heartfelt gratitude to the following, for the contribution they made towards the completion of this degree. Special thanks;

- ❖ To Him; who created man, heaven and earth, the Creator of the universe, the true source of light and wisdom, God, for strengthening me in all things and seeing me through all the challenging circumstances. For me to reach this far, it is not by my intelligence, but it is His will.
- ❖ To my supervisor, Professor Zenixole Tshentu, for his expert guidance, tremendous patience, countless discussions, ceaseless encouragement, immense understanding, and for the opportunity to be part of his research group. His invaluable input, unwavering support, and financial assistance made this journey an easier one.
- ❖ To my co-supervisor, Professor Michael Lee, for his input, encouragement, and practical criticism.
- ❖ To my co-supervisor and academic mentor, Professor Carminita Frost, for her invaluable time, precious care and concern, unwavering support, and pundit guidance towards the success of my academic journey.
- ❖ To Dr. Natasha Beukes for her tireless, much-treasured, and invaluable assistance with cell work studies, conference preparations, and dissertation finalisation.
- ❖ To the Mandela Rhodes Foundation, for their financial support towards the completion of my degree.
- ❖ To my non-academic mentors, Kim Elliot, Jennifer Winstead, Robin Minne, Fiona Heilbron, and Lynette Roodt, for the mentorship, consistent support, inspiration, and motivation throughout my university career.
- ❖ To my best friends, Nomfundo Mnisi, Zizopho Ngayeka, Mutenta Nyambe, Lerato Kekana, Innocent Zvovuranda, Brian Dzadoza, Pumza Mente, Victor Agbakoba, and Malvin Chironga for their love, care, emotional support, tremendous and immeasurable friendships, and assistance in all aspects of my life.
- ❖ To my family, for their patience, love, care, concern, and wholehearted support throughout my studies.
- ❖ To Candice Blom, Arno Janse van Vuuren, Rutendo Kupara, Amy De La Harpe, Recardia Schoeman, Simon Jackson, Carri-Ann Bloem, Lynn Cairncross, Shirley Pinchuck, Marvin Randall, and all other biochemistry and Centre for High Resolution Transmission

Electron Microscopy (HRTEM) team members whom I worked with for their much-appreciated help.

- ❖ To the best research groupmate ever, Sinelizwi Joseph, for her immense assistance, genuine friendship, support, and inspiration which is highly treasured.
- ❖ To my amazing and enriching research group, for their countless discussions, encouragement, fantastic laboratory experience, friendly atmosphere, considerate and loving personalities.
- ❖ To my caring and loving psychologist, Fareedah Sauls, and ingenious attorney, Varonique Philander, for their invaluable professional support in times of need.
- ❖ To all my friends, colleagues, acquaintances, and any other persons not mentioned by name who made this achievable.

## TABLE OF CONTENTS

<b>DEDICATION</b>	.....	i
<b>DECLARATION</b>	.....	ii
<b>ABSTRACT</b>	.....	iii
<b>CONFERENCES AND PUBLICATIONS</b>	.....	v
<b>ACKNOWLEDGEMENTS</b>	.....	vi
<b>TABLE OF CONTENTS</b>	.....	viii
<b>LIST OF TABLES</b>	.....	xii
<b>LIST OF FIGURES</b>	.....	xiv
<b>LIST OF SCHEMES</b>	.....	xxviii
<b>LIST OF ABBREVIATIONS</b>	.....	xxix
<b>LIST OF SYMBOLS</b>	.....	xxxiv
<b>CHAPTER 1: INTRODUCTION</b>	.....	1
1.1 <b>CANCER</b>	.....	1
1.1.1    History and statistics of cancer	.....	1
1.1.2    Cancer treatment methods	.....	3
1.1.3    Challenges/Limitations of current therapeutic methods	.....	4
1.2 <b>RADIOPHARMACEUTICALS</b>	.....	5
1.2.1    Diagnostic radiopharmaceuticals	.....	5
1.2.2    Therapeutic radiopharmaceuticals	.....	6
1.2.3    Design and development of theranostic radiopharmaceuticals	.....	7
1.2.4    Radionuclides	.....	8
1.2.5    Palladium as a radiopharmaceutical	.....	10
1.2.5.1    Palladium's key properties	.....	10
1.2.5.2    Palladium isotopes, radionuclides, and their properties	.....	11
1.3 <b>NANOPARTICLES</b>	.....	11
1.3.1    Synthesis of nanoparticles	.....	12
1.3.1.1    Top-down and bottom-up approach	.....	12
1.3.2    Important nanoparticle properties in drug development	.....	13
1.3.2.1    Particle size and dispersity	.....	13
1.3.2.2    Surface charge	.....	14
1.3.2.3    Shape/morphology and organisation	.....	15
1.3.2.4    Chemical composition/hydrophobicity	.....	15
1.3.2.5    Impurity and crystallinity	.....	16
1.3.2.6    Stability	.....	16

1.3.2.7	Toxicity .....	16
1.3.2.8	Stealth, specificity, and biodegradability .....	17
1.3.2.9	Reproducibility .....	17
1.3.3	Functionalisation of nanoparticles .....	17
1.3.3.1	Bioconjugate .....	18
1.4	NANOMEDICINE AND NANOTECHNOLOGY .....	18
1.4.1	Nanoparticle vehicle molecules .....	19
1.4.2	Nanoparticle based-targeting methods .....	20
1.4.2.1	Passive targeting .....	20
1.4.2.2	Active targeting .....	21
1.4.3	Uptake mechanism .....	22
1.4.4	Factors affecting nanoparticle cellular uptake .....	23
1.5	FOLATE-BASED DRUG DEVELOPMENT .....	24
1.5.1	Structure of folic acid .....	24
1.5.2	Importance and functions of folic acid .....	24
1.5.3	Folate antagonists .....	25
1.5.4	The folate receptors .....	25
1.5.4.1	Structure and composition of the folate receptor .....	25
1.5.4.2	Active targeting of folate receptors .....	27
1.5.5	Folate conjugation .....	27
1.5.6	Folate uptake .....	28
1.5.6.1	Folate receptor-mediated endocytosis .....	28
1.5.6.2	Reduced folate carrier .....	29
1.5.6.3	Proton-coupled folate transporter .....	30
1.5.7	Antifolates uptake .....	30
1.5.8	Challenges/Limitations of nanoparticle folate-targeted therapy .....	31
1.6	FOLATE RECEPTOR EXPRESSION .....	33
1.6.1	MDA-MB-468 .....	34
1.6.2	MCF-7 .....	34
1.6.3	MDA-MB-231 .....	35
1.6.4	MCF-10A .....	35
1.7	AIMS OF THE STUDY .....	35
1.8	SCOPE OF THE DISSERTATION .....	36
CHAPTER TWO: MATERIALS, TECHNIQUES, and EXPERIMENTAL METHODS .....		37

2.1	MATERIALS: REAGENTS USED .....	37
2.2	INSTRUMENTATION .....	39
2.2.1	<sup>1</sup> H-and <sup>13</sup> C-Nuclear magnetic resonance (NMR).....	39
2.2.2	UV-Vis absorption spectroscopy (UV-Vis).....	39
2.2.3	Fourier-transform infrared spectroscopy (FTIR).....	40
2.2.4	X-ray diffraction spectroscopy (XRD).....	40
2.2.5	Liquid Chromatography-Mass Spectroscopy (LC-MS) .....	40
2.2.6	Elemental Analysis .....	40
2.2.7	Zeta potential (ZP) and dynamic light scattering (DLS) .....	40
2.2.8	Transmission electron microscopy (TEM).....	40
2.2.9	Inductively coupled plasma-optical emission spectroscopy (ICP-OES). .....	41
2.2.10	Powerwave spectrophotometer (BioTek) .....	42
2.2.11	Centrifuge .....	42
2.2.12	Ultrasonicator .....	42
2.2.13	Incubator.....	42
2.2.14	Other instrumentation.....	42
2.3	PREPARATIVE ASPECTS.....	43
2.3.1	Synthesis of N-Boc-ethylenediamine-folate .....	43
2.3.2	Synthesis of folate-ethylenediamine .....	43
2.3.3	Synthesis of tetraaminophthalocyanine (TAPc) .....	44
2.3.4	Synthesis of folate conjugated TAPc/EDA .....	45
2.3.5	Synthesis of palladium nanoparticles .....	47
2.3.6	Synthesis of capped palladium nanoparticles .....	48
2.4	CELL LINES AND CULTURE CONDITIONS.....	50
2.5	CELL VIABILITY ASSAY .....	50
2.5.1	Trypan Blue Exclusion Assay .....	51
2.5.2	Methylthiazol tetrazolium (MTT) assay .....	52
2.6	CELL UPTAKE STUDIES: TRANSMISSION ELECTRON MICROSCOPY (TEM) .....	52
2.7	CELL UPTAKE STUDIES: INDUCTIVELY COUPLED PLASMA-OPTICAL EMISSION SPECTROSCOPY (ICP-OES) .....	53
2.8	STATISTICS .....	53
CHAPTER THREE: SYNTHESIS, OPTIMISATION, AND CHARACTERISATION OF CONJUGATES AND NANOPARTICLES .....		
3.1	GENERAL INTRODUCTION .....	54

3.2	SYNTHESIS AND CHARACTERISATION OF CAPPING AGENTS .....	55
3.2.1	Synthesis of tetraaminophthalocyanine (TAPc) .....	55
3.2.2	Synthesis of folate-phthalocyanine .....	58
3.2.3	Synthesis of folate-ethylenediamine .....	62
3.3	PRELIMINARY OPTIMISATION OF SYNTHESIS PARAMETERS.....	66
3.3.1	Reducing and capping agents .....	67
3.3.2	Temperature and time .....	79
3.3.3	Stability .....	81
3.4	GENERAL DISCUSSION: PRELIMINARY OPTIMISATION OF NANOPARTICLES.....	85
3.5	CHARACTERISATION OF THE NANOPARTICLES FROM THE OPTIMISED METHOD ..	85
3.5.1	Borohydride capped nanoparticles.....	87
3.5.2	Ethylenediamine capped nanoparticles .....	89
3.5.3	Phthalocyanine capped nanoparticles.....	91
3.5.4	Folate-ethylenediamine capped nanoparticles .....	94
3.5.5	Folate-phthalocyanine capped nanoparticles .....	97
3.6	GENERAL DISCUSSION: OPTIMISED NANOPARTICLES .....	100
CHAPTER FOUR: BIOCHEMICAL EVALUATION OF PALLADIUM NANOPARTICLES .....		101
4.1	GENERAL INTRODUCTION .....	101
4.2	CYTOTOXIC STUDIES .....	102
4.2.1	MDA-MB-468 cell viability screen.....	103
4.2.2	MCF-7 cell viability screen .....	107
4.2.3	MDA-MB-231 cell viability screen.....	109
4.2.4	MCF-10A cell viability screen .....	110
4.3	GENERAL DISCUSSION AND CONCLUSION: CYTOTOXICITY STUDIES .....	111
4.4	CELL UPTAKE STUDIES .....	114
4.4.1	Cell internalisation studies: Transmission electron microscopy (TEM).....	114
4.4.2	Cell internalisation studies: Inductively coupled plasma-optical emission spectroscopy (ICP-OES) .....	123
4.5	GENERAL DISCUSSION AND CONCLUSION: CELL UPTAKE STUDIES .....	125
CHAPTER FIVE: CONCLUSIONS AND FUTURE WORK .....		127
5.1	CONCLUSIONS .....	127
5.2	FUTURE WORK.....	127
LIST OF REFERENCES .....		131



## LIST OF TABLES

<b>Table 1.1:</b>	Estimated incidences and mortality rates per 100 000 in Africa and Eastern Asia, 2012. ....	3
<b>Table 1.2:</b>	Commonly used diagnostic radionuclides .....	6
<b>Table 1.3:</b>	Diagnostic radionuclides used for imaging .....	6
<b>Table 1.4:</b>	Physical characteristics of single-photon radionuclides used in clinical nuclear medicine .....	7
<b>Table 1.5:</b>	Physical characteristics of positron-emitting radionuclide .....	7
<b>Table 1.6:</b>	The commonly used radionuclides.....	9
<b>Table 1.7:</b>	Palladium isotopes and radionuclides.....	11
<b>Table 1.8:</b>	The four breast cell lines employed for the cytotoxicity and cell uptake studies.....	34
<b>Table 2.1:</b>	List of chemicals or materials used and their suppliers .....	37
<b>Table 2.2:</b>	Inductively coupled plasma-optical emission spectrometer parameters.....	41
<b>Table 2.3:</b>	An illustration of the varied concentrations of reducing and capping agents used during the concentration ratios optimisation. For each experiment, two parameters were kept constant and one concentration varied until the desired nanoparticle sizes were achieved. X denotes a known concentration. ....	48
<b>Table 2.4:</b>	The size ranges of the synthesised palladium nanoparticles.....	49
<b>Table 2.5:</b>	The treatments used to investigate the cytotoxicity of the compounds used. The reported concentration for the palladium nanoparticles is 10 $\mu$ M palladium(II) content. ....	51
<b>Table 3.1:</b>	The obtained elemental compositions (%) for the purchased folate and synthesised conjugates; folate-ethylenediamine (FA-EDA) and folate-phthalocyanine (FA-Pc). ....	66
<b>Table 3.2:</b>	Summary of the particle diameters calculated using Scherrer's method for XRD spectra presented (Figure 3.19). The FWHM ( $\beta$ ) values were determined using SigmaPlot™. ....	76
<b>Table 3.3:</b>	The zeta potential (surface charge) of the differently capped optimised palladium nanoparticles in DMEM cell media at 25 °C and pH 7.4. ....	82
<b>Table 3.4:</b>	Summary of the TEM sizes and surface charges (in DMEM media) of the optimised palladium nanoparticles. ....	86

**Table 4.1:** The important abbreviations and colours for interpreting cytotoxicity results .....102

**Table 4.2:** The inductively coupled plasma-optical emission spectroscopy (ICP-OES) results obtained for the various treatments from the cell lysate (N=6).....123

## LIST OF FIGURES

<b>Figure 1.1:</b>	Ten leading cancer types for the estimated new cancer cases and deaths by sex, United States, 2018. Estimates are rounded to the nearest 10 and cases exclude basal cell and squamous cell skin cancers and <i>in situ</i> carcinoma except for urinary bladder. The ranking is based on modelled projections and may differ from the observed .....2	2
<b>Figure 1.2:</b>	An illustration of top-down and bottom-up synthesis approaches .....13	13
<b>Figure 1.3:</b>	Some of the different arrangements of spherical nanoparticles; (a) random structure, (b) fractal structure, (c) structural alignment, (d) close-packed structure, (e) ordered structure (dispersion), and (f) ordered structure (dense). .....15	15
<b>Figure 1.4:</b>	A summary of the key properties of nanoparticles in drug delivery systems and targeted therapy that affect nanoparticle' cellular uptake, clearance, toxicity, etc.....23	23
<b>Figure 1.5:</b>	(A) The structure of folic acid and methotrexate, (B) the crystal structure of the folate receptor bound to folic acid, and (C) methotrexate binding to folate receptor. ....25	25
<b>Figure 1.6:</b>	The crystal structure of the $\alpha$ -FR showing surface distribution of $\alpha$ -FR with a close-up view of the ligand binding pocket entrance. Folic acid carbon atoms are coloured grey, nitrogen atoms blue, and oxygen atoms red.....26	26
<b>Figure 1.7:</b>	Folate receptor-mediated folate uptake. Folate linked to intracellular or extracellular active agents bind to the folate receptor; the folate linked to intracellular drug is internalised, develops into endosomes, and is released into the cytoplasm while the endosome gets recycled. On the contrary, folate linked extracellular active agents activate cytotoxic function(s) outside the cell.....29	29
<b>Figure 1.8:</b>	Antifolates mechanism of action. The folate conjugates bind to the folate receptor, internalised <i>via</i> endocytosis, and the drug is cleaved and released exerting activity on cell while folate receptor is recycled back to the cell surface.....31	31
<b>Figure 1.9:</b>	Folate receptor expression among a wide variety of human tumours. Ovarian and non-small cell lung cancer (NSCLC) have the highest tumour folate receptor expression and breast tumours have positive folate receptor expression in most tumours. ....33	33

- Figure 3.1:** The UV-Vis spectra of the different phthalocyanines compounds; zinc tetranitrophthalocyanine (TNZnPc), tetraaminophthalocyanine (TAPc), and zinc tetranitrophthalocyanine (TAZnPc).....55
- Figure 3.2:** The FTIR spectra of the different phthalocyanine compounds; zinc tetranitrophthalocyanine (TNZnPc), tetraaminophthalocyanine (TAPc), and tetranitrophthalocyanine (TAZnPc).....57
- Figure 3.3:** The <sup>13</sup>C-NMR spectrum of the synthesised tetraaminophthalocyanine.....58
- Figure 3.4:** The UV-Vis spectra of folate (FA), folate-ethylenediamine (FA-EDA), folate-phthalocyanine (FA-Pc), and phthalocyanine (Pc).....59
- Figure 3.5:** The LC-MS of the folate-phthalocyanine.....60
- Figure 3.6:** The FTIR spectra of folate (FA), folate-phthalocyanine (FA-Pc), and phthalocyanine (Pc).....61
- Figure 3.7:** The <sup>1</sup>H-NMR of the N-Boc-ethylenediamine-folate conjugate. ....62
- Figure 3.8:** The <sup>1</sup>H-NMR of the folate-ethylenediamine .....63
- Figure 3.9:** The LC-MS of the folate-ethylenediamine. ....64
- Figure 3.10:** The FTIR spectra of folate (FA), folate-ethylenediamine (FA-EDA), and N-Boc-ethylenediamine-folate conjugate (FA-EDA-Boc). ....65
- Figure 3.11:** UV-Vis spectra of the different reducing agents investigated in the reduction of palladium(II) salt at room temperature, synthesised from the reaction of 100 μM palladium(II) with 500 μM reducing agent at room temperature.....68
- Figure 3.12:** The X-ray diffraction (XRD) spectra of the amorphous nanoparticles obtained from the reduction of 100 μM palladium(II) salt with 50 mM of; (a) citrate, (b) sodium metabisulfite, (c) pyrogallol, and (d) hydrazine at room temperature. ....69
- Figure 3.13:** The stability studies (UV-Vis spectra) of ethylenediamine-capped nanoparticles synthesised from the reduction of palladium(II) by; (a) 1 mM sodium borohydride, and (b) 5 mM formaldehyde, obtained from the reduction of 10 μM and 50 μM palladium(II) salt, respectively. ....70
- Figure 3.14:** Bright-field TEM images of amorphous precipitates obtained from the reduction of 100 μM palladium(II) with 100 μM sodium borohydride in the presence of 100 μM of; (a) 1,6-hexamethylenediamine, (b) 4,4' - ethylenedianiline, (c) 1,2-diphenyl-1,2-diaminoethane, and (d) 1,4-

- diaminobenzene as capping agents. The inset shows a SAED for a non-crystalline precipitate, similar to the SAED patterns for the other three images.....72
- Figure 3.15:** Bright-field TEM images of crystalline nanoparticles obtained from the reduction of 10  $\mu\text{M}$  palladium(II) with 2mM sodium borohydride capped with 800  $\mu\text{M}$ ; (a) ethylenediamine, (b) 1,10-diaminodecane, and (c) 1,12-diaminododecane.....72
- Figure 3.16:** An XRD spectrum of the ethylenediamine-capped palladium nanoparticles synthesised from the reduction of 100  $\mu\text{M}$  palladium(II) with 10 mM sodium borohydride in the presence of 100  $\mu\text{M}$  ethylenediamine.....73
- Figure 3.17:** The scanning transmission electron microscope-energy dispersive X-ray spectroscopy (STEM-EDS) spectrum of the ethylenediamine-capped palladium(0) nanoparticles formed from the reduction of 100  $\mu\text{M}$  palladium(II) with 10 mM sodium borohydride in the presence of 100  $\mu\text{M}$  ethylenediamine. The inset shows the analysed region of the agglomerated ethylenediamine-capped palladium nanoparticles. ....74
- Figure 3.18:** The SAED patterns for; (a) folate-phthalocyanine capped crystalline palladium nanoparticles, (b) JEMS simulated SAED for palladium crystal, and (c) annotated JEMS simulated SAED for palladium showing the (1 1 1), (2 0 0), (2 2 0), (3 1 1), and (2 2 2) rings .....75
- Figure 3.19:** The XRD spectra showing the reproducibility of large-sized palladium nanoparticles capped with; (a) phthalocyanine, (b) borohydride, (c) folate-phthalocyanine, and (d) folate-ethylenediamine synthesised from the reduction of 100  $\mu\text{M}$  palladium(II) salt with 1 mM sodium borohydride.....76
- Figure 3.20:** The selected area electron diffraction (SAED) patterns of the synthesised and characterised nanoparticles; (a) small-sized ethylenediamine capped (sz-ED $\hat{\text{A}}$ ), (b) medium-sized phthalocyanine capped (mz-P $\hat{\text{C}}$ ), (c) medium-sized folate-ethylenediamine capped (mz-FA-ED $\hat{\text{A}}$ ), and (d) small-sized folate-phthalocyanine capped (sz-FA-P $\hat{\text{C}}$ ) nanoparticles synthesised from the reduction of 10  $\mu\text{M}$  palladium(II) salt with sodium borohydride. ....77

- Figure 3.21:** Bright-field TEM images showing the different shapes obtained from the synthesis of the nanoparticles; (a) circular shaped, (b) tetrahedral and semi-regular shaped, (c) circular flower-like shaped, (d) square shaped nanoparticles, (e) elongate shaped nanoparticles, (f) regular square shaped nanoparticles, and (g) flower-like undefined nanoparticles. ....78
- Figure 3.22:** The visual presentation of the palladium solutions; a) 100  $\mu\text{M}$  palladium(II) solution, (b) ethylenediamine-capped palladium(0), (c) borohydride-capped palladium(0), (d) phthalocyanine-capped palladium(0), (e) folate-ethylenediamine capped palladium(0), and (f) folate-phthalocyanine capped palladium (0) nanoparticles. (b) to (e) were synthesised from the reduction of 100  $\mu\text{M}$  Pd(II) solution by 20 mM sodium borohydride.....79
- Figure 3.23:** The UV-Vis spectra of palladium nanoparticles after different synthetic times; (a) 3, 10, and 30 min), and (b) 1 hour, 1 day, and 1 week. ....79
- Figure 3.24:** The UV-Vis spectra of palladium(0) nanoparticles depicting the effects of temperature on the synthesis at different temperatures a) UV-Vis spectra for nanoparticles synthesised at room temperature, 40  $^{\circ}\text{C}$ , 50  $^{\circ}\text{C}$ , and 60  $^{\circ}\text{C}$  (b) 70  $^{\circ}\text{C}$ , 80  $^{\circ}\text{C}$ , and 90  $^{\circ}\text{C}$ .....80
- Figure 3.25:** An illustration of the zeta potential distribution of the palladium nanoparticles capped with: phthalocyanine (green), borohydride (red), and ethylenediamine (blue) synthesised from 100  $\mu\text{M}$  palladium(II), 2 mM reducing and capping agents concentrations.....81
- Figure 3.26:** The UV-Vis stability analysis of ethylenediamine capped nanoparticles formed from the reduction of palladium(II) salt by sodium borohydride after 3 minutes, 1 hour, 12 hours, and 24 hours in Leibovitz-L15 cell media (the spectra's trend was the same for DMEM and Hams F12). ....83
- Figure 3.27:** The hydrodynamic size distributions of differently capped palladium nanoparticles were measured using dynamic light scattering (DLS) in DMEM cell media for; (a) small-sized ethylenediamine-capped palladium nanoparticles (sz-ED $\hat{\text{A}}$ -NPs) synthesised from the reduction of 10.15  $\mu\text{M}$  palladium(II) salt with 2 mM sodium borohydride solution in the presence of 1 mM ethylenediamine, (b) medium-sized phthalocyanine capped palladium nanoparticles (mz-P $\hat{\text{C}}$ -NPs) synthesised from the reduction of 10.11  $\mu\text{M}$  palladium(II) salt with 800

$\mu\text{M}$  sodium borohydride solution in the presence of  $100 \mu\text{M}$  phthalocyanine, (c) medium-sized ethylenediamine capped palladium nanoparticles synthesised from the reduction of  $10.15 \mu\text{M}$  palladium(II) salt with  $800 \mu\text{M}$  sodium borohydride solution in the presence of  $200 \mu\text{M}$  ethylenediamine, (d) medium-sized folate-phthalocyanine capped palladium nanoparticles (mz-FA-P $\hat{\text{C}}$ -NPs) synthesised from the reduction of  $10.49 \mu\text{M}$  palladium(II) salt with  $800 \mu\text{M}$  sodium borohydride solution in the presence of  $200 \mu\text{M}$  folate-phthalocyanine, (e) large-sized ethylenediamine capped palladium nanoparticles (Iz-ED $\hat{\text{A}}$ -NPs) synthesised from the reduction of  $10.38 \mu\text{M}$  palladium(II) salt with  $800 \mu\text{M}$  sodium borohydride in the presence of  $1.7 \text{ mM}$  ethylenediamine. The DLS runs were done after 5 min (red), 10 min (green), and 15 min (blue) for (b), (d), and (e), and after 5 min only for (a), (c), and (e).....84

**Figure 3.28:** (a) Bright-field TEM image of monodispersed small-sized borohydride-capped palladium nanoparticles with an average diameter of  $2.1 \pm 0.5 \text{ nm}$ , synthesised from the reduction of  $10.65 \mu\text{M}$  palladium(II) salt with  $2 \text{ mM}$  sodium borohydride solution, (b) A plot of nanoparticle size (nm) against frequency (y-axis), highlighting a narrow size distribution. The inset presents a magnified (5X) view of small-sized borohydride-capped palladium nanoparticles. ....87

**Figure 3.29:** (a) Bright-field TEM image of monodispersed small-sized borohydride-capped palladium nanoparticles with an average diameter of  $1.6 \pm 0.4 \text{ nm}$ , synthesised from the reduction of  $10.04 \mu\text{M}$  palladium(II) salt with  $800 \mu\text{M}$  sodium borohydride solution, and (b) A plot of nanoparticle size (nm) against frequency (y-axis), highlighting a narrow size distribution. ....87

**Figure 3.30:** (a) Bright-field TEM image of medium-sized borohydride-capped palladium nanoparticles with an average diameter of  $30 \pm 10 \text{ nm}$ , synthesised from the reduction of  $10.65 \mu\text{M}$  palladium(II) salt with  $500 \mu\text{M}$  sodium borohydride solution, and (b) A plot of nanoparticle size (nm) against frequency (y-axis), highlighting a broad size distribution. The inset presents borohydride-capped palladium nanoparticles at magnified view (10X) of (a). ....88

- Figure 3.31:** Bright-field TEM images of agglomerated large-sized borohydride-capped palladium nanoparticles synthesised from; (a) the reduction of 10.65  $\mu\text{M}$  palladium(II) salt with 100  $\mu\text{M}$  sodium borohydride solution, (b) the reduction of 10.04  $\mu\text{M}$  palladium(II) with 100  $\mu\text{M}$  sodium borohydride solution. The inset presents a magnified (2X) agglomerate of (a). From the measurable nanoparticles, the size ranges were found to be  $371 \pm 72$  nm and  $308 \pm 61$  nm for (a) and (b), respectively.....88
- Figure 3.32:** (a) Bright-field TEM image of monodispersed small-sized ethylenediamine-capped palladium nanoparticles with an average diameter of  $2.5 \pm 0.4$  nm, synthesised from the reduction of 10.38  $\mu\text{M}$  palladium(II) salt with 2 mM sodium borohydride solution in the presence of 800  $\mu\text{M}$  ethylenediamine capping agent, and (b) A plot of nanoparticle size (nm) against frequency (y-axis), highlighting a narrow size distribution. The inset presents ethylenediamine-capped palladium nanoparticles of size  $2.6 \pm 0.2$  nm and its size distribution (bottom right), synthesised from similar concentrations as in (a).....89
- Figure 3.33:** (a) Bright-field TEM image of polydispersed small-sized ethylenediamine-capped palladium nanoparticles with an average diameter of  $1.4 \pm 0.4$  nm, synthesised from the reduction of 10.15  $\mu\text{M}$  palladium(II) salt with 2 mM sodium borohydride solution in the presence of 1 mM ethylenediamine capping agent, and (b) A plot of nanoparticle size (nm) against frequency (y-axis), highlighting a narrow size distribution. ....89
- Figure 3.34:** (a) Bright-field TEM image of polydispersed medium-sized ethylenediamine-capped palladium nanoparticles with an average diameter of  $22 \pm 6$  nm, synthesised from the reduction of 10.38  $\mu\text{M}$  palladium(II) salt with 800  $\mu\text{M}$  sodium borohydride solution in the presence of 200  $\mu\text{M}$  ethylenediamine capping agent, and (b) A plot of nanoparticle size (nm) against frequency (y-axis), highlighting a broad size distribution. The nanoparticle-like light grey particles were confirmed to be amorphous using SAED; only crystalline palladium nanoparticle size distribution is presented. ....90
- Figure 3.35:** (a) Bright-field TEM image of polydispersed medium-sized ethylenediamine-capped palladium nanoparticles with an average



- diameter of  $37 \pm 6$  nm, synthesised from the reduction of  $10.15 \mu\text{M}$  palladium(II) salt with  $800 \mu\text{M}$  sodium borohydride solution in the presence of  $200 \mu\text{M}$  ethylenediamine capping agent, and (b) A plot of nanoparticle size (nm) against frequency (y-axis), highlighting a broad size distribution. The nanoparticle-like light grey particles were confirmed to be amorphous using SAED; only crystalline palladium nanoparticle size distribution is presented .....90
- Figure 3.36:** Bright-field TEM images of agglomerated large-sized ethylenediamine-capped palladium nanoparticles synthesised from; (a) the reduction of  $10.38 \mu\text{M}$  palladium(II) salt with  $800 \mu\text{M}$  sodium borohydride solution in the presence of  $1.7 \text{ mM}$  ethylenediamine capping agent, and (b) the reduction of  $10.15 \mu\text{M}$  palladium(II) salt with  $800 \mu\text{M}$  sodium borohydride solution in the presence of  $1 \text{ mM}$  ethylenediamine capping agent. From the measurable nanoparticles found on the grids, the size ranges were  $95.19 \pm 20.85 \text{ nm}$  and  $204.37 \pm 50.60 \text{ nm}$ , respectively. ....91
- Figure 3.37:** (a) Bright-field TEM image of dispersed small-sized phthalocyanine-capped palladium nanoparticles with an average diameter of  $2.8 \pm 0.4 \text{ nm}$  synthesised from the reduction of  $10.32 \mu\text{M}$  palladium(II) salt with  $2 \text{ mM}$  sodium borohydride solution in the presence of  $1 \text{ mM}$  phthalocyanine capping agent, and (b) A plot of nanoparticle size (nm) against frequency (y-axis), highlighting a narrow size distribution. The inset presents a magnified view (5X) of the encircled area showing phthalocyanine-capped palladium nanoparticles. ....91
- Figure 3.38:** (a) Bright-field TEM image of monodispersed small-sized phthalocyanine-capped palladium nanoparticles with an average diameter of  $3 \pm 0.5 \text{ nm}$ , synthesised from the reduction of  $10.11 \mu\text{M}$  palladium(II) salt with  $2 \text{ mM}$  sodium borohydride solution in the presence of  $1 \text{ mM}$  phthalocyanine capping agent, and (b) A plot of nanoparticle size (nm) against frequency (y-axis), highlighting a narrow size distribution. ....92
- Figure 3.39:** (a) Bright-field TEM image of medium-sized phthalocyanine-capped palladium nanoparticles with an average diameter of  $16 \pm 2 \text{ nm}$ , synthesised from the reduction of  $10.11 \mu\text{M}$  palladium(II) salt with  $800 \mu\text{M}$  sodium borohydride solution in the presence of  $100 \mu\text{M}$

- phthalocyanine capping agent, and (b) A plot of nanoparticle size (nm) against frequency (y-axis), highlighting a slightly broad size distribution ....92
- Figure 3.40:** (a) Bright-field TEM image of dispersed medium-sized phthalocyanine-capped palladium nanoparticles with an average diameter of  $27 \pm 6$  nm, synthesised from the reduction of  $10.32 \mu\text{M}$  palladium(II) salt with  $800 \mu\text{M}$  sodium borohydride solution in the presence of  $200 \mu\text{M}$  phthalocyanine capping agent, and (b) A plot of nanoparticle size (nm) against frequency (y-axis), highlighting a broad size distribution. The nanoparticle-like light grey particles were confirmed to be amorphous using SAED; only crystalline palladium nanoparticle size distribution is presented.....93
- Figure 3.41:** Bright-field TEM images of agglomerated large-sized phthalocyanine-capped palladium nanoparticles synthesised from; (a) the reduction of  $10.38 \mu\text{M}$  palladium(II) salt with  $800 \mu\text{M}$  sodium borohydride solution in the presence of  $1 \text{ mM}$  phthalocyanine capping agent, and (b) the reduction of  $10.11 \mu\text{M}$  palladium(II) salt with  $800 \mu\text{M}$  sodium borohydride solution in the presence of  $500 \mu\text{M}$  phthalocyanine capping agent. The estimated sizes from the measurable nanoparticles were  $134 \pm 6 \text{ nm}$  and  $252.06 \pm 36 \text{ nm}$  for (a) and (b), respectively. ....93
- Figure 3.42:** (a) Bright-field TEM image of polydispersed small-sized folate-ethylenediamine capped palladium nanoparticles with an average diameter of  $2.1 \text{ nm} \pm 0.1 \text{ nm}$ , synthesised from the reduction of  $10.83 \mu\text{M}$  palladium(II) salt with  $2 \text{ mM}$  sodium borohydride solution in the presence of  $1 \text{ mM}$  folate-ethylenediamine, and (b) A plot of nanoparticle size (nm) against frequency (y-axis), highlighting a narrow size distribution. ....94
- Figure 3.43:** (a) Bright-field TEM image of polydispersed small-sized folate-ethylenediamine capped palladium nanoparticles with an average diameter of  $4.9 \pm 0.8 \text{ nm}$ , synthesised from the reduction of  $10.41 \mu\text{M}$  palladium(II) salt with  $2 \text{ mM}$  sodium borohydride solution in the presence of  $500 \mu\text{M}$  folate-ethylenediamine, and (b) A plot of nanoparticle size (nm) against frequency (y-axis), highlighting a narrow size distribution. The inset shows folate-ethylenediamine capped palladium nanoparticles with an average size of  $1 \pm 0.1 \text{ nm}$  synthesised

- from 10.41  $\mu\text{M}$  palladium salt with 1 mM sodium borohydride solution in the presence of 500  $\mu\text{M}$  folate-ethylenediamine. ....94
- Figure 3.44:** (a) Bright-field TEM image of dispersed medium-sized folate-ethylenediamine capped palladium nanoparticles with an average diameter of  $28 \pm 6$  nm, synthesised from the reduction of 10.83  $\mu\text{M}$  palladium(II) salt with 800  $\mu\text{M}$  sodium borohydride solution in the presence of 200  $\mu\text{M}$  folate-ethylenediamine, and (b) A plot of nanoparticle size (nm) against frequency (y-axis), highlighting a broad size distribution. The insets show magnified views (5X top, 2X bottom) of folate-ethylenediamine capped palladium nanoparticles clearly showing well defined shapes. ....95
- Figure 3.45:** (a) Bright-field TEM image of medium-sized folate-ethylenediamine capped palladium nanoparticles with an average diameter of  $21 \pm 3$  nm, synthesised from the reduction of 10.41  $\mu\text{M}$  palladium(II) salt with 800  $\mu\text{M}$  sodium borohydride solution in the presence of 200  $\mu\text{M}$  folate-ethylenediamine, and (b) A plot of nanoparticle size (nm) against frequency (y-axis), highlighting a broad size distribution. The inset presents a magnified view (2X) of (a) from the encircled region.....95
- Figure 3.46:** (a) Bright-field TEM image of large-sized folate-ethylenediamine capped palladium nanoparticles with an average diameter of  $650 \pm 164$  nm, synthesised from the reduction of 10.41  $\mu\text{M}$  palladium(II) salt with 800  $\mu\text{M}$  sodium borohydride solution in the presence of 20  $\mu\text{M}$  folate-ethylenediamine, and (b) A plot of nanoparticle size (nm) against frequency (y-axis), highlighting a broad size distribution. The inset shows partially agglomerated folate-ethylenediamine capped palladium nanoparticles. ....96
- Figure 3.47:** (a) Bright-field TEM image of large-sized folate-ethylenediamine capped palladium nanoparticles with an average diameter of  $150 \pm 30$  nm, synthesised from the reduction of 10.83  $\mu\text{M}$  palladium(II) salt with 800  $\mu\text{M}$  sodium borohydride solution in the presence of 50  $\mu\text{M}$  folate-ethylenediamine, and (b) A plot of nanoparticle size (nm) against frequency (y-axis), highlighting the palladium nanoparticles size distribution range. ....96

- Figure 3.48:** (a) Bright-field TEM image of monodispersed small-sized folate-phthalocyanine capped palladium nanoparticles with an average diameter of  $3.5 \pm 0.9$  nm, synthesised from the reduction of  $10.99 \mu\text{M}$  palladium(II) salt with 2 mM sodium borohydride solution in the presence of 1 mM folate-phthalocyanine, and (b) A plot of nanoparticle size (nm) against frequency (y-axis), highlighting a narrow size distribution. ....97
- Figure 3.49:** (a) Bright-field TEM image of polydisperse small-sized folate-phthalocyanine capped palladium nanoparticles with an average diameter of  $1.2 \pm 0.2$  nm, synthesised from the reduction of  $10.49 \mu\text{M}$  palladium(II) salt with 2 mM sodium borohydride solution in the presence of  $800 \mu\text{M}$  folate-phthalocyanine, and (b) A plot of nanoparticle size (nm) against frequency (y-axis), highlighting a narrow size distribution. ....97
- Figure 3.50:** (a) Bright-field TEM image of dispersed medium-sized folate-phthalocyanine capped palladium nanoparticles with an average diameter of  $16 \pm 3$  nm, synthesised from the reduction of  $10.49 \mu\text{M}$  palladium(II) salt with  $800 \mu\text{M}$  sodium borohydride solution in the presence of  $200 \mu\text{M}$  folate-phthalocyanine, and (b) A plot of nanoparticle size (nm) against frequency (y-axis), highlighting a broad size distribution. ....98
- Figure 3.51:** (a) Bright-field TEM image of medium-sized folate-phthalocyanine capped palladium nanoparticles with an average diameter of  $23 \pm 5$  nm, synthesised from the reduction of  $10.99 \mu\text{M}$  palladium(II) salt with  $800 \mu\text{M}$  sodium borohydride solution in the presence of  $200 \mu\text{M}$  folate-phthalocyanine, and (b) A plot of nanoparticle size (nm) against frequency (y-axis), highlighting a broad size distribution. The inset shows a magnified view (5X) of the folate-phthalocyanine capped palladium nanoparticles. ....98
- Figure 3.52:** (a) Bright-field TEM image of large-sized folate-phthalocyanine capped palladium nanoparticles with an average diameter of  $168 \pm 28$  nm, synthesised from the reduction of  $10.49 \mu\text{M}$  palladium(II) salt with  $800 \mu\text{M}$  sodium borohydride solution in the presence of 1 mM folate-phthalocyanine, and (b) A plot of nanoparticle size (nm) against

- frequency (y-axis), highlighting a broad size distribution. The inset shows well-defined monodispersed large-sized folate-phthalocyanine capped palladium nanoparticles. ....99
- Figure 3.53:** (a) Bright-field TEM image of dispersed large-sized folate-phthalocyanine capped palladium nanoparticles with an average diameter of  $190 \pm 29$  nm, synthesised from the reduction of  $10.99 \mu\text{M}$  palladium(II) salt with  $800 \mu\text{M}$  sodium borohydride solution in the presence of  $1 \text{ mM}$  folate-phthalocyanine, and (b) A plot of nanoparticle size (nm) against frequency (y-axis), highlighting a broad size distribution. The inset shows dispersed large-sized folate-phthalocyanine capped palladium nanoparticles. ....99
- Figure 4.1:** The MDA-MB-468 cell line's cytotoxic profiles for the different treatments;  $100 \mu\text{M}$  (palladium content) palladium nanoparticles,  $13.6 \text{ mM}$  folic acid (FA),  $13.2 \text{ mM}$  methotrexate (MTX),  $13.5 \text{ mM}$  ethylenediamine (EDA),  $13.6 \text{ mM}$  phthalocyanine (Pc),  $12.5 \text{ mM}$  folate-ethylenediamine (FA-EDA),  $12.9 \text{ mM}$  folate-phthalocyanine (FA-Pc), and untreated (UT) MDA-MB-468 cell line. The experiments were completed in triplicate ( $N=3$ ), and the significance was marked with asterisks \*; for a p-value  $<0.05$  (significant), \*\* for a p-value  $<0.01$  (significant), and \*\*\* for a p-value  $<0.001$  (highly significant) was determined using one-way analysis of variance (ANOVA) relative to the control (untreated cells). ....104
- Figure 4.2:** The MDA-MB-468 cell line's cytotoxic profiles for the different treatments;  $10 \mu\text{M}$  (palladium content) palladium nanoparticles,  $1.36 \text{ mM}$  folic acid (FA),  $1.32 \text{ mM}$  methotrexate (MTX),  $1.35 \text{ mM}$  ethylenediamine (EDA),  $1.36 \text{ mM}$  phthalocyanine (Pc),  $1.25 \text{ mM}$  folate-ethylenediamine (FA-EDA),  $1.29 \text{ mM}$  folate-phthalocyanine (FA-Pc), and untreated (UT) MDA-MB-468 cells. The experiments were completed in triplicate ( $N=3$ ), and the significance was marked with asterisks \*; for a p-value  $<0.05$  (significant), \*\* for a p-value  $<0.01$  (significant), and \*\*\* for a p-value  $<0.001$  (highly significant) was determined using one-way analysis of variance (ANOVA) relative to the control (untreated cells). ....106
- Figure 4.3:** The MCF-7 cell line's cytotoxic profiles for the different treatments;  $10 \mu\text{M}$  (palladium content) palladium nanoparticles,  $1.36 \text{ mM}$  folic acid

(FA), 1.32 mM methotrexate (MTX), 1.35 mM ethylenediamine (EDA), 1.36 mM phthalocyanine (Pc), 1.25 mM folate-ethylenediamine (FA-EDA), 1.29 mM folate-phthalocyanine (FA-Pc), and untreated (UT) MCF-7 cell line. The experiments were completed in triplicate (N=3), and the significance was marked with asterisks \*; for a p-value <0.05 (significant), \*\* for a p-value <0.01 (significant), and \*\*\* for a p-value <0.001 (highly significant) was determined using one-way analysis of variance (ANOVA) relative to the control (untreated cells).....108

**Figure 4.4:** The MDA-MB-231 cell line's cytotoxic profiles for the different treatments; 10  $\mu$ M (palladium content) palladium nanoparticles, 1.36 mM folic acid (FA), 1.32 mM methotrexate (MTX), 1.35 mM ethylenediamine (EDA), 1.36 mM phthalocyanine (Pc), 1.25 mM folate-ethylenediamine (FA-EDA), 1.29 mM folate-phthalocyanine (FA-Pc), and untreated (UT) MDA-MB-231 cell line. The experiments were completed in triplicate (N=3), and the significance was marked with asterisks \*; for a p-value <0.05 (significant), \*\* for a p-value <0.01 (significant), and \*\*\* for a p-value <0.001 (highly significant) was determined using one-way analysis of variance (ANOVA) relative to the control (untreated cells). .....109

**Figure 4.5:** The MCF-10A cell line's cytotoxic profiles for the different treatments; 10  $\mu$ M (palladium content) palladium nanoparticles, 1.36 mM folic acid (FA), 1.32 mM methotrexate (MTX), 1.35 mM ethylenediamine (EDA), 1.36 mM phthalocyanine (Pc), 1.25 mM folate-ethylenediamine (FA-EDA), 1.29 mM folate-phthalocyanine (FA-Pc), and untreated (UT) MCF-10A cell line. The experiments were completed in triplicate (N=3), and the significance was marked with asterisks \*; for a p-value <0.05 (significant), \*\* for a p-value <0.01 (significant), and \*\*\* for a p-value <0.001 (highly significant) was determined using one-way analysis of variance (ANOVA) relative to the control (untreated cells).....110

**Figure 4.6:** Bright-field transmission electron microscope (TEM) images of unstained MCF-10A cells after 24 h treatment with 10  $\mu$ M (palladium content) small-sized folate-ethylenediamine capped palladium(0) nanoparticles (sz-FA-Pc-NPs). Higher magnifications were used, from (a) to (d) to acquire the images, with the encircled regions indicating the

- area where the following image was acquired. The nanoparticles were clearly visualised with no cell ultrastructure.....115
- Figure 4.7:** The STEM-EDS spectrum of the nanoparticles on the unstained sample. Palladium presence was observed. The presence of carbon (C), nitrogen (N), and oxygen (O) can be attributed to the presence of folate-phthalocyanine or cellular organelles. The presence of potassium (K) and chlorine (Cl) can be attributed to incomplete washing of PBSA with the cobalt (Co) and iron (Fe) attributed to system artefacts from the TEM chamber, while the presence of copper is attributed to the use of a copper TEM grid. ....116
- Figure 4.8:** Bright-field TEM images of osmicated MCF-10A cells (from Figure 4.6) after 24 h treatment with small-sized folate-phthalocyanine capped palladium(0) nanoparticles (sz-FA-Pc-NPs); (a) TEM image showing a well-defined cell ultrastructure; intact cell membranes (CM), protruding cell membranes (encircled CM), mitochondrion (M), endoplasmic reticulum (ER), and possible metal stains, artefacts, or nanoparticles (encircled), (b) A magnified cellular area showing well-defined ultrastructure; nuclear membrane (NM), mitochondrion (M), cell membrane (CM), and unclear possible nanoparticles or metal stains or artefacts (encircled), (c) Clear ultrastructure of magnified specimen area showing intact cell membranes (CM) and possible nanoparticles or metal stains or artefacts (encircled), (d) TEM image displaying the visualised zoomed cytoplasm area with endoplasmic reticulum (ER), and (e) Inset showing a highly magnified section of the cells showing notable metal precipitate or artefacts (encircled). ....117
- Figure 4.9:** Bright-field TEM images of osmicated MDA-MB-231 cells after 24 h treatment with large-sized folate-ethylenediamine capped palladium(0) nanoparticles (lz-FA-EDc-NPs); (a) Visible cell membrane (CM), endoplasmic reticulum (ER), nuclear membrane (NM), and nucleus (N) and possible metal nanoparticles or stains (encircled), (b) Visible cell membrane (CM) and mitochondrion (M) with possible nanoparticle or osmium stains (encircled), (c) Zoomed ultrastructure showing mitochondria (M), and possible nanoparticles or osmium stains (encircled), (d) Ultrastructure showing endoplasmic reticulum (ER) and

- possible nanoparticles or osmium stains (encircled). The ultrastructure was seen, with no confirmed crystalline palladium nanoparticles. ....119
- Figure 4.10:** Bright-field TEM images of non-osmicated, lead citrate and uranyl acetate stained MCF-7 cells treated with medium-sized phthalocyanine capped palladium(0) nanoparticles (mz-Pc-NPs) for 24 h; (a) Cell membrane (CM) is visible and no clear ultrastructure (b) unclear ultrastructure showing possible nanoparticle, artefacts or metal stains (encircled) and cell membrane (CM).....120
- Figure 4.11:** Bright-field TEM images showing osmicated, lead citrate, and uranyl acetate stained MCF-7 untreated cells (no nanoparticle treatments); (a) Mitochondrion (M) is visible and artefacts are shown by arrows, (b) Cell membrane (CM), mitochondrion (M), and possible artefacts (A) are highlighted, (c) and (d) presents untreated MCF-7 cells showing possible artefacts or unidentifiable organelles. ....121
- Figure 4.12:** Bright-field TEM images of osmicated, lead citrate and uranyl acetate stained MCF-7 cells treated with 10  $\mu$ M large-sized folate-phthalocyanine capped palladium(0) nanoparticles (Iz-FA-Pc-NPs); (a) shows an MCF-7 with an unclearly defined ultrastructure and some dark spots (encircled), (b) a magnified area on the specimen showing possible nanoparticles (encircled) and the dark spot area (arrowed) that gave image (c), (c) a crystalline palladium nanoparticle, and (d) a magnification of the encircled area (on (c)). ....122



## LIST OF SCHEMES

<b>Scheme 1.1:</b>	The structure of folate showing the pteridine ring (red), 4-aminobenzoate (blue), and the glutamate (black).....	24
<b>Scheme 2.1:</b>	The protection and deprotection steps for the synthesis of folate-ethylenediamine.....	43
<b>Scheme 2.2:</b>	The synthesis of metal-free tetraaminophthalocyanine from 4-nitrothalonitrile. ....	44
<b>Scheme 2.3:</b>	The activation of folate for phthalocyanine or diamine conjugation .....	45
<b>Scheme 2.4:</b>	Conjugation of activated folate with TAPc.....	46
<b>Scheme 2.5:</b>	Activation of folate and its conjugation to diamines. ....	46
<b>Scheme 2.6:</b>	The $\gamma$ -isomers of the folate conjugates; (a) N-Hydroxysuccinimide (NHS) activated folic acid (NHS-FA), (b) tert-Butyloxycarbonyl-ethylenediamine protected folic acid (FA-EDA-Boc), (c) folate-ethylenediamine (FA-EDA), and (d) folate-phthalocyanine (FA-Pc).....	47
<b>Scheme 2.7:</b>	The reaction scheme of the formation of Pd(0) nanoparticles; (a) the reduction of palladium(II) chloride with sodium borohydride, and (b) the reduction of potassium tetrachloropalladate(II) with sodium borohydride.....	48
<b>Scheme 2.8:</b>	The amine-stabilised palladium nanoparticles; (a) borohydride-capped ( $\text{B}^{\text{H}}$ ), (b) tetraaminophthalocyanine-capped (TAP $\hat{\text{C}}$ ), (c) ethylenediamine-capped (ED $\hat{\text{A}}$ ), (c) folate-ethylenediamine capped (FA-ED $\hat{\text{A}}$ ), and (d) folate-phthalocyanine capped (FA-TAP $\hat{\text{C}}$ ) palladium(0) nanoparticles, where n is unknown. ....	49
<b>Scheme 3.1:</b>	The different reducing agents investigated in the optimisation of the required nanoparticle sizes. ....	67
<b>Scheme 3.2:</b>	The commercially available symmetrical diamines employed in the optimisation of nanoparticle sizes. ....	70
<b>Scheme 5.1:</b>	The proposed new thiol-amine stabilised palladium(0) nanoparticles; (a) 4-aminophenol-, (b) 2-aminoethanethiol- (cysteamine), and (a) polyethyleneimine (PEI)-capped nanoparticles. For simplicity, one capping agent unit is shown, however, m, n, and y are unknown.....	128

**LIST OF ABBREVIATIONS**

$^{13}\text{C}$ -NMR	carbon 13 nuclear magnetic resonance
$^1\text{H}$ -NMR	proton nuclear magnetic resonance
Ag	silver
At	astatine
Au	gold
B.C	before Christ
BF	bright-field
B $\hat{\text{H}}$ -NPs	borohydride capped nanoparticles
Bi	bismuth
Boc	di- <i>tert</i> -butyl dicarbonate
C	carbon
Cl	chlorine
Co	cobalt
Cond	conductivity
Cu	copper
D <sub>2</sub> O	deuterium oxide
D <sub>average</sub>	average particle size
DCC	<i>N,N'</i> -dicyclohexylcarbodiimide
DCM	dichloromethane
DLS	dynamic light scattering
DMEM	Dulbeco's Modified Eagle's Medium
DMSO	dimethylsulfoxide
DMSO-d <sub>6</sub>	deuterated dimethylsulfoxide
DNA	deoxyribonucleic acid

Dy	dysprosium
EDA	ethylenediamine
EDA	ethylenediamine
EDÂ-NPs	ethylenediamine capped nanoparticles
EDL	electric double layer
EDS	energy dispersive X-ray spectroscopy
EDTA	ethylenediaminetetraaceticacid
EPR	enhanced permeability and retention
Er	erbium
FA	folate/folic acid
FA-EDA	folate-ethylenediamine
FA-EDÂ-NPs	folate-ethylenediamine capped nanoparticles
FA-Pc	folate-phthalocyanine
FA-PĈ-NPs	folate-phthalocyanine capped nanoparticles
FBS	foetal bovine serum
Fcc	face-centred cubic
Fe	iron
FR	folate receptor
FTIR	Fourier transform infrared spectroscopy
FWHM	full width half maximum in radians
GBM	glomerular basement membrane
Ge	germanium
H	hydrogen
HCl	hydrochloric acid

Ho	holmium
HREM	high resolution electron microscopy
HRTEM	high resolution transmission electron microscopy
I	iodine
IP	intraperitoneal
IV	intravenous
JEMS	Java electron microscopy software
K	potassium
L-15	Leibovitz-15 Medium
Lu	lutetium
lz	large-sized
MDR	multidrug resistance
Mob	electrophoretic mobility
MPS	mononuclear phagocyte system
MTD	maximum tolerated dose
MTT	3-(4,5-dimethylthiazol-2-yl)-2,5-diphenyltetrazolium bromide
MTX	methotrexate
MW	molecular weight
mz	medium-sized
N	nitrogen
Na	sodium
NHS	N-hydroxysuccinimide
NP(s)	nanoparticle(s)
NRP(s)	nanoradiopharmaceuticals

P	phosphorous
Pb	lead
PBSA	phosphate buffered saline with EDTA
Pc	phthalocyanine (or tetraaminophthalocyanine)
PCFT	proton-coupled folate transporter
Pc-NPs	phthalocyanine capped nanoparticle(s)
Pd	palladium
PEG	poly(ethylene glycol)
PEI	polyethyleneimine
Pt	platinum
Pte	pteroyl group
PVP	poly(vinylpyrrolidone)
Re	rhenium
RES	reticuloendothelial system
RFC	reduced folate carrier
Rh	rhodium
ROS	reactive oxygen species
RP(s)	radiopharmaceutical(s)
rpm	revolutions per minute
rt	room temperature
SAED	selective area electron diffraction
Sc	scandium
Sm	samarium
Sn	tin

SPECT	single photon emission spectroscopy
Sr	strontium
sz	small-sized
TAPc	tetraaminophthalocyanine
Tc	technetium
TEM	transmission electron microscopy
TNPc	tetranitrophthalocyanine
UHV	ultra-high vacuum
UT	untreated cells
UV-Vis	ultraviolet-visible spectroscopy
WHO	World Health Organisation
XPS	X-ray photoelectron spectroscopy
XRD	X-ray diffraction spectroscopy
Y	yttrium
ZP	zeta potential

## LIST OF SYMBOLS

%	percentage
$\leq$	less than or equal to
$\geq$	greater than or equal to
$\mu$	micro
d	days(s)
e <sup>-</sup>	electron(s)
h	hour(s)
$\kappa$	Scherrer's constant
kDa	kiloDaltons
keV	kiloelectron volts
MeV	megaelectron volts
mg	milligram
min(s)	minute(s)
mL	millilitre
nm	nanometre ( $10^{-9}$ m)
nM	nanomolar
$t_{1/2}$	half-life
$\gamma$	year(s)
$\alpha$	alpha
$\beta$	beta
$\gamma$	gamma
$\delta$	delta
$\epsilon$	epsilon
$\mu$ M	micromolar

**v**            wavenumber



## CHAPTER 1: INTRODUCTION

### 1.1 CANCER

With more than ten million new diagnoses annually, cancer remains a major fatal disease worldwide. In many countries, more than 25% of deaths are due to cancer. According to a published report by the World Health Organization (WHO) and International Agency for Research on Cancer (IARC), cancer mortality rates are expected to have an increase of 50% by 2020. The high mortality rates highlight the challenges regarding cancer therapy and the need for ongoing work by researchers in drug delivery fields [1].

Cancer progression occurs when the normal mechanisms that regulate cell growth and proliferation are disturbed, for example, uncontrolled replication of deoxyribonucleic acid (DNA) [2]. A tumour develops from a single cell that undergoes a mutation that blocks its apoptotic signalling pathway resulting in uncontrollable proliferation [3]. A cancerous cell surrounded by healthy tissue will replicate at a faster rate than the other cells, thus placing a strain on the nutrient supply and elimination of metabolic waste products. Once a tumour mass has formed, the surrounding healthy tissues are unable to compete with the cancer cells for the nutrients supply from the bloodstream. This leads to the displacement of healthy cells until a tumour reaches a diffusion-limited maximal size [4, 5].

There are several types of cancers, most of them form solid tumours; however, some cancers like leukaemia (blood cancer) do not form tumours. Instead, leukaemia cells are present in the blood and blood-forming organs, circulating throughout the tissues. Not all tumours are cancerous; some tumours are benign (non-cancerous) and not life-threatening [6].

#### 1.1.1 History and statistics of cancer

The word cancer came from a Greek word *karkinos* to describe carcinoma tumours by a physician Hippocrates (460–370 Before Christ (B.C)). Some of the earliest evidence of human bone cancer was found in mummies in ancient Egypt and ancient manuscripts dating back to around 1600 B.C. The world's oldest recorded case of breast cancer hails from ancient Egypt in 1500 B.C, and it was recorded that there was no treatment for cancer, only palliative treatment. According to inscriptions, surface tumours were surgically removed similarly to how they are removed today [6].

In 2012, cancer was the second leading cause of death in the world after cardiovascular diseases. The WHO attributed 8.2 million deaths to cancer in 2012, constituting approximately 13% of all recorded deaths. Within the next two decades, new global cancer incidences are

expected to increase from 14 million in 2012 to as many as 22 million by 2032. Half of the men and one-third of women in the world develop cancer during their lifetimes. In 2016, 1 685 210 new cancer cases and 595 690 cancer deaths were recorded in the United States. This was the equivalent of more than 4 600 new cancer diagnoses per day and approximately 1,600 deaths per day [7]. In 2018, 1 735 350 new cases and about 609 640 cancer deaths were projected to occur in the United States (**Figure 1.1**). This corresponds to approximately 1 700 deaths per day [8]. This is approximately a 6% increase in deaths over two years.

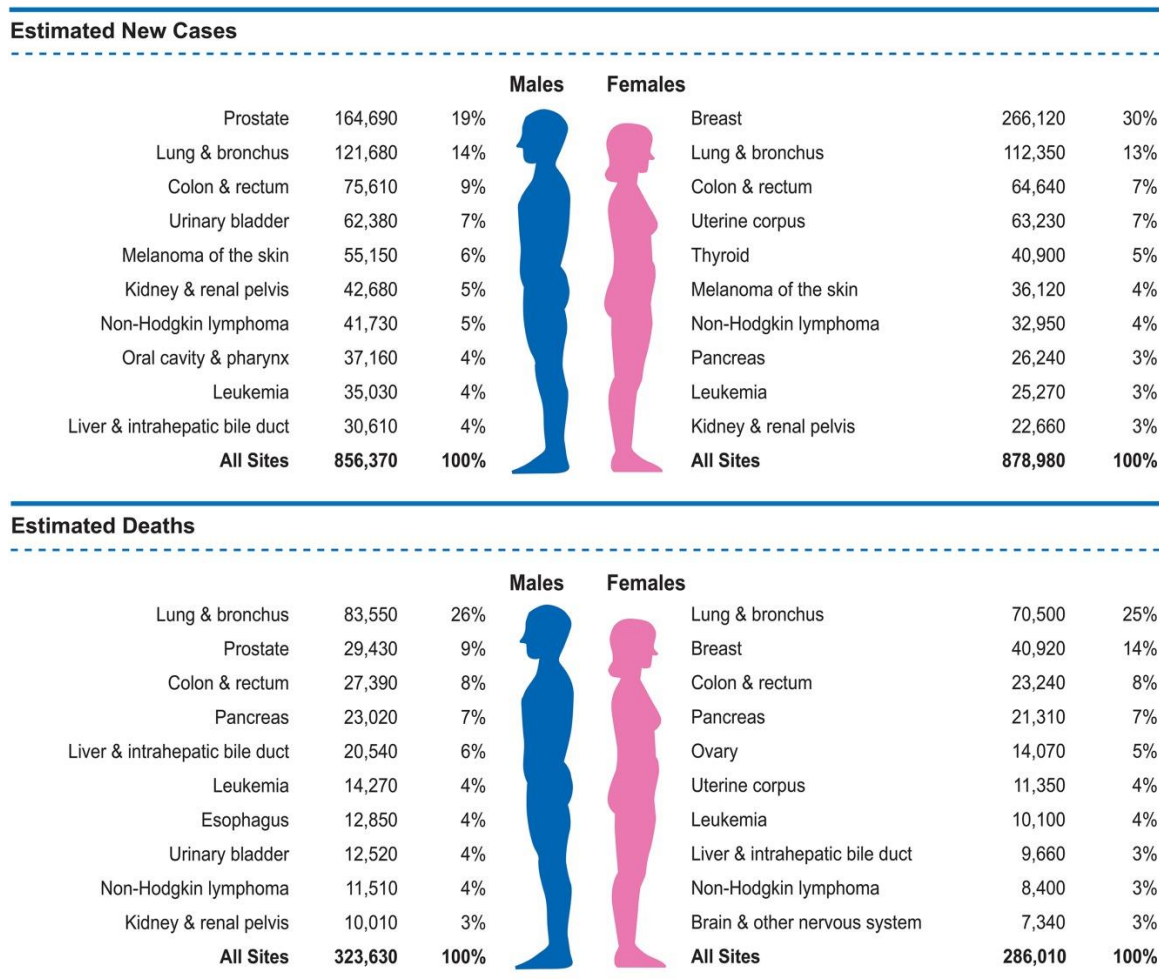


**Figure 1.1:** Ten leading cancer types for the estimated new cancer cases and deaths by sex, United States, 2018. Estimates are rounded to the nearest 10 and cases exclude basal cell and squamous cell skin cancers and *in situ* carcinoma except for urinary bladder. The ranking is based on modelled projections and may differ from the observed [8]. This image was reproduced from reference [8] with permission from Wiley Online (Copyright 2018).

Worldwide, millions of cancer patients extend their life expectancy due to early identification and treatment. The most common causes of deaths are lung, bronchial, prostate, colorectum,

and breast cancer [7]. In African countries, the lifetime probability of being diagnosed with an invasive cancer is higher for men than women (**Table 1.1**), with Southern Africa having the highest number of both cancer incidences and mortality cases [9]. The high mortality can be attributed to our inability to administer therapeutic agents selectively to the targeted sites without adverse effects on healthy tissue [10] and expensive therapeutic methods.

**Table 1.1:** Estimated age-standardised incidences and mortality rates per 100 000 in Africa and Eastern Asia by world area, 2012 and 2018 [11, 12].

Year	INCIDENCES				MORTALITY			
	Male		Female		Male		Female	
	2012	2018	2012	2018	2012	2018	2012	2018
Eastern Africa	120.7	112.4	154.7	150.7	103.8	87.0	110.5	107.6
Middle Africa	91.8	101.8	110.7	109.2	82.3	79.5	82.3	80.9
Northern Africa	133.5	138.9	127.7	137.3	99.9	102.1	75.7	76.9
Southern Africa	210.3	230.5	161.1	122.4	136.5	142.4	98.7	98.3
Western Africa	78.7	95.6	112.4	122.0	68.5	72.1	75.7	83.6
Eastern Asia	225.4	238.4	151.9	192.0	159.3	159.6	80.2	89.7
Totals	860.4	917.6	818.5	833.6	650.3	642.7	523.1	537

### 1.1.2 Cancer treatment methods

Cancer cells have non-uniform microvasculature in tumour tissues. The tumour blood vessels are highly disorganised with a high proportion of proliferating cells, increased tortuosity and relatively thin-walled, leaky, and less supporting pericytes. The pore sizes are between 100 and 780 nm, while normal cells have pore sizes less than 6 nm. The pore size difference can be exploited for selective cancer cell accumulation by nanoparticles [10]. In addition to that, there is a decreasing amount of oxygen available to peripheral tumour cells, this occurs due to the increased distance to the centralised blood vessels; thus, increasing the distance over which oxygen must diffuse to reach these cells. The oxygen availability is also decreased by the consumption of oxygen by tumour cells that have closer proximity to the blood vessels [10]. Tumours synthesise new blood vessels in a process known as angiogenesis; however, these vessels are abnormal and have an increased number of proliferating endothelial cells, increased vessel tortuosity, deficient pericytes, and abnormalities in the basement membrane with large gaps between adjacent endothelial cells ranging between 380 and 780 nm [13].

The current therapeutic strategies for most cancers involve a combination of surgical resection, radiation therapy, and chemotherapy [14]. These therapies are associated with significant morbidity and mortality rates, primarily due to their non-specific detrimental effects on normal cells. The tumour microenvironment provides unique challenges for the delivery of chemotherapeutic agents in doses that are effective while ensuring minimal systemic toxicity and reduced costs [15].

### **1.1.3 Challenges/Limitations of current therapeutic methods**

Once the tumour mass initiates angiogenesis, blood vessels proliferate resulting in an unorganised and abnormal vasculature [2]. Tumours contain regions with extensive vasculature and rich blood supply and regions with poor vasculature and little blood supply. The leaky vasculature in tumours is highly permeable due to the increased size and quantity of fenestrations as well as incomplete or abnormal basement membranes [16]. The variance in the level of the vasculature, and the tendency of the vessels to have poor smooth muscle or nerve innervation results in significantly heterogeneous blood flow through a tumour [17]. Tumour blood vessels are also inherently less vascular due to abnormal basement membranes and incomplete endothelial linings caused by the inability of pericytes to completely line the rapidly proliferating cells forming the vessel walls [13]. Tumours also have a reduced ability to drain fluid and waste from the interstitial space. The reduced drainage is due to a poorly-defined lymphatic system caused by the demand of the rapidly proliferating tumour cells [18].

Unlike healthy tissue which rapidly remove macromolecules and lipids from its interstitium, tumour cells accumulate these molecules. The highly permeable vasculature and poorly-defined lymphatic system result in the enhanced permeability and retention effect (EPR) [19]. The EPR has been the focus of much research, due to its ability to target macromolecules including nanoparticles, passively [20, 21]. The EPR is a unique feature, which allows macromolecules or drug delivery nanoparticles (cut-off size of >400 nm) to accumulate and diffuse in tumour tissues preferentially [13]. Drug delivery nanoparticles can extravasate into tumour tissues, accumulate, and release the therapeutic drug locally in the extracellular area [22].

The drug delivery specificity and non-selectivity between healthy and tumourigenic tissues lead to various side effects. Another detriment to systemic drug delivery is that the drug encounters numerous extra-and intracellular barriers before reaching the tumour site [23].

Moreover, the drug must retain its biological activity and reach the target site at high enough concentrations to have therapeutic efficacy. There is also a lack of drug accumulation in the centre of the tumour mass where the interstitial pressure is the highest [10]. In addition to that, the extracellular matrix possesses a physical barrier to chemotherapeutic drugs [24]. During cellular uptake of chemotherapeutic drugs *via* phagocytosis, the particles are shuttled from the early endosome to the late endosome and finally the lysosome for degradation. During which, the pH decreases from 7.4 to approximately 5.0, thus, the drug must maintain its activity through both decreased pH and rampant enzymatic activity [25].

Despite rapid advances in diagnostic procedures and treatments, the overall survival rate from cancer has not improved substantially over the past 30 years [26]. This is because of the EPR and multi-drug resistance (MDR) challenges [27]. Approximately 99% of chemotherapy drugs do not reach the cancer cells and hence the need to develop pharmaceuticals that are target specific [28]. There may also be drug resistance at the cellular tumour level due to physiological barriers, and the distribution, biotransformation, and clearance of anticancer drugs in the body is equally a major concern [22, 29, 30].

To address the challenges and limitations mentioned above, it is necessary to create effective cancer therapeutics that overcome biological barriers, ensure specific targeting, prevent rapid clearance and causes tumour deaths [31]. The development of nanoradiopharmaceutical cancer therapies has the potential to overcome both systemic and tumour barriers and provide specific, targeted delivery [32, 33]. There is a need, therefore, to develop novel approaches for the accurate detection of the early stage of cancer and for targeted therapies based on the cancer-specific markers, which could lead to personalised medicine [34, 35].

## 1.2 RADIOPHARMACEUTICALS

Radiopharmaceuticals portray physiological, biochemical, or pathological in the body without causing any detrimental effects [36]. They are referred to as *radiotracers* because they are given in sub-pharmacological doses that “trace” a physiological or pathological process in the body [37]. Most radiopharmaceuticals are a combination of a radioactive molecule that permits external detection and a biologically active molecule or drug that acts as a carrier and determines localisation and biodistribution [38].

### 1.2.1 Diagnostic radiopharmaceuticals

Radiopharmaceuticals are radiolabelled molecules designed for *in vivo* application. They consist of a molecular structure, which determines the fate of the radiopharmaceutical within

the organism (pharmacokinetics and pharmacodynamics) and a radionuclide being responsible for the signals detectability outside of the organism for subsequent visualisation with nuclear medical methods [39]. The half-life ( $t_{1/2}$ ) must be long enough to allow a radiochemist to carry out radiopharmaceutical synthesis (**Table 1.2**) and for nuclear medicine practitioners to collect useful images [26, 40].

**Table 1.2:** Commonly used diagnostic radionuclides [41].

Radionuclide	Half-life	Gamma energy (keV)	Decay mode	Source
$^{64}\text{Cu}$	12.3 h	511(10%), 185 (24%)	Electron capture	Reactor
$^{67}\text{Ga}$	78.3 h	93(10%), 185 (24%)	Electron capture	Generator
$^{99\text{m}}\text{Tc}$	6.02 h	141(89%)	Isomeric transition	Generator
$^{111}\text{In}$	2.83 d	171(88%), 247(94%)	Electron capture	Cyclotron
$^{117\text{m}}\text{Sn}$	14.0 d	159(87%)	Isomeric transition	Cyclotron

To allow for imaging (**Table 1.3**), the radionuclide should have  $\gamma$  energies in the range 100 - 510 keV and its half-life should be long enough for the preparation of the radiopharmaceutical and yet short enough to limit radiation exposure [42].

**Table 1.3:** Diagnostic radionuclides used for imaging [43].

Radioisotope	Half-life in hours	Image uses
$^{99\text{m}}\text{Tc}$	6,0	Bone, thyroid, brain, and kidneys
$^{201}\text{Tl}$	73,0	Heart
$^{123}\text{I}$	13,3	Thyroid
$^{67}\text{Ga}$	78,2	Various tumours
$^{18}\text{F}$	1,8	Brain

### 1.2.2 Therapeutic radiopharmaceuticals

Several  $\beta$ -emitting radionuclides ( $^{64}\text{Cu}$ ,  $^{89}\text{Sr}$ ,  $^{90}\text{Y}$ ,  $^{109}\text{Pd}$ ,  $^{153}\text{Sm}$ ,  $^{165}\text{Dy}$ ,  $^{166}\text{Ho}$ ,  $^{169}\text{Er}$ ,  $^{177}\text{Lu}$ ,  $^{186}\text{Re}$ , and  $^{198}\text{Au}$ ) have been proposed for radionuclide therapy [44] for bone pain palliation, tumour therapy, and radiation synovectomy. Some single-photon radionuclides have been used in clinical medicine (**Table 1.4**), and so as positron-emitting radionuclides (**Table 1.5**).

**Table 1.4:** Physical characteristics of single-photon radionuclides used in clinical nuclear medicine [45].

Radionuclide	Principal mode of decay	Physical half-life	Principal photon energy in keV (abundance %)	Production method
<sup>99</sup> Mo	Beta minus	2.8 d	740 (12), 780 (4)	Reactor
<sup>99m</sup> Tc	Isomeric transition	6 h	140 (89)	Generator <sup>99</sup> Mo
<sup>131</sup> I	Beta minus	8 d	364 (81)	Reactor
<sup>123</sup> I	Electron capture	13.2 h	159 (83)	Cyclotron
<sup>67</sup> Ga	Electron capture	78.3 h	93 (37), 185 (20), 300 (17), 395 (5)	Cyclotron
<sup>201</sup> Tl	Electron capture	73.1 h	69-83 (Hg x-rays), 135 (2.5), 167 (10)	Cyclotron
<sup>111</sup> In	Electron capture	2.8 d	171 (90), 245 (94)	Cyclotron
<sup>127</sup> Xe	Electron capture	36 d	172 (26), 203 (7), 375 (17)	Cyclotron
<sup>133</sup> Xe	Beta minus	5.2 d	81 (37)	Reactor
<sup>57</sup> Co	Electron capture	272 d	122 (86)	Cyclotron

**Table 1.5:** Physical characteristics of positron-emitting radionuclide [46].

Radionuclide	Physical half-life (min)	Positron energy (MeV)	Range in soft tissues (mm)	Production Method
<sup>11</sup> C	20	0.96	4.1	Cyclotron
<sup>13</sup> N	10	1.19	5.4	Cyclotron
<sup>15</sup> O	2	1.73	7.3	Cyclotron
<sup>18</sup> F	110	0.635	2.4	Cyclotron
<sup>68</sup> Ga	68	1.9	8.1	Generator <sup>68</sup> Ge
<sup>82</sup> Rb	1.3	3.15	15.0	Generator <sup>82</sup> Sr

### 1.2.3 Design and development of theranostic radiopharmaceuticals

Radiopharmaceuticals require unique properties that need to be considered, such as half-life, radiation energy, and tissue penetration that are associated with the onset of response, duration, and toxicity [47, 48].

Essential factors in developing therapeutic radiopharmaceuticals include the selection choice of the radionuclide, local production conditions, and carrier molecule biokinetics [17, 49]. For therapeutic purposes, the selection of a suitable radioisotope should consider not only the physical characteristics (type of energy, tissue penetration range, and half-life), however, specificity of localisation and pharmacokinetics [50, 51].

#### 1.2.4 Radionuclides

A radionuclide is an atom that has excess energy, that can be emitted from the nucleus as gamma radiation or as a “new” alpha or beta particle during a radioactive decay process [52]. The preferred isotopes are the  $\gamma$ -emitters for imaging as  $\gamma$ -radiation is less damaging to the body compared to  $\alpha$  or  $\beta$  radiation [53]. Good therapeutic results would be obtained if the half-life of the radionuclide was not shorter than 12 h and not longer than 5 days for successful radiolabelling, and the period of the imaging procedure [54]. The emission energies should be significantly high enough to deliver a radiation dose [40]. In the case of radioimmunotherapy, where a limited number of binding sites are available, carrier-free radionuclides are ideal to achieve high binding affinities to the receptors [51]. Radionuclide decay should result in gamma emissions with sufficient energy for external detection. The radionuclide can contain particulate radiation (e.g., beta emissions), which increases patient radiation dose (**Table 1.6**). Beta emissions are also suitable for therapeutic radiopharmaceuticals [55]. The effective half-life should be long enough for only the intended application. Radionuclides that decay by  $\beta$ -particle emission are the most extensively used [41].

The radionuclide should be carrier-free, i.e. not contaminated by either stable radionuclides or other radionuclides of the same element [56]. Carrier material can negatively influence biodistribution and labelling efficiency. A carrier-free radionuclide has the highest specific activity [57, 58]. The pharmaceutical component should be free of any toxicity or physiological effects. The radiopharmaceutical should not disassociate *in vitro* or *in vivo* and should be readily available or easily compounded [54]. The radiopharmaceutical should rapidly and specifically localise according to the intended application, and a rapid background clearance is essential to ensure a good target-to-background ratio [26, 45]. Radiopharmaceutical should be inexpensive, relatively pure, can be produced in industrial quantities, appropriate physical properties, and be easily bound to a ligand [59]. The availability of the radionuclide, good physical characteristics of the radionuclide, radiochemical and radiopharmacological properties are of paramount importance for an excellent radionuclide [60]. The use of several



radionuclides has been documented; however, for this study, the radionuclide of interest was palladium.

**Table 1.6:** The commonly used radionuclides.

Radionuclide	Decay mode	Half-life	$E_{\text{max}}\alpha/\beta$ (MeV)	$E_{\text{max}}\gamma$ (keV)
$^{212}\text{Bi}$	$\alpha$	60.5 min	7.8	
$^{213}\text{Bi}$	$\alpha$	45.6 min	5.8	
	$\beta$		1.4	
$^{212}\text{Pb}$	$\alpha$	10.64 h	0.28 (83%) 0.57 (12%)	
$^{99\text{m}}\text{Tc}$	$\gamma$	6 h		141
$^{211}\text{At}$	$\alpha$	7.2 h	6.76	
$^{186}\text{Re}$	$\beta$	3.7 d	1.07	137
$^{188}\text{Re}$	$\beta$	17 h	2.11	155
$^{166}\text{Ho}$	$\beta$	1.1 d	1.6	81
$^{153}\text{Sm}$	$\beta$	1.95 d	0.8	103
$^{109}\text{Pd}$	$\beta$	13 h	1.10	
$^{131}\text{I}$	$\beta$	8 d	0.81	364 (81%) 637 (7%)
$^{125}\text{I}$	Low energy $e^-$	60 d		
$^{123}\text{I}$	Low energy $e^-$	13.3 h		
$^{32}\text{P}$	$\beta$	14.3 d	1.71	
$^{47}\text{Sc}$	$\beta$	3.4 d	0.6	
$^{64}\text{Cu}$	$\beta$	0.5 d	0.57	
$^{67}\text{Cu}$	$\beta$	2.6 d	0.57	
$^{89}\text{Sr}$	$\beta$	50.5 d	1.46	
$^{90}\text{Y}$	$\beta$	2.7 d	2.27	
$^{105}\text{Rh}$	$\beta$	1.5 d	0.57	
$^{111}\text{Ag}$	$\beta$	7.5 d	1.05	
$^{117\text{m}}\text{Sn}$	$\beta$	13.6 d	0.13	

The table above was constructed from the data collected from multiple references [42, 44, 62].

### 1.2.5 Palladium as a radiopharmaceutical

Current major classes of metal-based anticancer drugs include platinum(II), platinum(IV), palladium(II), gold(I) and gold(III), ruthenium(II) and ruthenium(III), and tin(IV) complexes [61]. An attempt to use Pd(II) complexes as chemotherapeutic anti-cancer agents towards cisplatin-resistant cells has been discouraged by the high lability and fast hydrolysis reactions presented by the Pd(II) complexes compared to platinum(II) complexes [61]. Moreover, multidrug resistance (MDR), specificity, efficiency, biotransformation, and clearance of drugs in the body (**Section 1.1.3**) remain problematic for metal complexes anti-cancer agents [13, 15, 61]. To circumvent these challenges, nanomedicine (**Section 1.4**) provide solutions; tissue and cell distribution profiles of anti-cancer drugs can be controlled while increasing anti-tumour efficacy and reducing systemic side effects through use of nanoparticles (**Section 1.3**) [24, 59]. A gap exists in the biomedical applications of palladium(0) nanoparticles in targeted therapy and nanoradiopharmaceuticals, highlighting its prospects in the development of palladium-based nanoradiopharmaceuticals.

#### 1.2.5.1 Palladium's key properties

Palladium, (atomic number 46), was discovered in 1803 by William Wollaston during his studies on the refining of platinum. It was named after a newly discovered asteroid, Pallas, which bears the name of the Greek goddess of wisdom. Palladium (Pd) occurs in association with other platinum group metals (PGMs), and the extraction processes depend on the ore used. It is the second most abundant platinum group metal and its primary sources are in South Africa and Russia [63]. Palladium belongs to the periodic table's group 10 and has the ground-state electronic configuration: [Kr] 4d<sup>10</sup>. Pd chemistry is dominated by the oxidation state +II (the most stable for the element) and exhibits rich organometallic chemistry [64].

Palladium exhibits similar chemistry to its 5d analogue, platinum (Pt); however, palladium is more reactive in comparison to platinum. It exhibits the oxidations states 0, +I, +II, and +IV. Many of the metal complexes in the 0 and I oxidation states form metal-metal bonded clusters [65] while the +II oxidation state forms a variety of monomeric complexes [66]. Palladium(0) has a face-centred cubic (fcc) lattice structure (Fm3m space group) with a lattice constant 3.89 nm [67, 68]. Palladium nanoparticles may be amorphous [69–71] or crystalline [72–74]. When viewed in a transmission electron microscope at high resolution, the crystalline palladium nanoparticles may exhibit lattice fringes unique to palladium [75].

Palladium is used in catalysis, electronics, technology, dentistry, jewellery, and photography [76]. Palladium is stable at room temperature, has low toxicity, is poorly absorbed by the human body when ingested and has limited toxicological effects [77–79], highlighting its possibility for use in pharmaceutical-related research.

### 1.2.5.2 Palladium isotopes, radionuclides, and their properties

Palladium has six naturally occurring isotopes have been found for palladium:  $^{102}\text{Pd}$  (1.02%),  $^{104}\text{Pd}$  (11.14%),  $^{105}\text{Pd}$  (22.33%),  $^{106}\text{Pd}$  (27.33%),  $^{108}\text{Pd}$  (26.46%), and  $^{110}\text{Pd}$  (11.72%) [80], and ten common radioisotopes and stable isotopes (**Table 1.7**). The radioisotope of interest is  $^{109}\text{Pd}$ , with a half-life of 13 hours which undergoes a  $\beta$  decay [81].

**Table 1.7:** Palladium isotopes and radionuclides.

Isotope	Abundance	Half-life( $t_{1/2}$ )	Decay mode	Product
$^{100}\text{Pd}$	Synthetic radionuclide	3.63 d	$\epsilon$	$^{100}\text{Rh}$
			$\gamma$	–
$^{102}\text{Pd}$	1.02%	stable		
$^{103}\text{Pd}$	Synthetic radionuclide	16.991 d	$\epsilon$	$^{103}\text{Rh}$
$^{104}\text{Pd}$	11.14%	stable		
$^{105}\text{Pd}$	22.33%	stable		
$^{106}\text{Pd}$	27.33%	stable		
$^{107}\text{Pd}$	Trace radionuclide	$6.5 \times 10^6$ y	$\beta^-$	$^{107}\text{Ag}$
$^{108}\text{Pd}$	26.46%	stable		
$^{109}\text{Pd}$	None	13 h	$\beta$	$^{109}\text{Ag}$
$^{110}\text{Pd}$	11.72%	stable		

The above table was constructed from information from references [42, 81].

## 1.3 NANOPARTICLES

Nanoparticles (NPs) are classified as particles with one dimension within the 1–100 nm size range and behave as a single unit with respect to transport and reactivity [82]. It has been demonstrated that NPs have a wide variety of unique applications, including cell targeting, intravenous nucleic acid delivery, environmental remediation, catalysis, bactericidal effects, etc. [83].

The nanoparticle's nanoscopic size facilitates intracellular uptake. NPs can encapsulate therapeutic drugs and release them in a controlled manner to specifically target diseased cells [84]. Additional advantages of NPs have brought widespread attention to the field of nanomedicine, including their large ratio of volume-to-surface area, modifiable external shell, biodegradability, and low cytotoxicity [30]. Metal nanomaterials have been found to have numerous applications such as in electronics, optics, magnetic devices as well as in catalysis. As the physical and chemical properties depend on the size and shape of the nanoparticles; their applications require non-agglomerated, uniform particles with a controlled mean size, narrow size distribution, and large surface-to-volume ratios [85].

The unique properties of nanoparticles allow the encapsulation of variety of drugs, whereas the tuneable surface chemistry is advantageous over their bulky counterparts [86]. Nanoparticles can be synthesised, assembled into desirable geometries and configurations, and coated with targeting agents and provide novel material properties for various applications in molecular and cellular labelling, tracking, detection, drug delivery, and medical imaging highlighting high levels of sensitivity and functionality [87]. To fully realise the promise they hold, nanoparticles must be capable of reaching their biological targets with high efficiency and specificity. In particular, delivery and targeting at the subcellular level have recently become increasingly important as we strive to decipher complex events that occur within living cells [88].

### 1.3.1 Synthesis of nanoparticles

Physical, chemical, or electrochemical methods have been used to prepare uniform nanoparticles. Chemical methods include reduction of metal salts in solution-phase, microemulsion, or sol-gel process have been employed to obtain well-defined mono- and bi-metallic particles [89–91].

Nanomaterials, including nanoparticles, can be constructed by the moulding or etching, top-down approach, or by assembling structures atom by atom or molecule by molecule, bottom-up approach [92].

#### 1.3.1.1 Top-down and bottom-up approach

Top-down technologies utilise mechanical forces to break down macroscopic particles to nanoscale size. Bottom-up technologies build-up nanoscale particles from molecular or atomic bond (**Figure 1.2**).

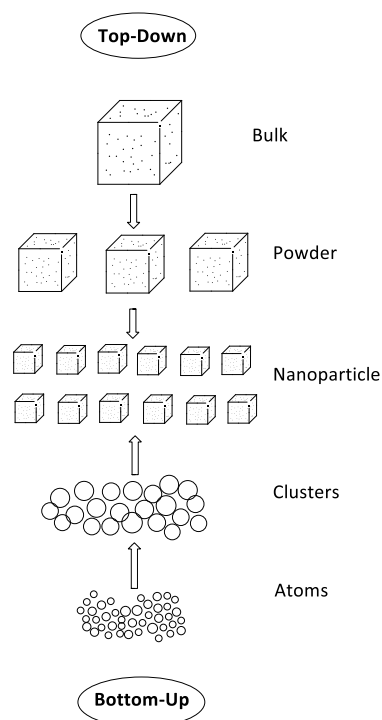


**Figure 1.2:** An illustration of top-down and bottom-up synthesis approaches [92].

### 1.3.2 Important nanoparticle properties in drug development

The key parameters or characteristics include particle size, size dispersity, structure, surface characteristic, crystallinity, composition, and dissolution [93]. The nanoparticle ability to penetrate biological membranes, allowing accessibility to remote tissues and increased residence time in the body offers a more diverse portfolio of treatment options and improve the efficacy through both local and systemic targeting [9, 18, 94, 95].

#### 1.3.2.1 Particle size and dispersity

The size of nanoparticle governs its interactions with biological systems, including absorption, distribution, cellular internalisation, metabolism, and excretion [96]. Furthermore, nanoparticle size allows for interactions with various biomolecules on the cell membrane surfaces and within the cells, that do not necessarily alter the behaviour and biochemical properties of those molecules [93].

Nanoparticles with a diameter between 30 nm and 50 nm are more efficiently internalised by cells with greater efficiency than smaller (less than 30 nm) or larger (about 70 to 240 nm) particles. Nanoparticles with a diameter of 30 to 50 nm efficiently recruit and interact with membrane receptors and are subsequently taken up by receptor-mediated endocytosis [97]. The largest particle size of harnessing the EPR effect is 400 nm [98]. Particles with diameters

less than 200 nm will be cleared faster than particles with diameters over 200 nm. Varying particle sizes from 50 to 500 nm showed higher levels of agglomeration for the nanoparticles in the liver [22]. Therefore, to be an effective drug carrier, the nanoparticle should have a diameter between 10 and 150 nm [99, 100]. This size range will ensure longer circulation time and increased accumulation in the tumour interstitial [101, 102]. Cancer vascular pores range from 300-700 nm, therefore, the nanoparticles should be less than 250 nm for maximum efficacy [103]. Nanoparticles between 150 and 250 nm are also internalised by cells [99], [104].

### 1.3.2.2 Surface charge

The surface of a particle is the primary medium by which it interacts with its environment. The uptake and translocation of nanoparticles by organisms are affected by the nanoparticle surface charge [101]. For example, the nanoparticle surface charge has been documented to alter blood-brain barrier integrity and permeability [96]. Surface charge is responsible for a range of biological effects of NPs including cellular uptake, toxicity, and dissolution [105]. In one study, neutral and zwitterionic nanoparticles demonstrated longer circulation time *via* both intraperitoneal (IP) and intravenous (IV) administration, whereas negatively and positively charged nanoparticles possessed relatively short half-lives. Neutral and zwitterionic-charged nanoparticles are preferentially internalised *via* passive targeting [106]. Positively charged particles interact strongly with the slightly anionic plasma membrane [107]. They are taken up more readily or may disrupt plasma membrane integrity. Positively charged NPs are taken up *via* adsorptive mediated pinocytosis, whereas negatively charged NPs use alternative uptake routes, and are taken up *via* receptor-mediated or facilitated processes [108, 109]. Non-ionic particles tend not to interact with the cell membrane [97]. Positively charged nanoparticle surfaces enhance endocytosis [110]. pH affects net charge, and nanoparticles' surface charge at cellular pH range is critical [111, 112].

The modification of the nanoparticles surface by the addition of hydrophilic polymers results in decreased clearance by the mononuclear phagocyte system (MPS) or reticuloendothelial system (RES). A hydrophilic polymer, poly(ethylene glycol) (PEG), imparts stealth characteristics by shielding the nanoparticles from opsonin adsorption and subsequent clearance by the MPS/RES once attached to nanoparticle surface [22].

### 1.3.2.3 Shape/morphology and organisation

Elongated or filamentous nanoparticles have been shown to have distinct advantages over spherical particles regarding surface area-to-volume ratio, the rate of clearance from the body, and elimination mechanism [102, 113]. Cylindrical nanoparticles (NPs) have the highest percentage of cellular internalisation [22]. Spherical NPs (**Figure 1.3**) are efficiently taken up at a higher rate than rod-shaped NPs, presumably due to the longer membrane wrapping time required for the longer rod-shaped particles [97].

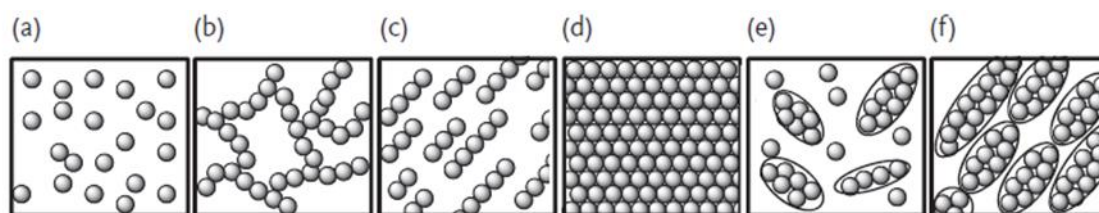


**Figure 1.3:** Some of the different arrangements of spherical nanoparticles; (a) random structure, (b) fractal structure, (c) structural alignment, (d) close-packed structure, (e) ordered structure (dispersion), and (f) ordered structure (dense). This image was reproduced from reference [114] with permission from Wiley Online (Copyright 2018).

The effects of particle shape and curvature on cellular internalisation showed that 14 and 75 nm spherical nanoparticles were up-taken by cells 3.75 to 5 times more than 14 by 74 nm rod-shaped particles, leading to the hypothesis that the significant difference in uptake could be due to the difference in particle curvature, affecting the contact area with the cell membrane receptors as well as the distribution of targeting ligands on the particles [115–117].

### 1.3.2.4 Chemical composition/hydrophobicity

Nanoparticles are usually taken up by the liver, spleen, and other parts of the reticuloendothelial system depending on the surface composition and hydrophobicity [101]. For instance, particles with more hydrophobic surfaces would preferentially be taken up by the liver, followed by the spleen, and lungs. Whereas, hydrophilic nanoparticles (35 nm diameter), such as those prepared from poly(vinylpyrrolidone) (PVP), showed less than 1% initial uptake by the spleen and liver and 8 h after injection showed 5 to 10% still circulating in the bloodstream [95].

Longer circulation time increases the nanoparticle ability to target deeper lying site of interests easily, and should be 100 nm or less in diameter and have a hydrophilic surface to

reduce clearance by macrophages [118]. Hydrophilic polymer coatings create particle surfaces that repel plasma proteins and adsorb surfactants thereby achieving easy targeting by avoiding RES [119].

The chain length of the PEG spacer between the ligand and the nanoparticle surface also requires consideration [120]. When the chain length of the PEG spacer is longer than the other PEG chains involved in the PEG-brush, the conjugated ligand can become buried within the brush layer. The extra units of a longer PEG spacer are subject to mushroom-like folding, which results in the limited exposure of the ligand [98].

#### **1.3.2.5 Impurity and crystallinity**

The nanoparticles purity is vital for proper analysis, characterisation, and understanding of the outcome of the study. Purification of nanoparticles is performed during synthesis, mainly through centrifugation of the newly synthesised nanoparticles [121]. Preferred metal nanoparticles must be crystalline, and their crystallinity can be investigated using X-ray diffraction spectroscopy (XRD), or transmission electron microscope-selective-area electron diffraction spectroscopy (TEM-SAED analysis) [71].

#### **1.3.2.6 Stability**

Their tuneable size, shape, and surface characteristics enable nanoparticles to have a higher stability, higher carrier capacity, the ability to incorporate both hydrophilic and hydrophobic substances and compatibility with different administration routes, thereby making them highly attractive in many aspects of oncology [27]. The nanoparticles stability during synthesis and *in vitro* or *in vivo* stability is key for proper drug development and must be reported for all studies [122]. Nanoparticles can be formulated to exhibit stability, in both shelf storage life, uptake rates, and specificity within the body, and response by the body to treatment [123, 124].

#### **1.3.2.7 Toxicity**

Nanoparticles should not cause adverse health side effects [125]. Nanoparticles should be non-toxic to the cells, biodegradable, pure and non-immunogenic [126–128]. The nanotoxicology of NPs should be minimum for the successful design and development of radiopharmaceuticals [96].



### 1.3.2.8 Stealth, specificity, and biodegradability

The nanoparticle-drug complex must remain stable in the serum to allow the systemic delivery of the drug. The nanoparticle-drug complex must be delivered to tumour cells (either by receptor-mediated interactions or *via* the EPR effect), thereby reducing any unwanted complications from nontargeted delivery [22, 129]. The nanoparticle must be able to release the drug once at the site of the tumour. Nanoparticles that are used as carriers will either bind to the drug surface or entrap and encapsulate the drug to protect it from degradation or denaturation [130]. The residual nanoparticle carrier should ideally be made of a biological or biologically inert material with a limited lifespan to allow safe degradation [131, 132]. Alternatively, if a nonbiodegradable material is used, it must have proven to be safe at the doses needed or be easily cleared from the subject.

### 1.3.2.9 Reproducibility

Batch to batch reproducibility in nanoparticle synthesis is vital for the development of radiopharmaceuticals. The successful reproducibility of *in vitro* studies paves way for the *in vivo* studies, and subsequent preclinical trials upon the success of *in vivo* studies. This needs to be investigated and reported.

## 1.3.3 Functionalisation of nanoparticles

Functionalisation of nanoparticles to create a stealth surface from opsonisation is necessary to increase circulation times through removal avoidance by the reticuloendothelial systems (RES). Short circulation times, decrease the efficiency of the delivery of the nanoparticle to the tumour site [110]. Blood circulation residence, maximal tolerated dose (MTD), specificity, and selectivity are the principal factors for achieving a high therapeutical index and corresponding clinical success [22].

The surface functionalisation can be designed to provide either a controlled release or a triggered release of the therapeutic molecule. The nanoparticle surface can thus be functionalised by various methods. Tissue defects, stealth properties, targeting, and the size of the nanoparticles are major factors affecting the biodistribution and clearance of polymeric nanoparticles [22, 129]. Due to their unique size, and amenability to surface functionalisation to allow for the incorporation of the desired characteristics, nanoparticles are particularly well suited to overcoming most common drug delivery barriers [22]. Thus, over the past 20 years, numerous approaches to improving nanoparticle blood residence and accumulation in specific tissues for the treatment of disease have been developed [133, 134].

### 1.3.3.1 Bioconjugate

A limited number of chemical functionalities allow for the facile release of a covalently attached drug after targeted cell uptake. To facilitate this process, drugs must contain at least one of a limited number of functional groups (-SH, -COOH, -OH, or-NH<sub>2</sub>) that can be modified for cellular targeting or intracellular release [135]. An efficient drug release mechanism must be designed for the conjugate: i.e. the release mechanism needs to be inert during transit to the pathologic lesion but is rapidly activated after target cell binding and internalisation, enabling release of the therapeutic cargo only at the site of disease [94].

Prerequisites for an ideal bioconjugate include selectivity for tumour cells, chemical and physical stability, ensures maximum accumulation within the tumour tissues, optimal tissue penetration, have a small size, be easy to synthesise and modify, have good tumour penetration ability, excellent compatibility, and rapid clearance from the body [136]. The bioconjugates should enhance extended circulation, to allow maximum interaction with the target site to ensure sufficient delivery and dosing to target cells [97]. In addition, bioconjugates should be biocompatible/biodegradable, limiting immune response and facilitating degradation, and eventual removal from the body [137]. An excellent example of which is folic acid (**Section 1.5**). Folic acid is stable, inexpensive, and non-immunogenic [138], and is commonly linked to PEG [139] and has been considered for targeting [140]. However, in this study, we will explore the effects of palladium nanoparticles stabilised with diamine and phthalocyanine folate conjugates.

## 1.4 NANOMEDICINE AND NANOTECHNOLOGY

Nanotechnology is the creation, manipulation, and application of structures in the nanometre size range [141]. Nanomedicine is the application of nanotechnology to design and develop therapeutics and diagnostic tools [142]. It has drug delivery systems in the nanoscopic scale, and may include delivery vehicles and diagnostic agents [143], multivalent surface modifications with targeting ligands, efficient navigation of the complex *in vivo* environment, increased intracellular trafficking, and sustained release of the drug payload [30]. These nanoparticle advantages increase the potential of nanoparticles to be a superior treatment option to conventional cancer therapies [144, 145].

Nanotechnology allows for improved delivery of poorly water-soluble drugs, targeted delivery of drugs in a cell or tissue-specific manner, transcytosis of drugs across tight epithelial and endothelial barriers [146, 147]. Nanotechnology also entails the delivery of large

macromolecule drugs to intracellular sites of action, the co-delivery of two or more drugs or therapeutic modality for combination therapy [148], visualisation of sites of drug delivery by combining therapeutic agents with imaging modalities [29], and real-time read on the *in vivo* efficacy of a therapeutic agent [149].

#### 1.4.1 Nanoparticle vehicle molecules

In the modern era of medicine, cellular hitchhiking of circulatory cells offer an attractive option for therapies capable of performing functions which are often limited to applications of synthetic materials [150]. Red blood cells, macrophages, monocytes, T-cells, B-cells, and other circulatory cells are nature's own 'delivery vehicles' as they have evolved to perform delivery functions *in vivo* optimally [137]. The nanoparticle must be able to bind or contain the desired drug(s) [151].

Synthetic materials are significantly limited in their ability to circulate, target, and negotiate cellular barriers limiting clinical use [83]. Thus, it is essential to develop technologies to overcome these inherent limitations. Extensive research efforts are focusing on improving drug delivery through the use of nanoparticles to improve the biological outcome of therapeutic drugs [87, 152–157].

The biophysiochemical properties of the nanoparticle vehicle molecules, such as size, charge, surface hydrophilicity, nature and density of the ligands on their surface impacts the circulating half-life of the particles as well as their biodistribution [158]. The presence of targeting ligands on nanoparticle vehicle molecules can increase the interaction of the drug delivery system with increased cells specificity in the target tissue, enhancing cellular uptake by receptor-mediated endocytosis [159]. It is believed that targeting anchors drug delivery systems thereby decreasing the efficiency of diffusion and increasing uniform tissue distribution [160, 161].

For optimal targeting ability, it is imperative for delivery vehicles to have controlled particle size, size distribution, shape, crystal structure and composition [162]. To achieve this, nanoparticles purity, aggregation, physical properties stabilisation, possible reactants, increased reproducibility, increased mass produce, and low production cost are essential factors to consider [114, 163]. The possibility of our designed nanoparticles acting as delivery vehicles will be advantageous to our study.

### 1.4.2 Nanoparticle based-targeting methods

Nanoparticles have the advantage of targeting cancer by simply being accumulated and entrapped in tumours (passive targeting) [134]. The phenomenon is called the enhanced permeation and retention effect, caused by leaky angiogenic vessels, poor lymphatic drainage and has been used to explain why macromolecules and nanoparticles are found in higher ratios in tumours, compared to normal tissues [59]; however, selective active targeting is preferred. The types of nanoparticles currently used in research for cancer therapeutic applications include dendrimers, liposomes, polymeric nanoparticles [164], micelles, protein nanoparticles, ceramic nanoparticles, viral nanoparticles, metallic nanoparticles, and carbon nanotubes [93].

The therapeutic index of the majority of drugs currently being used would be improved if delivery to their biological targets was nanotechnology-based and more efficient [165]. The efficacy can be increased, reducing the toxicity of a cancer drug to non-tumorigenic tissues, if a directed target system was employed at the target site for a sufficient amount of time [166]. Most common nanoparticles deliveries include injection, oral delivery, ocular delivery, delivery to the brain and gene delivery [167].

Nanoparticles are capable of encapsulating drugs limiting degradation or deactivation before the drug reaches a target site *in vivo*, improving tissue-specific targeting ligands [168, 169]. Nanoparticles are subjected to rapid clearance from blood and majority of formulated nanoparticles drug systems do not reach clinical trials [137], highlighting the need for effective drug design.

Nanoparticles offer significant improvements in therapeutics through site specificity, ability to escape from multi-drug resistance, and efficient delivery of drugs [147, 170]. This is achieved *via* passive or active targeting [152].

#### 1.4.2.1 Passive targeting

Passive targeting of nanoparticles takes advantage of the abnormal tumour physiology and structure that results in the EPR effect [171]. The permeability of the vasculature and retention by an insufficient lymphatic system can result in passive accumulation of macromolecules to increase their tumour concentration by 70-fold. This accumulation will only be observed if the macromolecules avoid clearance by mechanisms such as renal clearance and uptake by the MPS/RES [134].

Efficacy of nanoparticles as delivery vehicles is highly size- and shape-dependent. The size of the nanoparticles affects their movement in and out of the vasculature, whereas the margination of particles to the vessel wall is impacted by their shape [24]. Particles tend to passively extravasate through the leaky vasculature, which is characteristic of solid tumours and inflamed tissue, and preferentially accumulate through the EPR effect [172]. If this occurs, the drug may be released into the extracellular matrix and diffuse throughout the tissue for bioactivity [149, 171].

Passive targeting has been demonstrated for nanoparticles with sizes ranging from 10 to 500 nm. It was found that particles (40–100 nm) accumulation depends on the blood residence half-life and is independent of nanoparticle size for the tested size range. In contrast, smaller particles (around 20 nm) accumulation depends on size and residence time [173, 174]. However, small particles have a relatively short residence time at the tumour site when compared with larger particles (> 40 nm). The blood residence time is a crucial parameter for therapeutic efficiency, as the nanoparticles are initially transported by the blood, followed by passive diffusion from the blood vessel into the tumour [175, 176].

Passive targeting has disadvantages similar to traditional chemotherapy, i.e. inability to actively and effectively distinguish between healthy tissue from tumour tissues [177]. Passive targeting also involves the use of other innate characteristics of the nanoparticle highlighting the need for active targeting [139].

#### **1.4.2.2 Active targeting**

Once nanoparticles have extravasated in the target tissue, the presence of ligands on the particle surface can result in the active targeting of particles to receptors present on the target cell or tissue, resulting in enhanced accumulation and cell uptake through receptor-mediated endocytosis [145], enhancing the therapeutic efficacy of drugs, that not readily permeate the cell membrane and require an intracellular site of action for bioactivity [178].

Active targeting involves the use of peripherally conjugated targeting moieties for the enhanced delivery of nanoparticle systems [179]. The four major advantages of targeting tumour vasculature in comparison to conventional therapies include; by-passing the physiological barrier that prohibits the dissemination of nanoparticles through a tumour vasculature, destroying the vasculature to decreases the growth and metastatic capabilities of a tumour, the phenotypic changes in neovascular endothelial cells are inhibited diminishing

the possibilities of acquired drug resistance, which is conventional cancer therapies, and the tumour vasculature is not specific for the type of cancer [110, 180].

Active targeting takes advantage of ligand-receptor, antigen-antibody and other forms of molecular recognition, to deliver a nanoparticle or drug to a specific location. For cancer therapy, active targeting of cancer-specific receptors is beneficial because it reduces or eliminates the delivery of potentially toxic drugs to healthy tissue [98].

Active targeting takes advantage of the overexpression of receptors, such as folate and transferrin, on the tumour cell surface [110]. These targeted nanodelivery systems have performed significantly better than their non-targeted counterparts resulting in increased cytotoxicity to tumour cells and reduction of side effects [181].

### 1.4.3 Uptake mechanism

Both targeted and non-targeted nanoparticles arrive at the tumour vicinity *via* the EPR effect. Tumour cell internalisation is enhanced by the presence of surface ligands [139]. Faster clearance from circulation generally corresponds to increased accumulation in the liver and spleen *via* the RES [98]. The internalisation of nanoparticles is vital for effective delivery of some anticancer drugs, especially in gene delivery therapies, gene silencing, and other biotherapeutics [110, 182].

The targeting moieties are essential to the mechanism of cellular uptake. Long circulation times allows for effective transport of the nanoparticles to the tumour site *via* the EPR effect, where the targeting molecule can induce the endocytosis of nanoparticles [159]. The internalisation of nanoparticle drug delivery systems has shown an increased therapeutic effect [183]. The nanoparticle attaches to vascular endothelial cells *via* a non-internalising epitope, high local concentrations of the drug will be available on the outer surface of the target cell [184].

It is widely accepted that nanoparticles are suitable to crossing biological barriers through tissue diffusion, extravasation, and escape from hepatic filtration [185]. Historically, the administration of therapeutic agents has been limited by multiple factors, primarily low solubility, stability, and rapid clearance, resulting in a short circulation half-life and low efficacy, thus, requiring the frequent administration of the drug [186]. The uptake and internalisation of nanoparticles are affected by a few factors.

### 1.4.4 Factors affecting nanoparticle cellular uptake

The most important properties of effective nanocarriers are the carriers' increased blood residence time, ability to target specific tissues selectively, and to overcome biological barriers (**Figure 1.4**); depending on a particle's shape, size, and surface characteristics [186]. Particle size is a crucial factor in the biodistribution of circulating nanoparticles and achieving therapeutic efficacy [103]. Nanoparticles carrying a positively charged surface have a high nonspecific internalisation rate with a short blood circulation half-life. Whereas, nanoparticles with a negative surface charge showed a marked reduction in the rate of non-receptor mediated cellular uptake [22]. The surface functionality is another critical parameter in controlling the development of long-circulating nanoparticles [187]. Nanoparticle's uniform size distribution, ease of detection, purity (lack contamination), and commercial availability are essential for improved cellular uptake [188, 189].

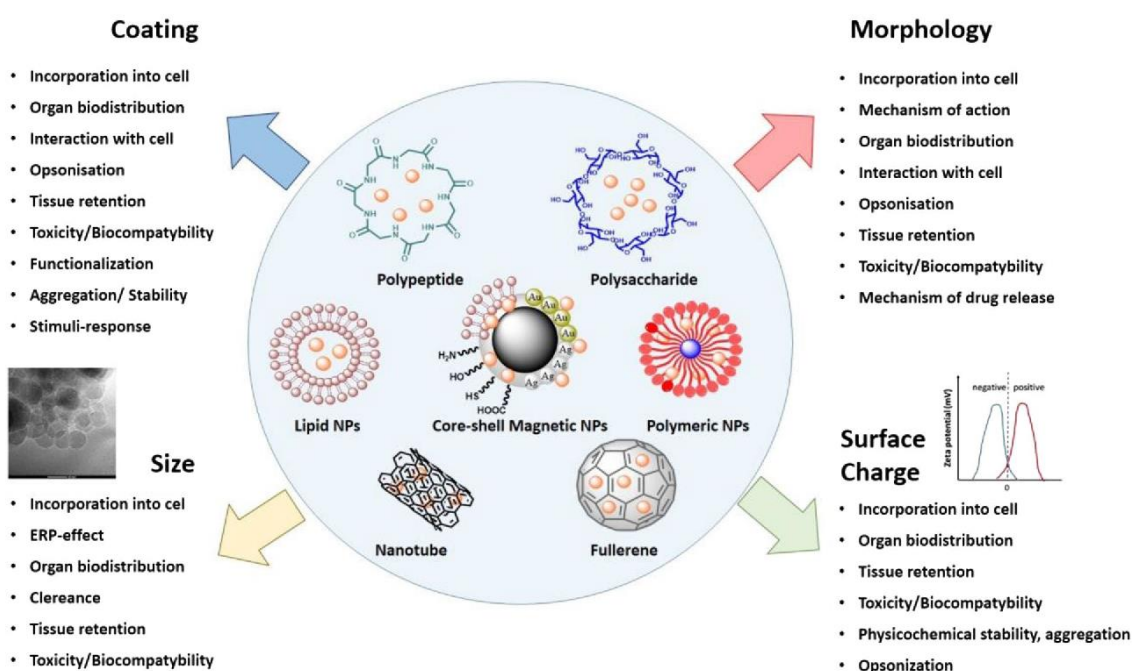


**Figure 1.4:** A summary of the key properties of nanoparticles in drug delivery systems and targeted therapy that affect nanoparticle cellular uptake, clearance, toxicity, etc. [190]. This image was reproduced from reference [190] with permission from Springer (Copyright 2018).

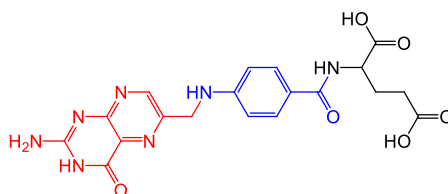
The effectiveness of the prediscussed factors is cell specific. In normal tissues and organs, FR-expression is restricted to only a few sites where it is confined to the luminal surface of polarised epithelia and is overexpressed on tumour cells [181]. Thus, using folate receptor-based nanoparticle systems to selectively and effectively deliver drugs to tumour cells has been explored for the last two decades [191], and folate receptor-targeted radionuclide therapy has great prospects [146, 192].

## 1.5 FOLATE-BASED DRUG DEVELOPMENT

Folate receptors are overexpressed in numerous cancers to meet the demand of folate by the rapidly dividing cells. This folate dependency of tumours has been therapeutically and diagnostically exploited in cancer folate-receptor mediated tumour targeting [164, 193].

### 1.5.1 Structure of folic acid

Folic acid is also known as pteroylglutamic acid (**Scheme 1.1**). It has the chemical formula  $C_{19}H_{19}N_7O_6$  (MW = 441.4 Da). Folic acid is a well-known water-soluble vitamin in the vitamin B-complex group. Folate, the folic acid salt, or pteroylglutamate, is water-soluble [194], stable, inexpensive, and non-immunogenic chemical, with a high affinity as a cell surface receptor [195].



**Scheme 1.1:** The structure of folate showing the pteridine ring (red), 4-aminobenzoate (blue), and the glutamate (black) [196].

### 1.5.2 Importance and functions of folic acid

Folic acid is an essential vitamin required for DNA nucleotide synthesis (synthesis of purines and pyrimidines) and cell division [197]. Folic acid (or folate), binds explicitly with a folate receptor existing on the surface of tumoral cells. Tumour cells require more folate than healthy cells [198]. The deficiency of folate is linked to anaemia, foetal neural tube defects, cardiovascular diseases, and cancer [199].



### 1.5.3 Folate antagonists

Antifolates are folate analogues that inhibit vitamin B<sub>9</sub> (folic acid) cellular uptake, primarily *via* widely expressed facilitative membrane transporters [200]. Human folate receptors (FRs) transport folate *via* endocytosis with high affinity, are proposed targets for the specific delivery of new classes of antifolates or folate conjugates to tumours or sites of inflammation [201].

Three antifolates (**Figure 1.5**); pemetrexed, aminopterin, and methotrexate are commonly used due to structural similarity to folate [193, 202].

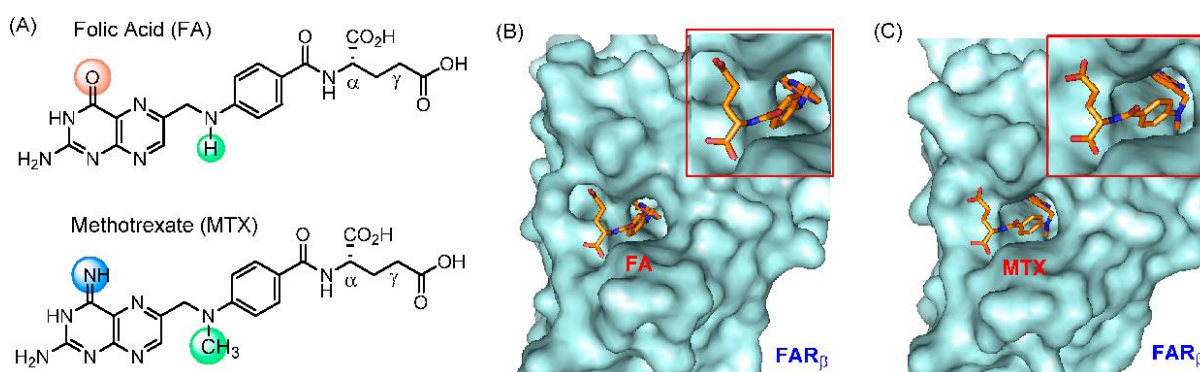


**Figure 1.5:** (A) The structure of folic acid and methotrexate, (B) the crystal structure of the folate receptor bound to folic acid, and (C) methotrexate binding to folate receptor [203]. This image was reproduced from reference [203] with permission from PubMed (Copyright 2018).

### 1.5.4 The folate receptors

Nearly all cells express the folate receptor; for normal DNA replication and cell division, however, cancerous cells express a much higher amount of folate receptors (500+ times more than healthy cells) [204]. Cancer cells overexpress the folate receptor due to their increased folate requirements [205, 206]. As a result, the high affinity of folic acid and folate presents a unique opportunity to use these molecules as targeting ligands to deliver nanoparticles to cancer cells [207].

#### 1.5.4.1 Structure and composition of the folate receptor

FRs, also known as folate-binding proteins (FBP), are *N*-glycosylated proteins with high binding affinity to folate. FRs include at least four isoforms,  $\alpha$ ,  $\beta$ ,  $\gamma$  /  $\gamma'$ , and  $\delta$  [208]. The  $\alpha$ ,  $\beta$ , and  $\delta$  isoforms are glycosylphosphatidylinositol (GPI) anchored membrane proteins, whereas  $\gamma$ / $\gamma'$ -FR- is constitutively secreted by lymphoid cells [209]. The affinities of folic acid for the FRs are  $\alpha$ -FR,  $K_d \sim 0.1$  nM;  $\beta$ -FR,  $K_d \sim 1$  nM; and  $\gamma$ -FR,  $K_d \sim 0.4$  nM.  $\alpha$ -FR and  $\beta$ -FR share high

amino acid sequence identity (~70%) and are distinguishable by differential affinities for folic acid and stereoisomers of reduced folates [193, 199, 210].

The  $\alpha$ -FR, a 38 kDa glycosyl-phosphatidylinositol-anchored glycoprotein, has restricted expression in the kidney, lung, choroid plexus, placenta, and normal cells [211]. In these sites, the  $\alpha$ -FR is confined to the luminal surface of polarised epithelia and is not in contact with circulating folates or intravenously administered folic acid conjugates. The  $\alpha$ -FR is over-expressed in a variety of tumours such as ovarian carcinomas, choriocarcinomas, meningiomas, uterine sarcomas, osteosarcomas, and non-Hodgkin's lymphomas [212]. The  $\beta$ -FR expression is restricted mainly to the placenta, white blood cells of myeloid lineage, and activated macrophages [209, 213]. The presence of the folate receptors on a cell surface is regulated by the cell function [164].

The crystal structure of the folate receptor was reported to be 2.8 Angstroms. The  $\alpha$ -folate receptor has a globular structure, stabilised by eight disulphide bonds. It contains a deep and open folate-binding pocket comprised of residues that are conserved in all folate receptors [201]. The folate pteroyl moiety is buried inside the receptor, whereas its glutamate moiety is exposed and protrudes from the pocket entrance (**Figure 1.6**), allowing it to be conjugated to drugs without affecting the  $\alpha$ -FR binding [193].

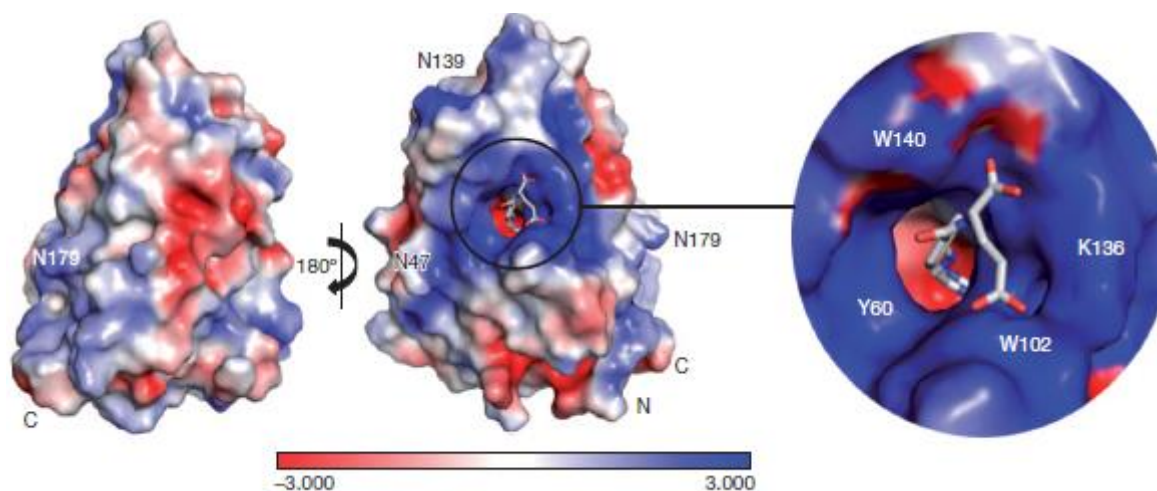


**Figure 1.6:** The crystal structure of the  $\alpha$ -FR showing surface distribution of  $\alpha$ -FR with a close-up view of the ligand binding pocket entrance. Folic acid carbon atoms are coloured grey, nitrogen atoms blue, and oxygen atoms red [199]. This image was reproduced from reference [199] with permission from PubMed (Copyright 2018).

Folic acid is oriented with its basic pteroyl moiety docked deep inside of the negatively charged pocket and the two negatively charged carboxyl groups of its glutamate moiety extruding from the positively charged entrance of the ligand-binding pocket [193]. The folate receptor constitutes a useful target for tumour-specific drug delivery.

#### 1.5.4.2 Active targeting of folate receptors

As previously mentioned, targeted delivery *via* selective cellular markers can potentially increase the efficacy and reduce the toxicity of therapeutic agents. Conjugates of folic acid and anti-FR molecules can be taken up by cancer cells *via* receptor-mediated endocytosis, thus providing a mechanism for targeted delivery to FR+ cells [210].

The FR-targeted radionuclides have several advantages, including relatively easy and cost-effective synthesis, potential broad applications for the treatment of several tumours, and favourable tumour-to-background ratios [214]. However, current radiotracer-based imaging techniques are limited in anatomic resolution, which necessitates additional imaging modalities and other techniques to localise the detected tumour [123].

FR density appears to increase as the cancer worsens. However, in some tissues, FR access is limited due to the FR location on the apical (externally-facing) membrane of polarised epithelia [215]. Nonetheless, FR active targeting is achievable when folate is conjugated to a drug-containing molecule or compound [212].

#### 1.5.5 Folate conjugation

FRs mediate cellular internalisation of folate conjugates *via* receptor-mediated endocytosis, thus constituting a method for targeted intracellular delivery of therapeutic agents to FR+ cells [210, 216].

Folate conjugation presents an alternative method of targeting the folate receptor. Folate receptor-specific delivery of protein toxins, anti-T-cell receptor antibodies, interleukin-2, chemotherapy agents,  $\gamma$ -emitting radiopharmaceuticals, magnetic resonance imaging contrast agents, liposomal drug carriers, and gene transfer vectors [212]. The small size, convenient availability, simple conjugation chemistry, and lack of immunogenicity of folic acid make it an ideal ligand for folate conjugation and targeted delivery to tumours [212].

Folate conjugation has been successfully used for the delivery of small molecules, macromolecules, and nanocarriers in numerous preclinical studies [147]. For nanocarriers, which include liposomes, polymeric nanoparticles, and several types of nucleic acid vectors,

a drug carrier is typically conjugated to folate, through a PEG linker to overcome steric hindrance surrounding the FR on the cell surface [217]. Among macromolecules, folate has been conjugated to protein toxins, antibodies, polymeric drug carriers, and prodrug converting enzyme [215]. Folate conjugates can target both  $\alpha$ -FR- and  $\beta$ -FR. This potentially enables the targeting of tumours that are low in  $\alpha$ -FR but high in  $\beta$ -FR (e.g., tumours that are highly infiltrated by  $\beta^+$ -FR tumour associated macrophages, and chronic inflammatory diseases like rheumatoid arthritis [218]). However, this reduces the selectivity for the tumour cells, but may expand the range of disease targets and subsequently patient population that are responsive to FR-targeted therapy [219].

A low molecular weight (MW) folate conjugate is rapidly distributed into tumour tissues and is rapidly cleared from systemic circulation, reducing the concentration in the plasma and non-target tissues. This typically leads to a higher tumour-to-normal tissue ratio. The low MW conjugates are typically not immunogenic and are not subject to denaturation and the associated loss of biological activity and can be produced by total synthesis as a single pure chemical entity, which is not always feasible for macromolecular conjugates [215]. In addition to low toxicity, biodegradability, and biocompatibility of these folate conjugates [220], the small size, convenient availability, simple conjugation chemistry, and lack of immunogenicity of folic acid makes it an ideal biomolecule for targeted drug delivery to tumours [212] with effective cellular uptake.

### 1.5.6 Folate uptake

Folic acid and its reduced derivatives, including 5-methyltetrahydrofolate and 10-formyltetrahydrofolate, are transported *via* the widely expressed folate receptors, and the two facilitative transporters, namely; reduced folate carrier (RFC) and proton-coupled folate transporter (PCFT) [221].

#### 1.5.6.1 Folate receptor-mediated endocytosis

A universal anion channel with a low folate-binding affinity ( $K_m$  5-10mM) is responsible for the uptake of folate in adult tissues. The folate food supplement had a high binding affinity of  $K_d$ , 1nM and the physiologically prevalent folate  $N^5$ -methyltetrahydrofolate (5-mTHF), requires the function of three subtypes of folate receptor ( $\alpha$ -FR,  $\beta$ -FR, and  $\gamma$ -FR), which are cysteine-rich glycoproteins that mediate folate uptake through endocytosis, in which the  $\alpha$ -FR is the mostly expressed [222]. Inside the cell, the acidic environment of the endosome promotes the release of folate from receptors [223]. In normal tissues, the exception for folate

receptors overexpression and increased folate uptake is essential and restricted to embryonic development (for example, placenta and neural tubes) and folate resorption (kidney) [199].

Most eukaryotic cells are unable to produce folate [224] and folates cannot directly penetrate the cell membrane because of their hydrophilic anionic nature; cellular uptake also occurs *via* endocytosis through folate receptors (FRs) [162]. Substantial targeting efficacy has been found both *in vitro* and *in vivo* [210], although the precise mechanism of FR transport of folic acid into cells remains unresolved, folate conjugates are primarily taken up non-destructively (Figure 1.7) by mammalian cells *via* folate receptor-mediated endocytosis [225].

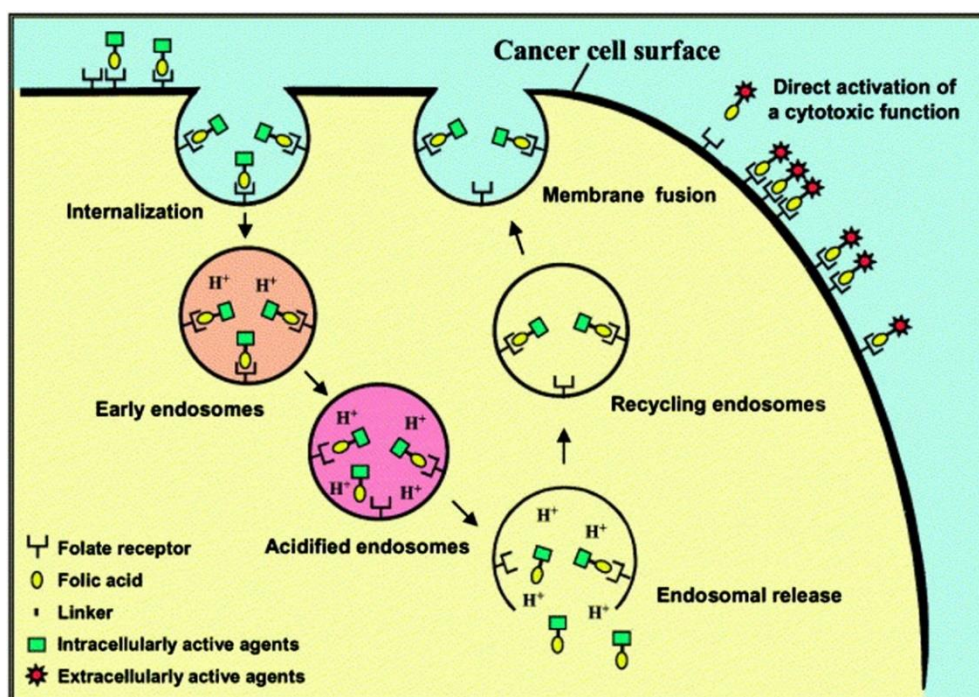


**Figure 1.7:** Folate receptor-mediated folate uptake [226]. Folate linked to intracellular or extracellular active agents bind to the folate receptor; the folate linked to intracellular drug is internalised, develops into endosomes, and is released into the cytoplasm while the endosome gets recycled. On the contrary, folate linked extracellular active agents activate cytotoxic function(s) outside the cell. This image was reproduced from reference [226] with permission from Elsevier (Copyright 2018).

#### 1.5.6.2 Reduced folate carrier

The reduced folate carrier (RFC) is a ubiquitously expressed anion transporter primarily responsible for the transmembrane transport of reduced folates, with  $K_t$  values in the  $\mu\text{M}$  range. RFC is the primary pathway for reduced folate uptake into various tissues under physiological pH. Reduced folates and antifolates, such as methotrexate, pralatrexate, and



pemetrexed, are transported into cells through the RFC and are subsequently retained in the cytoplasm through polyglutamylation by the poly(*p*-glutamate) synthetase [221, 227]. RFC, however, has a relatively low affinity for folic acid relative to the FRs and is not expected to transport folate derivatives across the cellular membrane. In contrast,  $\alpha$ -FR binds folate derivatives with high affinity and mediates their internalisation by endocytosis *via* a pathway that is associated with caveolae and receptor recycling [210].

### 1.5.6.3 Proton-coupled folate transporter

Folate uptake *via* the proton-coupled folate transporter (PCFT), which is responsible for intestinal folate absorption at the acidic pH of the upper small [228]. The key role of PCFT in obligatory intestinal folate absorption has been established in studies with hereditary folate malabsorption, a congenital disorder in which loss-of-function mutations in PCFT, results in low folate levels in the blood and cerebrospinal fluid [202]. PCFT is a proton-driven folate cotransporter whose activity can be upregulated by the folate receptor to satisfy heightened needs [229]. PCFT regulates folate homeostasis and is known for internalising antifolates [230] and not folate conjugates [210].

### 1.5.7 Antifolates uptake

Antifolates are also taken up by the mechanisms mentioned above for folate uptake (**Figure 1.8**). For over 60 years, antifolates have been developed to treat a variety of cancer types and inflammatory diseases[231]. More recently, the emphasis in folate-mediated drug therapy has shifted to obtain a better understanding of transport mechanisms of antifolates because dose-limiting toxicities arise from their transport *via* RFC, and possibly PCFT, into normal cells [232].

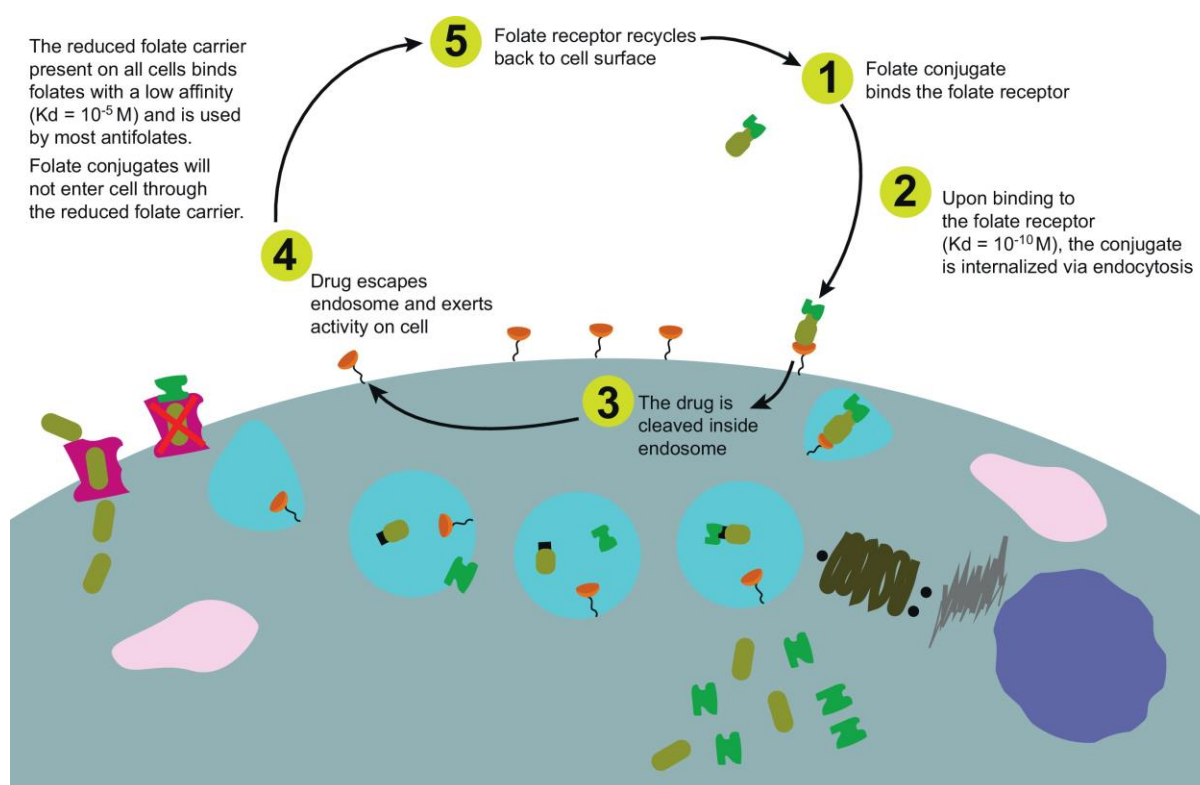


**Figure 1.8:** Antifolates mechanism of action [211]. The folate conjugates bind to the folate receptor, internalised *via* endocytosis, and the drug is cleaved and released exerting activity on cell while folate receptor is recycled back to the cell surface. This image was reproduced from reference [211] with permission from Elsevier (Copyright 2018).

To date, antifolates approved for clinical use are transported primarily *via* RFC, although one of the most recently developed antifolates, pemetrexed (PMX), may also transit through PCFT [210]. Despite the published successes, folate-targeted therapy has limitations and challenges.

### 1.5.8 Challenges/Limitations of nanoparticle folate-targeted therapy

One of the potential limitations of FR-targeted nanomedicines could be their high renal uptake. Significant amounts of FA-conjugated nanoparticles have been observed in the liver and kidneys [233]. Nanoparticles may accumulate in the liver, spleen, and lungs based on their size distribution, i.e., nanoparticles of 50–100 nm tend to accumulate in the liver due to non-continuous endothelia with vascular fenestrations; nanoparticles of 200–500 nm tend to accumulate in the spleen due to inter-endothelial cell slits; and microparticles of 2–5  $\mu m$  tend to accumulate in the capillaries of the lungs [59].

Only nanoparticles of 5 nm or smaller can be filtered out by the kidneys. Physiologically, folate binding proteins (FBP) including  $\alpha$ -FR,  $\beta$ -FR, and RFC are highly expressed in the kidneys. FBP is in the brush board membrane of the proximal tubule cells and participates in folate reabsorption from the convoluted proximal tubules. Hence, these proximal tubular cells are not directly exposed to the circulating FA-conjugated nanoparticles unless they are filtered from glomeruli. Filtration initially occurs at the interface of glomerulus and Bowman's capsule [234]. Filtered molecules or nanoparticles need to pass through three filtration layers: the endothelium, glomerular basement membrane (GBM), and foot processes of the podocytes. The endothelium serves as an initial physical barrier with a pore size of 80–100 nm in diameter. The GBM with a high concentration of heparin sulphate in the middle layer provides a negative charge to repel negatively charged molecules electrostatically but attract positively charged molecules or nanoparticles, e.g., dendrimers, from the blood. The foot processes of podocytes with a pore size of 15–20 nm in diameter represent the last filtration barrier [234].

Another potential disadvantage of the strategy of using folate conjugates includes interference of FR targeting by circulating folate, which may be influenced by a patient's diet. Conversely, it is worth noting that dietary folate has not been a significant issue in clinical studies. Folic acid has been given to the patient in clinical trials to reduce normal tissue uptake of etarfolatide in a clinical trial, suggesting that low concentrations of circulating folate may be helpful for targeting tumour cells *in vivo* [235].

The high-level accumulation of folate-based radiopharmaceutical suggests that kidney uptake of low MW folate conjugates is extremely high since both types of agents similarly bind the FR. The accumulation of these conjugates in the kidneys has been found to be persistent rather than transient, reducing the prospective applications of low MW folate conjugate-based radiopharmaceuticals for targeted therapy [215]. The lack of FR subtype specificity of folate conjugates is also viewed as a disadvantage [236].

Another limitation is that folate-linked macromolecules do not appear to target normal tissues. This is primarily limited by the poor penetration of macromolecular conjugates into solid tumours. This problem may be addressed by inducing a two-stage targeting strategy, in a similar manner to the folate–haptent therapy. A reduction in the size of the targeted complex to facilitate better tumour penetration and application of strategies to increase the permeability of solid tumours. Alternatively, the use of more potent therapeutic agents that are effective at the lower doses that penetrate the tumour masses [237].



Folate targeting shows considerable promise for the development of tumour-specific therapeutic agents, but obstacles must still be overcome before it can reach its full potential. [226]. The above-mentioned challenges have solutions [145], and the experimental design factored in the published limitations.

## 1.6 FOLATE RECEPTOR EXPRESSION

Different cells express different amounts of folate receptors on their surfaces (**Figure 1.9**).

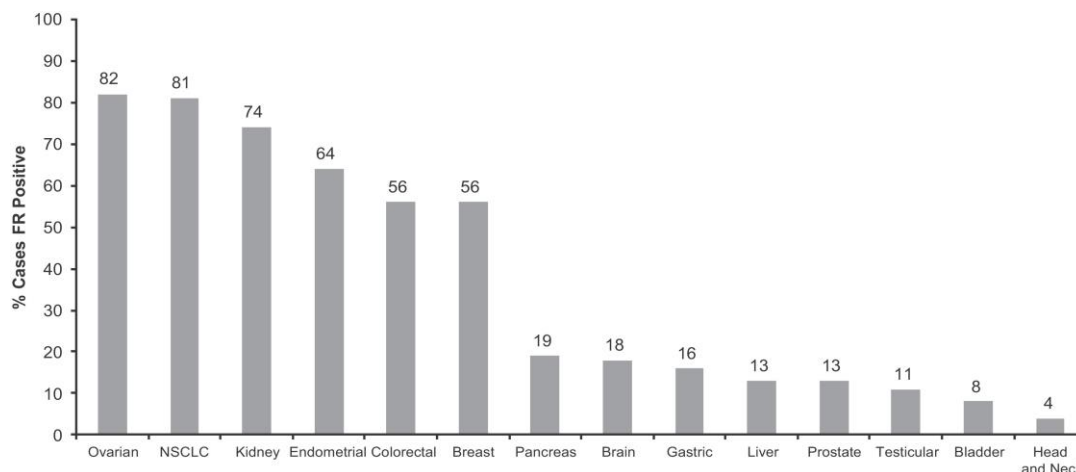


**Figure 1.9:** Folate receptor expression among a wide variety of human tumours [211]. Ovarian and non-small cell lung cancer (NSCLC) have the highest tumour folate receptor expression and breast tumours have positive folate receptor expression in most tumours. This image was reproduced from reference [211] with permission from Elsevier (Copyright 2018).

Among normal tissues, the  $\alpha$ -FR expression is mostly limited to the apical plasma membrane of the polarised kidney and specific epithelial cells and other areas as previously elaborated [216]. In this study, four breast cell lines were selected based on their  $\alpha$ -folate receptor expression levels [238], namely; MDA-MB-468, MCF-7, MDA-MB-231, and MCF-10A (**Table 1.8**).

**Table 1.8:** The four breast cell lines employed for the cytotoxicity and cell uptake studies.

Cell line	MDA-MB-468	MCF-7	MDA-MB-231	MCF-10A
<b>α-folate receptor expression levels</b>	-	+	++	+*
<b>Oestrogen receptor</b>	-	+	-	+
<b>Progesterone receptor</b>	+	+	-	+
<b>HER2 receptor</b>	-	-	-	+
<b>Epidermal growth factor (EGF) receptor</b>	+	-	-	+
<b>Endogenous A<sub>2B</sub> receptor</b>	-	-	+	-
<b>Tumorigenicity</b>	yes	yes	yes	no
<b>Tissue source</b>	M(PE)	M(PE)	M(PE)	M(PE)
<b>Tumour identification</b>	basal A	luminal	basal B (invasive)	basal B (non-invasive)
<b>Cell morphology</b>	grape-like	mass	stellate	round
<b>Proliferative index</b>	82.4	56.7	9.42	49.5

The above table was constructed from multiple references [238–245]. For the alpha folate receptor levels; - denotes negative receptor expression, + denotes low levels of receptor overexpression, ++ denotes high levels of receptor overexpression, and +\* denotes normal. For the other receptors, the levels of expression are unreported; - denotes negative receptors, + denotes positive receptors, M = metastasis, and PE = pleural effusion.

### 1.6.1 MDA-MB-468

The MDA-MB-468 breast cancer cell line was first derived from a pleural effusion of a 51-year-old breast cancer patient in 1977 [245]. It does not have any folate receptor on its surface and has disorganised nuclei with poor cell-cell adhesion [244].

### 1.6.2 MCF-7

The Michigan Cancer Foundation-7 (MCF-7) is an adherent breast cancer cell line isolated in 1970 from a 69-year-old Caucasian woman [246]. The MCF cell line has a low folate receptor expression [244] with disorganised nuclei and robust cell-cell adhesion.

### 1.6.3 MDA-MB-231

It is an epithelial human breast cancer cell line with high folate receptor expression [247], disorganised nuclei and elongated cell body with invasive processes [244].

### 1.6.4 MCF-10A

The Michigan Cancer Foundation-10 (MCF-10A) is a non-tumorigenic human epithelial human breast mammary gland cell [248] with normal cell folate receptor expression, organised nuclei and robust cell-cell adhesion [249].

## 1.7 RATIONALE AND MOTIVATION

Folate-conjugate based radiopharmaceuticals are hypothesised to have favourable pharmacokinetic properties than other radiolabelled agents [181], but with no folate-targeting drugs that are past clinical trials [250], only six folate-targeted drugs, four folate-targeted imaging agents, and an  $\alpha$ -FR specific monoclonal body are in clinical trials [164, 249, 251]. Therefore, there is a gap in folate receptor-targeted therapy.

South Africa has the world's second largest reserves of palladium [63], and palladium-109 has the key properties required for a nanoradiopharmaceutical (**Section 1.2.5**). Palladium has been reported to be a prospective key element in the nanomedical field [252]. To the best of our knowledge, palladium use as a biofunctionalised radionuclide for cancer-specific receptor-mediated targeted endocytosis has not been previously reported, highlighting prospects for the development of palladium-based nanoradiopharmaceuticals.

## 1.8 AIMS OF THE STUDY

The study primarily aims to design new nanoradiopharmaceuticals based on the  $^{109}\text{Pd}$  nuclide. A cold  $^{108}\text{Pd}$  was used for the development stage in this study, and the palladium was in the form of palladium(II) which was reduced to palladium(0) nanoparticles.

The key objectives are summarised as follows:

- (i) The *in situ* synthesis of palladium(II) complexes with capping agents followed by their *in situ* reduction to Pd(0) nanoparticles.
- (ii) Preliminary synthesis, characterisation, and optimised synthesis (at room temperature) of palladium(0) nanoparticles capped with tetraaminophthalocyanine, diamines, and folate conjugates as biomolecules for cancer cell localisation.

- (iii) The *in vitro* cell cytotoxic studies were carried out to determine the required non-cytotoxic concentration of palladium nanoparticles for active targeting.
- (iv) The cell uptake and localisation studies were investigated using transmission electron microscopy (TEM) and inductively coupled plasma-optical emission spectroscopy (ICP-OES). The size- and capping agent-dependency with respect to cancer cell accumulation *via* folate receptor-mediated endocytosis was explored.

The preliminary development of a unique class of folate-conjugated palladium-based nanoradiopharmaceuticals providing theranostic (therapy and diagnosis) abilities, designed to reach their specific target (cancerous cells) selectively and efficiently ensuring tissue bioavailability was conducted.

## 1.9 SCOPE OF THE DISSERTATION

The dissertation is composed of five themed chapters and list of references.

**Chapter 1:** As described in detail in the preceding pages, **Chapter 1** delivers an in-depth and thorough introduction of a variety of concepts that are fundamental to this study.

**Chapter 2:** This chapter provides a comprehensive list, summary, and descriptions of the materials used, preparative and synthetic methods, and instrumentation used.

**Chapter 3:** A detailed synthesis, optimisation, and characterisation of conjugates and nanoparticles is presented in this chapter. Stepwise elimination of reducing agents, capping agents, and preferred synthetic conditions and methods are explained.

**Chapter 4:** The *in vitro* cytotoxic effects of the palladium nanoparticles are reported in this chapter. It further presents the qualitative and quantitative cell uptake of the palladium nanoparticles by the four breast cell lines.

**Chapter 5:** The last chapter provides summarised conclusions and suggested future work for this study.

**List of references:** This section lists all the bibliography.

## CHAPTER TWO: MATERIALS, TECHNIQUES, AND EXPERIMENTAL METHODS

### 2.1 MATERIALS: REAGENTS USED

All the glassware and magnetic bars were soaked with aqua-regia for a few days, then rinsed with distilled water, and dried in an oven before use. A list of the chemicals used is provided (Table 2.1).

**Table 2.1:** List of chemicals or materials used and their suppliers

Chemical name	Percentage purity	Supplier
1,10-diaminodecane	97.0	Sigma-Aldrich
1,2,3-trihydroxybenzene	98.0	Sigma-Aldrich
1,2-diphenyl-1,2-diaminoethane	98.0	Sigma-Aldrich
1,4-diaminobenzene	99.0	Sigma-Aldrich
1,8-diazabicyclo [5.4.0] undec-7-ene	98.0	Sigma-Aldrich
1.5 mL Eppendorf tubes	sterile	Sigma-Aldrich
15 mL falcon tubes	sterile	Sigma-Aldrich
3-(4,5-dimethylthiazol-2-yl)-2,5-diphenyltetrazolium bromide	99.9	Sigma-Aldrich
4,4'-ethylenedianiline	95.0	Sigma-Aldrich
4-Nitrophthalonitrile	99.9	Sigma-Aldrich
Acetic acid	Glacial	Sigma-Aldrich
Acetone	98.0	Merck-Chemicals
Agar 100 resin	-	Agar Scientific
Cacodylate buffer	99.0	Agar Scientific
Camptothecin	99.9	Sigma-Aldrich
Citric acid	99.5	Sigma-Aldrich
Corning® cell scrapersblade L 1.8 cm, handle L 25 cm	sterile	Sigma-Aldrich
Dichloromethane (DCM)	99.0	Merck- Chemicals
Diethyl ether	98.0	Sigma- Aldrich
Dimethyl sulfoxide (DMSO)	99.5	ACE Chemicals

**Table 2.1:** Continued.

Disodium hydrogen phosphate	98.0	Sigma-Aldrich
Dulbecco's Modified Eagle's Medium (DMEM)	sterile	Biowest
Ethanol	99.0	Merck-Chemicals
Ethyl acetate	Analytical grade	Merck-Chemicals
Ethylenediamine	98.0	Sigma-Aldrich
Foetal bovine serum (FBS)	99.9	Thermofisher & Biowest
Folic acid (FA)	98.8	Sigma-Aldrich
Formaldehyde	38.0 (w/v)	Sigma-Aldrich
Glass Pasteur pipettes	sterile	Sigma-Aldrich
Glutaraldehyde	50.0 (w/v)	Agar Scientific
HAMS F12	sterile	Biowest
Hexamethylenediamine	98.0	Sigma-Aldrich
Hexane	97.0	Sigma-Aldrich
Hydrazine hydrate	98.0	Sigma-Aldrich
Hydrochloric acid	97.0	Merck-Chemicals
Hydrocortisone	99.9	Sigma-Aldrich
Insulin	99.9	Gibco
Lead citrate	98.0	Sigma Aldrich
Leibovitz's L-15 Medium	sterile	Gibco
Methotrexate	99.9	Sigma-Aldrich
Molecular grade ethanol	99.0	Sigma-Aldrich
N,N'-Dicyclohexylcarbodiimide (DCC)	98.0	Sigma-Aldrich
N,N'-Dimethyl formamide (DMF)	99.0	Fluka
N-Boc-Ethylene diamine	Analytical grade	Sigma-Aldrich
N-Hydroxysuccinimide (NHS)	98.0	Sigma-Aldrich
n-Octanol	99.9	FluoroChem
Osmium tetroxide	98.0	Sigma-Aldrich
Parafilm	-	Sigma-Aldrich
Paraformaldehyde	98.0	Agar Scientific

**Table 2.1:** Continued.

Potassium chloride	99.0	Sigma-Aldrich
Potassium dihydrogen phosphate	99.5	Sigma-Aldrich
Potassium tetrachloropalladate	99.0	Sigma-Aldrich
Propylene oxide	98.0	Sigma-Aldrich
Pyridine	99.0	Sigma-Aldrich
Pyridine-HCl	90.0	Merck-Chemicals
Sodium borohydride	99.0	ACE Chemicals
Sodium chloride	99.5	Sigma-Aldrich
Sodium metabisulphite	98.0	Sigma-Aldrich
Sodium sulphide hydrate	60.0	Sigma-Aldrich
Triethylamine	99.0	Merck- Chemicals
Trifluoroacetic acid	99.0	Sigma-Aldrich
Trypan blue	99.5	ACE chemicals
Trypsin	sterile	Sigma-Aldrich
Uranyl acetate	99.9	Lonza Chemical
Zinc(III) chloride	98.0	Sigma-Aldrich

## 2.2 INSTRUMENTATION

Various instruments were employed for analytical and spectroscopy analysis.

### 2.2.1 <sup>1</sup>H-and <sup>13</sup>C-Nuclear magnetic resonance (NMR)

The <sup>1</sup>H-Nuclear Magnetic Resonance (NMR) and <sup>13</sup>C-NMR measurements were acquired on a Bruker NMR (400 MHz) spectrometer in deuterated DMSO (DMSO-d<sub>6</sub>) solution and reported relative to tetramethylsilane ( $\delta$  0.00). The NMR spectra were used to confirm the chemical structures.

### 2.2.2 UV-Vis absorption spectroscopy (UV-Vis)

UV-Vis absorption spectra of the synthesised nanoparticles (NPs) and compounds were recorded on a Thermo Scientific spectrophotometer on a wavelength interval between 200 nm and 800 nm. Quartz square spectrophotometer cuvettes with a path length of 10 mm were used. Water and DMSO were used as the solvents.

### 2.2.3 Fourier-transform infrared spectroscopy (FTIR)

The infrared spectra were recorded on a Bruker Tensor 27 Platinum ATR-FTIR spectrophotometer in the range 4000–400  $\text{cm}^{-1}$ .

### 2.2.4 X-ray diffraction spectroscopy (XRD)

The crystallinity of the nanoparticles was confirmed using powder XRD data obtained using a Bruker Kappa Apex II diffractometer with a monochromated Cu K $\alpha$  radiation ( $\lambda = 0.71073 \text{ \AA}$ ). (The use of XRD was limited to only large-sized nanoparticles that were precipitated, collected, dried, powdered, and analysed).

### 2.2.5 Liquid chromatography-mass spectroscopy (LC-MS)

LC-MS spectra were acquired from a Water Synapt G2 liquid chromatography-mass spectroscopy using methanol as a solvent at 15 V.

### 2.2.6 Elemental analysis

Elemental analysis was conducted using a Vario Elementary ELIII Microcube CHNS elemental analyser. Calibration of the instrument was done with the use of the following standards in a linear curve adjustment within the total working range.

Standard 1: Sulfanamide: C - 41.81; H - 4.65; N - 16.25; S - 18.62%

Standard 2; Acetanilide: C - 71.09; H - 0.67; N - 10.36%

### 2.2.7 Zeta potential (ZP) and dynamic light scattering (DLS)

The surface charge (zeta potential) and hydrodynamic sizes of nanoparticles were determined by analysing sonicated particle suspensions using a Malvern Zetasizer Nano ZS particle size analyser (Malvern Instruments GmbH, Herrenberg, Germany). The mean value and standard deviation of three readings were reported.

### 2.2.8 Transmission electron microscopy (TEM)

Transmission electron microscope (TEM) images of the palladium nanoparticles and culture cells were acquired using a Zeiss Libra 120 and JEOL JEM2100 LaB6 transmission electron microscope operated at 120 and 200 kV, respectively. Nanoparticle solutions in ethanol were ultrasonicated for 30 s and the carbon-coated copper grids or 300-mesh carbon coated grids purchased from Electron Microscopy Sciences and SPI carbon coated grids, respectively, were used to collect the nanoparticles from the homogenous solution. The grids were completely dried in vacuum for at least 60 min and the images were acquired using a Mega-view III digital



camera's embedded self-imaging system. The diameter of the smallest circle of best fit was measured using ImageJ™ software for 30 to 50 nanoparticles and the nanoparticle size distribution constructed. For the agglomerated large-sized nanoparticles, the sizes were obtained from the measurable nanoparticles.

Selective area electron diffraction (SAED) patterns and energy dispersive X-ray (EDS) spectra were acquired from the JEOL JEM2100 LaB6 TEM, with the latter acquired in scanning transmission electron microscope (STEM) mode.

### 2.2.9 Inductively coupled plasma-optical emission spectroscopy (ICP-OES).

The nanoparticle analysis was carried out with an Avio 200 ICP-OES (**Table 2.2**). The metal standards, dissolved in 0.5 M HNO<sub>3</sub>, were used to prepare standard solutions for the construction of calibration curves using distilled, deionised, Milli-Q water with a resistivity of 18.2 MΩcm<sup>-1</sup> for dilution [253]. The solutions were analysed at 248.89 nm for minimal interferences [254]. The instrument was calibrated by using 0.01, 0.1, 1, 10, 50, and 100 ppm standard solutions for the palladium(II) ions.

**Table 2.2:** Inductively coupled plasma-optical emission spectrometer parameters.

Applied radio frequency (RF) power	1500 W
Plasma gas flow rate	10 L/min
Auxiliary gas flow rate	0.2 L/min
Nebulizer gas flow rate	0.55 L/min
Sampling depth	8.5 mm
Sample pump rate	50 rpm
Sample flow rate	1 mL/min
Sample flush time	10 s
Time scan acquisition	50 ms/point
Cooled spraying chamber temperature	4°C
The camera temperature	46.63°C
Generator temperature	24°C
Optics temperature	36.9°C
Total integration time	30 s per analyte
Autosampler wash rate	2.5 mL/min

**Table 2.2:** Continued.

Autosampler wash normal time	20 s
Autosampler source equilibration delay	1 s
Plasma view	axial
Number of replicates	6
Number of points per peak	7
Purge gas flow	normal
Delay time	25 s
Palladium wavelength	248.89 nm
Potential interferences	$^{92}\text{Zr}^{16}\text{O}^+$ , $^{92}\text{Mo}^{16}\text{O}^+$ , $^{68}\text{Zn}^{40}\text{Ar}^+$

### 2.2.10 Powerwave spectrophotometer (BioTek)

The Powerwave Epoch | 2 microplate reader Biotek spectrophotometer was used to measure absorbance in 96-well microplate after cell counting using haemocytometer.

### 2.2.11 Centrifuge

Labofuse 200 Heraeus sepatech centrifuge was used for centrifugation.

### 2.2.12 Ultrasonicator

Ultrasonication of nanoparticles was done by a Bransonic 1800 Lasec 150W ultrasonic water bath.

### 2.2.13 Incubator

Thermo Electron Corporation Forma Direct Heat CO<sub>2</sub> Incubator 311 was used to grow and culture the different cell lines. It maintained optimal temperature (37°C), Carbon dioxide (% CO<sub>2</sub> = 5%), and humidity (95%) needed for cell growth.

### 2.2.14 Other instrumentation

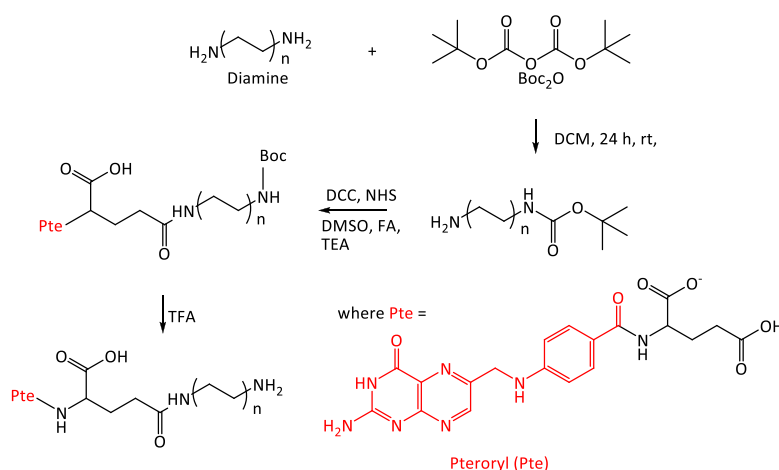
A 691-pH meter (Metrohm Herisau, Switzerland), micro weighing balance (A&D Company Limited, Japan), temperature-controlled heating stove (Lasec, South Africa), millipore water dispenser (Simplicity 185, France), gyrotory G16 water bath shaker (model G76 New Brunswick Scientific, USA), and an inverted light microscope (Zeiss Primo Star, Axiovert 40 C, 100-240 V), CSV 90 Auto Vortex Mixer (Crown Scientific, 100 W, 220-240 V), PowerTome XL ultra-microtome (Labtech, UK), and a special diamond knife for microtome were also used.

## 2.3 PREPARATIVE ASPECTS

Several methods were used to prepare the different compounds. A summary of the preparative aspects is presented.

### 2.3.1 Synthesis of N-Boc-ethylenediamine-folate

According to the literature [258], *tert*-Butyloxycarbonyl (Boc) protecting group can be used to protect one side of the diamine and allow the conjugation of folate. The method was modified as reported by Lee *et al.*, (2007) [259].



**Scheme 2.1:** The protection and deprotection steps for the synthesis of folate-ethylenediamine.

In a round-bottomed flask 640 mg of folic acid (1.34 mmol, 1 eq. dehydrated powder) was dissolved in 25 mL of dimethylsulfoxide (DMSO). After the dissolution was complete (about 30 minutes with mild heating), 308 mg (2 eq.) of *N*-hydroxysuccinimide (NHS), and 552 mg of *N,N'*-Dicyclohexylcarbodiimide (DCC) were added successively (**Scheme 2.1**). The reaction mixture was gently stirred for 16 h at room temperature, after which the urea was filtered off. The solution was added to 0.376 mL (2 eq.) of triethylamine followed by 429 mg (2 eq) of *N*-Boc-ethylene diamine dissolved in 5 mL of DMSO, and the mixture was stirred overnight followed by addition of a mixture of 20% acetone in diethyl ether. A yellow precipitate was carefully centrifuged and washed four times with acetone and two times with diethyl ether and dried under vacuum [258].

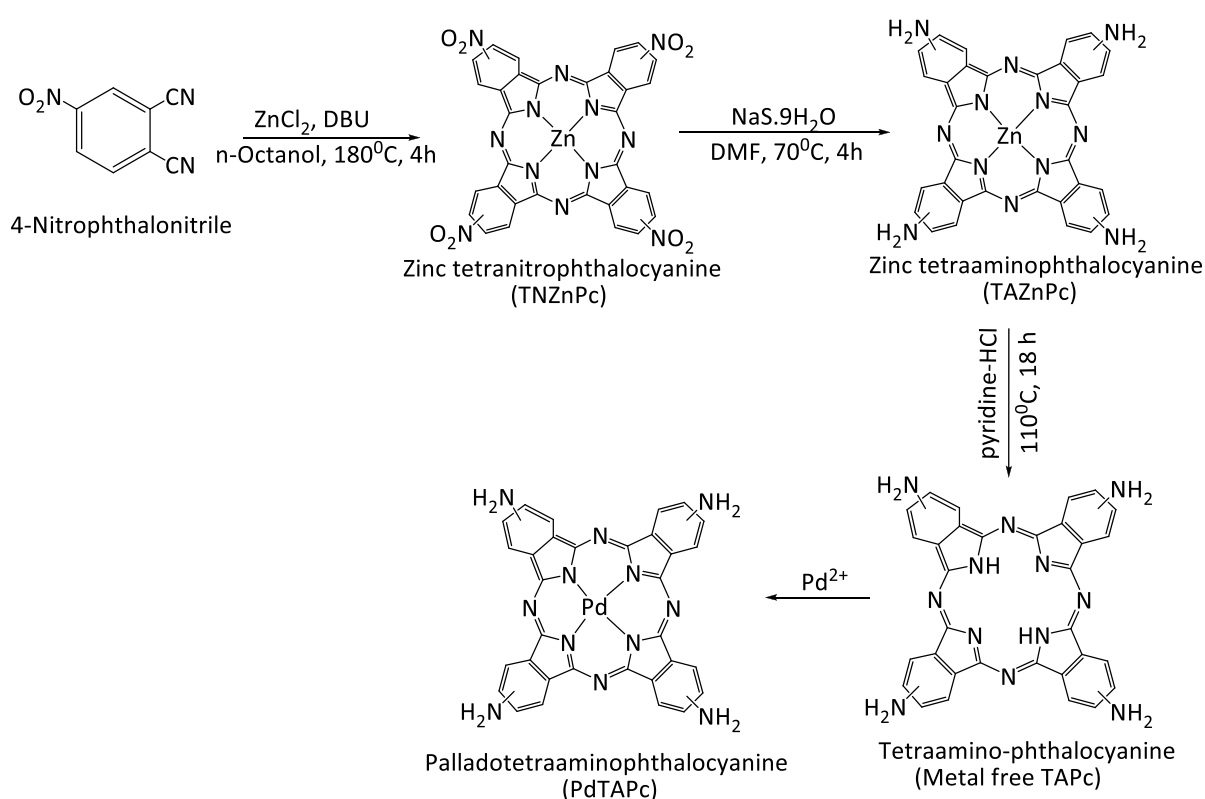
### 2.3.2 Synthesis of folate-ethylenediamine

The folate-ethylenediamine was prepared (**Scheme 2.1**) as per published literature [258]. *N*-Boc-ethylenediamine-folate conjugate (205 mg) was dissolved in 2 mL of trifluoroacetic acid

(TFA) and stirred for 2 hours. The solvent was removed under pressure with the aid of dichloromethane (DCM), and the red residue was dissolved with a minimal amount of dry dimethylformamide (DMF). The addition of triethylamine (TEA) resulted in the precipitation of a yellow powder which was washed and centrifuged four times, and twice with diethyl ether (80% yield, 136 mg). Further purification was done [138].

### 2.3.3 Synthesis of tetraaminophthalocyanine (TAPc)

The synthesis of TAPc (**Scheme 2.2**) was conducted as reported in literature [260]. 4-Nitrophthalonitrile (5.14 g, 29.7 mmol) and zinc chloride (1.23 g, 7.42 mmol) were added to n-octanol (8 mL), and catalytic amounts of 1,8-diazabicyclo-[5.4.0]-undec-7-ene (DBU) was added to the reaction mixture. The reaction was allowed to proceed at 180°C for 4 h. After that, the reaction mixture was cooled and diluted with toluene (80 mL), and the precipitate that resulted was collected by centrifugation at 6400 rpm for 30 min. The solid was filtered and washed with toluene, water, MeOH/ether (1:9), and lastly EtOAc/hexane (2:1). The dark green solid (TNZnPc) that resulted was dried and weighed.



**Scheme 2.2:** The synthesis of metal-free tetraaminophthalocyanine from 4-nitrophthalonitrile.

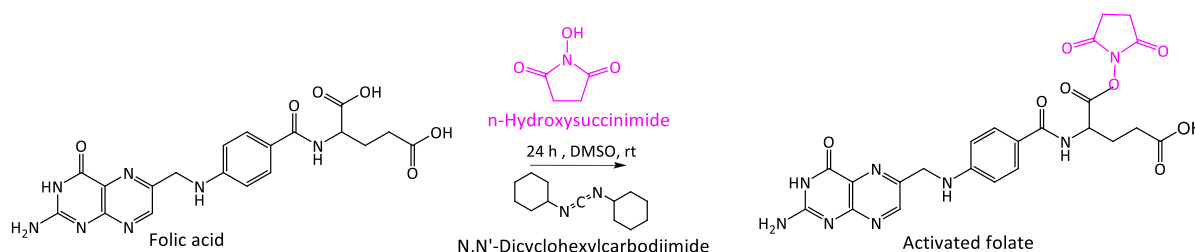
TAZnPc was synthesised under a nitrogen atmosphere at 65°C by dissolving 4.08 g (5.35 mmol) of TNZnPc in 80 mL DMF, followed by addition of 15.88 g (66.1 mmol) of sodium sulfide

nonahydrate. The reaction mixture was allowed to continue overnight and then cooled to room temperature (**Scheme 2.2**). It was then diluted with cold water (200 mL), and the resulting precipitate was collected by centrifugation at 6400 rpm for 30 min. The precipitate was repeatedly washed with MeOH/ether (1:9), EtOAc, and dried to afford a dark green solid.

TAZnPc was demetalated to form TAPc by dissolving 0.75 g in a solution of pyridine (4 mL), and pyridine HCl (2 g) while being stirred, under nitrogen, at 110 °C for 17 h. The reaction was stopped, and 20 mL of H<sub>2</sub>O was used to cool the mixture. Centrifugation was used to collect the dark green precipitate at 6400 rpm for 30 min, followed by filtration and repeated washing with H<sub>2</sub>O, MeOH, and EtOAc [260].

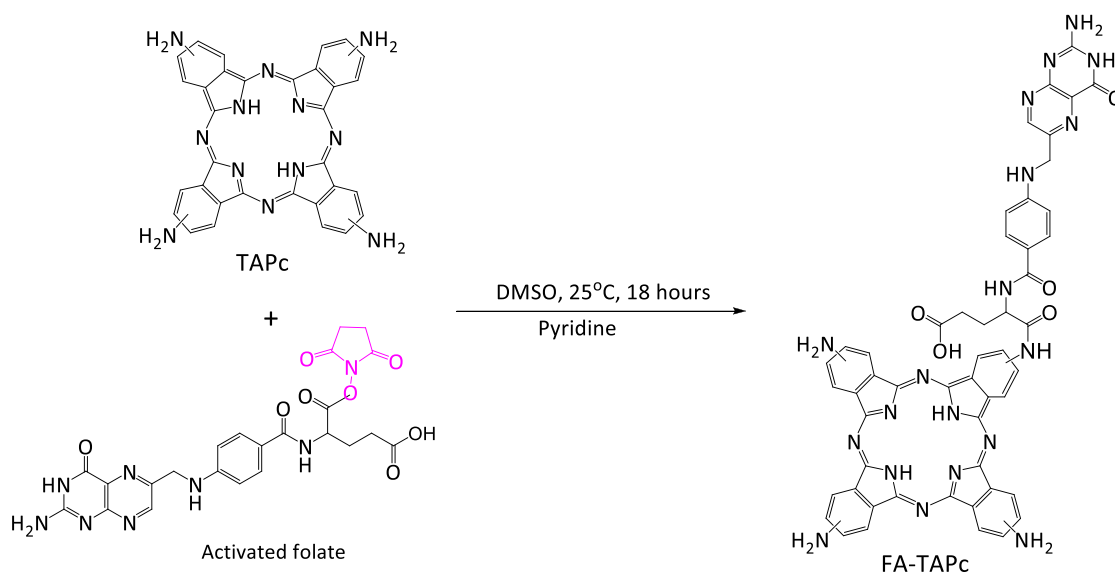
### 2.3.4 Synthesis of folate conjugated TAPc/EDA

Firstly, folic acid was activated (**Scheme 2.3**) using a published method [226].

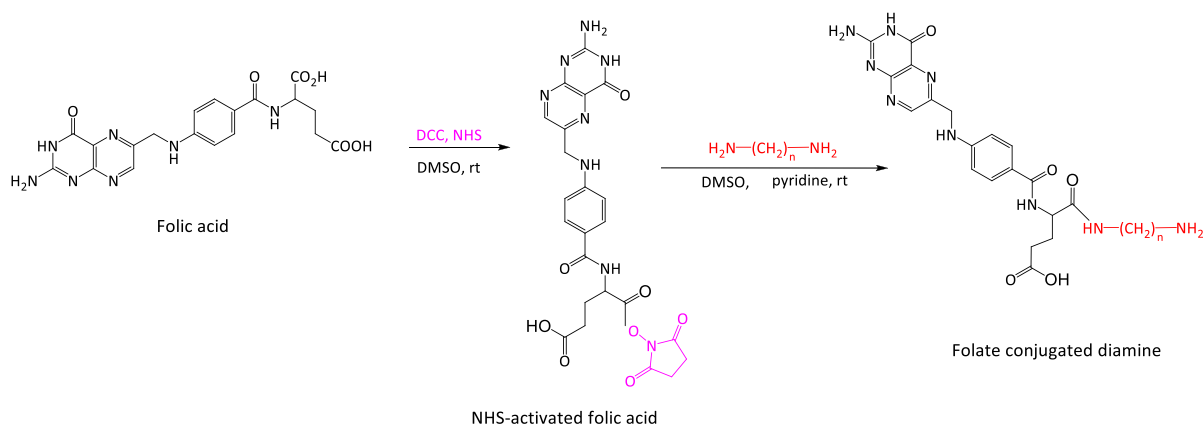


**Scheme 2.3:** The activation of folate for phthalocyanine or diamine conjugation [261].

A solution of TAPc (313 mg) in DMSO was then added to activated folate, and the solution was further stirred at room temperature for 48 h. The solid product was acquired through centrifugation of the resulting solution at 7000 rpm for 10 min (**Scheme 2.4**), and was weighed as described in the literature [258, 262]. Diamines were conjugated to folate (**Scheme 2.5**) as per published literature [223].

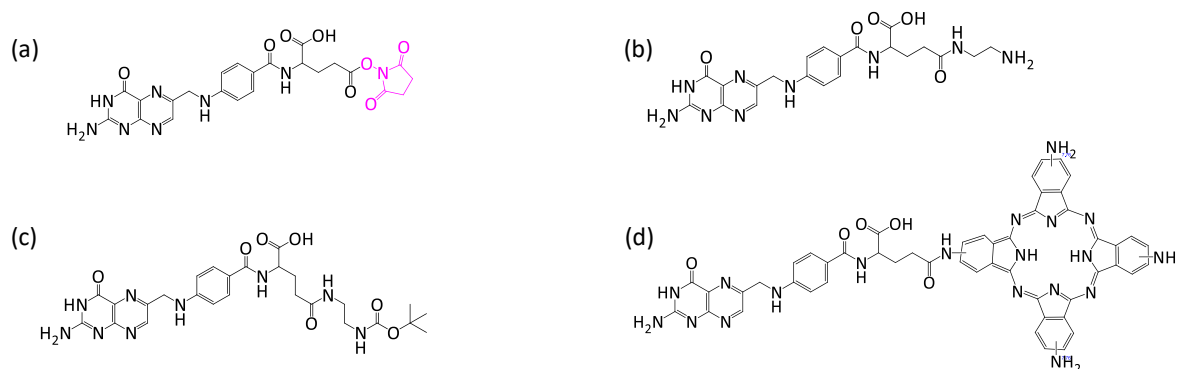


**Scheme 2.4:** Conjugation of activated folate with TAPC [263].



**Scheme 2.5:** Activation of folate and its conjugation to diamines.

After the first step, excess acetonitrile is added for removal of DCC and NHS. Unreacted DCC and NHS precipitate out, and the solution is filtered [263]. A ratio of 1:2:1 (FA:DCC:NHS) gives a yield of 99% activation at the  $\alpha$  position and 90% selectivity. These are the stoichiometric ratios used for all direct conjugation reactions [258]. The conjugation reactions result in both the  $\alpha$  and  $\gamma$  isomers. These isomers were not separated and with the structures of the  $\alpha$ -conjugates presented in-text, the structures of the  $\gamma$ -conjugates are presented (**Scheme 2.6**).



**Scheme 2.6:** The  $\gamma$ -isomers of the folate conjugates; (a) N-Hydroxysuccinimide (NHS) activated folic acid (NHS-FA), (b) tert-Butyloxycarbonyl-ethylenediamine protected folic acid (FA-EDA-Boc), (c) folate-ethylenediamine (FA-EDA), and (d) folate-phthalocyanine (FA-Pc).

### 2.3.5 Synthesis of palladium nanoparticles

The method used was a modification of the previously published methods [264–266]. The adopted synthesis was designed to meet the conditions inherent from the production of the hot isotope [267]. A small amount of  $\text{PdCl}_2$  was dissolved in acidified (10% HCl) millipore water to obtain  $\text{H}_2\text{PdCl}_4$  of known concentration. Gentle continuous stirring was done at room temperature to ensure homogeneity of the mixture. Freshly prepared sodium borohydride solution of known concentration was added dropwise to the brownish palladium chloride solution. The solution was further stirred, and aliquots analysed using UV-Vis to confirm the complete reduction of palladium(II) to palladium(0). Visually, this was noted by the colour change from the brownish solution to a blackish colour. The solution was then transferred to polyethylene tubes and the nanoparticles were subjected to purification by centrifugation at 15 000 rpm for 10 minutes. The obtained precipitate (large nanoparticle sizes) was washed with ethanol and collected by filtration for further analysis. For smaller nanoparticles in solution, the supernatant was carefully removed by using a pasteur pipette or precipitated out using acetone. The nanoparticles were prepared for TEM analysis by ultrasonication in ethanol solution for 30 seconds and collected on the TEM grids.

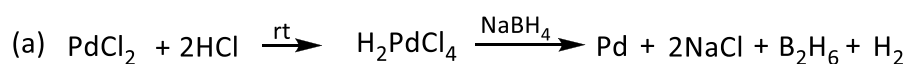
The above was also repeated for the nanoparticles synthesised from potassium tetrachloropalladate ( $\text{K}_2\text{PdCl}_4$ ). The method was the same except for the addition of 10 % HCl. The pH of the nanoparticle's solution was maintained at 7.4.

During preliminary stages, different reducing agents and capping agents were investigated, and the concentrations were optimised with the best conditions retained for future experimentation. The stoichiometric concentration variations employed during optimisation are presented (**Table 2.3**) and the optimal concentrations reported (**Table 3.4**).

**Table 2.3:** An illustration of the varied concentrations of reducing and capping agents used during the concentration ratios optimisation. For each experiment, two parameters were kept constant and one concentration varied until the desired nanoparticle sizes were achieved. X denotes a known concentration.

Sample	Moles of metal salt	Moles of reducing agent	Moles of capping agent
P1	X	0.5X	0.5X
P2	2X	0.5X	0.5X
P3	X	X	X
P4	X	X	5X
P5	X	5X	X
P6	X	5X	10X
P7	X	10X	20X
P8	X	20X	50X

The reducing agent used after optimisation was sodium borohydride and the reaction scheme is presented (**Scheme 2.7**).



**Scheme 2.7:** The reaction scheme of the formation of Pd(0) nanoparticles; (a) the reduction of palladium(II) chloride with sodium borohydride, and (b) the reduction of potassium tetrachloropalladate(II) with sodium borohydride.

### 2.3.6 Synthesis of capped palladium nanoparticles

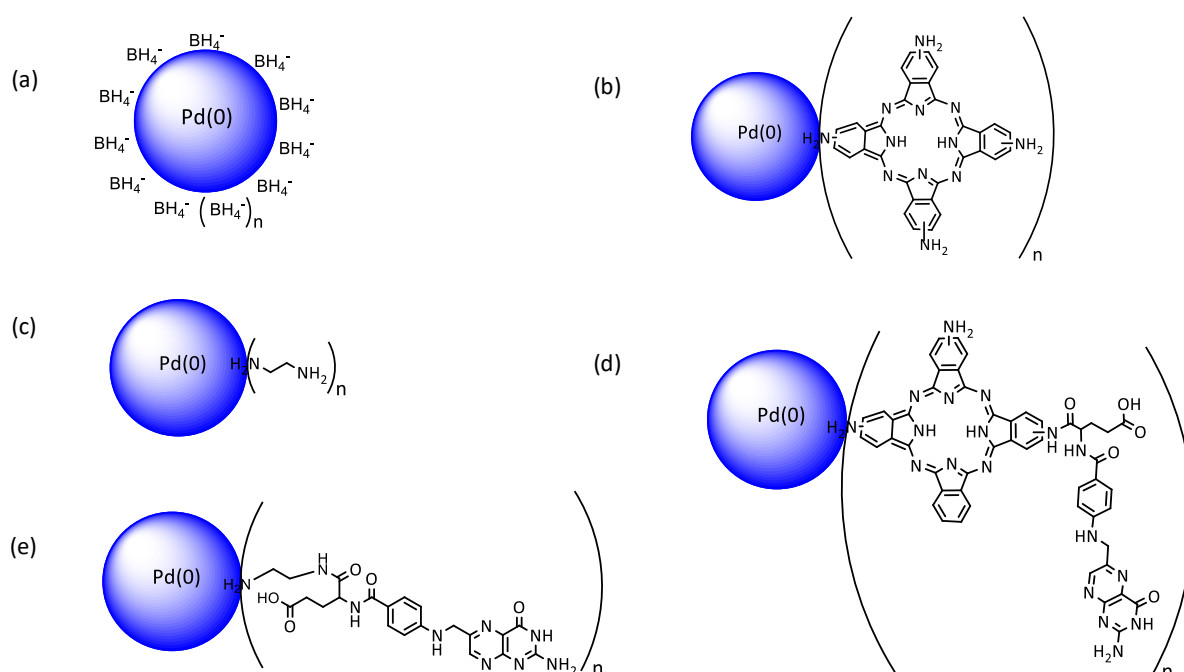
The accurately weighed palladium(II) salt was dissolved in 10% HCl water. The capping agents (known concentration) were mixed with the palladium solution and stirred for at least 10 min before the dropwise addition of the reducing agent. Continuous stirring was done at room temperature (rt) to obtain the capped palladium nanoparticles.



The differently capped palladium nanoparticles; borohydride capped ( $B\hat{h}$ ), tetraaminophthalocyanine-capped ( $TAP\hat{c}$ ), ethylenediamine-capped ( $ED\hat{a}$ ), folate-ethylenediamine capped ( $FA-ED\hat{a}$ ), and folate-tetraaminophthalocyanine-capped ( $FA-TAP\hat{c}$ ), were reported (**Scheme 2.8**). The nanoparticles were categorised into small-, medium-, and large-sized nanoparticles (**Table 2.4**).

**Table 2.4:** The size ranges of the synthesised palladium nanoparticles.

Sample description (abbreviation)	Size range
Small-sized (sz)	Less than 10 nm
Medium sized (mz)	Between 10 and 80 nm
Large-sized (lz)	Between 80 and 300 nm



**Scheme 2.8:** The amine-stabilised palladium nanoparticles; (a) borohydride-capped ( $B\hat{h}$ ), (b) tetraaminophthalocyanine-capped ( $TAP\hat{c}$ ), (c) ethylenediamine-capped ( $ED\hat{a}$ ), (c) folate-ethylenediamine capped ( $FA-ED\hat{a}$ ), and (d) folate-phthalocyanine capped ( $FA-TAP\hat{c}$ ) palladium(0) nanoparticles, where  $n$  is unknown.

## 2.4 CELL LINES AND CULTURE CONDITIONS

The following cell lines were used in this study; MDA-MB-468, MCF-7, MCF-10A, and MDA-MB-231. The cell lines (MCF-7 and MCF-10A) were cultured at 37 °C with 5% carbon dioxide. The MDA-MB-468 cell line were cultured at 37 °C, in a 100% air (CO<sub>2</sub> free atmosphere). The MDA-MB-231 and MDA-MB-468 cell lines were cultured in Leibovitz's (L-15) media supplemented with 10% (v/v) FBS. The MCF-7 cell line was cultured in Dulbecco's Modified Eagle's Medium (DMEM) supplemented with 10 % (v/v) foetal bovine serum (FBS). The MCF-10A cell line was cultured in Hams F 12 media supplemented with 5% (v/v) donor horse serum, 20 ng/mL epidermal growth factor (EGF), 10 µg/mL insulin, and 0.5 µg/mL hydrocortisone. Upon reaching 70-80% confluence, the cells were subcultured from a ratio of 1:4 to a ratio of 1:8 depending on the growth rate of the cell line. Subculturing was performed as follows: the cells were washed thrice with phosphate-buffered saline (PBSA) supplemented with ethylenediaminetetraacetic acid (EDTA) (137 mM NaCl, 2.68 mM KCl, 10 mM Na<sub>2</sub>HPO<sub>4</sub>.12H<sub>2</sub>O, 1.47 mM KH<sub>2</sub>PO<sub>4</sub>, and 0.68 mM of EDTA), with pH 7.4. The cells were trypsinised with a 0.25% (w/v) trypsin PBSA solution for 5 to 15 minutes at 37 °C, the cell detachment was confirmed using a microscope. Cryopreservation was done where necessary by using 10% DMSO (v/v) with the appropriate media and stored in nitrogen vapor. Cell subculturing and or medium change was done every 2 to 3 days, depending on the degree of confluence. The cells were resuspended in the respective media and subcultured in 10 cm<sup>2</sup> tissue culture treated petri-dishes.

## 2.5 CELL VIABILITY ASSAY

The trypan blue exclusion assay and the methythiazol tetrazolium (MTT) assay were routinely used to assess the cell morphology, cell viability, and determine seeding densities during experiments.

The cells were seeded at 50 000 cells per ml in 96-well plate and allowed to attach for 24 h. Initially, the MDA-MB-468 was treated with 100 µM nanoparticle concentrations, however, this concentration was cytotoxic. All cell lines (MDA-MB-238, MCF-7, MDA-MB-231, and MCF-10A) were subsequently treated with 10 µM nanoparticle concentrations (**Table 2.5**).

**Table 2.5:** The treatments used to investigate the cytotoxicity of the compounds used. The reported concentration for the palladium nanoparticles is 10  $\mu$ M palladium(II) content.

Treatment	Abbreviation	Concentration
Untreated	UT	-
Folic acid	FA	1.36 mM
Methotrexate	MTX	1.32 mM
Ethylenediamine	EDA	1.35 mM
Phthalocyanine	Pc	1.36 mM
Folate-ethylenediamine	FA-EDA	1.25 mM
Folate-phthalocyanine	FA-Pc	1.29 mM
Small-sized borohydride capped nanoparticles	sz-B <sup>h</sup> -NPs	10 $\mu$ M
Medium-sized borohydride capped nanoparticles	mz-B <sup>h</sup> -NPs	
Large-sized borohydride capped nanoparticles	lz-B <sup>h</sup> -NPs	
Small-sized ethylenediamine capped nanoparticles	sz-ED <sup>A</sup> -NPs	
Medium-sized ethylenediamine capped nanoparticles	mz-ED <sup>A</sup> -NPs	
Large-sized ethylenediamine capped nanoparticles	lz-ED <sup>A</sup> -NPs	
Small-sized phthalocyanine capped nanoparticles	sz-P <sup>c</sup> -NPs	
Medium-sized phthalocyanine capped nanoparticles	mz-P <sup>c</sup> -NPs	
Large-sized phthalocyanine capped nanoparticles	lz-P <sup>c</sup> -NPs-	
Small-sized folate-ethylenediamine capped nanoparticles	sz-FA-ED <sup>A</sup> -NPs	
Medium-sized folate-ethylenediamine capped nanoparticles	mz-FA-ED <sup>A</sup> -NPs	
Large-sized folate-ethylenediamine capped nanoparticles	lz-FA-ED <sup>A</sup> -NPs	
Small-sized folate-phthalocyanine capped nanoparticles	sz-FA-P <sup>c</sup> -NPs	
Medium-sized folate-phthalocyanine capped nanoparticles	mz-FA-P <sup>c</sup> -NPs	
Large-sized folate-phthalocyanine capped nanoparticles	lz-FA-P <sup>c</sup> -NPs	

### 2.5.1 Trypan Blue Exclusion Assay

A 20  $\mu$ L aliquot of 0.4% trypan blue solution was mixed with 20  $\mu$ L of cell suspension and vortexed. The cells (10 $\mu$ L) were counted using a haemocytometer and a Zeiss Primo Star light microscope. Trypan blue penetrates dead cells staining their cytoplasm blue while live cells remain clear. Unstained (viable) and stained (nonviable) cells were counted in the 16 squares

in the corner of the grid. The cells were diluted to the appropriate cell densities (equation 1), seeded as per the assay requirements, and cell viability determined (equation 2).

$$\text{Cell density (number of cell per mL)} = \text{number of cells (mm}^{-2}\text{)} \times 2 \text{ (dilution factor)} \times 10^4 \quad (1)$$

$$\text{Cell viability (\%)} = \frac{\text{Number of viable cells (stained cells)}}{\text{Total number of cells (stained and unstained cells)}} \times 100 \quad (2)$$

### 2.5.2 Methylthiazol tetrazolium (MTT) assay

To determine cell viability, the MTT assay was performed. After 24 hours of treatments exposure, the medium was aspirated and replaced with 200  $\mu\text{L}$  of fresh media containing 0.5 mg/mL MTT and incubated for 2 hours for the MDA-MB-468, MDA-MB-231, and MCF-7 cell line, and 3 hours for the MCF-10A cell line. Subsequently, the excess MTT was removed and the formazan crystals were solubilised using DMSO. The absorbance was read at 540 nm and recorded on an Epoch 2 Powerwave spectrophotometer (BioTek) The formation of purple formazan from the reduction of yellow (3-(4,5-dimethylthiazol-2-yl)-2,5-diphenyltetrazolium bromide by mitochondrial reductase enzymes only occurs in live cells.

A standard curve of 0–100 000 cells was used to determine cell number and allow for normalisation. The cells were allowed to attach for 4-8 h, and MTT assay was performed. All treatments were conducted in triplicate (N=3).

## 2.6 CELL UPTAKE STUDIES: TRANSMISSION ELECTRON MICROSCOPY (TEM)

The cells were split and grown in 10  $\text{cm}^2$  petri dishes until  $\pm$  80% confluence. The cells were treated for 24 hours with the following palladium nanoparticles; small-sized and medium-sized borohydride, folate-phthalocyanine, and folate-ethylenediamine capped nanoparticles (Untreated cell lines were used as control). After the 24-hour treatment exposure, the cells were washed thrice with PBS at 37  $^{\circ}\text{C}$ . The cells were fixed using a prewarmed (37  $^{\circ}\text{C}$ ) 2.5% glutaraldehyde and 2% paraformaldehyde in media in a 0.1 M cacodylate buffer at a controlled pH of 7.4 at room temperature. After an hour, the cells were gently scraped off the plate using a scrapper, aliquoted into test tubes, pelleted loosely and fixed for 3 hours. The cell pellet was washed thrice with cacodylate buffer at 5 min intervals and spun between the washes.

The cells were stained with 1% osmium tetroxide in cacodylate buffer for 1.5 hours at 4  $^{\circ}\text{C}$ . The cells were washed several times with cacodylate buffer, dehydrated in 10% and 70% ethanol for 10 minutes and further dehydrated in 100% ethanol for 15 minutes, and. in propylene

oxide twice for 15 minutes. The pellet was infiltrated with epoxy resin/propylene oxide 1:1 ratio mixture for at least 1.5 hours on a rotary. An overnight infiltration with 100% epoxy resin was done at room temperature. The cells pellet was embedded on the epoxy resin in dried plastic and polymerise at 60-70°C for 18–24 hours. Ultrathin sections of 70–100 nm were cut using glass microtome a diamond knife, collected on carbon-coated copper grids, and stained with uranyl acetate and lead citrate [268]. Specimens were analysed using TEM.

Some specimens were viewed unstained (without the osmium tetroxide, uranyl acetate and lead citrate contrasting steps), some with only osmium tetroxide staining, and others with only uranyl acetate and lead citrate providing the contrast (**Section 4.4.1**).

## **2.7 CELL UPTAKE STUDIES: INDUCTIVELY COUPLED PLASMA-OPTICAL EMISSION SPECTROSCOPY (ICP-OES)**

Cells were cultured and grown as previously described (**Section 2.4**). After 24 hour exposure to treatments (10 µM palladium content small-sized and medium-sized borohydride, folate-phthalocyanine, and folate-ethylenediamine capped nanoparticles and untreated cell line was used as control), cells were carefully washed thrice with 3 mL PBS solution. Each cell well was treated with 0.5 mL of 0.5 M HNO<sub>3</sub> for 1-1.5 h at room temperature. The cell well contents were transferred and stored in eppendorfs. Milli-Q water was used to fill 15 mL tubes and the metal ions concentration determined using ICP-OES [269, 270].

## **2.8 STATISTICS**

For the cytotoxic effects of the nanoparticles, the presented data are a mean ± standard deviation from the three measurements (N=3) and were analysed using descriptive statistics and single factor analysis of variance.

The significance of the results in comparison to the control was determined using Microsoft Excel 2016 by one way analysis of variance (ANOVA) function. The significance was marked with asterisks \* for p-value <0.05 (statistically significant), \*\* for p-value <0.01 (statistically significant), and \*\*\* for p-value <0.001 (statistically highly significant).

## CHAPTER THREE: SYNTHESIS, OPTIMISATION, AND CHARACTERISATION OF CONJUGATES AND NANOPARTICLES

### 3.1 GENERAL INTRODUCTION

Several novel nanotechnology methods are currently under investigation and development for cancer therapy, with nanotechnology offering the opportunity to produce specific nanoparticles holding capabilities [49, 271]. Over the past few years, the synthesis of nanoparticles with optimal catalytic or bio-friendly properties has been the focus of extensive research [272–274]. The synthesis and use of nanoparticles constitute a major research area that attracts both academic and industrial interest [275]. As intensively discussed (**Section 1.3**), the synthesis and optimisation of nanoparticles is critical in ensuring cellular uptake and internalisation. A great deal of previous research has focused on the synthesis of nanoparticles and cellular uptake, delivery, and cell membrane interactions are key considerations in the nanoradiopharmaceutical design [276–278]. The size, shape or morphology, surface charge, stability, and other physical and chemical properties were carefully monitored, and the experimental reproducibility investigated. The unique physical and chemical characteristics of nanoparticles results in the differences in chemical and biological activities, highlighting the importance of constant synthesis parameters [279].

The investigation of the following nanoparticle synthetic parameters was conducted; temperature, time, pH and importantly the concentrations of precursor salt, capping and reducing agents used. With limited synthesis procedures available in the literature, different stoichiometric ratios, and reducing agents were used to synthesise different sizes of the nanoparticles [264, 280–282].

Generally, a fast, simple, reliable, and eco-friendly process for the synthesis of nanoradiopharmaceutical is critical [283, 284]. In this study, of foremost importance was the need to employ a green chemistry synthesis procedure while controlling physical and chemical parameters, lowering immunogenicity, and minimising the cost of production for future clinical use. The preferred capping agent or conjugate should uniquely target cells and be characterised by optimal binding affinity and minimal immunogenicity [161].

More recent attention has focused on the synthesis of nanoparticles using greener synthetic routes [285, 286]. Green chemistry is all about reducing and eliminating the use of substances hazardous to human health and the environment [125, 287]. Strategies of addressing the

mounting environmental concerns with the current approach include the use of benign solvents, biodegradable polymers, and non-toxic chemicals [284]. The use of simple diamines, tetraaminophthalocyanines, and their folate conjugates as capping agents was considered and explored.

### 3.2 SYNTHESIS AND CHARACTERISATION OF CAPPING AGENTS

The amine groups-containing diamines and tetraaminophthalocyanine were used as capping agents. Ethylenediamine was subsequently chosen as the best diamine, by elimination. The folate conjugation of ethylenediamine and tetraaminophthalocyanine is outlined (**Section 3.2.1 - 3.2.3**).

#### 3.2.1 Synthesis of tetraaminophthalocyanine (TAPc)

Phthalocyanines are planar molecules with 18- $\pi$  electron systems which are known for their intense dark green colour [288]. They are thermodynamically and chemically stable and have medical applications [289–291]. The obtained UV-Vis spectroscopy characterisation of the intermediates synthesised during the synthesis of tetraaminophthalocyanine (TAPc) (**Scheme 2.2**) were presented (**Figure 3.1**).

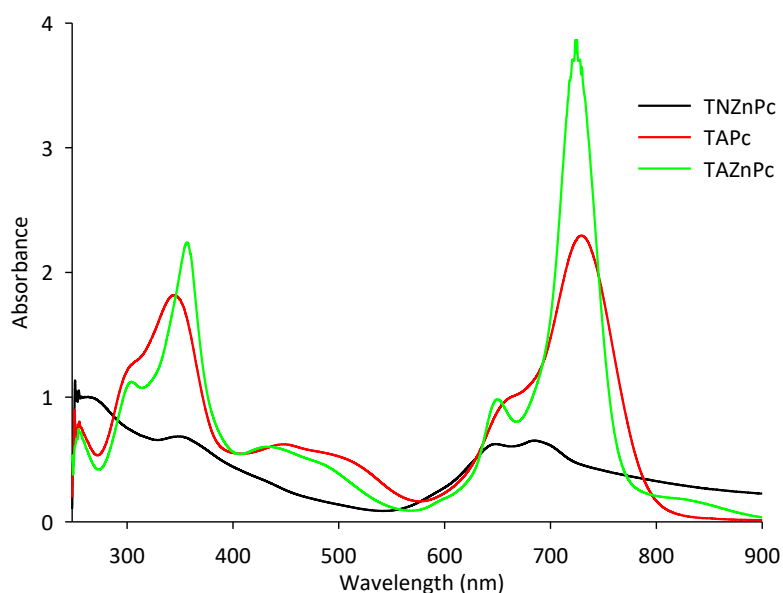


**Figure 3.1:** The UV-Vis spectra of the different phthalocyanine compounds; zinc tetranitrophthalocyanine (TNZnPc), tetraaminophthalocyanine (TAPc), and zinc tetranitrophthalocyanine (TAZnPc).

The lack of sharpness of bands for TNZnPc is possibly due to possible aggregation. It is evident (for TNZnPc) that nitro (-NO) group causes slight splitting of the Q-band. The amino (-NH<sub>2</sub>) group on the TAPc shows a bathochromic shift that occurred due to the negative inductive effect of NH<sub>2</sub> (**Figure 3.1**). Splitting of the Q-band indicates the presence of both monomeric and dimeric forms of the complexes in formation. The shoulder or splitting of the observed peak can also be due to the fine vibronic structure in addition to dimeric species in solution [292].

Phthalocyanines have a strong absorption band in the far red in the visible region of the spectrum, near 670 nm, known as a Q-band, usually accompanied by a vibronic shoulder which is caused by their intense green colour. A less intense band is usually observed near 340 nm and is known as the B-band [293]. An unmetalated Pc exhibits a split Q-band due to a non-degenerate LUMO, giving rise to 2 allowed electronic transitions of different energies.

Gourtaman's four orbital theory suggests that these bands arise due to the electronic transitions between the HOMO ( $a_{1u}$  and  $a_{2u}$ ) to the LUMO (doubly degenerate  $e_g$ ) [294]. Q-band is a result of the transition from  $a_{2u}$  of HOMO to degenerate  $e_g$  of LUMO. B-band is a result of the superimposition of  $B_1$  and  $B_c$  that arises from transitions between  $a_{2u}$  and  $b_{2u}$  of HOMO to the  $e_{2g}$  of LUMO [294, 295]. The reproducibility of the synthesis of tetraaminophthalocyanine was confirmed and corroborated with published literature [262, 296–298]. The products were further characterised with FTIR (**Figure 3.2**).



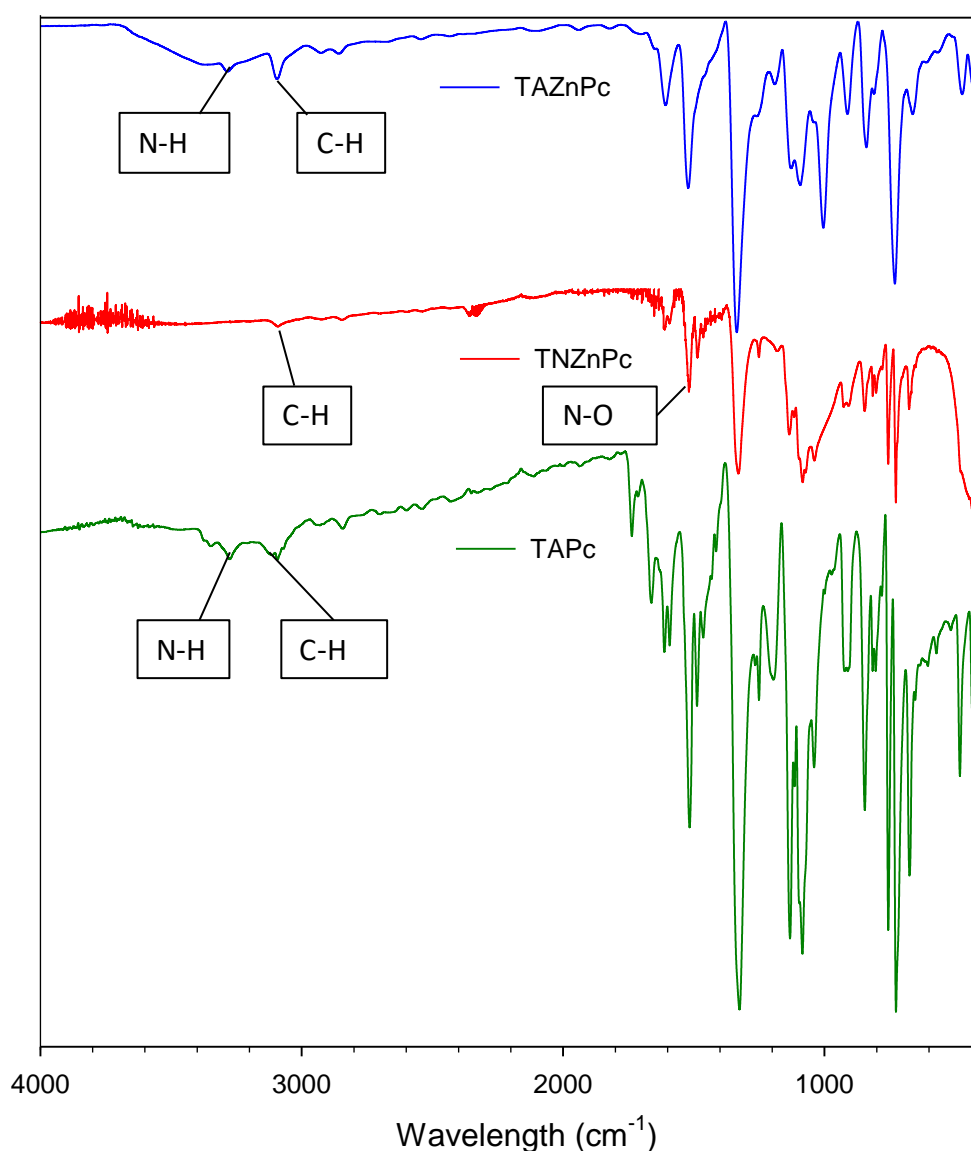


**Figure 3.2:** Overlaid FTIR spectra of the different phthalocyanine compounds; zinc tetranitrophthalocyanine (TNZnPc), tetraaminophthalocyanine (TAPc), and tetranitrophthalocyanine (TAZnPc).

The spectrum of TNZnPc (**Figure 3.2**) displayed a  $\nu(\text{N-O})$  peak at  $1538\text{ cm}^{-1}$ . An aromatic  $\nu(\text{C-N})$  bond peak at  $1332\text{ cm}^{-1}$  and the  $\nu(\text{C-H})$  stretch peak around  $3100\text{ cm}^{-1}$  are significant and consistent for all the phthalocyanine compounds. The amine  $\nu(\text{N-H})$  peaks were notable around  $3362\text{ cm}^{-1}$  for both the amino group-containing phthalocyanines.

The notable disappearance of the nitro (-NO) group and the successful formation of the amino (-NH<sub>2</sub>) group (Figure 3.2) confirmed the success of the reaction (Scheme 2.2). A comparison of the TAZnPc and TAPc spectra does not explicitly show the difference between the two compounds. This might be due to the limitation of the FTIR technique and the incomplete demetallation of TAZnPc. However, there is a difference in the NH bending region the visual difference (intensity of the green colour) and the UV-Vis confirmation concurred with the published literature on the two compounds [262, 296–298].

With little to no reported <sup>13</sup>C-NMR spectrum for tetraaminophthalocyanines. The obtained spectrum (Figure 3.3) showed more than 80% similarity to the expected spectrum as estimated by ChemDraw [299]. This further confirmed the success of the synthesis. For the rest of this thesis, tetraaminophthalocyanine (TAPc) is referred to as phthalocyanine (Pc).

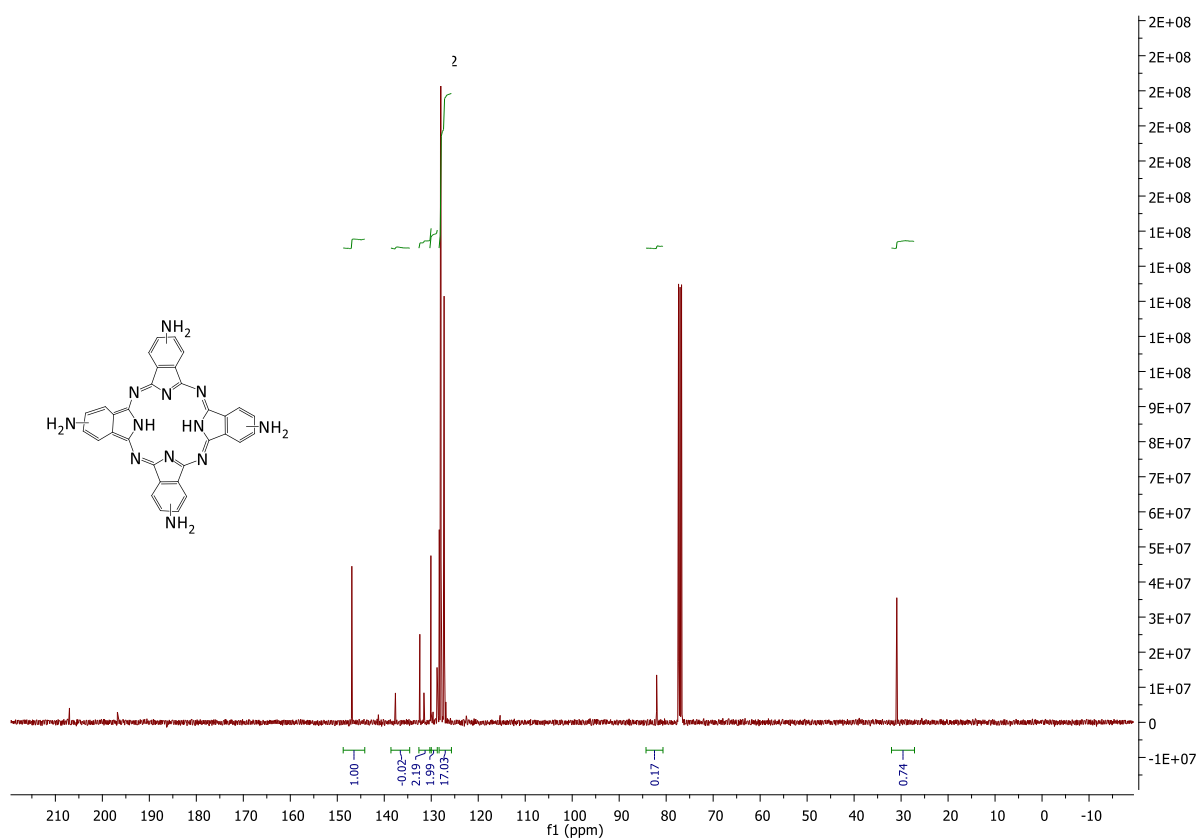
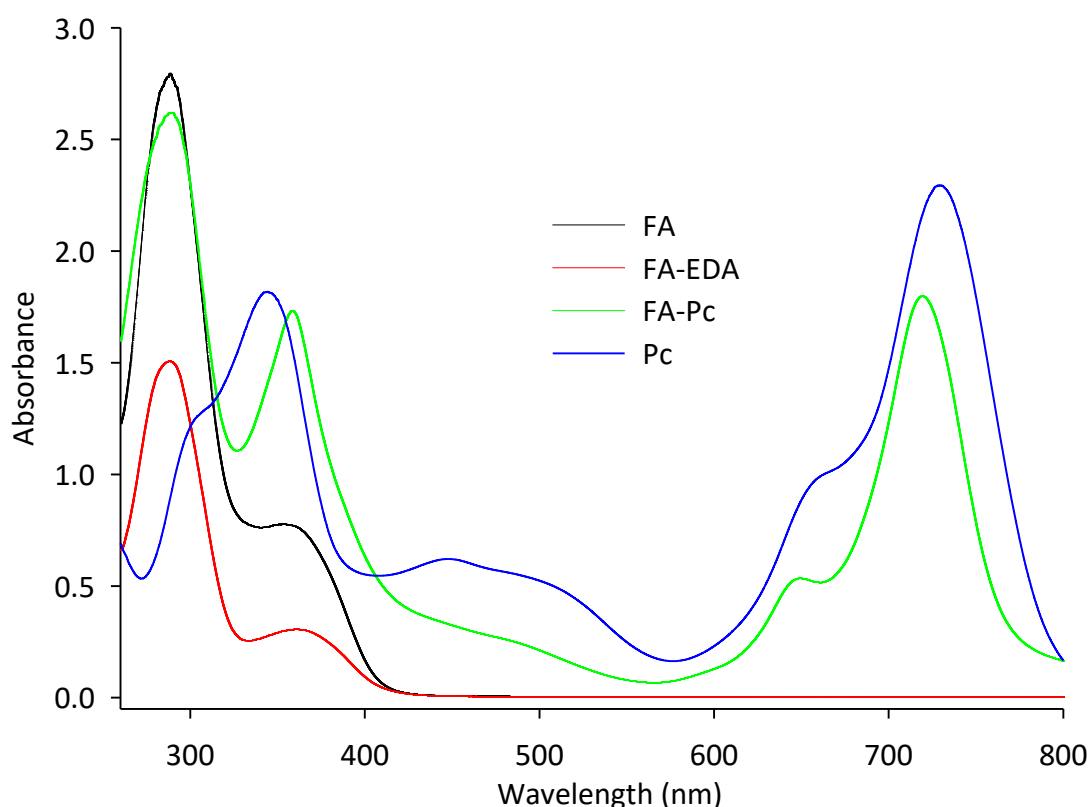


Figure 3.3: The <sup>13</sup>C-NMR spectrum of the synthesised tetraaminophthalocyanine.

### 3.2.2 Synthesis of folate-phthalocyanine

The folate-phthalocyanine was synthesised (Scheme 2.4) and the obtained final product was characterised using UV-Vis (Figure 3.4), LC-MS (Figure 3.5), and FTIR (Figure 3.6).



**Figure 3.4:** The UV-Vis spectra of folate (FA), folate-ethylenediamine (FA-EDA), folate-phthalocyanine (FA-Pc), and phthalocyanine (Pc).

Folate (FA) showed two peaks, around 290 and 360 nm. The formation of the additional amide bond between the folic acid carboxylic group and the amine group of the ethylenediamine or phthalocyanine resulted in spectral shifts. The presence of the peaks at 670 and 730 nm for the folate-phthalocyanine (FA-Pc) confirmed the presence of phthalocyanine  $\pi$ -bond systems in the FA-Pc compound, absent in folate-ethylenediamine (FA-EDA) and folate spectra [300]. A notable folate bathochromic shift from 350 nm to 380 nm (B-band) confirmed the folate-phthalocyanine conjugation, together with the phthalocyanine hypsochromic shift 735 nm to 715 nm (**Figure 3.4**). These shifts can be attributed to the phthalocyanine-folate auxochrome-chromophore effect. Folate-phthalocyanine had different molecular spectra from either folate or phthalocyanine. The prominent peak at 715 nm (Q-band) confirmed the success of the FA-Pc conjugation.

$\gamma$ -conjugates are intrinsically obtained as the primary product (between 55 to 90% selectivity using carbodiimide chemistry), and both conjugates have reported medicinal relevance [258]. The  $\gamma$ -carboxyl conjugate also maintains a high affinity to the folate receptor, and the

mechanism of cellular uptake is as effective as that of folic acid [301, 302]. With this in mind, the separation of the two isomers was not conducted. The reported characterisation and analysis are for the unseparated isomers. However, the structures of the  $\gamma$ -isomers were presented (**Scheme 2.6**). The liquid chromatography-mass spectrometry (LC-MS) data of the folate-phthalocyanine (**Figure 3.5**) was analysed.

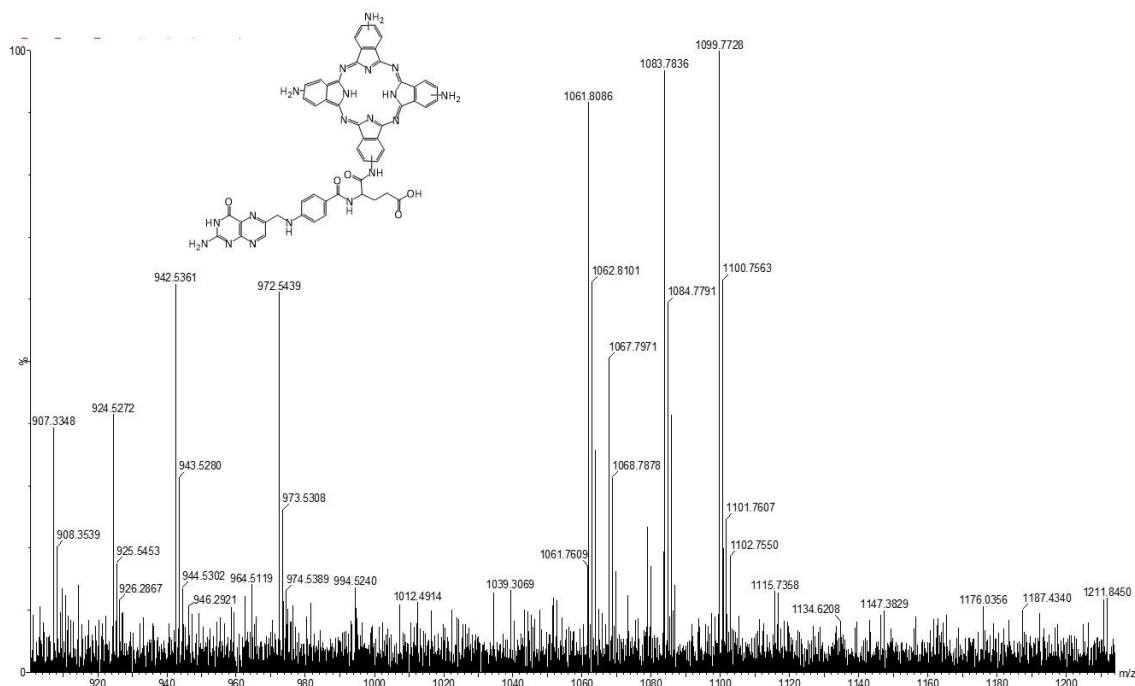


**Figure 3.5:** The LC-MS of the folate-phthalocyanine.

The successful formation of folate-phthalocyanine ( $C_{55}H_{55}N_{19}O_5$ ) is evidenced by the  $m/z$  of 1061.81. The prominent peaks at 1062.81 and 1063.81 are undoubtedly allocated to  $M+1$  and  $M+2$ , respectively. The other unexpected and unwanted peaks are due to fragmentation, dimerisation, and impurity of the obtained compound. The peak at 1147.38 is due to the formation of activated folate-phthalocyanine ( $M+1$ ) which is an impurity of the final product. Phthalocyanines are known to fragment. The used (commercial) folate was found to contain some impurities (**Table 3.1**) and also contributed to the presence of many peaks. FTIR spectra of the precursor compounds and conjugates were analysed and compared (**Figure 3.6**).

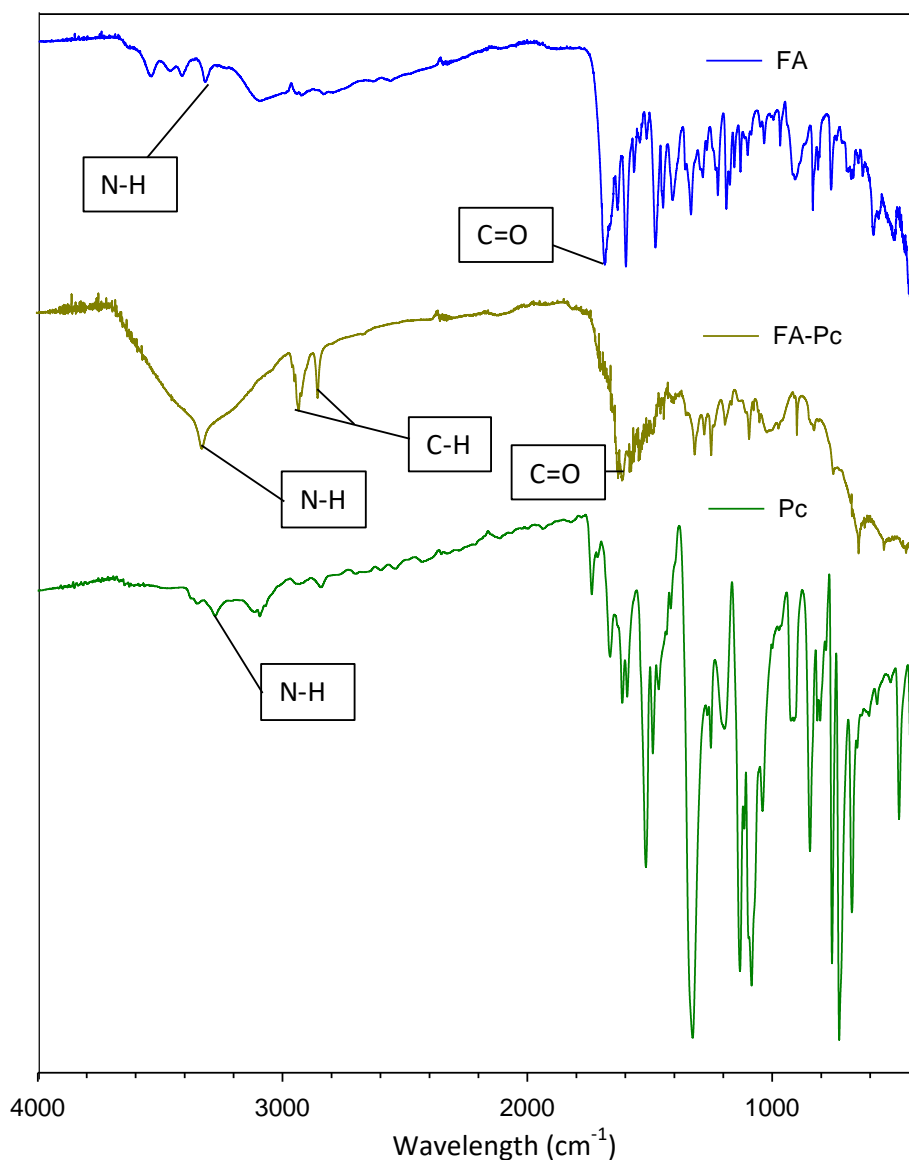


**Figure 3.6:** The FTIR spectra of folate (FA), folate-phthalocyanine (FA-Pc), and phthalocyanine (Pc).

The spectrum for folic acid (FA) shows a peak corresponding to the carbonyl  $\nu(\text{C}=\text{O})$  stretch around  $1675\text{ cm}^{-1}$ . Furthermore, the in-ring carbon to carbon  $\nu(\text{C}=\text{C})$  stretch at  $1591\text{ cm}^{-1}$  is common for folate and also appeared in folate-phthalocyanine (FA-Pc). FA-Pc shows an amine  $\nu(\text{N}-\text{H})$  sharp stretch at  $3308\text{ cm}^{-1}$ . Notable  $\nu(\text{C}-\text{H})$  stretches at  $2928\text{ cm}^{-1}$  and  $2836\text{ cm}^{-1}$ , and the prominent medium intensity  $\nu(\text{C}=\text{O})$  stretch at  $1645\text{ cm}^{-1}$  specific for FA-Pc are observed. An  $\nu(\text{N}-\text{H})$  bend for primary amines around  $1620\text{ cm}^{-1}$  is shared across the three compounds. Pc exhibits a unique peak for  $\nu(\text{C}=\text{C})$  aromatic stretch at  $1525\text{ cm}^{-1}$ . FA-Pc FTIR corresponds to

reported literature. The obtained UV-Vis and FTIR for Pc-conjugation are in agreement with recently published literature [303, 304].

### 3.2.3 Synthesis of folate-ethylenediamine

The folate-ethylenediamine was analysed and the characterisation of the N-Boc protected folate-ethylenediamine's  $^1\text{H-NMR}$  reported (**Figure 3.7**).

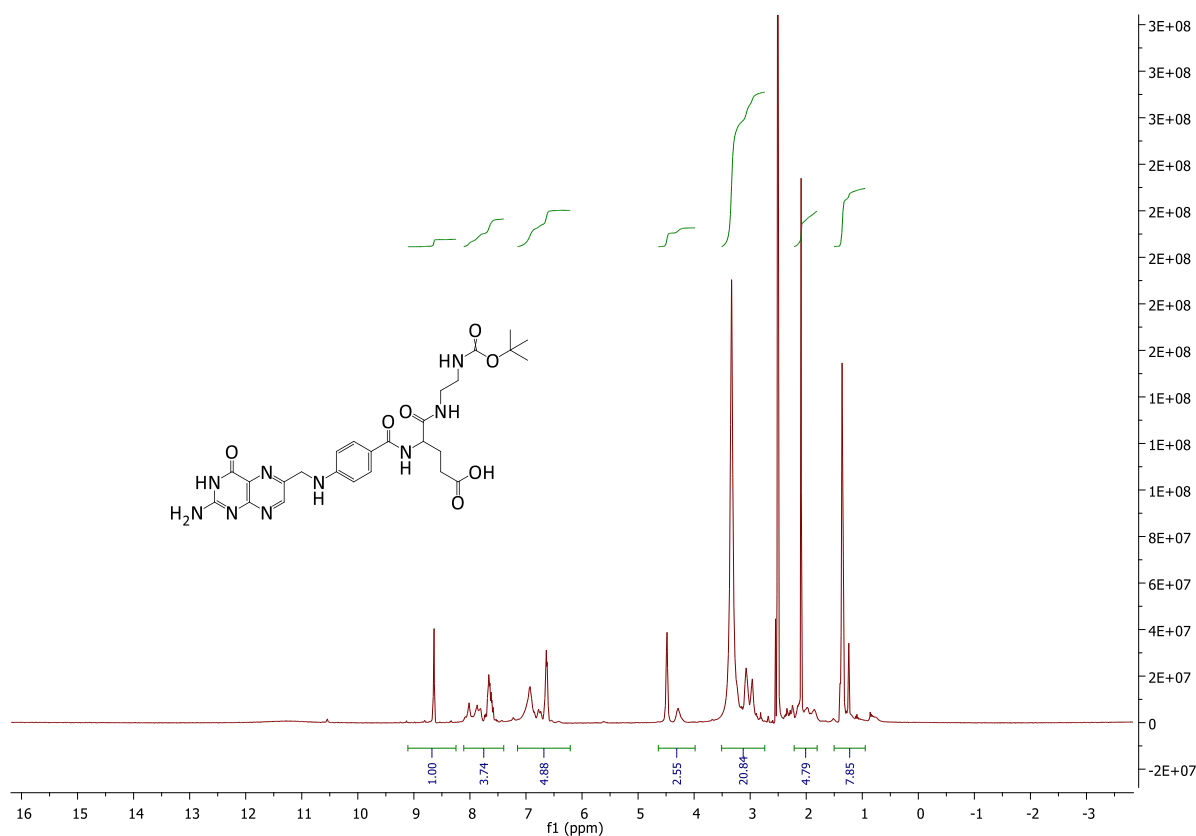


**Figure 3.7:** The  $^1\text{H-NMR}$  of the N-Boc-ethylenediamine-folate conjugate.

The obtained  $^1\text{H-NMR}$  is consistent with the one available in the literature [258].  $^1\text{H-NMR}$  (400 MHz,  $\text{D}_6\text{MSO}$ ) ( $\delta$ ): 8.64 (s, 1H, pterin), 8.04 - 7.86 (m, 2H), 7.68 - 7.62 (m, 2H, aromatic), 7.10 - 6.82 (m, 3H), 6.65 - 6.53 (d, 2H, aromatic), 4.48 (bs, 2H, aromatic), 4.27 (m, 1H,  $\alpha\text{H}$ ), 3.43 (bs, water), 3.06 - 2.88 (m, 4H, ethylenediamine), 2.28 - 1.85 (m, 4H, glutamic moiety), 1.35 (s, 9H, Boc). After the deprotection step of N-Boc, ethylenediamine-folate  $^1\text{H-NMR}$  was reported (**Figure 3.8**).

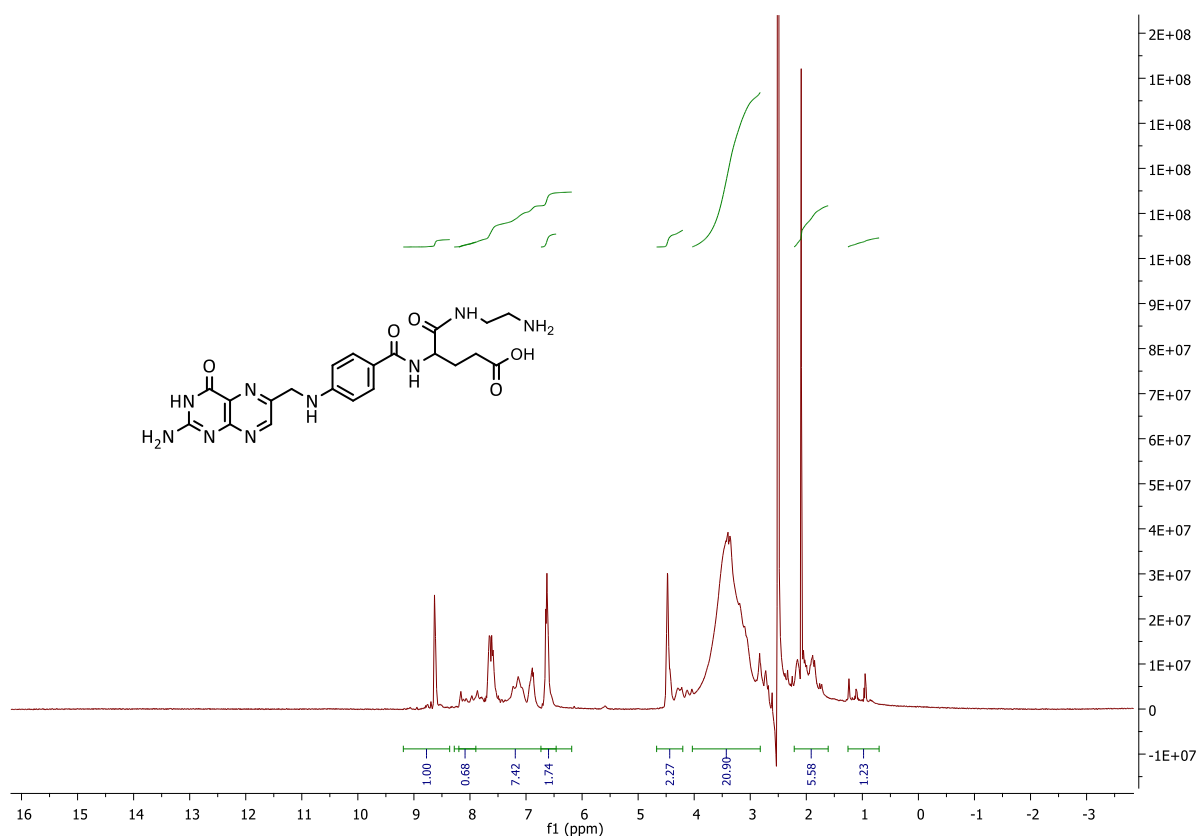


**Figure 3.8:** The  $^1\text{H-NMR}$  of the folate-ethylenediamine

$^1\text{H-NMR}$  measurement obtained from a 400 MHz using  $\text{D}_6\text{MSO}$  as a solvent exhibited the following peaks ( $\delta$ ): 8.64 (s, 1H, pterin), 8.19 - 7.96 (m, 1H), 7.66 - 7.58 (m, 2H, aromatic), 7.18 - 6.91 (m, 3H), 6.66 - 6.53 (m, 2H, aromatic), 4.47 (bs, 2H, benzylic), 4.31 - 4.07 (m, 1H), 3.52 (water), 2.92 - 2.60 (m, 2H, ethylenediamine), and 2.24 - 1.93 (m, 4H, glutamic moiety). The obtained  $^1\text{H-NMR}$  was as expected [258].

The LC-MS of the synthesised folate-ethylenediamine ( $\text{C}_{21}\text{H}_{25}\text{N}_9\text{O}_5$ ) (**Figure 3.9**) was analysed. The formation of the expected product is irrefutably confirmed with the prominent  $m/z$  peaks at 484.20 and 485.20 which correspond to  $M+1$  and  $M+2$ , respectively, for folate-ethylenediamine (**Figure 3.9**). The possible presence of folate at 442.14 ( $M+1$ ) and the presence of some activated folate (NHS-folate) can also be suggested as the unlabelled peaks at 523.16 and 524.17 for  $M+1$ , and  $M+2$ , respectively, are significant. It is further noted that there is a possibility of some unreacted N-Boc-ethylenediamine-folate due to the presence of the unlabelled 584.25 and 585.26 peaks which can be assigned to  $M+1$  and  $M+2$  of N-Boc-EDA-FA. The peaks at 569.36, 570.36, and 557.38 are attributed to possible folate-ethylenediamine with Boc fragments attached to it.

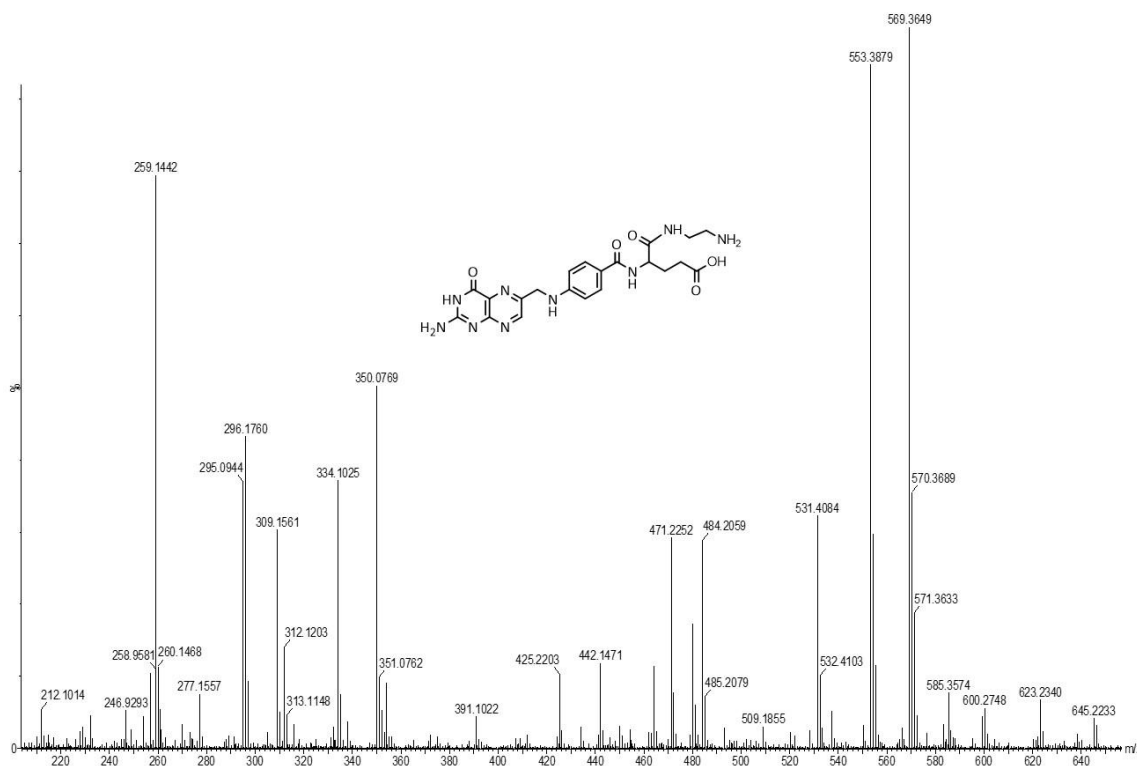


**Figure 3.9:** The LC-MS of the folate-ethylenediamine.

Due to possible dimerisation, fragmentation and incomplete purifications, few unexpected peaks are seen (**Figure 3.9**). However, the toxicity of all the reactants and all the formed products were investigated (**Chapter 4**), and their possible presence were not significant to our study. For further characterisation, FTIR analysis was performed (**Figure 3.10**).



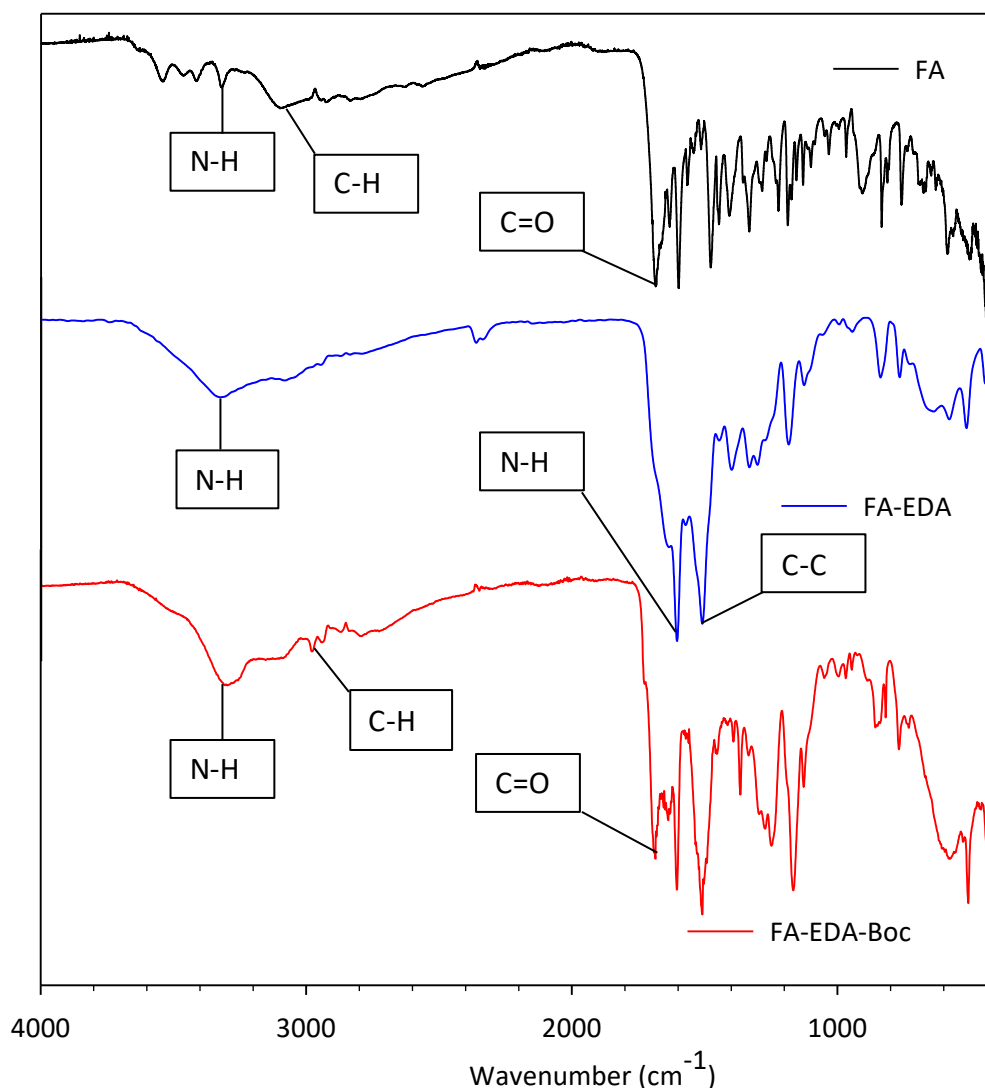


**Figure 3.10:** The FTIR spectra of folate (FA), folate-ethylenediamine (FA-EDA), and N-Boc-ethylenediamine-folate conjugate (FA-EDA-Boc).

Folate (FA) showed an amine  $\nu(\text{N-H})$  peak at  $3318\text{ cm}^{-1}$ , alkane  $\nu(\text{C-H})$  peak at  $3109\text{ cm}^{-1}$ , and a carbonyl  $\nu(\text{C=O})$  peak at  $1693\text{ cm}^{-1}$  (**Figure 3.10**). FA-EDA exhibited a peak for the amide  $\nu(\text{N-H})$  group at  $3311\text{ cm}^{-1}$  and the amine  $\nu(\text{N-H})$  group's peak at  $1590\text{ cm}^{-1}$ . Carbon to carbon  $\nu(\text{C=C})$  in ring peak at  $1499\text{ cm}^{-1}$  is significant and clearly seen for FA-EDA. FA-EDA-BOC showed a broad amide N-H bend at  $3299\text{ cm}^{-1}$ , a carbonyl  $\nu(\text{C=O})$  at  $1692\text{ cm}^{-1}$ , and an alkane  $\nu(\text{C-H})$  at  $3005\text{ cm}^{-1}$ .

Elemental analysis of folate (FA), folate-ethylenediamine (FA-EDA), and folate-phthalocyanine (FA-Pc) was determined (**Table 3.1**).

**Table 3.1:** The obtained elemental compositions (%) for the purchased folate and synthesised conjugates; folate-ethylenediamine (FA-EDA) and folate-phthalocyanine (FA-Pc).

Element	Folate (C <sub>19</sub> H <sub>19</sub> N <sub>7</sub> O <sub>6</sub> )		FA-EDA (C <sub>21</sub> H <sub>25</sub> N <sub>9</sub> O <sub>5</sub> )		FA-Pc (C <sub>55</sub> H <sub>55</sub> N <sub>19</sub> O <sub>5</sub> )	
	Expected	Obtained	Expected	Obtained	Expected	Obtained
C	51.70	49.48	52.17	46.37	62.19	44.1
H	4.34	6.81	5.21	5.81	5.22	0.54
N	22.21	20.24	26.07	22.82	25.06	19.01

The elemental analysis of the commercially purchased folate was done as an instrumentation control. From its values, a  $\pm 2\%$  variation was obtained for the reported data. However, the obtained results for folate-ethylenediamine and folate-phthalocyanines did not correlate with the expected values. The deviation agrees with the LC-MS spectra (**Figure 3.5** and **Figure 3.9**), and this is attributed to impurities. These results should be accepted given that the commercial folate used was not free of impurities. After the successful synthesis of phthalocyanines, folate-ethylenediamine and folate-phthalocyanine, the synthesis of nanoparticles was conducted.

### 3.3 PRELIMINARY OPTIMISATION OF SYNTHESIS PARAMETERS

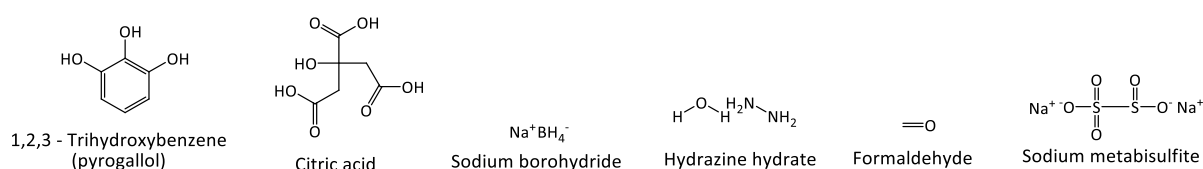
With size and morphology being primarily dependent on capping agent used, employing a reducing agent, reaction time, the ratio of the precursor to the other reagents, and ionic strength of solvent used is key [305]. To optimise the essential size and desired morphology, the effects of using different reducing and capping agents were investigated. The cost-effectiveness, time-efficiency, ease of synthesis, and reproducibility of the results were vital. Taking into account all the principal factors previously discussed (**Section 1.3.2**), the selection of the reducing and capping agents was conducted.

The use of a greener solvent, water, was preferred to organic solvents. Water is non-flammable, non-toxic, and non-tumorigenic. Dispersity of the nanoparticles in water without loss of physical and chemical properties over extended periods of time was studied. The water-based synthesis of nanoparticles is fraught with the problem as a result of ionic interactions, which were overcome by using low concentrations of the precursor molecule (about  $5 \times 10^{-4}$  M) [275]. Literature exists that support the need for the development of an environmentally friendly medium in place of the commonly used volatile, toxic organic, ionic solvents, and polyionic liquids synthesis [306, 307].

The reducing power of the reducing agent is reported to be pH dependent [308]. As a result, a neutral pH was carefully monitored and controlled. Strong reducing agents rapidly increase nucleation [309] and makes it difficult to obtain nanoparticles with a uniform size. Weaker reductants are usually preferred at higher temperatures and stronger reductants preferred at low temperatures [305, 309]. Pd(II) is reported to be reduced by alcohols, sodium borohydride, ascorbic acid, hydrazine, poly(ethylene glycol) (PEG), dimethylamine borane in supercritical carbon dioxide, thermal induced reduction and sonochemical reduction under different reaction conditions [310–318]. Commonly used capping agents include long chain hydrocarbons, polymers, dendrimers, block copolymers, small molecules, polysaccharides etc. [319]. The size, shape, and morphology of the palladium nanoparticles can be controlled in a narrow range by changing the concentration of the starting materials as previously reported [320]. Taking into account the above, the selection of reducing and capping agents was conducted as detailed below.

### 3.3.1 Reducing and capping agents

One of the primary aims of this study was to develop a greener synthesis method of palladium nanoparticles at room temperature in water with minimum time. Unlike most of the organic solvents, water is non-flammable, non-toxic, and non-tumorigenic. With the reducing and capping agent being key determinants on most of the nanoparticle's properties, the different reducing agents (**Scheme 3.1**) and commercially available capping agents (**Scheme 3.2**) were used.



**Scheme 3.1:** The different reducing agents investigated in the optimisation of the required nanoparticle sizes.

Firstly, the reducing abilities of the reducing agents were investigated without any capping agents used. Some reducing agents can reduce and cap or stabilise the formed nanoparticles. However, the primary focus was on the reducing agent strength to reduce Pd(II) to crystalline Pd(0) at room temperature in an aqueous medium.

The strength of a reducing agent is important in the formation of dispersed crystalline nanoparticles of good morphology [114]. Varying concentrations were used to reduce

palladium chloride ( $\text{PdCl}_2$ ) to palladium(0) with no capping agent. UV-Vis was used as the primary characterisation technique to confirm the reduction of palladium(II). The disappearance of the palladium chloride peak and the notable colour change of the solution was evident for the possible formation of Pd(0) nanoparticles [287, 311, 321]. At this stage, the crystallinity was confirmed by X-ray powder diffraction. The optical properties for the nanoparticles formed from the different reducing agents were investigated (**Figure 3.11**).

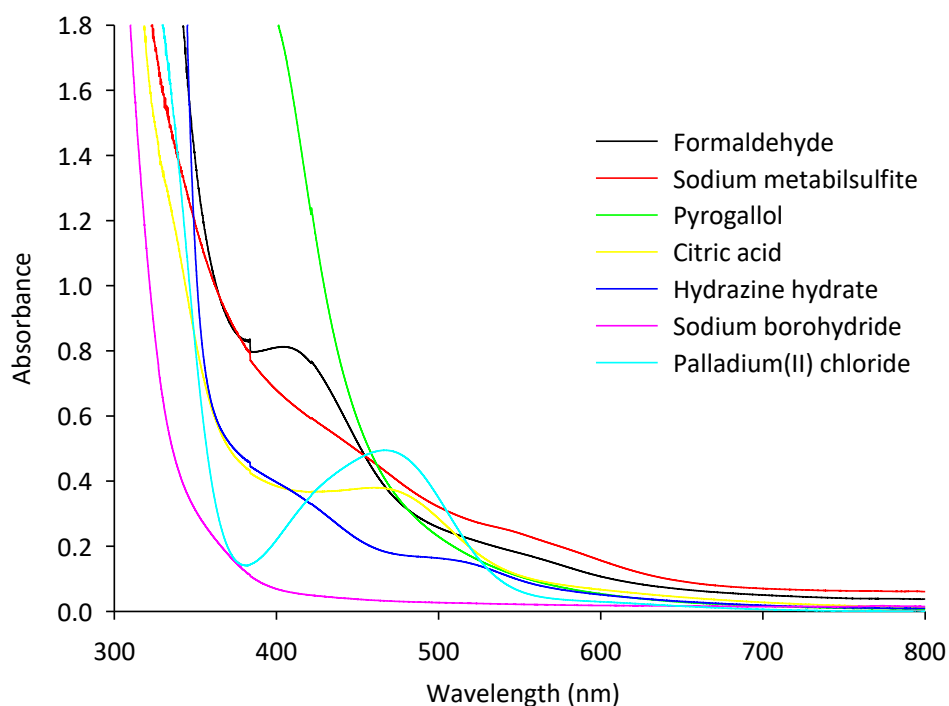


**Figure 3.11:** UV-Vis spectra of the different reducing agents investigated in the reduction of palladium(II) salt at room temperature, synthesised from the reaction of  $100 \mu\text{M}$  palladium(II) with  $500 \mu\text{M}$  reducing agent at room temperature.

Aqueous  $\text{Pd}^{2+}$  absorb at  $465 \text{ nm}$  while palladium nanoparticles do not. The disappearance of this prominent  $\text{Pd}^{2+}$  peak and a single strong absorption maxima appearing at  $324 \text{ nm}$  are an indication of the formation of palladium nanoparticles (PdNPs) [322, 323]. All the spectra showed the disappearance of the  $\text{Pd}^{2+}$  absorption peak, confirming the reduction. However, due to instrumentation limitations, only a few of spectra clearly showed the  $324 \text{ nm}$  peak (**Figure 3.18a**). The sharpness of the peak indicates the size distribution of the particles. The expected blue shift confirms the formation of NPs with the  $\pi\text{-}\pi^*$  transitions [324]. The lower intensity is attributed to the lower concentration of Pd(0). Further characterisation techniques such as XRD were used to confirm this conclusion.

One of the most important things is the greener synthesis of the nanoparticles. Despite citric acid and sodium borohydride being labelled as corrosive (hazard code), formaldehyde and hydrazine being toxic, these were preferred due to their reducing strength (**Figure 3.11**). Other reducing agents like ethanol, carbon monoxide, oleylamine, ethylene glycol, and 1-octadecene are known to have low reducing power at room temperature [125]. As a result, these were not used in this study.

Hydrazine has been used to reduce palladium(II) to palladium(0) with ammonium derivatised isocyanides as stabilising agents at high temperatures [325]. Hydrazine and borohydride produced similar NPs. These nanoparticles were well defined and circular. This agrees with the available literature [310]. Despite being a conventional method, the citrate method did not work for the reduction and capping of palladium nanoparticles at room temperature, and pyrogallol and sodium metabisulfite. The obtained products were characterised using XRD (**Figure 3.12**).

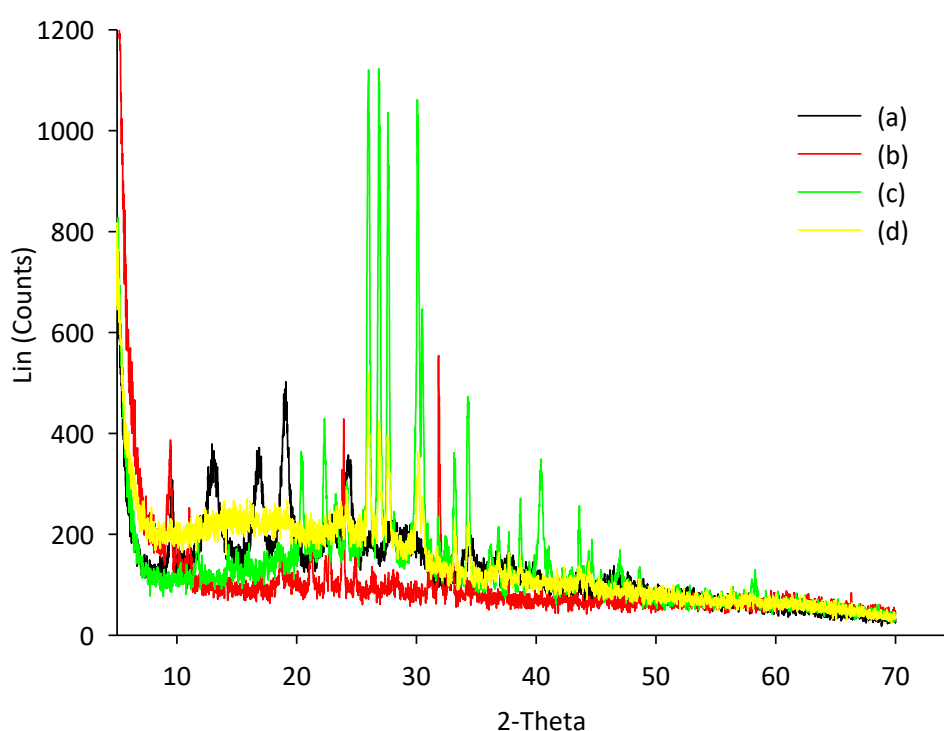


**Figure 3.12:** The X-ray diffraction (XRD) spectra of the amorphous particles obtained from the reduction of 100  $\mu\text{M}$  palladium(II) salt with 50 mM of; (a) citrate, (b) sodium metabisulfite, (c) pyrogallol, and (d) hydrazine at room temperature.

It was concluded that sodium borohydride and formaldehyde were the best-reducing agents (**Figure 3.11**). A comparison of the UV-Vis spectra of the two reducing agents (**Figure 3.12**), showed that sodium borohydride achieved complete reduction, therefore, it was preferred to formaldehyde. Sodium borohydride and formaldehyde can reduce palladium(II) to palladium(0) at low concentrations at room temperature. The obtained UV-Vis spectra of the palladium(0) nanoparticles obtained from their reduction (**Figure 3.13**).

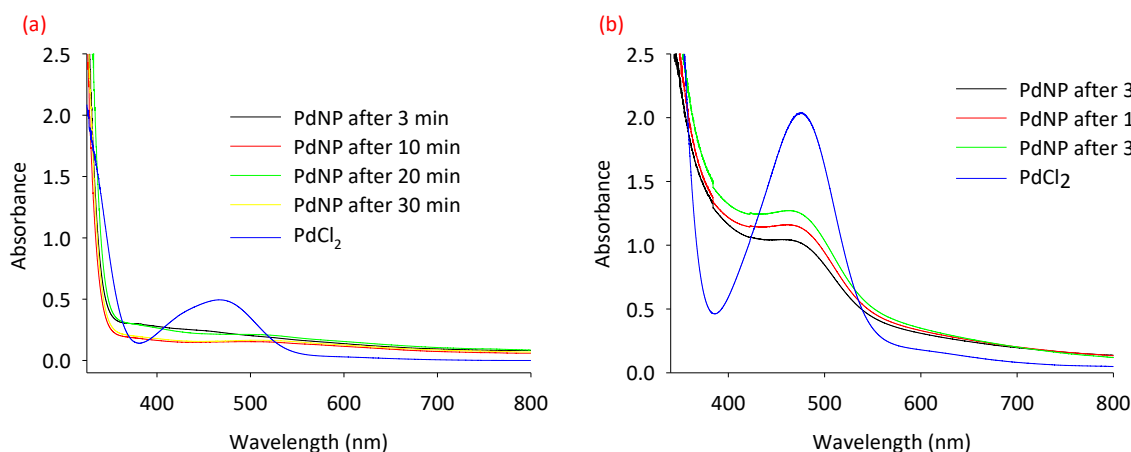
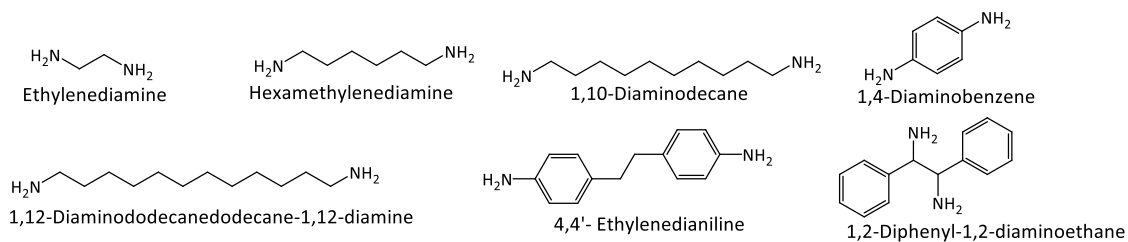


**Figure 3.13:** The stability studies (UV-Vis spectra) of ethylenediamine-capped nanoparticles synthesised from the reduction of palladium(II) by; (a) 1 mM sodium borohydride, and (b) 5 mM formaldehyde, obtained from the reduction of 10  $\mu\text{M}$  and 50  $\mu\text{M}$  palladium(II) salt, respectively.

Varying concentrations of the reducing agents was carried out to investigate the best capping agents. Palladium nanoparticles primary nuclei are known to have extremely high surface energy [308]. Owing to this, they tend to aggregate a lot as seen for uncapped nanoparticles, hence the need for the nitrogen-containing capping agents. It has been confirmed that amine-group containing compounds can stabilise palladium nanoparticles [326]. Diamines and amine containing phthalocyanines were used in this study with preference given to the less toxic diamines that are highly biocompatible. Selected commercially available aliphatic, aromatic, short, and lengthy diamines were used in the preliminary studies (**Scheme 3.2**).



**Scheme 3.2:** The commercially available symmetrical diamines employed in the optimisation of nanoparticle sizes.

The primary aim of the preliminary studies was to determine a diamine that meets all the requirements previously discussed (**Section 1.3**). The chosen diamine (ethylenediamine) was then conjugated to folate, and its capping agent abilities and that of its conjugate explored. The effects of the chosen diamine on nanoparticles properties were later compared to the effects of synthesised phthalocyanines and the folate conjugates. Amine-containing molecules have been used in radiopharmaceutical conjugation [327].

The use of hexamethylenediamine as a capping agent has been reported [305, 328]. However, the aspect of solubility and the need for heating caused its elimination from the list. Palladium(II) amine complexes are very sensitive to preparative conditions, and several forms are often stabilised in the powders produced (polymorphism) such that single crystals are not easily obtained [329]. Amine molecules provide hydrophilicity in aqueous solution [323]. The diamines that produced amorphous precipitates are reported (**Figure 3.14**), and were expected to stabilise crystalline palladium(0) nanoparticles similarly to how they stabilise palladium(II) complexes.

The determination of the crystallinity of the synthesised nanoparticles was conducted. Amorphous nanoparticles have been considered for use in pharmaceutical industry [330–333]. Some amorphous nanoparticles have better prospects to crystalline nanoparticles [334, 335], however, water solubility and size determination remain challenges [336, 337]. On the other hand, crystalline nanoparticles are easier to characterise and more stable compared to amorphous nanoparticles [72, 73, 331, 338–340], despite their tendency to agglomerate at larger sizes [341]. With special focus on improved solubility, controlled size, well-defined morphology, and easy characterisation; capping agents that produced amorphous palladium nanoparticles were eliminated (**Figure 3.14**).

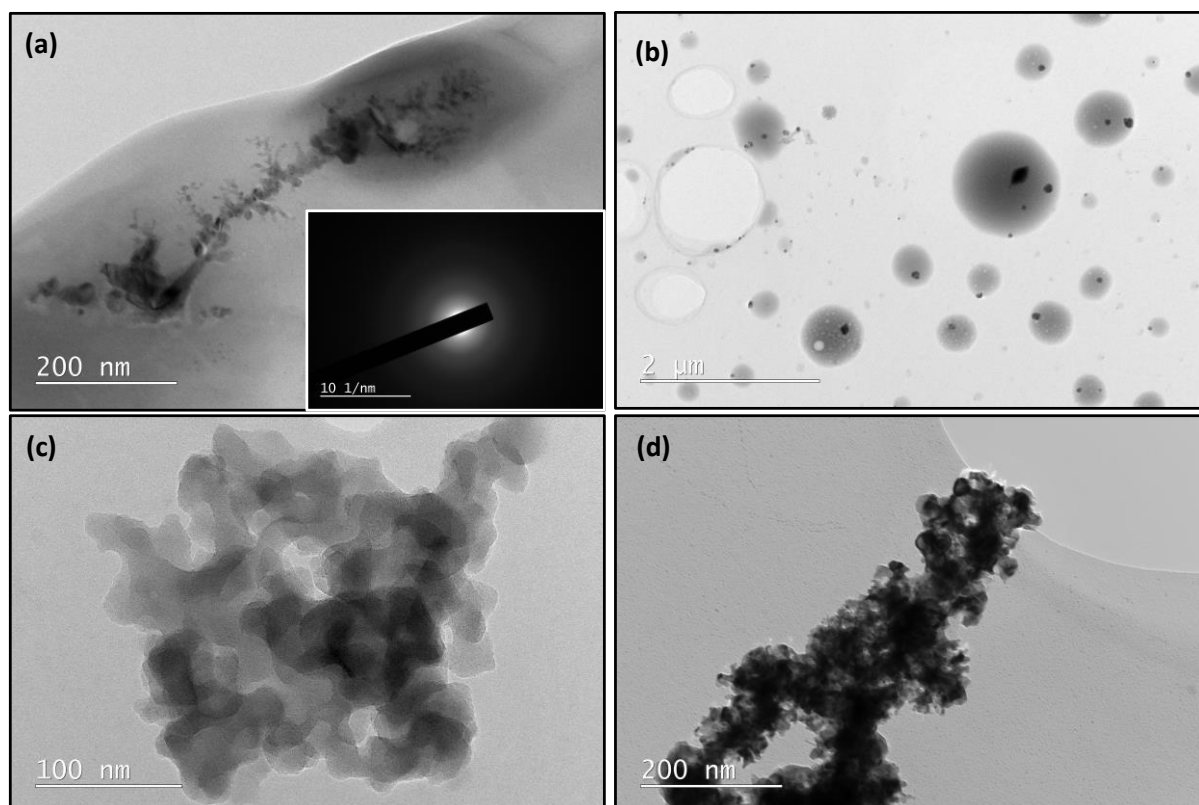


**Figure 3.14:** Bright-field TEM images of amorphous precipitates obtained from the reduction of  $100\ \mu\text{M}$  palladium(II) with  $100\ \mu\text{M}$  sodium borohydride in the presence of  $100\ \mu\text{M}$  of; (a) 1,6-hexamethylenediamine, (b) 4,4'-ethylenedianiline, (c) 1,2-diphenyl-1,2-diaminoethane, and (d) 1,4-diaminobenzene as capping agents. The inset shows a SAED for a non-crystalline precipitate, similar to the SAED patterns for the other three images.

Palladium nanoparticles exist in amorphous or crystalline form [69–71, 74, 342]. Ethylenediamine, 1,10-diaminododecane, and 1,12-diaminododecane produced crystalline nanoparticles (**Figure 3.15**).

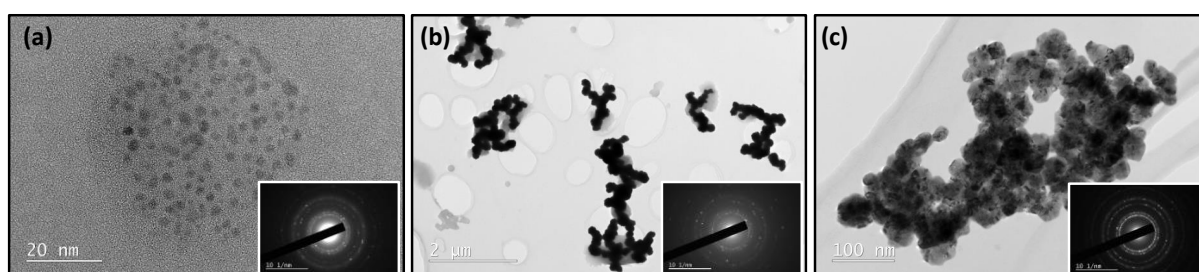


**Figure 3.15:** Bright-field TEM images of crystalline nanoparticles obtained from the reduction of  $10\ \mu\text{M}$  palladium(II) with  $2\text{mM}$  sodium borohydride capped with  $800\ \mu\text{M}$ ; (a) ethylenediamine, (b) 1,10-diaminododecane, and (c) 1,12-diaminododecane.



The UV-Vis spectra were similar; independent of the capping agent (diamine) used, and this agreed with the published work [324]. Longer diamines were expected to result in more stable NPs [314], however, the obtained results showed more dispersed and non-aggregated nanoparticles for ethylenediamine. Further investigation was conducted to confirm crystallinity and the absence of PdO using X-ray diffraction spectroscopy (XRD) (**Figure 3.16**), scanning transmission electron microscopy-energy dispersive X-ray spectroscopy (STEM-EDS) (**Figure 3.17**), and selective area electron diffraction (SAED) (**Figure 3.18**).

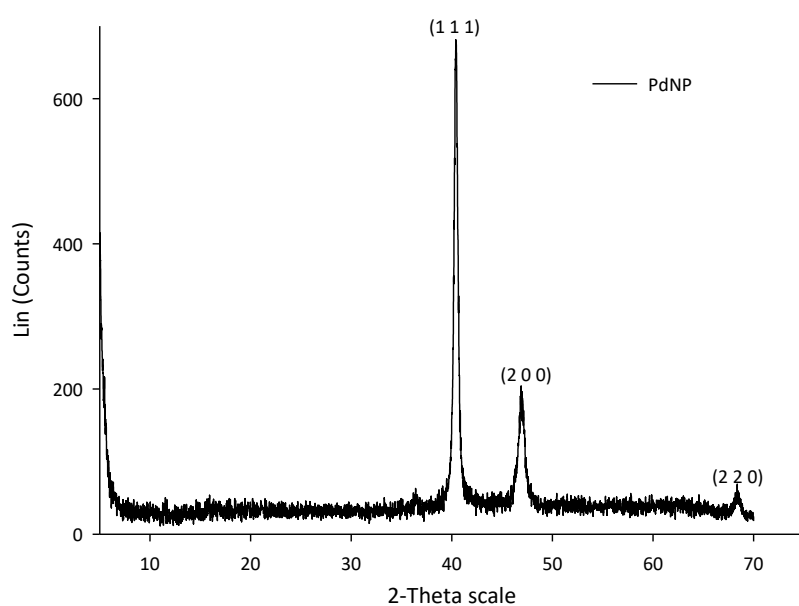


**Figure 3.16:** An XRD spectrum of the ethylenediamine-capped palladium nanoparticles synthesised from the reduction of 100  $\mu\text{M}$  palladium(II) with 10 mM sodium borohydride in the presence of 100  $\mu\text{M}$  ethylenediamine.

The above X-ray diffraction profile of the synthesised PdNPs, with the indices (1 1 1), (2 0 0), and (2 2 0), corresponds to the palladium XRD crystal structure open database [68] and the particle size calculated using Scherrer's equation [343]. The three fringe patterns with plane distances of 0.225, 0.195, and 0.138 nm were consistent with the indices (1 1 1), (2 0 0), and (2 2 0) of pure face-centred cubic (fcc) palladium as confirmed by SAED estimation (**Figure 3.18**) [344, 345].

There was no obvious diffraction peak of Pd(II) species. In addition, no peaks were found on the XRD pattern which could be attributed to PdO [68, 346], confirming the absence of PdO. Different capping agents gave PdNPs which exhibited similar XRD spectra (**Figure 3.19**) and

complementary SAED (**Figure 3.20**), highlighting the reproducibility of crystalline PdNPs synthesis irrespective of optimised capping agent used.

Despite XRD being primarily used to confirm crystallinity (**Figure 3.16**), the crystal particle size was calculated using Scherrer equation [343];

$$D = \frac{\kappa\lambda}{\beta\cos\theta} \quad (3)$$

Where D is particle size,  $\kappa$  is Scherrer constant (0.94),  $\lambda$  is wavelength of the X-ray source (0.15406 nm),  $\beta$  is the full width half maximum (FWHM),  $\theta$  is peak position ( $2\theta/2$ ), and  $\beta\cos\theta$  is in radians. At (1 1 1);  $d = 110.63$  nm, at (2 0 0);  $d = 90.48$  nm, at (2 2 0);  $d = 83.73$  nm, and  $D_{\text{average}} = 92.79$  nm. The obtained size was within the large-sized nanoparticles range (**Table 2.4**) as expected.

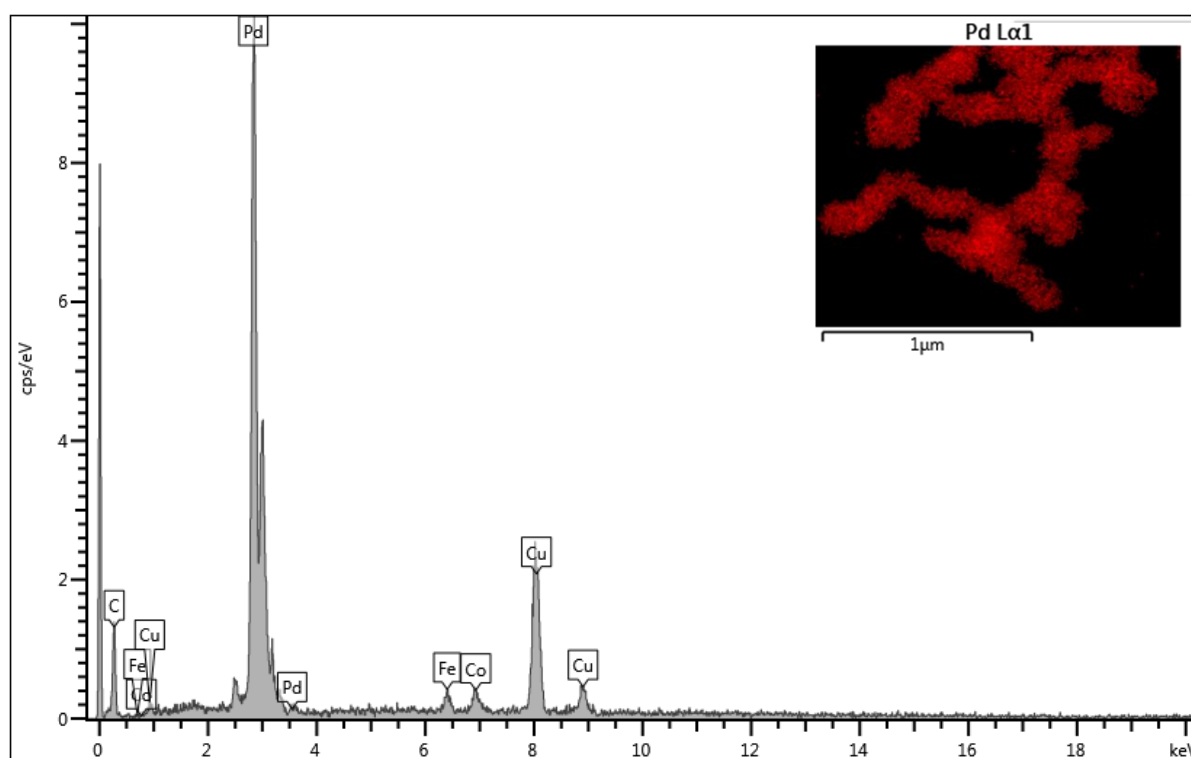


**Figure 3.17:** The scanning transmission electron microscope-energy dispersive X-ray spectroscopy (STEM-EDS) spectrum of the ethylenediamine-capped palladium(0) nanoparticles formed from the reduction of 100 μM palladium(II) with 10 mM sodium borohydride in the presence of 100 μM ethylenediamine. The inset shows the analysed region of the agglomerated ethylenediamine-capped palladium nanoparticles.

The STEM-EDS spectrum confirmed the presence of palladium. The detection of copper can be attributed to the copper grid used and the presence of iron and cobalt (**Figure 3.17**) can be attributed to system artefacts as the TEM chamber is made of iron and cobalt. The carbon can be attributed to the ethylenediamine carbon atoms. SAED was employed (**Figure 3.18**) to further affirm the findings from XRD and STEM-EDS. The obtained SAED spectra were compared with the simulated Java Electron Microscopy Software (JEMS) and it corresponded [345], affirming the crystallinity and elemental composition of the palladium nanoparticles (**Figure 3.16** and **Figure 3.19**).

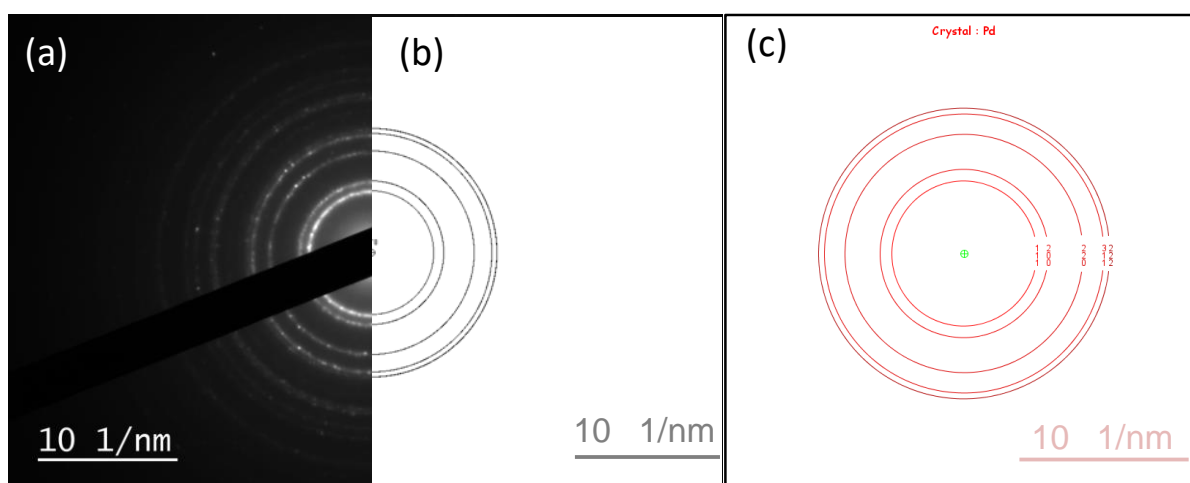


**Figure 3.18:** The SAED patterns for; (a) folate-phthalocyanine capped crystalline palladium nanoparticles, (b) JEMS simulated SAED for palladium crystal, and (c) annotated JEMS simulated SAED for palladium showing the (1 1 1), (2 0 0), (2 2 0), (3 1 1), and (2 2 2) rings.

The XRD spectra (**Figure 3.19**) did not show the (3 1 1), (2 2 2), and other peaks due to instrumentation settings (maximum  $2\theta$  value was  $70^\circ$ ), while the (3 1 1) and (2 2 2) peaks occur at  $2\theta = 82$  and  $86^\circ$ , respectively. New runs with maximum  $2\theta = 90^\circ$  will be conducted. The XRD spectra were used to confirm crystallinity and absence of PdO for the differently capped large-sized palladium nanoparticles. The particle sizes of the large-sized nanoparticles (**Figure 3.19**) was confirmed using Scherrer's equation (**Table 3.2**). The findings confirmed that the differently capped palladium nanoparticle had a relatively similar average particle size. XRD could not be employed for all nanoparticles as small- and medium-sized nanoparticles could not be precipitated and collected in solid form for XRD analysis. Due to this limitation, XRD use in this study was limited to confirming crystallinity and the absence of PdO, and not for particle size analysis, resulting in XRD particle sizes not being compared to other particle size analysis techniques used.

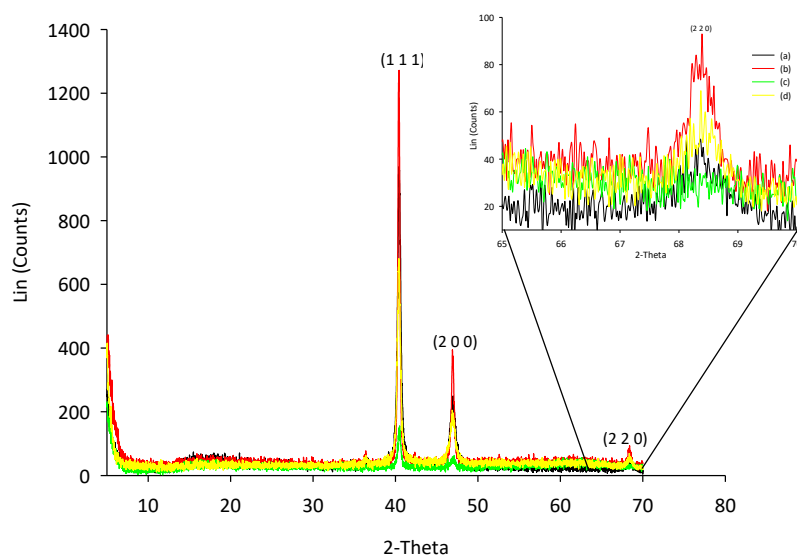


**Figure 3.19:** The XRD spectra showing the reproducibility of large-sized palladium nanoparticles capped with; (a) phthalocyanine (Pc), (b) borohydride (Bh), (c) folate-phthalocyanine (FA-Pc), and (d) folate-ethylenediamine (FA-EDA) synthesised from the reduction of 100  $\mu\text{M}$  palladium(II) salt with 1 mM sodium borohydride.

**Table 3.2:** Summary of the particle diameters calculated using Scherrer's method for XRD spectra presented (Figure 3.19). The FWHM ( $\beta$ ) values were determined using SigmaPlot™.

Capping agent	Parameter	For (1 1 1) peak	For (2 0 0) peak	For (2 2 0) peak	D average (nm)
Pc	$2\theta$ ( $^\circ$ )	40.8	47.1	68.5	96.19
	$\beta$ (cm)	0.08	0.1	0.115	
	D (nm)	110.70	90.55	87.33	
Bh	$2\theta$ ( $^\circ$ )	40.8	47.1	68.5	96.19
	$\beta$ (cm)	0.08	0.1	0.115	
	D (nm)	110.70	90.55	87.33	
FA-Pc	$2\theta$ ( $^\circ$ )	40.3	47.0	68.6	96.14
	$\beta$ (cm)	0.08	0.1	0.115	
	D (nm)	110.53	90.52	87.39	
FA-EDA	$2\theta$ ( $^\circ$ )	40.5	47.2	68.5	96.17
	$\beta$ (cm)	0.08	0.1	0.115	
	D (nm)	110.60	90.59	87.33	

The obtained average particle diameters (**Table 3.2**) are within the large-sized nanoparticle size range or category (**Table 2.4**). With the small and medium-sized nanoparticles difficult to precipitate out, collect and analyse using powder XRD; selective area electron diffraction (SAED) was used (**Figure 3.20**) to primarily confirm crystallinity for the small- and medium-sized palladium nanoparticles.

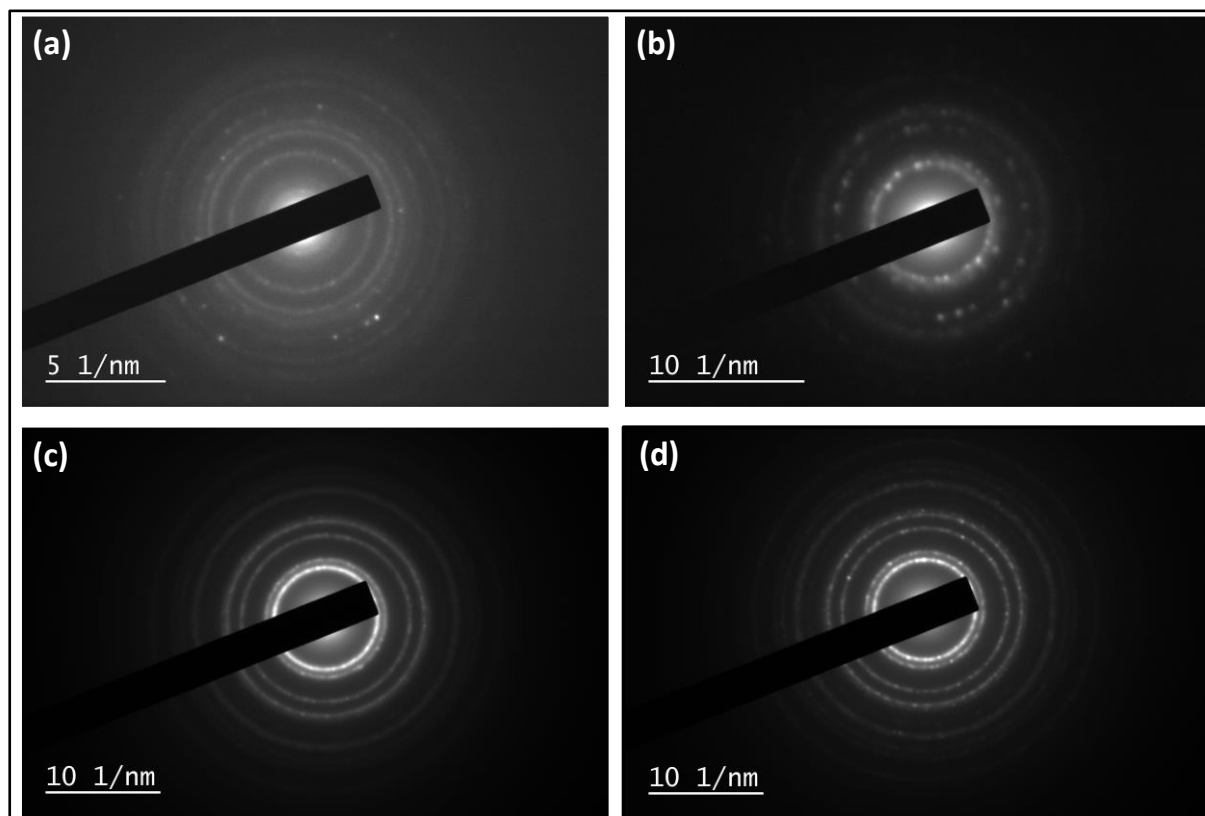


**Figure 3.20:** The selected area electron diffraction (SAED) patterns of the synthesised and characterised nanoparticles; (a) small-sized ethylenediamine capped (sz-EDÂ), (b) medium-sized phthalocyanine capped (mz-PĈ), (c) medium-sized folate-ethylenediamine capped (mz-FA-EDÂ), and (d) small-sized folate-phthalocyanine capped (sz-FA-PĈ) nanoparticles synthesised from the reduction of 10  $\mu\text{M}$  palladium(II) salt with sodium borohydride.

The SAED patterns were as expected [345]. With this success, special focus was shifted to the shape and morphology of the nanoparticles. However, it was difficult to obtain uniform sizes when using strong reducing agents, because they increase rate of nucleation and result in agglomeration. Changing the temperature, time, and pH also play a vital role in the synthesis [347]. The shape and morphology of the nanoparticles were investigated using TEM (**Figure 3.21**). Palladium nanoparticles exist in different shapes ranging from triangular, rhomboidal or square, pentagonal, symmetrical, round NPs, irregular shaped, or elongated, cuboidal,

cuboctahedron, octahedron, tetrahedron, decahedron, icosahedron, spherical, polyhedral shaped nanoparticles, 4-sided rhombohedral, hexagonal, pentagonal, sponge-like structures, and nanoflowers [264, 266, 305, 342, 348]. A few of the shapes were observed (**Figure 3.21**).

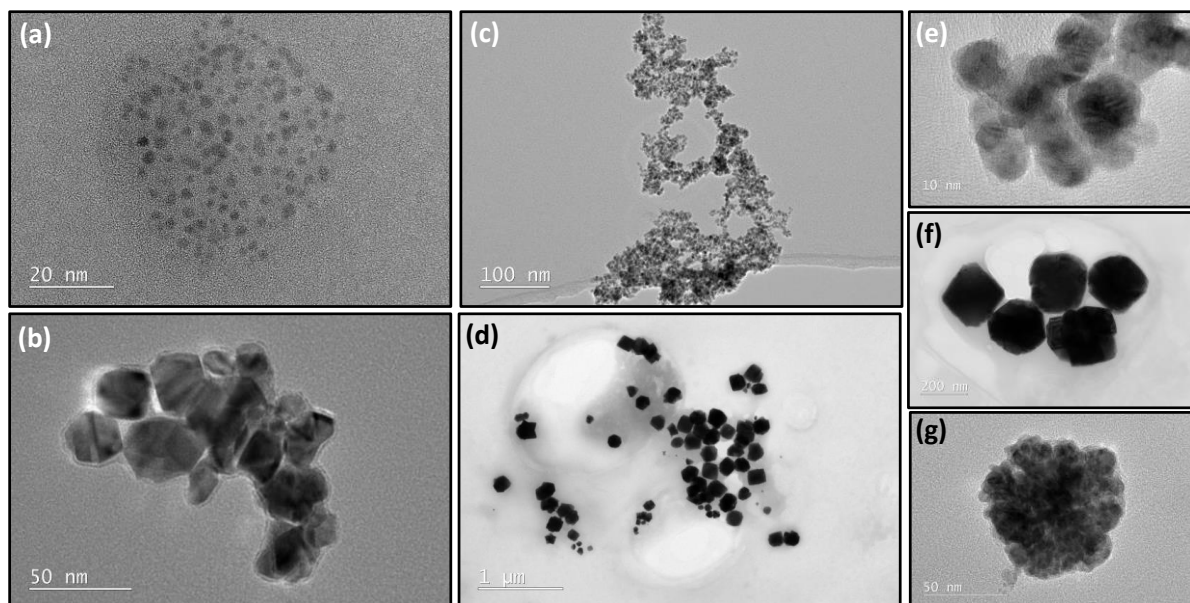


**Figure 3.21:** Bright-field TEM images showing the different shapes obtained from the synthesis of the nanoparticles; (a) circular shaped, (b) tetrahedral and semi-regular shaped, (c) circular flower-like shaped, (d) square shaped nanoparticles, (e) elongate shaped nanoparticles, (f) regular square shaped nanoparticles, and (g) flower-like undefined nanoparticles.

The proportion of the different morphologies can be varied by changing synthesis conditions including the molar ratios of precursor salt: reducing agent and stabilising agent [347]. Monodispersity, shape, size, and the surface charge of the particles are dependent on the precursor, nature of ligands, and nature of solvent [305, 349]. The success of the reduction of the palladium(II) salt were primarily confirmed using UV-Vis (**Figure 3.11**). The success of the reduction was confirmed visually. The colour change of palladium solution (**Figure 3.22**), from brown to the black-greyish colourless solution further confirmed the successful reduction of palladium(II) to palladium(0). When in solution, palladium nanoparticles are black-greyish. However, when agglomerated and out of solution, the shiny silver-greyish colour was observed. Visually, the success of the synthesis could be observed (**Figure 3.22**). The temperature and time effects on palladium nanoparticles were investigated.



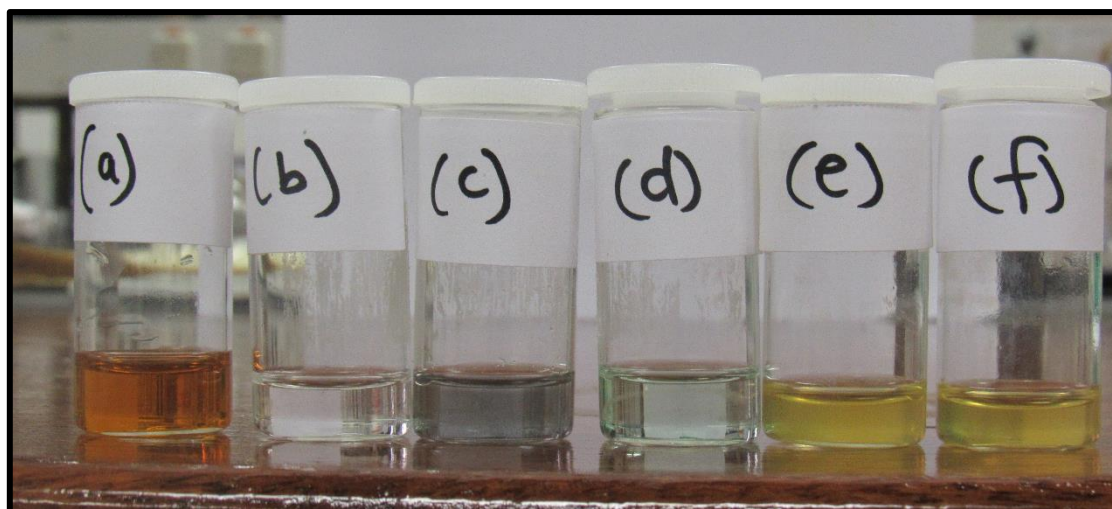


**Figure 3.22:** The visual presentation of the palladium solutions; a) 100  $\mu\text{M}$  palladium(II) solution, (b) ethylenediamine-capped palladium(0), (c) borohydride-capped palladium(0), (d) phthalocyanine-capped palladium(0), (e) folate-ethylenediamine capped palladium(0), and (f) folate-phthalocyanine capped palladium (0) nanoparticles. (b) to (e) were synthesised from the reduction of 100  $\mu\text{M}$  Pd(II) solution by 20 mM sodium borohydride.

### 3.3.2 Temperature and time

The synthesis temperature is known to affect the shape of nanoparticles. In this study, higher temperatures triggered coagulation and formation of crumps or agglomerates were noted, and preference was given to room temperature. The effects of synthesis time were investigated (**Figure 3.23**).

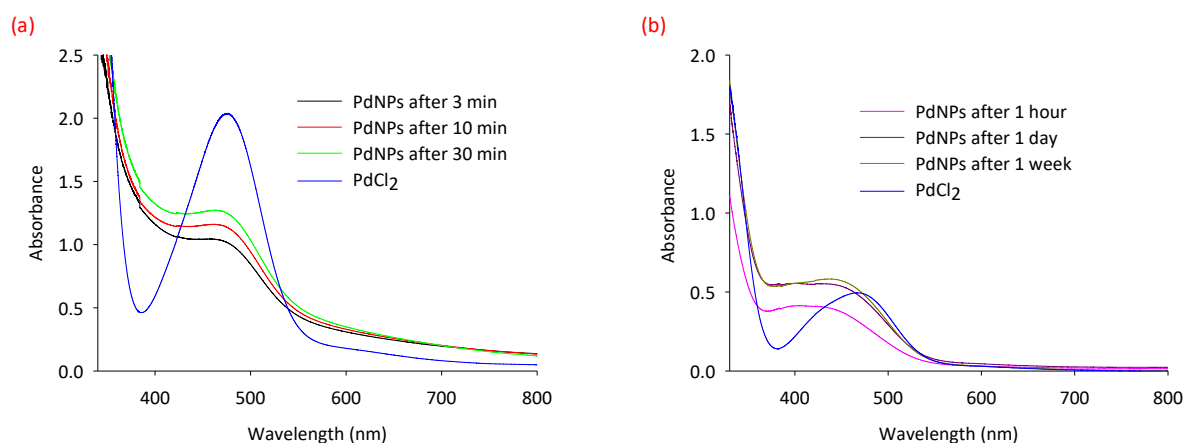


**Figure 3.23:** The UV-Vis spectra of palladium nanoparticles after different synthetic times; (a) 3, 10, and 30 min), and (b) 1 hour, 1 day, and 1 week.

There is no significant UV-Vis absorption difference between after 3 and 10 minutes reduction time (**Figure 3.23a**). Three minutes was reported in literature as the time taken to completely reduce palladium(II) to palladium(0) under optimal conditions and concentration [314]. At 100  $\mu\text{M}$  the palladium(II) salt exhibited higher absorbance values compared to the palladium(0) systems and this will be investigated further in future studies. With no reported significant UV-Vis absorption increase after three minutes to 8 hours from synthesis [314], and the obtained UV-Vis spectra being repeatedly obtained, the effects of temperature were investigated (**Figure 3.24**).

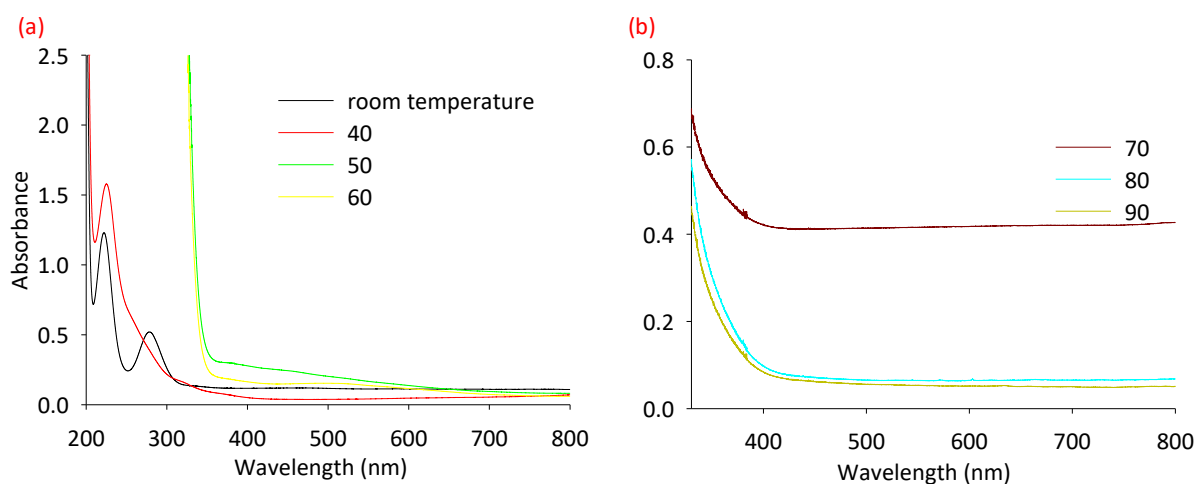


**Figure 3.24:** The UV-Vis spectra of palladium(0) nanoparticles depicting the effects of temperature on the synthesis at different temperatures a) UV-Vis spectra for nanoparticles synthesised at room temperature, 40 °C, 50 °C, and 60 °C (b) 70 °C, 80 °C, and 90 °C.

As expected, higher temperatures accelerated reduction by introducing more reaction energy into the reaction system (**Figure 3.24**), hence promoting nucleation [308]. The atoms nucleate under thermodynamically controlled processes to achieve the formation of nucleating centres and capping agents stabilising the nucleating centres to achieve controlled growth [314]. The presence of a broad continuous absorption throughout the visible region is a characteristic feature of palladium nanoparticles (**Figure 3.24**). Kinetic nucleation is accelerated at 70 °C [350], and hence the unusual high absorbance.

Since the concentration of palladium atoms in the reaction system would quickly drop below the minimum supersaturation level after the formation of copious primary nuclei, generation of new nuclei would be inhibited, eventually leading to the smaller nanoparticles with narrow distribution aggregating [350]. At higher temperatures, agglomerates were observed upon the addition of a few drops of the reducing agent. As observed (**Figure 3.24**), the UV-Vis



spectra at room temperature is as published in literature [65, 351]. It was concluded that the synthesis of palladium nanoparticles at room temperature could be safely employed in this study, and the stability of the nanoparticles investigated. NPs dispersed in solution can agglomerate because of thermodynamic effects and can also leach molecular species promoted by solvent, ligands or other reaction parameters [349].

### 3.3.3 Stability

With the concentration of precursor reported to significantly affect or directly influence the size of obtained nanoparticles [352], the experiments were conducted at low concentrations. pH is known to affect protonation and thereby changing the reduction rate, resulting in nanoparticles of different sizes and morphologies [307]. Palladium nanoparticles capped with N-containing stabiliser are reported to aggregate more at lower pH. This is due to the protonation of the N-groups and unavailability for bonding to the nanoparticle surface, subsequently becoming deprotected causing aggregation [275]. To prevent any pH-related variation, pH was kept constant. The zeta potential (surface charge) of the nanoparticles in different media at a pH of 7.4 (**Figure 3.25**) was presented.

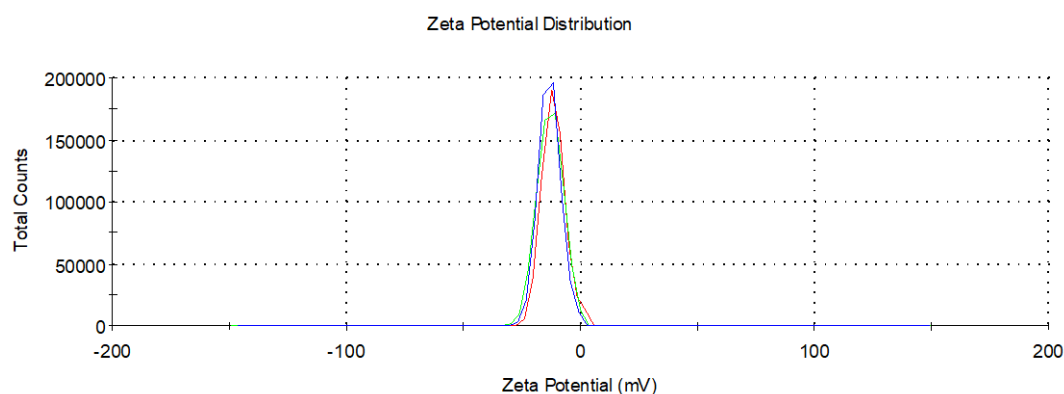


**Figure 3.25:** An illustration of the zeta potential distribution of the palladium nanoparticles capped with: phthalocyanine (green), borohydride (red), and ethylenediamine (blue) synthesised from 100  $\mu\text{M}$  palladium(II), 2 mM reducing and capping agents' concentrations.

The borohydride-, phthalocyanine-, and ethylenediamine-capped nanoparticles possessed surface charge that is within the preferred -30 mV to +30 mV zeta potential range as published in literature [96, 353]. Characterisation of the nanoparticles used in cellular uptake was inevitable. The summary of the surface charge of the nanoparticles used for the cell studies was presented (**Table 3.3**).

**Table 3.3:** The zeta potential (surface charge) of the differently capped optimised palladium nanoparticles in DMEM cell media at 25 °C and pH 7.4.

Sample Name	ZP (mV)	Mob ( $\mu\text{mcm/Vs}$ )	Cond (mS/cm)
sz-B $\hat{h}$ -NPs	-2.86 $\pm$ 0.64	-0.2241	216
lz-B $\hat{h}$ -NPs	-10.9 $\pm$ 2.10	-0.8572	214
sz-ED $\hat{A}$ -NPs	-0.66 $\pm$ 0.07	-0.0520	30.1
lz-ED $\hat{A}$ -NPs	+1.34 $\pm$ 0.18	-0.087	90.2
sz-P $\hat{C}$ -NPs	+0,063 $\pm$ 0.02	-0,0049	189
lz-P $\hat{C}$ -NPs	+2.81 $\pm$ 0.78	-0.1109	249
sz-FA-ED $\hat{A}$ -NPs	-0,051 $\pm$ 0.09	-0,0040	193
lz-FA-ED $\hat{A}$ -NPs	-0,101 $\pm$ 0.14	-0,0079	258
sz-FA-P $\hat{C}$ -NPs	-3,96 $\pm$ 0.24	-0,3106	521
lz-FA-P $\hat{C}$ -NPs	-4,70 $\pm$ 0.57	-0,3684	519

sz=small sized, mz=medium-sized, lz=large-sized, ED $\hat{A}$ =ethylenediamine capped, B $\hat{h}$ =borohydride, NPs=nanoparticles, P $\hat{C}$ =phthalocyanine capped, FA-ED $\hat{A}$ =folate-ethylenediamine capped, FA-P $\hat{C}$ =folate-phthalocyanine capped, Mob=electrophoretic mobility, Cond=conductivity.

Most of the nanoparticles had a preferred negative charge (**Table 3.3**). Negatively charged nanoparticles are not easily taken up *via* endocytosis [354, 355], however, they are taken up *via* receptor mediated endocytosis. In this case, negatively charged nanoparticles could be taken up *via* folate receptor mediated endocytosis despite their sizes. With the positive charged nanoparticles being ethylenediamine-capped and phthalocyanine capped, these were not employed for cell studies (**Section 4.4**). The trend of the small negative charges within the -30 to +30 mV was noted for all the characterised nanoparticles (**Table 3.4**). Folate-conjugates capped nanoparticles exhibited negative charges that synergises their uptake *via* folate receptor-mediated uptake and not passive diffusion, or any other endocytosis mechanisms. It can be noted that borohydride-capped nanoparticles also exhibited negative charges in both the preliminary and optimised characterisation (**Table 3.3** and **Table 3.4**). The low electrophoretic mobility values (**Table 3.3**) also confirm the stability of the nanoparticles in cell media. The cell lines were exposed to the palladium nanoparticles for 24 hours, and the stability of palladium nanoparticles in cell culture media was performed and the findings reported (**Figure 3.26**).

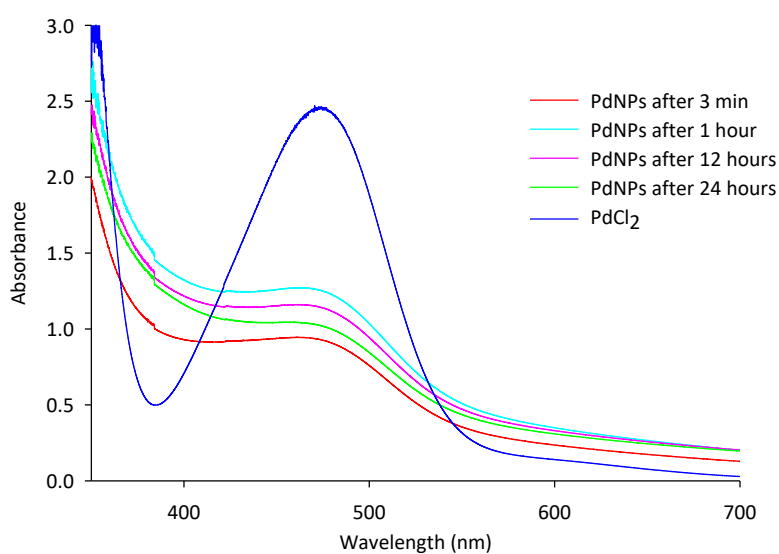


**Figure 3.26:** The UV-Vis stability analysis of ethylenediamine capped nanoparticles formed from the reduction of palladium(II) salt by sodium borohydride after 3 minutes, 1 hour, 12 hours, and 24 hours in Leibovitz-L15 cell media.

The stability of the nanoparticles in cell media was key to the success of this study. Over 24 hours, the nanoparticles were stable in Leibovitz-L15 media (and exhibited similar UV-Vis spectra for DMEM and Hams F-12 media) (Figure 3.26). The spectra's trend was the same for DMEM and Hams F12. The UV-Vis stability studies confirmed that the palladium nanoparticles were stable in both aqueous (Figure 3.13), and *in vitro* (Figure 3.26) and it can be suggested that the nanoparticles could be stable *in vivo*.

Hydrodynamic size investigation (Figure 3.27) showed that the nanoparticles can have broad size distributions with a possibility of bi or multimodality (Figure 3.27 (b), (d), and (f)). However, for this study the synthesis was optimised to obtain nanoparticles of narrow distributions and non-overlapping sizes (Table 2.4). Broader size distributions were noted in some of the optimised nanoparticles, more prominent in the large-sized nanoparticles (Table 3.4). However, the size range non-overlap allowed the nanoparticles to be employed for applications in *in vitro* studies. The nanoparticle solutions were stable after 5 min, 10 min, and 15 min with no significant size change (Figure 3.27).

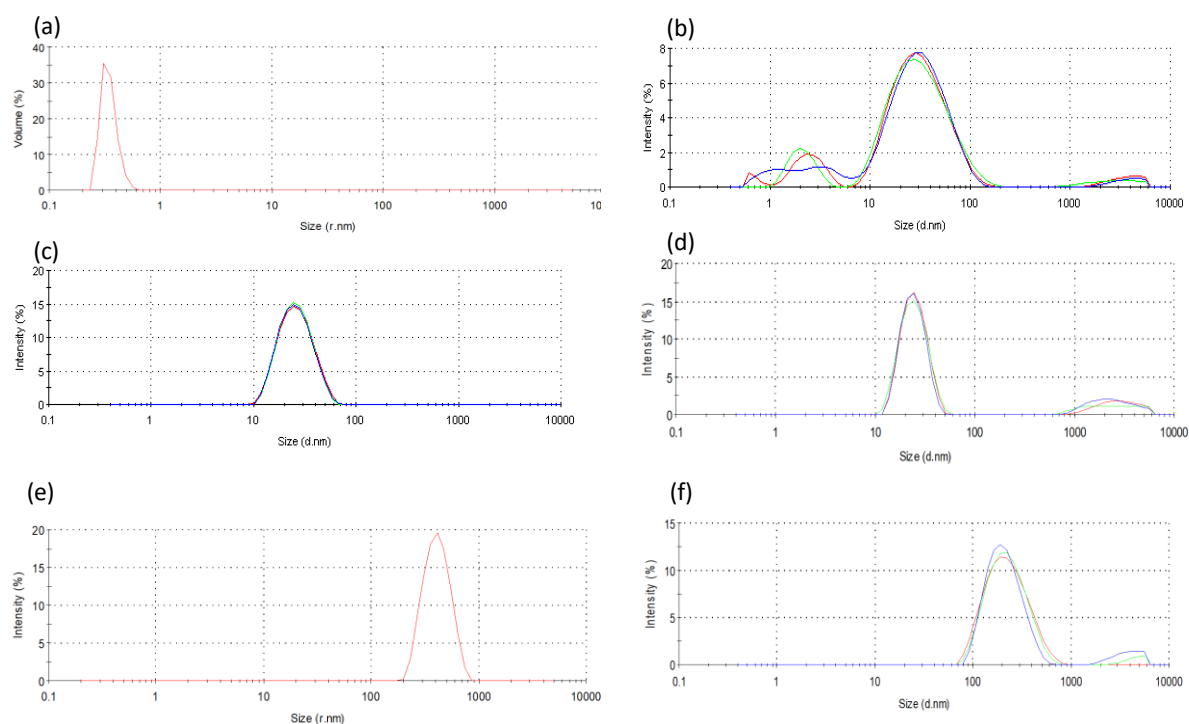


**Figure 3.27:** The hydrodynamic size distributions of differently capped palladium nanoparticles were measured using dynamic light scattering (DLS) in DMEM cell media for; (a) small-sized ethylenediamine-capped palladium nanoparticles (sz-ED $\hat{A}$ -NPs) synthesised from the reduction of 10.15  $\mu\text{M}$  palladium(II) salt with 2 mM sodium borohydride solution in the presence of 1 mM ethylenediamine, (b) medium-sized phthalocyanine capped palladium nanoparticles (mz-P $\hat{C}$ -NPs) synthesised from the reduction of 10.11  $\mu\text{M}$  palladium(II) salt with 800  $\mu\text{M}$  sodium borohydride solution in the presence of 100  $\mu\text{M}$  phthalocyanine, (c) medium-sized folate-ethylenediamine capped palladium nanoparticles synthesised from the reduction of 10.15  $\mu\text{M}$  palladium(II) salt with 800  $\mu\text{M}$  sodium borohydride solution in the presence of 200  $\mu\text{M}$  folate-ethylenediamine, (d) medium-sized folate-phthalocyanine capped palladium nanoparticles (mz-FA-P $\hat{C}$ -NPs) synthesised from the reduction of 10.49  $\mu\text{M}$  palladium(II) salt with 800  $\mu\text{M}$  sodium borohydride solution in the presence of 200  $\mu\text{M}$  folate-phthalocyanine, (e) large-sized folate-phthalocyanine capped palladium nanoparticles (lz-ED $\hat{A}$ -NPs) synthesised from the reduction of 10.38  $\mu\text{M}$  palladium(II) salt with 800  $\mu\text{M}$  sodium borohydride in the presence of 1.7 mM folate-phthalocyanine. The DLS runs were done after 5 min (red), 10 min (green), and 15 min (blue) for (b), (d), and (f), and after 5 min only for (a), (c), and (e).

### 3.4 GENERAL DISCUSSION: PRELIMINARY OPTIMISATION OF NANOPARTICLES SYNTHESSES

Palladium nanoparticles were successfully synthesised at room temperature. The dropwise addition of reducing agent allowed nucleation under thermodynamically controlled processes achieving the formation of nucleating centres. In aqueous solution, the capping agents stabilised the nucleating centres resulting in achieved controlled growth with monodispersed nanoparticles being obtained. It was difficult to obtain uniform sizes when using strong reducing agents at higher temperatures. Strong reducing agents made the nucleation process faster and triggered agglomeration as published in literature [314]. Sodium borohydride produced well defined and various shaped palladium nanoparticles. Controlled reactant concentration variations produced nanoparticles of different sizes as expected [356].

The investigated capping agents showed strong ability to attach to the surface of nanoparticles and consistent results were obtained. Being essential for biological applications [310], the stability of the nanoparticles and favourable surface charges provided remarkable results. Phthalocyanines and phthalocyanine conjugates were able to stabilise the palladium nucleating centres as expected [304]. Ethylenediamine also proved to successfully conjugate to folate on one end, with the free end being available to attach to the solid surface of the nanoparticles.

The generalisability of much-published research on this topic is problematic. The nanoparticle synthesis findings at room temperature do not correlate to those obtained at higher temperatures. The stability of the bioconjugates, their precursors, and the nanoparticles in aqueous and cell media conditions was a great advantage for the intended *in vivo* use of the palladium nanoparticles as reported in literature [122, 357, 358].

### 3.5 CHARACTERISATION OF THE NANOPARTICLES FROM THE OPTIMISED METHOD

Recently, particle size, shape, and morphology have been emphasised as key physical parameters which have exerted a tremendous impact on cellular uptake and biodistribution [99, 102, 117, 359]. Prior to *in vitro* studies of the nanoparticles, three varied sizes (**Table 2.5**) of nanoparticles were synthesised from the reduction of palladium(II) to palladium(0) nanoparticles by sodium borohydride. Considering the important properties of nanoparticles in drug development (**Section 1.3.2**), the optimised nanoparticles were synthesised (**Table 3.4**).

**Table 3.4:** Summary of the TEM sizes and surface charges (in DMEM media) of the optimised palladium nanoparticles.

Capping agent	Figure	Nanoparticle size $\pm$ standard deviation (nm)	Surface charge $\pm$ standard deviation (mV)	[Pd(II)] $\mu$ M	[NaBH <sub>4</sub> ]	[Capping agent]
Bh	3.28	2.1 $\pm$ 0.5	-12.2 $\pm$ 0.8	10.65	2 mM	2 mM
	3.29	1.6 $\pm$ 0.4	-10.8 $\pm$ 0.6	10.04	800 $\mu$ M	800 $\mu$ M
	3.30	30 $\pm$ 10	-12.8 $\pm$ 1.7	10.65	500 $\mu$ M	500 $\mu$ M
	3.31	371 $\pm$ 72	-12.6 $\pm$ 1.8	10.65	100 $\mu$ M	100 $\mu$ M
		308 $\pm$ 61	-13.35 $\pm$ 1.1	10.04	100 $\mu$ M	100 $\mu$ M
EDA	3.32	2.5 $\pm$ 0.4	+3.2 $\pm$ 0.3	10.38	2 mM	800 $\mu$ M
	3.33	1.4 $\pm$ 0.2	+4.4 $\pm$ 0.8	10.15	2 mM	1 mM
	3.34	22 $\pm$ 6	+3.9 $\pm$ 0.5	10.38	800 $\mu$ M	200 $\mu$ M
	3.35	37 $\pm$ 6	+2.3 $\pm$ 0.3	10.15	800 $\mu$ M	200 $\mu$ M
	3.36	95 $\pm$ 16	+4.8 $\pm$ 0.9	10.38	800 $\mu$ M	1.7 mM
		122 $\pm$ 48	+5.9 $\pm$ 0.7	10.15	800 $\mu$ M	1 mM
Pc	3.37	2.8 $\pm$ 0.4	+12.1 $\pm$ 0.4	10.32	2 mM	1 mM
	3.38	3 $\pm$ 0.5	+13.6 $\pm$ 1.3	10.11	2 mM	1 mM
	3.39	16 $\pm$ 2	+8.9 $\pm$ 0.8	10.11	800 $\mu$ M	100 $\mu$ M
	3.40	27 $\pm$ 5	+10.9 $\pm$ 0.3	10.32	800 $\mu$ M	200 $\mu$ M
	3.41	134 $\pm$ 30	+11.2 $\pm$ 0.9	10.32	800 $\mu$ M	1 mM
		252 $\pm$ 36	+10.7 $\pm$ 1.1	10.11	800 $\mu$ M	500 $\mu$ M
FA-EDA	3.42	2.1 $\pm$ 0.3	-3.4 $\pm$ 0.1	10.83	2 mM	1 mM
	3.43	4.9 $\pm$ 0.8	-2.6 $\pm$ 0.4	10.41	2 mM	500 $\mu$ M
	3.44	28 $\pm$ 6	-1.8 $\pm$ 0.6	10.83	800 $\mu$ M	200 $\mu$ M
	3.45	21 $\pm$ 3	-1.1 $\pm$ 0.7	10.41	800 $\mu$ M	200 $\mu$ M
	3.46	650 $\pm$ 164	-3.9 $\pm$ 0.5	10.41	800 $\mu$ M	20 $\mu$ M
	3.47	150 $\pm$ 30	-2.7 $\pm$ 0.4	10.83	800 $\mu$ M	50 $\mu$ M
FA-Pc	3.48	3.5 $\pm$ 0.9	-3.7 $\pm$ 0.9	10.99	2 mM	1 mM
	3.49	1.2 $\pm$ 0.2	-1.6 $\pm$ 0.3	10.49	2 mM	800 mM
	3.50	16 $\pm$ 0.63	-3.2 $\pm$ 0.7	10.49	800 $\mu$ M	200 $\mu$ M
	3.51	23 $\pm$ 5	-2.5 $\pm$ 0.7	10.99	800 $\mu$ M	200 $\mu$ M
	3.52	168 $\pm$ 28	-2.8 $\pm$ 0.3	10.99	800 $\mu$ M	1 mM
	3.53	190 $\pm$ 29	-2.4 $\pm$ 0.1	10.99	800 $\mu$ M	1 mM

The reproducibility of the synthesis with acceptable variation was conducted, and the size and surface charge presented (**Figure 3.28 - Figure 3.53; Table 3.4**). The nanoparticle distribution range was considered narrow (if less than 10 nm) and broad (if more than 10 nm).

### 3.5.1 Borohydride capped nanoparticles

With the capping of nanoparticles by borohydride ions having been previously reported [360, 361], the reduction of palladium(II) ions with sodium borohydride was reported (**Figure 3.28- Figure 3.31**).

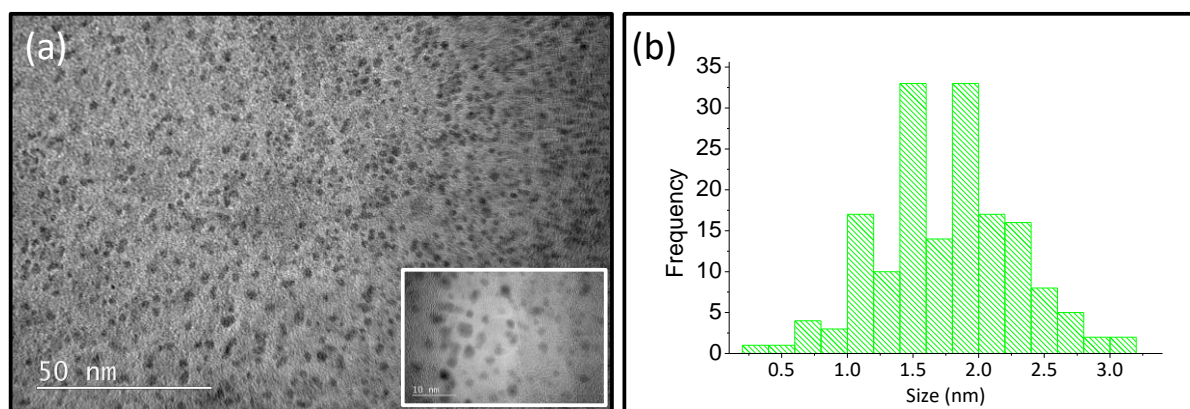


**Figure 3.28:** (a) Bright-field TEM image of monodispersed small-sized borohydride-capped palladium nanoparticles with an average diameter of  $2.1 \pm 0.5$  nm, synthesised from the reduction of  $10.65 \mu\text{M}$  palladium(II) salt with 2 mM sodium borohydride solution, (b) A plot of nanoparticle size (nm) against frequency (y-axis), highlighting a narrow size distribution. The inset presents a magnified (5X) view of small-sized borohydride-capped palladium nanoparticles.

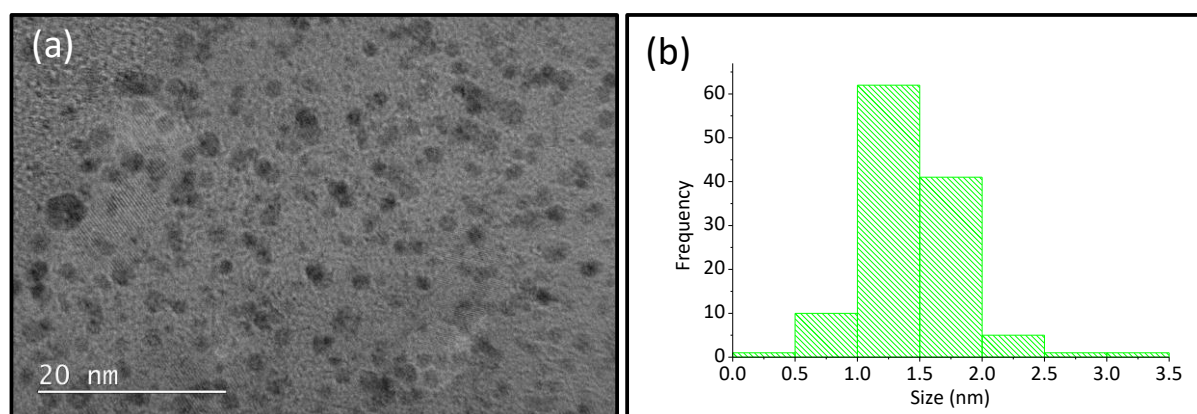


**Figure 3.29:** (a) Bright-field TEM image of monodispersed small-sized borohydride-capped palladium nanoparticles with an average diameter of  $1.6 \pm 0.4$  nm, synthesised from the reduction of  $10.04 \mu\text{M}$  palladium(II) salt with  $800 \mu\text{M}$  sodium borohydride solution, and (b) A plot of nanoparticle size (nm) against frequency (y-axis), highlighting a narrow size distribution.



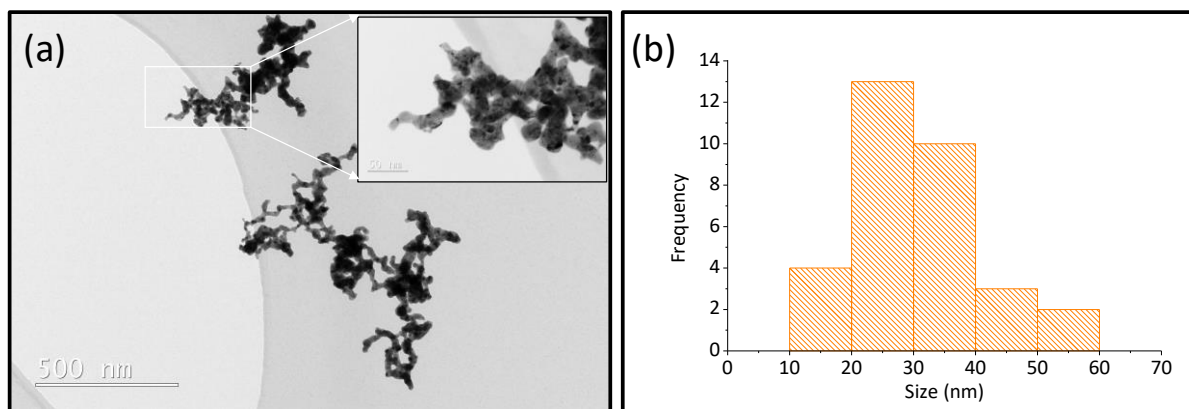


**Figure 3.30:** (a) Bright-field TEM image of medium-sized borohydride-capped palladium nanoparticles with an average diameter of  $30 \pm 10$  nm, synthesised from the reduction of  $10.65 \mu\text{M}$  palladium(II) salt with  $500 \mu\text{M}$  sodium borohydride solution, and (b) A plot of nanoparticle size (nm) against frequency (y-axis), highlighting a broad size distribution. The inset presents borohydride-capped palladium nanoparticles at magnified view (10X) of (a).

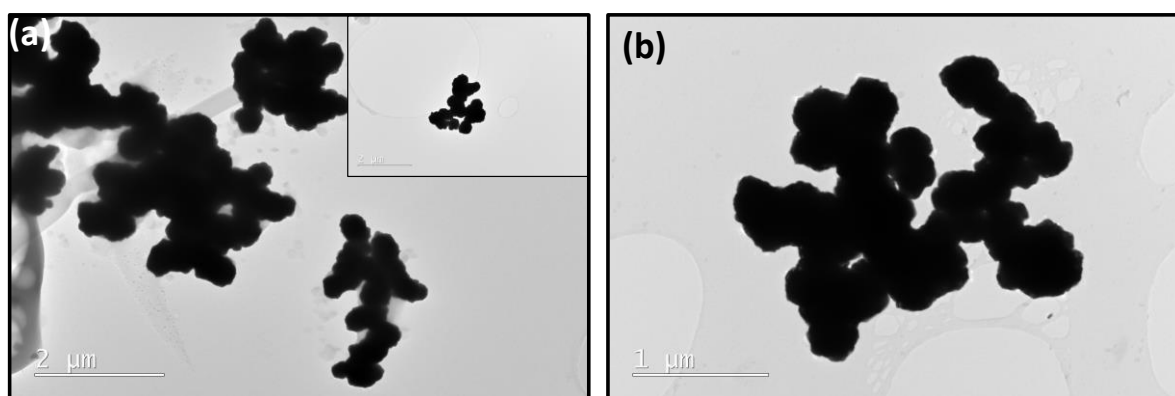


**Figure 3.31:** Bright-field TEM images of agglomerated large-sized borohydride-capped palladium nanoparticles synthesised from; (a) the reduction of  $10.65 \mu\text{M}$  palladium(II) salt with  $100 \mu\text{M}$  sodium borohydride solution, (b) the reduction of  $10.04 \mu\text{M}$  palladium(II) with  $100 \mu\text{M}$  sodium borohydride solution. The inset presents a magnified (2X) agglomerate of (a). From the measurable nanoparticles, the size ranges were found to be  $371 \pm 72$  nm and  $308 \pm 61$  nm for (a) and (b), respectively.

The synthesis of borohydride-capped palladium nanoparticles provided remarkable results. The nanoparticles (**Figure 3.28 – Figure 3.31**) has a relatively similar negative surface charge (**Table 3.4**) attributed to the negatively charged borohydride ions. Borohydride ions are small and were unable to fully stabilise the nucleating centres resulting in formation of agglomerates (**Figure 3.30**).



### 3.5.2 Ethylenediamine capped nanoparticles

Diamines can stabilise metal nanoparticles and ethylenediamine was employed in the optimised synthesis and the obtained results reported (**Figure 3.32** – **Figure 3.36**).

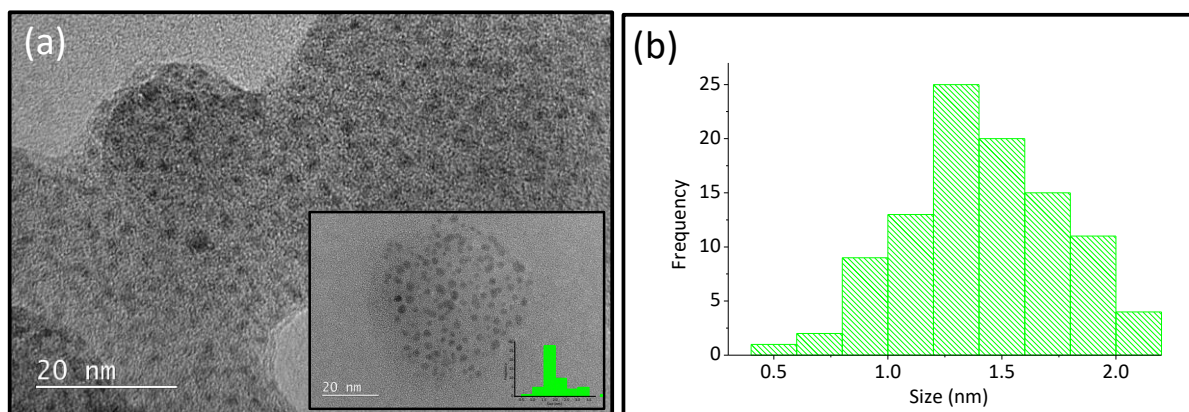


**Figure 3.32:** (a) Bright-field TEM image of monodispersed small-sized ethylenediamine-capped palladium nanoparticles with an average diameter of  $2.5 \pm 0.4$  nm, synthesised from the reduction of  $10.38 \mu\text{M}$  palladium(II) salt with 2 mM sodium borohydride solution in the presence of  $800 \mu\text{M}$  ethylenediamine capping agent, and (b) A plot of nanoparticle size (nm) against frequency (y-axis), highlighting a narrow size distribution. The inset presents ethylenediamine-capped palladium nanoparticles of size  $2.6 \pm 0.2$  nm and its size distribution (bottom right), synthesised from similar concentrations as in (a).

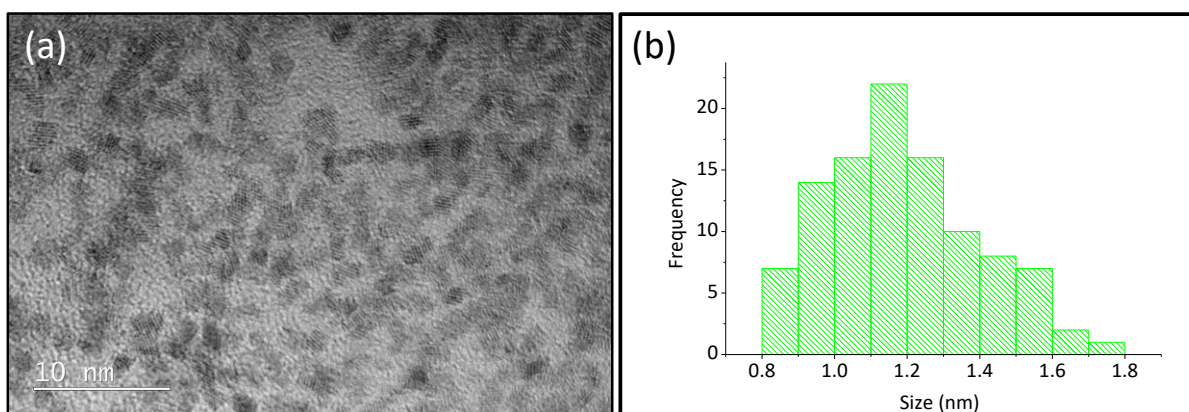


**Figure 3.33:** (a) Bright-field TEM image of polydispersed small-sized ethylenediamine-capped palladium nanoparticles with an average diameter of  $1.4 \pm 0.4$  nm, synthesised from the reduction of  $10.15 \mu\text{M}$  palladium(II) salt with 2 mM sodium borohydride solution in the presence of 1 mM ethylenediamine capping agent, and (b) A plot of nanoparticle size (nm) against frequency (y-axis), highlighting a narrow size distribution.

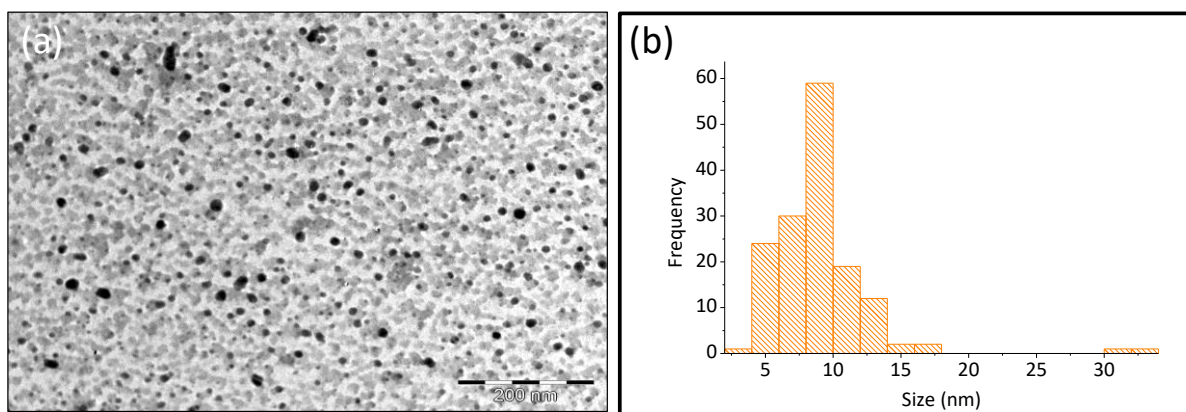


**Figure 3.34:** (a) Bright-field TEM image of polydispersed medium-sized ethylenediamine-capped palladium nanoparticles with an average diameter of  $22 \pm 6$  nm, synthesised from the reduction of  $10.38 \mu\text{M}$  palladium(II) salt with  $800 \mu\text{M}$  sodium borohydride solution in the presence of  $200 \mu\text{M}$  ethylenediamine capping agent, and (b) A plot of nanoparticle size (nm) against frequency (y-axis), highlighting a broad size distribution. (This image was acquired using a 120 kV TEM hence the low contrast between the background and the nanoparticles).

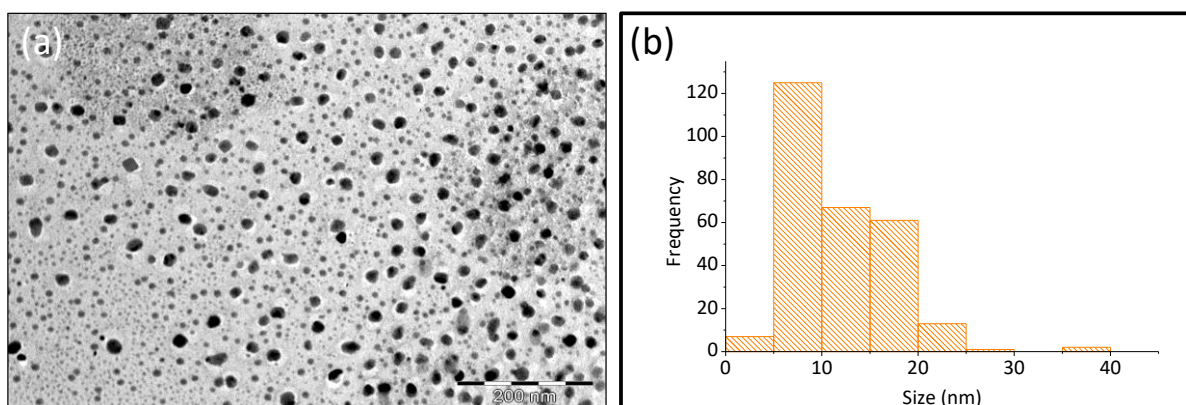


**Figure 3.35:** (a) Bright-field TEM image of polydispersed medium-sized ethylenediamine-capped palladium nanoparticles with an average diameter of  $37 \pm 6$  nm, synthesised from the reduction of  $10.15 \mu\text{M}$  palladium(II) salt with  $800 \mu\text{M}$  sodium borohydride solution in the presence of  $200 \mu\text{M}$  ethylenediamine capping agent, and (b) A plot of nanoparticle size (nm) against frequency (y-axis), highlighting a broad size distribution. (This image was acquired using a 120 kV TEM hence the low contrast between the background and the nanoparticles).

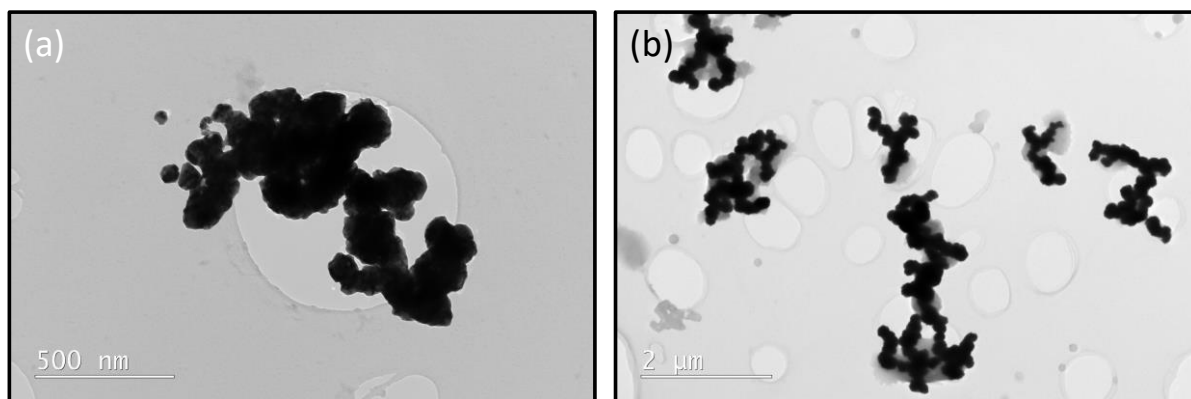


**Figure 3.36:** Bright-field TEM images of agglomerated large-sized ethylenediamine-capped palladium nanoparticles synthesised from; (a) the reduction of 10.38  $\mu\text{M}$  palladium(II) salt with 800  $\mu\text{M}$  sodium borohydride solution in the presence of 1.7 mM ethylenediamine capping agent, and (b) the reduction of 10.15  $\mu\text{M}$  palladium(II) salt with 800  $\mu\text{M}$  sodium borohydride solution in the presence of 1 mM ethylenediamine capping agent. From the measurable nanoparticles found on the grids, the size ranges were  $95.19 \pm 20.85$  nm and  $204.37 \pm 50.60$  nm, respectively.

### 3.5.3 Phthalocyanine capped nanoparticles

Tetraaminophthalocyanine (referred as phthalocyanine) has free amine groups available to interact with metal orbitals. Phthalocyanine was used to stabilise palladium nanoparticles and the obtained results presented (**Figure 3.37** – **Figure 3.41**).

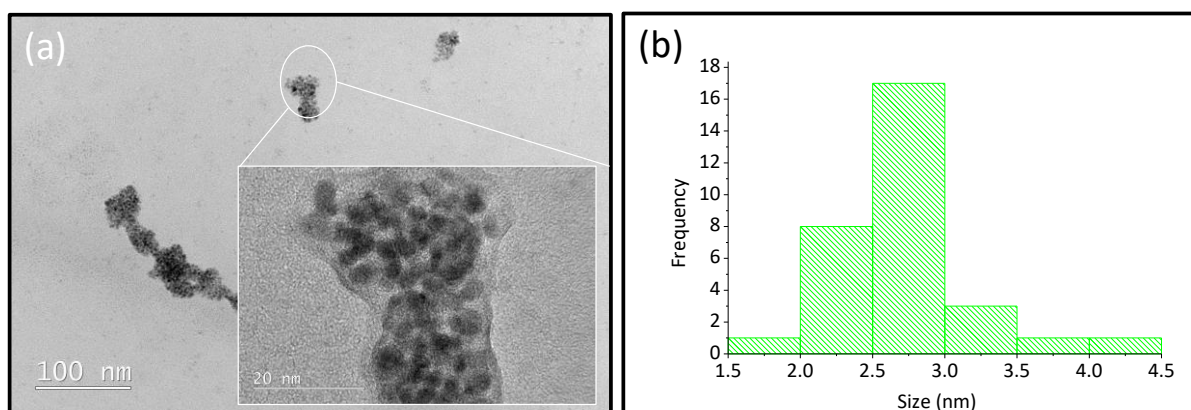


**Figure 3.37:** (a) Bright-field TEM image of dispersed small-sized phthalocyanine-capped palladium nanoparticles with an average diameter of  $2.8 \pm 0.4$  nm synthesised from the reduction of 10.32  $\mu\text{M}$  palladium(II) salt with 2 mM sodium borohydride solution in the presence of 1 mM phthalocyanine capping agent, and (b) A plot of nanoparticle size (nm) against frequency (y-axis), highlighting a narrow size distribution. The inset presents a magnified view (5X) of the encircled area showing phthalocyanine-capped palladium nanoparticles.



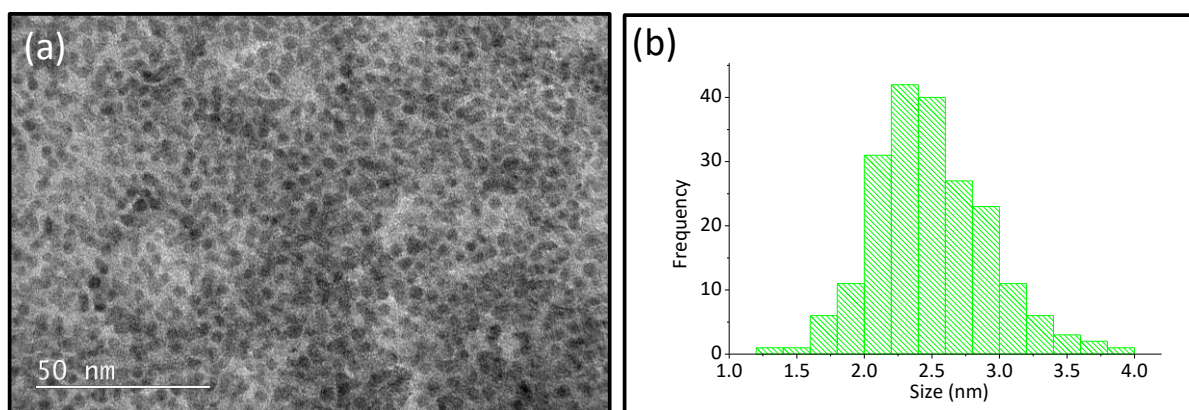


**Figure 3.38:** (a) Bright-field TEM image of monodispersed small-sized phthalocyanine-capped palladium nanoparticles with an average diameter of  $3 \pm 0.5$  nm, synthesised from the reduction of  $10.11 \mu\text{M}$  palladium(II) salt with 2 mM sodium borohydride solution in the presence of 1 mM phthalocyanine capping agent, and (b) A plot of nanoparticle size (nm) against frequency (y-axis), highlighting a narrow size distribution.

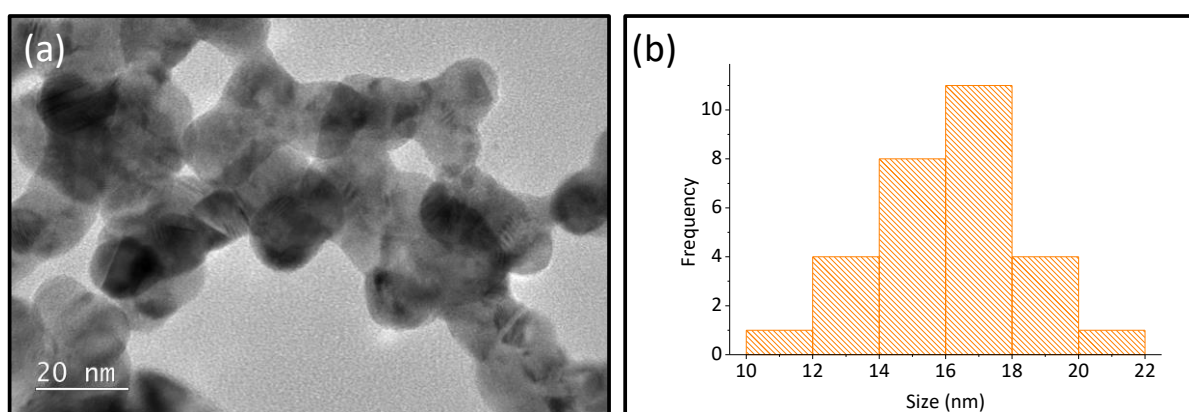


**Figure 3.39:** (a) Bright-field TEM image of medium-sized phthalocyanine-capped palladium nanoparticles with an average diameter of  $16 \pm 2$  nm, synthesised from the reduction of  $10.11 \mu\text{M}$  palladium(II) salt with  $800 \mu\text{M}$  sodium borohydride solution in the presence of  $100 \mu\text{M}$  phthalocyanine capping agent, and (b) A plot of nanoparticle size (nm) against frequency (y-axis), highlighting a slightly broad size distribution.

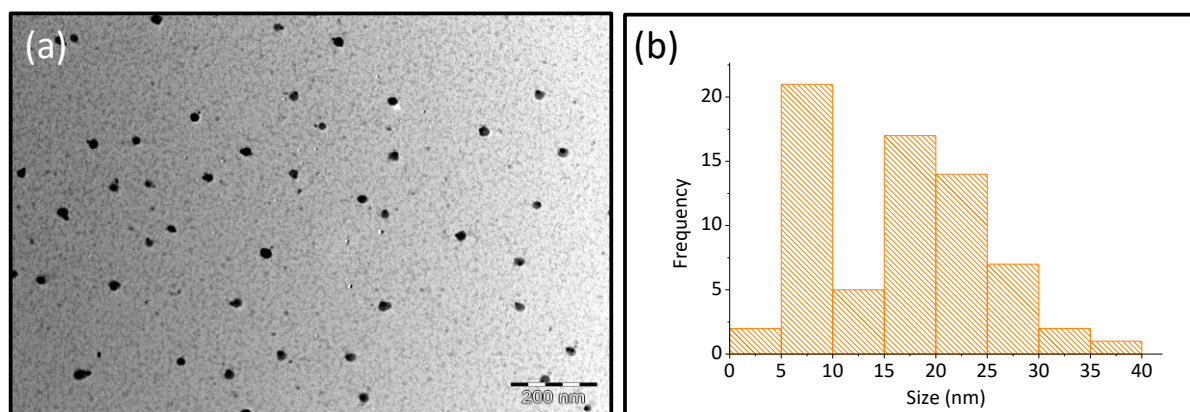


**Figure 3.40:** (a) Bright-field TEM image of dispersed medium-sized phthalocyanine-capped palladium nanoparticles with an average diameter of  $27 \pm 6$  nm, synthesised from the reduction of  $10.32 \mu\text{M}$  palladium(II) salt with  $800 \mu\text{M}$  sodium borohydride solution in the presence of  $200 \mu\text{M}$  phthalocyanine capping agent, and (b) A plot of nanoparticle size (nm) against frequency (y-axis), highlighting a broad size distribution.

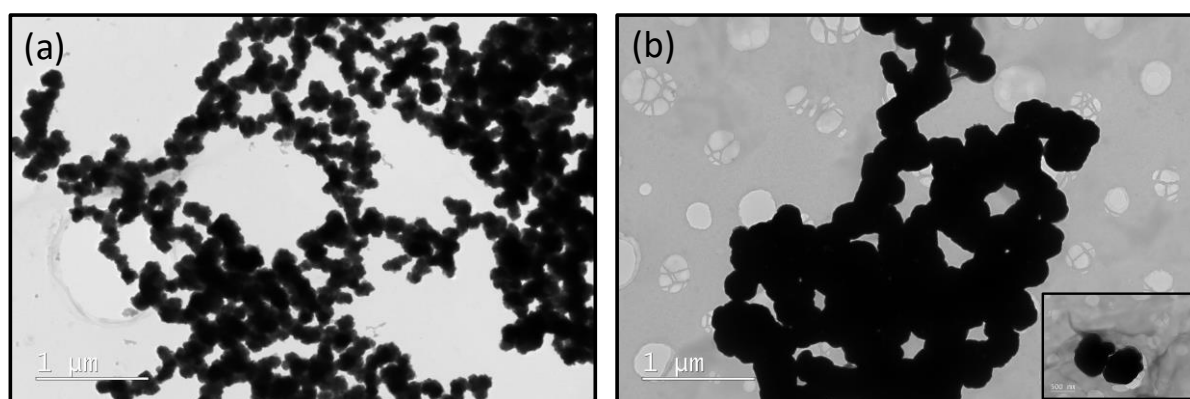


**Figure 3.41:** Bright-field TEM images of agglomerated large-sized phthalocyanine-capped palladium nanoparticles synthesised from; (a) the reduction of  $10.38 \mu\text{M}$  palladium(II) salt with  $800 \mu\text{M}$  sodium borohydride solution in the presence of  $1 \text{ mM}$  phthalocyanine capping agent, and (b) the reduction of  $10.11 \mu\text{M}$  palladium(II) salt with  $800 \mu\text{M}$  sodium borohydride solution in the presence of  $500 \mu\text{M}$  phthalocyanine capping agent. The estimated sizes from the measurable nanoparticles were  $134 \pm 6$  nm and  $252.06 \pm 36$  nm for (a) and (b), respectively.

The nanoparticles were dispersed and could easily be measured exhibiting acceptable size distributions (**Figure 3.37** – **Figure 3.40**). However, agglomerated nanoparticles are seen for large-sized nanoparticles (**Figure 3.41**) due to the tendency of the nanoparticles of large sizes to coagulate. The borohydride solution ( $800 \mu\text{M}$ ) produced highly reactive nucleation centres which were possibly not fully stabilised by the phthalocyanines.

### 3.5.4 Folate-ethylenediamine capped nanoparticles

The synthesised folate-phthalocyanine was used to stabilise the palladium(0) nanoparticles (Figure 3.42 – Figure 3.47).

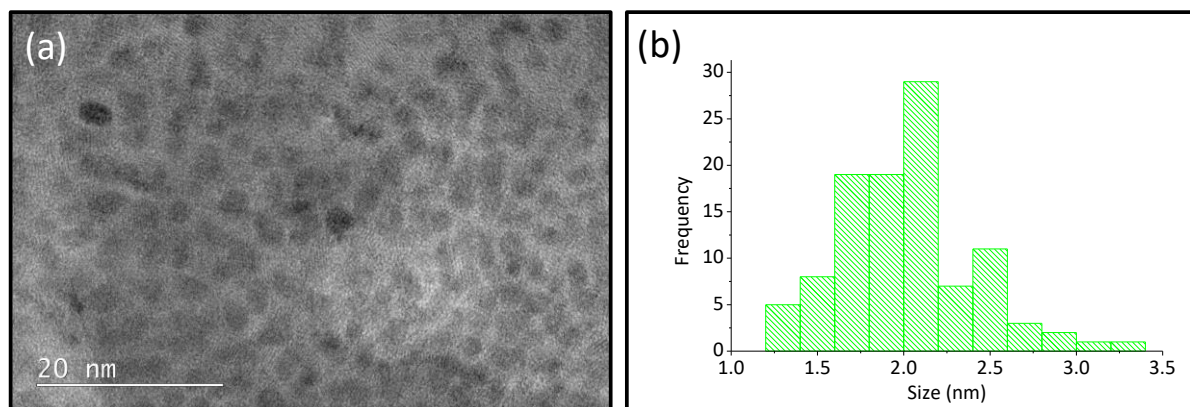


**Figure 3.42:** (a) Bright-field TEM image of polydispersed small-sized folate-ethylenediamine capped palladium nanoparticles with an average diameter of  $2.1 \text{ nm} \pm 0.1 \text{ nm}$ , synthesised from the reduction of  $10.83 \text{ } \mu\text{M}$  palladium(II) salt with  $2 \text{ mM}$  sodium borohydride solution in the presence of  $1 \text{ mM}$  folate-ethylenediamine, and (b) A plot of nanoparticle size (nm) against frequency (y-axis), highlighting a narrow size distribution.

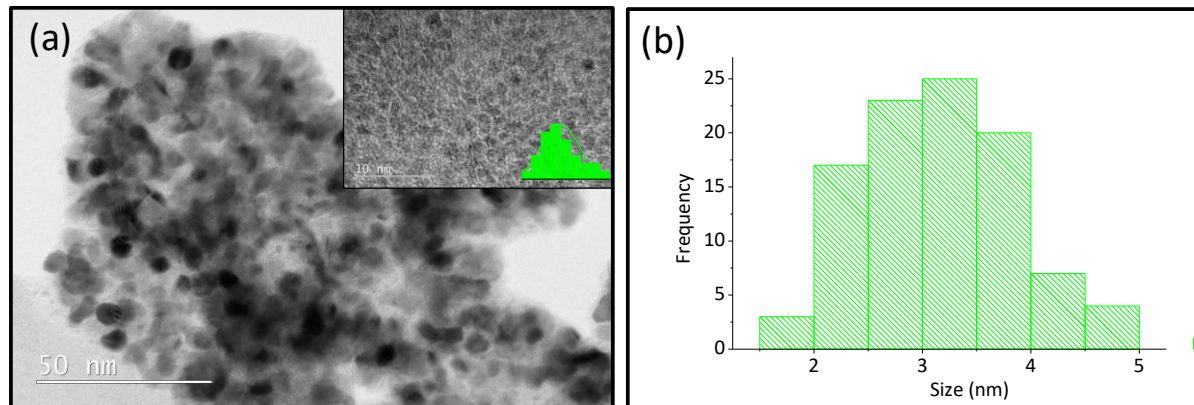


**Figure 3.43:** (a) Bright-field TEM image of polydispersed small-sized folate-ethylenediamine capped palladium nanoparticles with an average diameter of  $4.9 \pm 0.8 \text{ nm}$ , synthesised from the reduction of  $10.41 \text{ } \mu\text{M}$  palladium(II) salt with  $2 \text{ mM}$  sodium borohydride solution in the presence of  $500 \text{ } \mu\text{M}$  folate-ethylenediamine, and (b) A plot of nanoparticle size (nm) against frequency (y-axis), highlighting a narrow size distribution. The inset shows folate-ethylenediamine capped palladium nanoparticles with an average size of  $1 \pm 0.1 \text{ nm}$  synthesised from  $10.41 \text{ } \mu\text{M}$  palladium salt with  $1 \text{ mM}$  sodium borohydride solution in the presence of  $500 \text{ } \mu\text{M}$  folate-ethylenediamine.

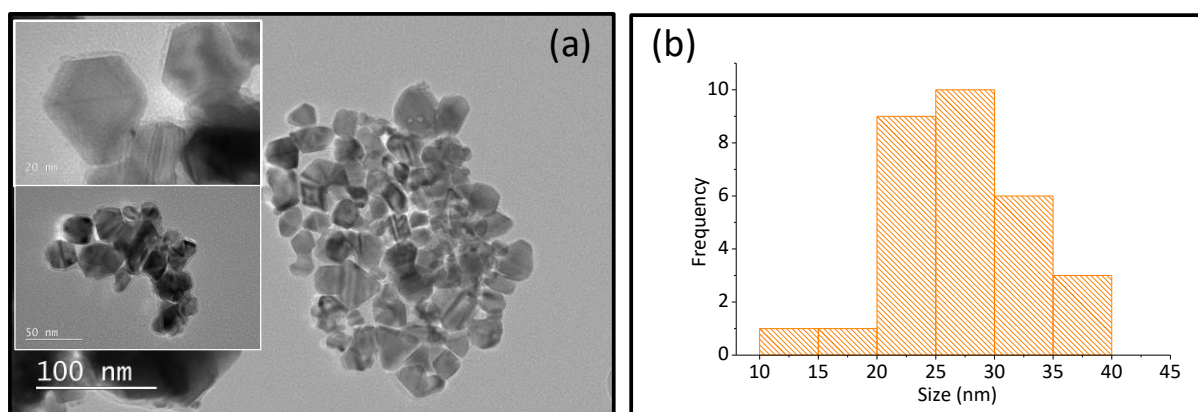


**Figure 3.44:** (a) Bright-field TEM image of dispersed medium-sized folate-ethylenediamine capped palladium nanoparticles with an average diameter of  $28 \pm 6$  nm, synthesised from the reduction of  $10.83 \mu\text{M}$  palladium(II) salt with  $800 \mu\text{M}$  sodium borohydride solution in the presence of  $200 \mu\text{M}$  folate-ethylenediamine, and (b) A plot of nanoparticle size (nm) against frequency (y-axis), highlighting a broad size distribution. The insets show magnified views (5X top, 2X bottom) of folate-ethylenediamine capped palladium nanoparticles clearly showing well defined shapes.

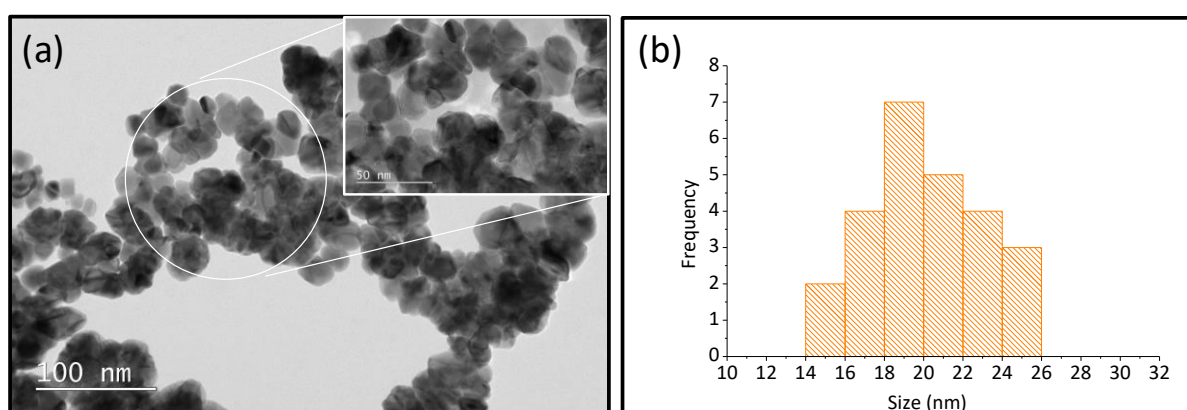


**Figure 3.45:** (a) Bright-field TEM image of medium-sized folate-ethylenediamine capped palladium nanoparticles with an average diameter of  $21 \pm 3$  nm, synthesised from the reduction of  $10.41 \mu\text{M}$  palladium(II) salt with  $800 \mu\text{M}$  sodium borohydride solution in the presence of  $200 \mu\text{M}$  folate-ethylenediamine, and (b) A plot of nanoparticle size (nm) against frequency (y-axis), highlighting a broad size distribution. The inset presents a magnified view (2X) of (a) from the encircled region.



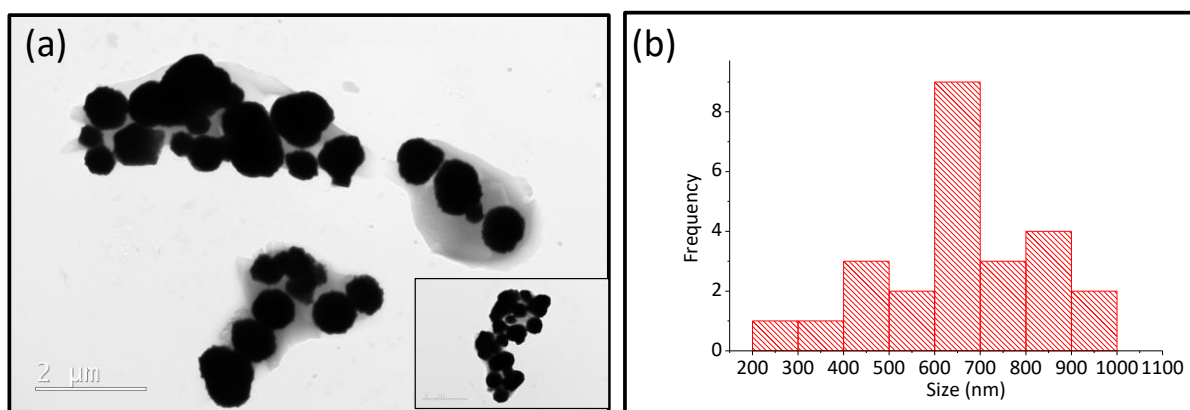


**Figure 3.46:** (a) Bright-field TEM image of large-sized folate-ethylenediamine capped palladium nanoparticles with an average diameter of  $650 \pm 164$  nm, synthesised from the reduction of  $10.41 \mu\text{M}$  palladium(II) salt with  $800 \mu\text{M}$  sodium borohydride solution in the presence of  $20 \mu\text{M}$  folate-ethylenediamine, and (b) A plot of nanoparticle size (nm) against frequency (y-axis), highlighting a broad size distribution. The inset shows partially agglomerated folate-ethylenediamine capped palladium nanoparticles.

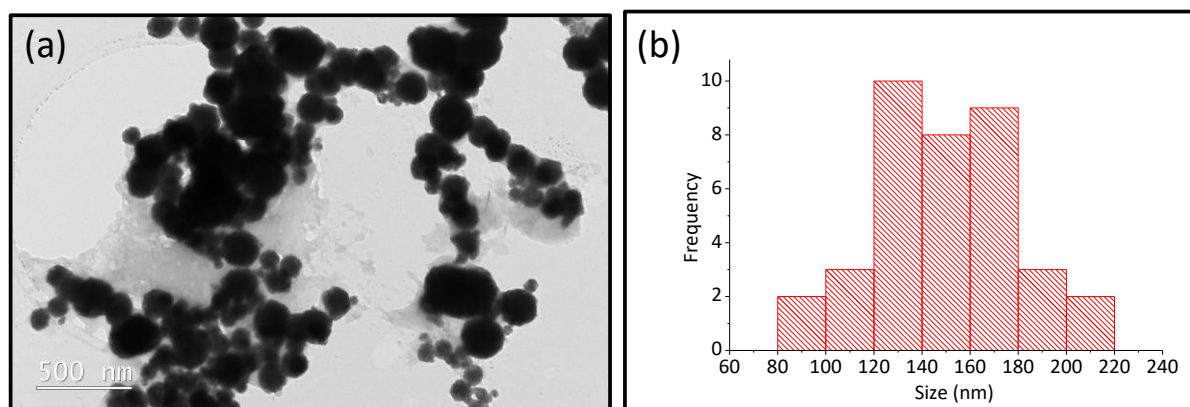


**Figure 3.47:** (a) Bright-field TEM image of large-sized folate-ethylenediamine capped palladium nanoparticles with an average diameter of  $150 \pm 30$  nm, synthesised from the reduction of  $10.83 \mu\text{M}$  palladium(II) salt with  $800 \mu\text{M}$  sodium borohydride solution in the presence of  $50 \mu\text{M}$  folate-ethylenediamine, and (b) A plot of nanoparticle size (nm) against frequency (y-axis), highlighting the palladium nanoparticles size distribution range.

The folate-ethylenediamine stabilised palladium nanoparticles better than borohydride, ethylenediamine, and phthalocyanine. This can be attributed to its relatively larger size compared to borohydride, ethylenediamine, and phthalocyanine. However, folate-phthalocyanine (larger conjugate) stabilised nanoparticles better than the other capping agents (**Figure 3.48 – Figure 3.53**).



### 3.5.5 Folate-phthalocyanine capped nanoparticles

The synthesised folate-phthalocyanine was used to stabilise palladium(0) nanoparticles (Figure 3.48 – Figure 3.53).

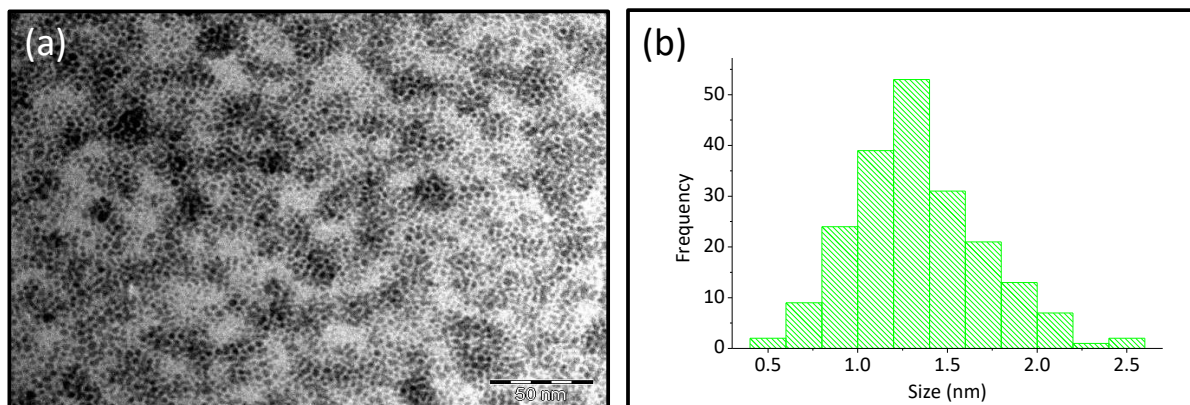


**Figure 3.48:** (a) Bright-field TEM image of monodispersed small-sized folate-phthalocyanine capped palladium nanoparticles with an average diameter of  $3.5 \pm 0.9$  nm, synthesised from the reduction of  $10.99 \mu\text{M}$  palladium(II) salt with 2 mM sodium borohydride solution in the presence of 1 mM folate-phthalocyanine, and (b) A plot of nanoparticle size (nm) against frequency (y-axis), highlighting a narrow size distribution.

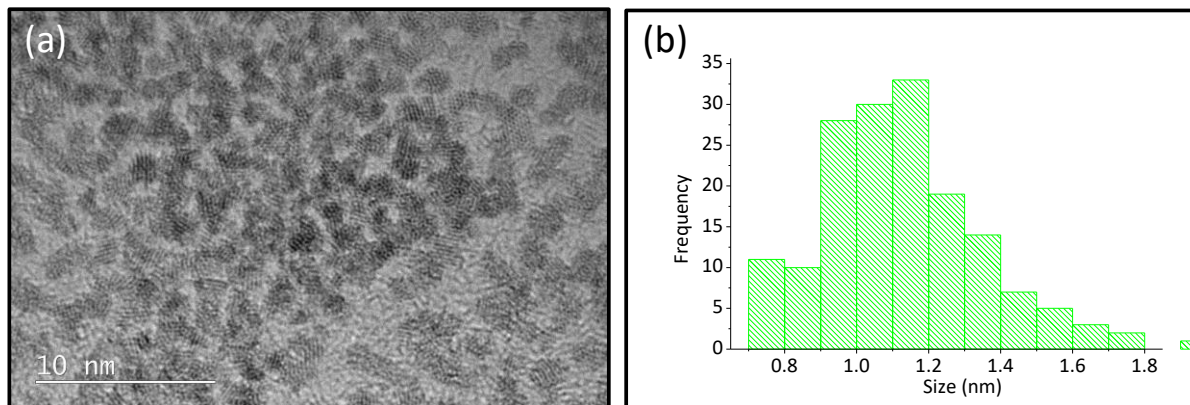


**Figure 3.49:** (a) Bright-field TEM image of polydisperse small-sized folate-phthalocyanine capped palladium nanoparticles with an average diameter of  $1.2 \pm 0.2$  nm, synthesised from the reduction of  $10.49 \mu\text{M}$  palladium(II) salt with 2 mM sodium borohydride solution in the presence of  $800 \mu\text{M}$  folate-phthalocyanine, and (b) A plot of nanoparticle size (nm) against frequency (y-axis), highlighting a narrow size distribution.

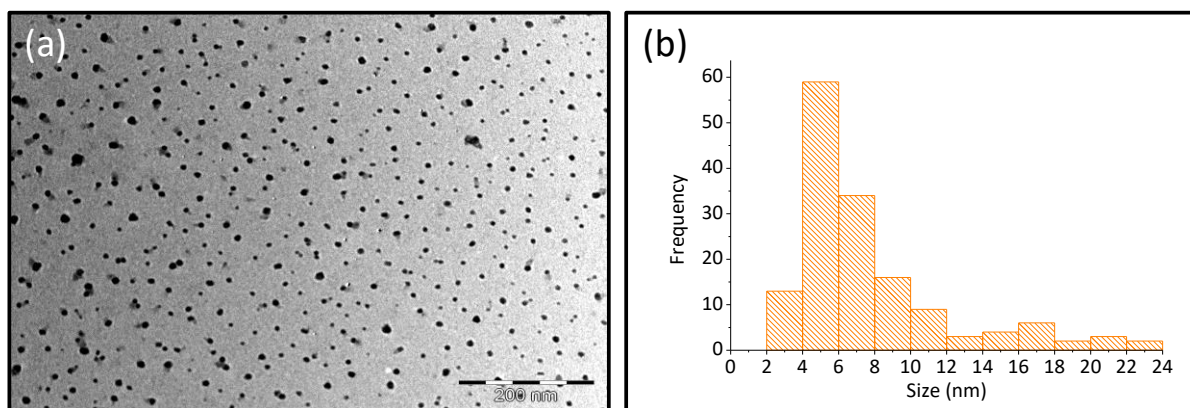


**Figure 3.50:** (a) Bright-field TEM image of dispersed medium-sized folate-phthalocyanine capped palladium nanoparticles with an average diameter of  $16 \pm 3$  nm, synthesised from the reduction of  $10.49 \mu\text{M}$  palladium(II) salt with  $800 \mu\text{M}$  sodium borohydride solution in the presence of  $200 \mu\text{M}$  folate-phthalocyanine, and (b) A plot of nanoparticle size (nm) against frequency (y-axis), highlighting a broad size distribution.

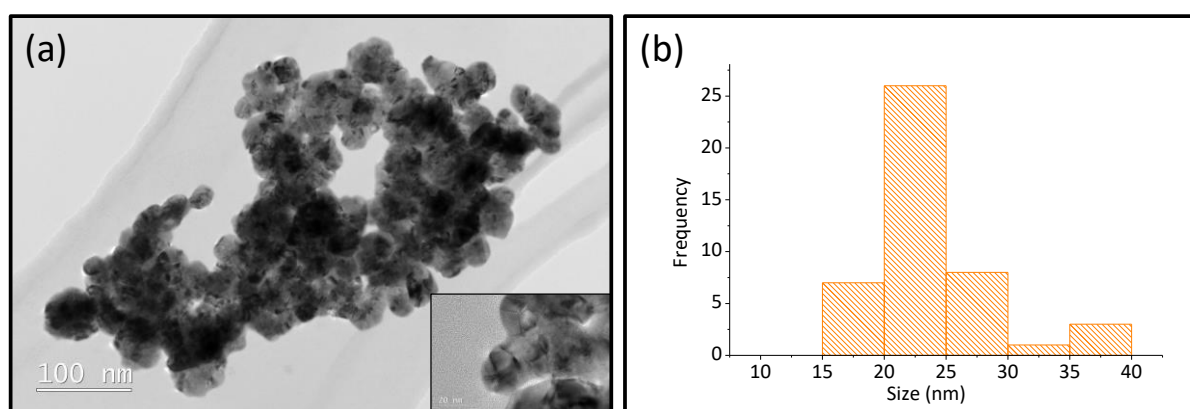


**Figure 3.51:** (a) Bright-field TEM image of medium-sized folate-phthalocyanine capped palladium nanoparticles with an average diameter of  $23 \pm 5$  nm, synthesised from the reduction of  $10.99 \mu\text{M}$  palladium(II) salt with  $800 \mu\text{M}$  sodium borohydride solution in the presence of  $200 \mu\text{M}$  folate-phthalocyanine, and (b) A plot of nanoparticle size (nm) against frequency (y-axis), highlighting a broad size distribution. The inset shows a magnified view (5X) of the folate-phthalocyanine capped palladium nanoparticles.

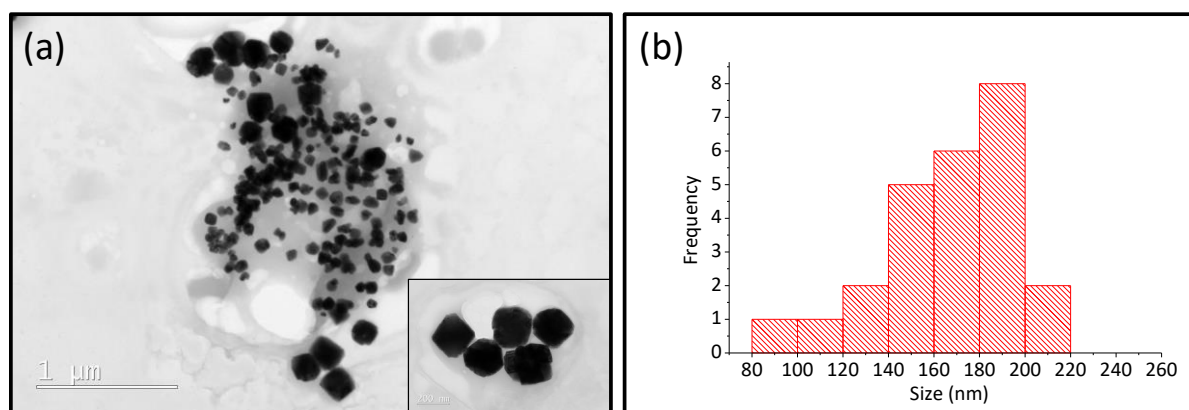


**Figure 3.52:** (a) Bright-field TEM image of large-sized folate-phthalocyanine capped palladium nanoparticles with an average diameter of  $168 \pm 28$  nm, synthesised from the reduction of  $10.49 \mu\text{M}$  palladium(II) salt with  $800 \mu\text{M}$  sodium borohydride solution in the presence of  $1$  mM folate-phthalocyanine, and (b) A plot of nanoparticle size (nm) against frequency (y-axis), highlighting a broad size distribution. The inset shows well-defined monodispersed large-sized folate-phthalocyanine capped palladium nanoparticles.

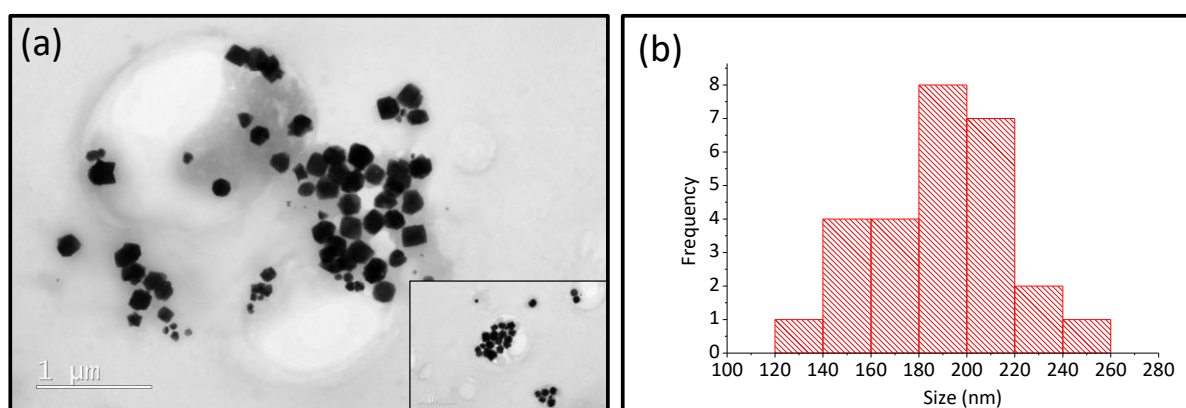


**Figure 3.53:** (a) Bright-field TEM image of dispersed large-sized folate-phthalocyanine capped palladium nanoparticles with an average diameter of  $190 \pm 29$  nm, synthesised from the reduction of  $10.99 \mu\text{M}$  palladium(II) salt with  $800 \mu\text{M}$  sodium borohydride solution in the presence of  $1$  mM folate-phthalocyanine, and (b) A plot of nanoparticle size (nm) against frequency (y-axis), highlighting a broad size distribution. The inset shows dispersed large-sized folate-phthalocyanine capped palladium nanoparticles.

The folate conjugates provided the most well defined negatively charged nanoparticles. This finding is of great significance to the application of palladium nanoparticles *in vitro* and subsequent *in vivo* studies in the development of palladium nanoradiopharmaceuticals.

### 3.6 GENERAL DISCUSSION: OPTIMISED NANOPARTICLES SYNTHESSES

The synthesis of the optimised nanoparticles is reproducible. The small-sized borohydride capped nanoparticles were spherical and evenly dispersed. The dispersity was consistent for all the small-sized nanoparticles. The medium-sized borohydride-capped nanoparticles were agglomerated together forming a flower-like crump. The large-sized borohydride-capped nanoparticles agglomerated together. The average sizes of the agglomerates (obtained from the measurable nanoparticles) were slightly outside the discussed range (**Table 2.3**). However, it was challenging to obtain smaller and more dispersed desired nanoparticles.

Ethylenediamine had spherical and elongated-like small-sized nanoparticles and slightly crumbed together large-sized nanoparticles forming elongates. The same trend was obtained for phthalocyanine capped nanoparticles. The small and medium-sized nanoparticles had dispersed nanoparticles and the large-sized palladium nanoparticles were agglomerated forming some branches. The size distributions were acceptable; there are no size overlaps, nullifying any results misinterpretation.

The folate-ethylenediamine produced evenly distributed nanoparticles of defined shapes. They had non-overlapping narrow size distributions and small negative charges (**Table 3.4**). Folate-phthalocyanine nanoparticles gave dispersed nanoparticles for all the sizes. This agrees to the known trend that smaller capping agents prevent agglomeration less compared to their bigger or large-sized counterparts. Folate-phthalocyanine has a bulkier structure, and hence it could easily stabilise the nucleating centres preventing agglomeration, relative to the smaller capping agents.

It can be concluded that different sized nanoparticles can be synthesised under controlled conditions and be reproduced (**Figure 3.28 - Figure 3.53**). As expected, it was confirmed that different shapes of palladium(0) nanoparticles exist and can be obtained from the reduction of palladium(II) by sodium borohydride and capped with amine-containing compounds.

The optimised nanoparticles meet the required characteristics of nanoparticles for biological applications (**Section 1.3.2**). Despite the large-sized nanoparticles being in the micro- range (**Table 3.4**), they can be used in drug delivery applications [362].

This success led to the investigation of the cytotoxicity, cellular uptake, and internalisation using the optimised palladium nanoparticles (**Chapter 4**).

## CHAPTER FOUR: BIOCHEMICAL EVALUATION OF PALLADIUM NANOPARTICLES

### 4.1 GENERAL INTRODUCTION

Nanoparticle applications have increasingly contributed towards the advancement of research development in several biomedical fields, e.g. the use of nanoradiopharmaceuticals [363]. Specific *in vitro* receptor delivery systems have been reported for protein toxins, such as anti-T-cell receptor antibodies, chemotherapy agents, and magnetic resonance imaging contrast agents [212], highlighting interest in the use of low molecular weight radiopharmaceuticals (RPs).

Literature focuses on the ease of functionalisation and conjugation of nanoparticles with various biomolecules to enhance drug targeting and biodiagnostics. Metals and metal-derived compounds have been used in medicine for several thousands of years [364–366]. Metal nanoparticles are utilised in various diagnostic and therapeutic purposes [367], due to metal nanoparticles having the ability to translocate to tissues without having a detrimental effect on cell viability [364]. At higher concentrations, nanoparticles are usually toxic to biological systems because of their inherent ability to cross biomembranes and interference with basal metabolic reactions within the cell [128, 368].

Folic acid conjugated nanoparticles are reported to have less cytotoxicity, increased dispersibility, bio- and cytocompatibility, and increased specificity with other bioactive molecules [194, 218]. As foreign substances and with concerns around the safety of the application of nanomaterials in humans [126, 368], their cytotoxicity studies were conducted on four cell lines with varied alpha folate receptor (FR) expression (**Table 1.8**), namely; MDA-MB-468 ( $\alpha$ -FR negative), MCF-7 (overexpressed  $\alpha$ -FR), MDA-MB-231 (overexpressed  $\alpha$ -FR), and MCF-10A (normal  $\alpha$ -FR expression).

One of the primary aims of this study was to preferentially target cancer cells by exploiting the overexpressed levels alpha folate receptor ( $\alpha$ -FR) levels in cancer cell lines using non-toxic concentrations of palladium nanoparticles. The FR is generally not overexpressed in most normal tissues [369], thus the  $\alpha$ -FR overexpression in cancer cells was targeted as a potential target for folate conjugated palladium nanoparticles.

## 4.2 CYTOTOXIC STUDIES

Recent studies showed successful folate receptor targeting [370], however, the potential toxicity of nanoparticles remains a major concern [126, 371]. The cytotoxicity of the different nanoparticles and their precursors (**Table 4.1**) for *in vitro* studies was conducted using the four cell lines (**Table 1.8**). Treatment screening concentrations were 10 and 100  $\mu\text{M}$  palladium(0) content (**Table 2.5** and **Table 4.2**). The main focus of this section was to determine the relevant concentrations that did not result in low cell viability (i.e. non-cytotoxic concentrations) since the hot isotopes would have an effect on the theranostic aspects for the *in vivo* studies.

**Table 4.1:** The important abbreviations and colours for interpreting the cytotoxic results.

	Colour used to denote small-sized ( <i>sz</i> ) nanoparticles (NPs) of less than 10 nm
	Colour used to denote medium-sized ( <i>mz</i> ) nanoparticles (NPs) with sizes between 10 and 80 nm
	Colour used to denote large-sized ( <i>lz</i> ) nanoparticles (NPs) with sizes between 80 and 300 nm
	Colour used to denote an untreated cell line (UT)
	Colour used to denote a control treatment
UT	Untreated cells
FA	Folic acid
MTX	Methotrexate
EDA	Ethylenediamine
Pc	Phthalocyanine
FA-EDA	Folate-ethylenediamine
FA-Pc	Folate-phthalocyanine
B <sup>h</sup> -NPs	Small-sized borohydride capped nanoparticles ( <i>sz</i> -B <sup>h</sup> -NPs)
B <sup>h</sup> -NPs	Medium- sized borohydride capped nanoparticles ( <i>mz</i> -B <sup>h</sup> -NPs)
B <sup>h</sup> -NPs	Large-sized borohydride capped nanoparticles ( <i>lz</i> -B <sup>h</sup> -NPs)
ED <sup>h</sup> -NPs	Small sized ethylenediamine capped nanoparticles ( <i>sz</i> -ED <sup>h</sup> -NPs)
ED <sup>h</sup> -NPs	Medium-sized ethylenediamine capped nanoparticles ( <i>mz</i> -ED <sup>h</sup> -NPs)
ED <sup>h</sup> -NPs	Large-sized ethylenediamine capped nanoparticles ( <i>lz</i> -ED <sup>h</sup> -NPs)
P <sup>c</sup> -NP	Small-sized phthalocyanine capped nanoparticles ( <i>sz</i> -P <sup>c</sup> -NPs)



**Table 4.1:** Continued.

PĈ-NP	Medium-sized phthalocyanine capped nanoparticles (mz-PĈ-NPs)
PĈ-NP	Large-sized phthalocyanine capped nanoparticles (lz-PĈ-NPs)
FA-EDĀ-NP	Small-sized folate-ethylenediamine capped nanoparticles
FA-EDĀ-NP	Medium-sized folate-ethylenediamine capped nanoparticles
FA-EDĀ-NP	Large-sized folate-ethylenediamine capped nanoparticles
FA-PĈ-NP	Small-sized folate-phthalocyanine capped nanoparticles
FA-PĈ-NP	Medium-sized folate-phthalocyanine capped nanoparticles
FA-PĈ-NP	Large-sized folate-phthalocyanine capped nanoparticles
	Colour used to denote the MCF-10A cell line
	Colour used to denote the MDA-MB-231 cell line
	Colour used to denote the MCF-7 cell line
	Colour used to denote the MDA-MB-231 cell line

Palladium has no known negative therapeutic effects [372] and is non-toxic to the skin [373]. Its ability to possibly coordinate with amino acids, proteins, DNA, and other macromolecules (e.g. vitamin B<sub>6</sub>), makes it capable of inhibiting some cellular functions [374]. Palladium's toxicity is dependent on its covalent state [375]. At 500  $\mu\text{M}$ , palladium(II) inactivates trypsin [376] and is known to competitively inhibit creatine kinase and non-competitively inhibit aldolase, succinate dehydrogenase, and alkaline phosphatase [372]. Higher concentrations (>100  $\mu\text{M}$ ) of palladium nanoparticles are reported to induce mitochondrial dysfunction [377, 378] in some cell lines, however, at the lower concentrations, there are no reported cytotoxic effects. As a result, the cytotoxicity effects of the palladium nanoparticles in this study were initially screened at 100  $\mu\text{M}$  (palladium content) using the MDA-MB-468 cell line, and subsequently at 10  $\mu\text{M}$  (palladium content) using MDA-MB-468, MCF-7, MDA-MB-231, and MCF-10A cell lines.

#### 4.2.1 MDA-MB-468 cell viability screen

The MDA-MB-468 cell line has no folate receptors (**Table 1.8**). The cytotoxic effects of the 100  $\mu\text{M}$  palladium nanoparticles (palladium content), and control treatments at the higher concentrations than the amounts used to cap the nanoparticles were investigated (**Figure 4.1**).

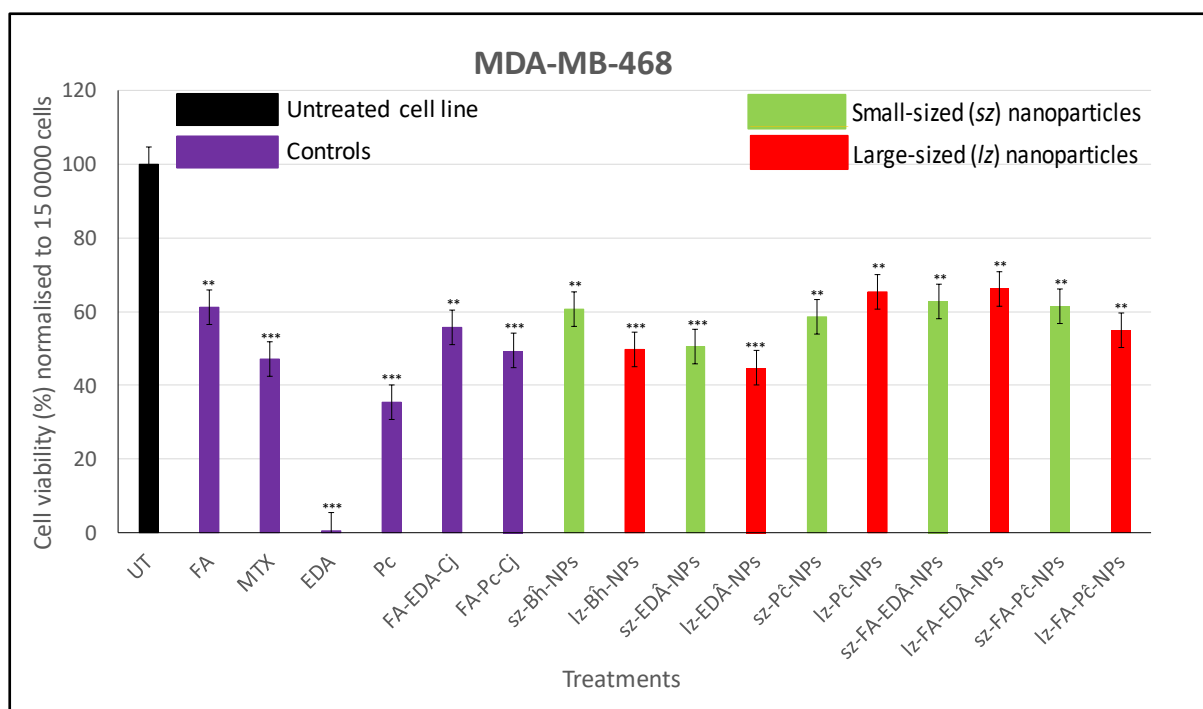


**Figure 4.1:** The MDA-MB-468 cell line's cytotoxic profiles for the different treatments; 100  $\mu$ M (palladium content) palladium nanoparticles, 13.6 mM folic acid (FA), 13.2 mM methotrexate (MTX), 13.5 mM ethylenediamine (EDA), 13.6 mM phthalocyanine (Pc), 12.5 mM folate-ethylenediamine (FA-EDA), 12.9 mM folate-phthalocyanine (FA-Pc), and untreated (UT) MDA-MB-468 cell line. The experiments were completed in triplicate (N=3), and the significance was marked with asterisks \*; for a p-value <0.05 (significant), \*\* for a p-value <0.01 (significant), and \*\*\* for a p-value <0.001 (highly significant) was determined using one-way analysis of variance (ANOVA) relative to the control (untreated cells).

Treatments that resulted in cell viability values higher than 80% were considered non-toxic [379]. The treatments that resulted in cell viability values below 80% relative to the untreated (UT) cells (**Figure 4.1**) were folic acid (control), small-sized borohydride capped, large-sized phthalocyanine capped, small-sized folate-ethylenediamine capped, large-sized folate-ethylenediamine capped, and the small-sized folate-phthalocyanine capped palladium nanoparticles treated cells exhibited cell viability values above 60%.

The small-sized and large-sized folate-phthalocyanine capped nanoparticles exhibited a highly significant ( $p < 0.001$ ) decrease in cell viability relative to the untreated cell line, a significant ( $p < 0.01$ ) increase in cell viability for the folate-phthalocyanine treatment (control). The small-sized folate-phthalocyanine capped nanoparticles treatment displayed a higher cell viability relative to the large-sized folate-phthalocyanine capped nanoparticles treatment. The small-



sized and large-sized folate-ethylenediamine capped nanoparticles treatments had a highly significant ( $p < 0.001$ ) decrease in cell viability relative to the untreated cell line, and a significant increase in viability relative to the folate-ethylenediamine (control). The small-sized folate-ethylenediamine capped nanoparticles treatments displayed a significant ( $p < 0.01$ ) increase in cell viability relative to the large-sized folate-ethylenediamine capped nanoparticles. The small-sized and large-sized phthalocyanine capped nanoparticles treatments exhibited highly significant ( $p < 0.01$ ) decrease in cell viability relative to the untreated cell line, and a significant ( $p < 0.05$ ) increase in viability relative to the folate-ethylenediamine (control). The small-sized and large-sized ethylenediamine capped nanoparticles treatments exhibited a highly significant ( $p < 0.001$ ) decrease in cell viability relative to the untreated cell line, and significant ( $p < 0.01$ ) increase in cell viability relative to free ethylenediamine (control). The large-sized ethylenediamine capped nanoparticles treatments displayed a lower cell viability relative to the small-sized ethylenediamine capped. The small-sized borohydride capped nanoparticles treatments showed significant ( $p < 0.01$ ) decrease in cell viability relative to the untreated cells, with the large-sized borohydride capped nanoparticles displaying a highly significant ( $p < 0.001$ ) decrease in cell viability relative to the untreated cells and a lower cell viability relative to the small-sized borohydride capped nanoparticles.

Folic acid unexpectedly showed low cell viability; however, it has previously been shown to possibly be toxic at 13.6 mM [380]. In this case, the folate may not be taken up *via* the folate receptor [230], but potentially *via* the low affinity (micromolar range) reduced folate carrier (RFC) [381]. MDA-MB-468 cell line is folate receptor negative, methotrexate (MTX), a folate-analogue cancer drug, gave a decrease in cell viability as expected [381–383], and is attributed to the uptake of MTX *via* non-folate receptor-mediated processes. Ethylenediamine (EDA) exhibited the highest toxicity; this may be attributed to the selective ability of diamines to interact with cellular components triggering apoptosis [384]. It is possible that the cell line MDA-MB-468 is poorly resistant to ethylenediamine, possibly due to its chelating nature to metal ions. Ethylenediamine containing palladium nanoparticles were cytotoxic at 100  $\mu$ M. This can be attributed to possible DNA denaturation since palladium(II) ethylenediamine containing complexes are cytotoxic [385] at 100  $\mu$ M [386] and this finding should be discussed further. The low cell viability for the phthalocyanine control treatment was unexpected since phthalocyanines are known to be non-cytotoxic [387–390], and have no reported cytotoxicity at this concentration [391] and as we are aware no available literature exists reporting Pc effects on the MDA-MB-468 cell line. The MDA-MB-468 cell line's response to amine-

containing compounds (EDA and Pc) at 13 mM will be further deconvoluted in future studies to provide an experiment-based explanation. It is possible, therefore, that the absence of oestrogen, progesterone, HER2, and adenosine receptors, play an unknown and unpublished role in the MDA-MB-468 cell line being more reactive to the amine functional group at the reported concentrations. Nanoparticles have peculiar physical properties, and their potential toxic effects cannot be assumed or predicted from the metal ion properties; however, at 100  $\mu\text{M}$  the palladium(0) nanoparticles showed cytotoxicity similar to palladium(II) [392]. The absence of literature on palladium's role in cancer development [392], the toxicity of palladium(0) nanoparticles, and the pending mechanistic assays studies on palladium compounds [393], limit explanations for unexpected findings.

For this study, a non-toxic concentration was required. The preferred results in this study are those that have no significant cytotoxicity (**Figure 4.2 - Figure 4.5**), since this is a preliminary study for radiation-induced apoptosis (cell death). Treatments at 100  $\mu\text{M}$  studies displayed cytotoxic effects over the palladium nanoparticles on MDA-MB-468, as such the experiment was repeated at 10  $\mu\text{M}$  palladium nanoparticles (**Figure 4.2**), with the addition of medium-sized nanoparticles treatments.

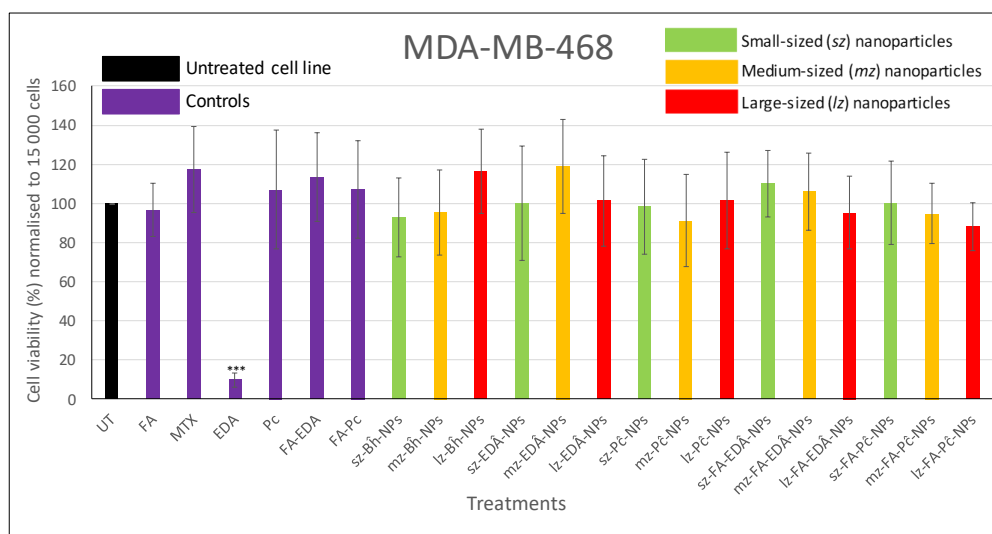


**Figure 4.2:** The MDA-MB-468 cell line's cytotoxic profiles for the different treatments; 10  $\mu\text{M}$  (palladium content) palladium nanoparticles, 1.36 mM folic acid (FA), 1.32 mM methotrexate (MTX), 1.35 mM ethylenediamine (EDA), 1.36 mM phthalocyanine (Pc), 1.25 mM folate-ethylenediamine (FA-EDA), 1.29 mM folate-phthalocyanine (FA-Pc), and untreated (UT) MDA-MB-468 cells. The experiments were completed in triplicate (N=3), and the significance was marked with asterisks \*, for a p-value <0.05 (significant), \*\* for a p-value <0.01 (significant), and \*\*\* for a p-value <0.001 (highly significant) was determined using one-way analysis of variance (ANOVA) relative to the control (untreated cells).

Reducing the nanoparticles treatment concentration to 10  $\mu\text{M}$  did significantly ( $p < 0.05$ ) increase in cell viability as reported in literature [379]. Only ethylenediamine exhibited cytotoxicity of greater than 80% (**Figure 4.2**). Ethylenediamine and its derivatives are known to be toxic at amounts ( $>100 \mu\text{M}$ ) [394]. However, this could be attributed to the sensitivity of the MDA-MB-468 cell line to free ethylenediamine. The ethylenediamine capped nanoparticles treatment exhibited an increased cell viability relative to the free ethylenediamine (control), this may be due to known unavailability of lone pairs on capping agents as they electronically stabilise the metal nanoparticles [395].

At 1.32 mM, FA was not cytotoxic as previously reported [380]. MTX uptake is non-folate receptor-dependent; however, it is time- and concentration-dependent. At this concentration (1.32 mM), it can be concluded that the cellular uptake was not significant at decreasing cell viability. A similar trend has been previously documented using a similar concentration (2.2 mM) and exposure time (24 h) [396], and may be attributed to the affinity of reduced folate carrier (RFC) affinity's for MTX [397]. At lower concentrations, phthalocyanine and folate conjugates showed increased cell viability as expected [398, 399]. There is no significant cell viability difference or notable trend in cell viability across the different sizes and capping agents used. With MDA-MB-468 cell line being folate receptor negative and the nanoparticles optimised for differential uptake based on capping agent, any possible uptake and internalisation was expected to be a similar rate and independent of size and capping agents (**Section 4.5**). As a result, since palladium nanoparticles at 10  $\mu\text{M}$  are non-toxic [392], the difference in the cell viability was not significant across all the investigated treatments.

#### 4.2.2 MCF-7 cell viability screen

No significant difference in cell viability was reported for MDA-MB-468 (folate receptor negative) cell line; the cytotoxic effects were investigated (**Figure 4.3**) using the MCF-7, which is considered a low folate receptor expression cell line.

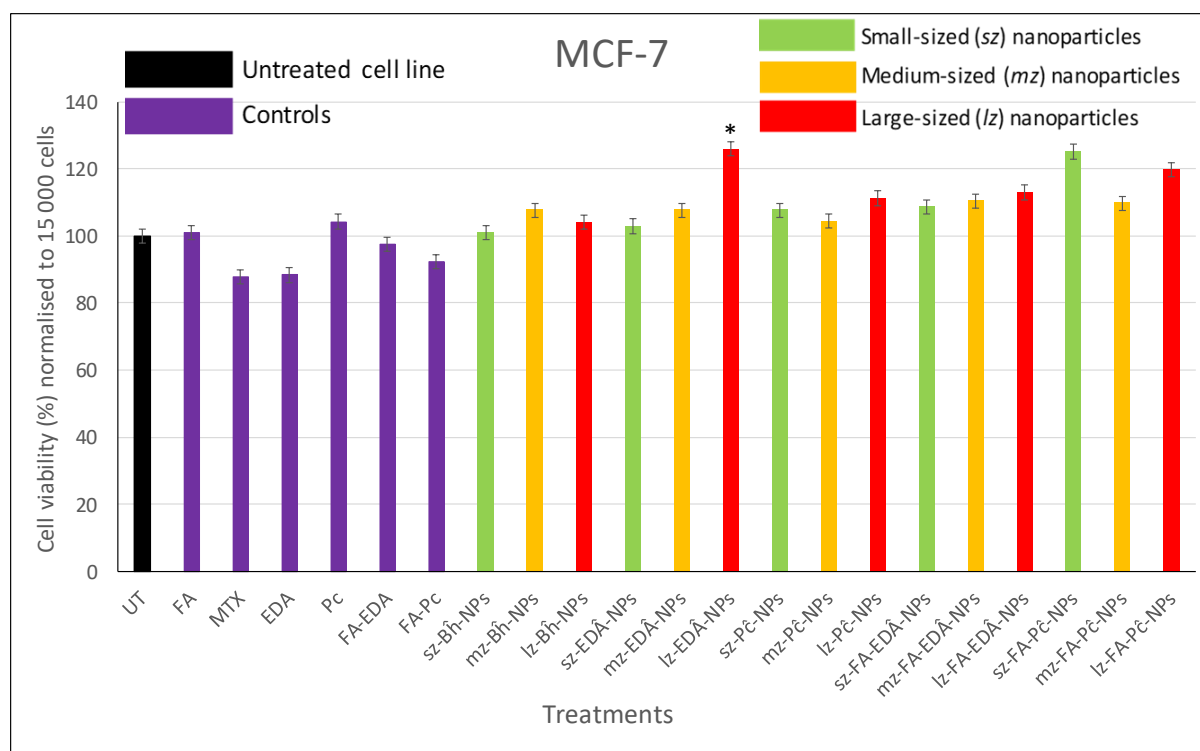


**Figure 4.3:** The MCF-7 cell line's cytotoxic profiles for the different treatments; 10  $\mu\text{M}$  (palladium content) palladium nanoparticles, 1.36 mM folic acid (FA), 1.32 mM methotrexate (MTX), 1.35 mM ethylenediamine (EDA), 1.36 mM phthalocyanine (Pc), 1.25 mM folate-ethylenediamine (FA-EDA), 1.29 mM folate-phthalocyanine (FA-Pc), and untreated (UT) MCF-7 cell line. The experiments were completed in triplicate ( $N=3$ ), and the significance was marked with asterisks \*; for a  $p$ -value  $<0.05$  (significant), \*\* for a  $p$ -value  $<0.01$  (significant), and \*\*\* for a  $p$ -value  $<0.001$  (highly significant) was determined using one-way analysis of variance (ANOVA) relative to the control (untreated cells).

Folic acid (FA) treatment had no significant change (**Figure 4.3**) in cell viability compared to the untreated cell line (control), potentially indicating that at the investigated folic acid concentration no up-regulation of the folate receptors did not lead to increased folate uptake to trigger proliferation as reported in literature [210]. As expected, methotrexate (MTX) treatment had the lowest cell viability (compared to other treatments), due to the reported decrease in the antiproliferative action on MCF-7 cells [400]. Literature reported that to a lesser extent MCF-7 cell line is resistant to low levels of MTX [396, 401, 402]. Unlike for the MDA-MB-468 cells, the MCF-7 cells displayed a cell viability of about 86% for the ethylenediamine (EDA) treatment. Phthalocyanine (Pc) treatment was non-toxic confirming previous findings documented in literature [389, 398, 403]. The folate conjugates (FA-EDA and FA-Pc) treatments demonstrated similar cytotoxicity levels (between 105 and 122%). All

the palladium nanoparticle treatments exhibited the preferred and expected increase in cell viability [378] between 90 and 100%. The large-sized nanoparticle treatments gave a higher cell viability compared to the small and medium-sized nanoparticles, with the large-sized ethylenediamine capped nanoparticles showing the most mitochondrial activity relative to all other treatments. The small-sized borohydride capped nanoparticles showed the lowest cell viability compared to other capping agents of similar sizes. This contradicts the notable observation for the MDA-MB-231 cell line, which also overexpresses folate receptors.

#### 4.2.3 MDA-MB-231 cell viability screen

Compared to the MCF-7 cells, the MDA-MB-231 cells have a high folate receptor expression (Table 1.8). The cytotoxicity of the 10  $\mu$ M palladium nanoparticles and control treatments (Table 2.5) were investigated (Figure 4.4).

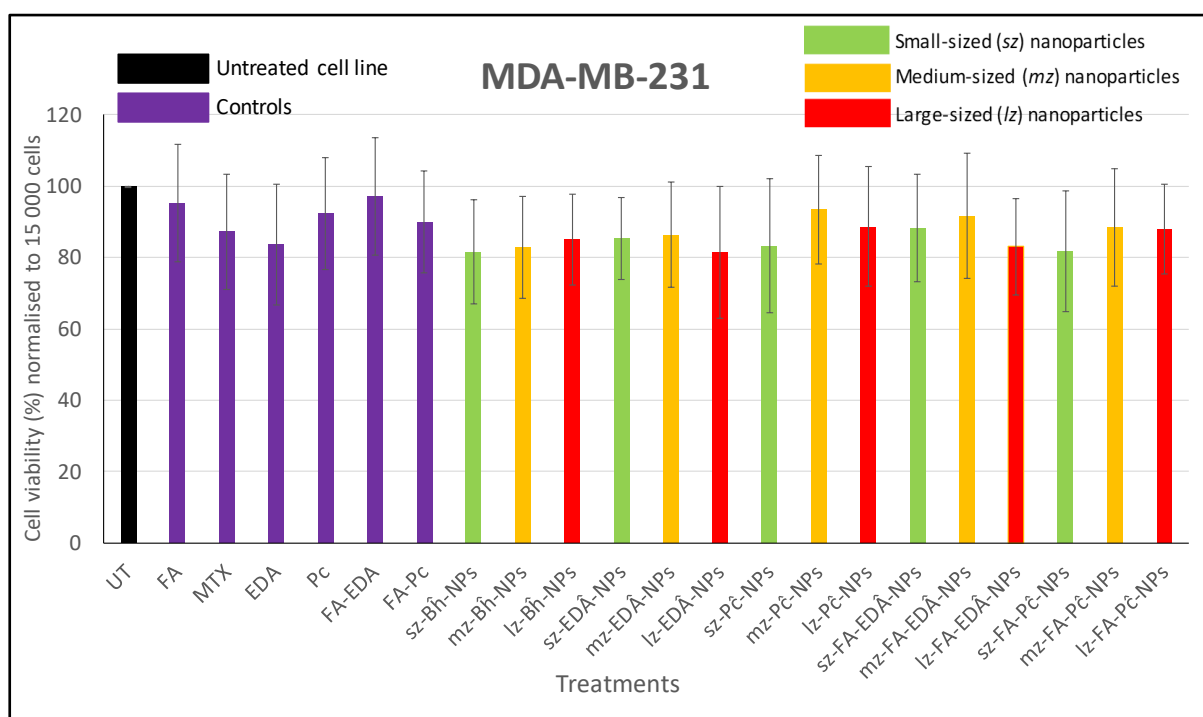


**Figure 4.4:** The MDA-MB-231 cell line's cytotoxic profiles for the different treatments; 10  $\mu$ M (palladium content) palladium nanoparticles, 1.36 mM folic acid (FA), 1.32 mM methotrexate (MTX), 1.35 mM ethylenediamine (EDA), 1.36 mM phthalocyanine (Pc), 1.25 mM folate-ethylenediamine (FA-EDA), 1.29 mM folate-phthalocyanine (FA-Pc), and untreated (UT) MDA-MB-231 cell line. The experiments were completed in triplicate (N=3), and the significance was marked with asterisks \*: for a p-value <0.05 (significant), \*\* for a p-value <0.01 (significant), and \*\*\* for a p-value <0.001 (highly significant) was determined using one-way analysis of variance (ANOVA) relative to the control (untreated cells).

All treatments had between 80 and 100% cell viability (**Figure 4.4**), with folate-ethylenediamine recording the highest cell viability (96%) relative to other control treatments. MTX, EDA, Pc, FA-Pc, and FA-EDA showed cell viability values lower than the untreated cells. However, the MDA-MB-231 cell line was found to be resistant to MTX [223], and had very low toxicity for N-containing compounds [394]. Therefore, low cell viability values were unexpected. Furthermore, the cell viability of the controls was insignificantly different to the nanoparticles as expected, but lower than the untreated cell line. Thus, pending further investigations, it can be accepted that the cell line exhibited decreased viability for palladium nanoparticles treatments relative to the untreated cell line (control).

#### 4.2.4 MCF-10A cell viability screen

MCF-10A cell line was a non-tumorigenic control and for the purpose of this study was considered the normal cell line with extremely low expression of  $\alpha$ -folate receptor expression [404]. The cytotoxic effects of 10  $\mu$ M palladium nanoparticles and control treatments (**Table 2.5**) on the MCF-10A cell line were investigated (**Figure 4.5**).

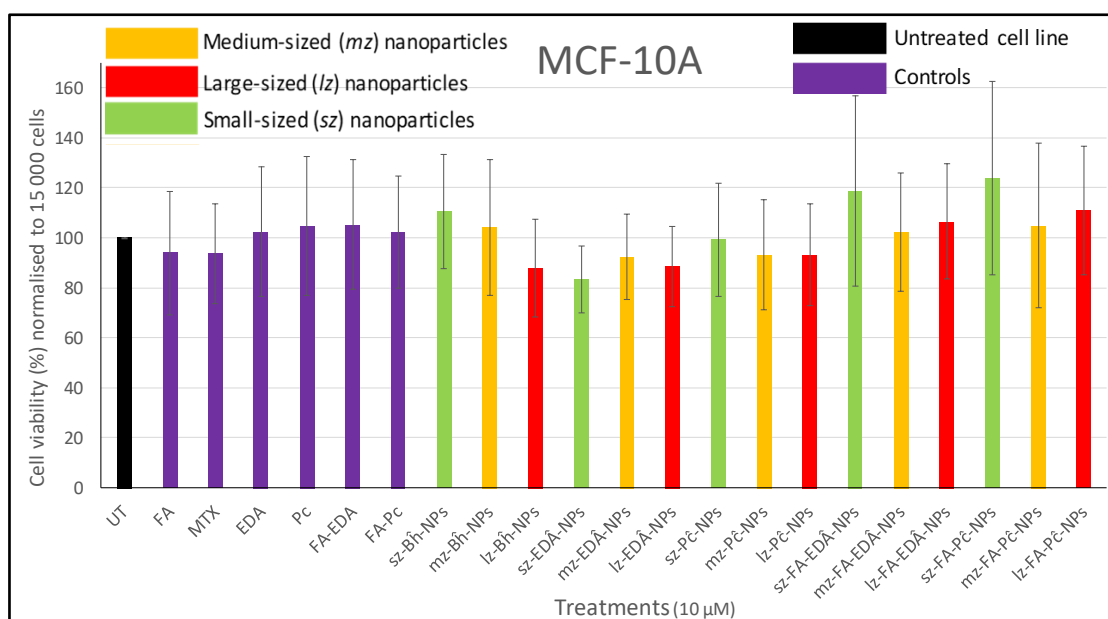


**Figure 4.5:** The MCF-10A cell line's cytotoxic profiles for the different treatments; 10  $\mu$ M (palladium content) palladium nanoparticles, 1.36 mM folic acid (FA), 1.32 mM methotrexate (MTX), 1.35 mM ethylenediamine (EDA), 1.36 mM phthalocyanine (Pc), 1.25 mM folate-ethylenediamine (FA-EDA), 1.29 mM folate-phthalocyanine (FA-Pc), and untreated (UT) MCF-10A cell line. The experiments were completed in triplicate (N=3), and the significance was marked with asterisks \*; for a p-value <0.05 (significant), \*\* for a p-value <0.01 (significant), and \*\*\* for a p-value <0.001 (highly significant) was determined using one-way analysis of variance (ANOVA) relative to the control (untreated cells).

All treatments had cell viability between 84 and 122% at the investigated concentrations (**Figure 4.5**). At 1.36 mM, folic acid has been documented to be nontoxic [380] and promote cell proliferation [197]. Therefore, it was expected that the folate-containing controls have increased proliferation relative to the untreated cell line (control). Methotrexate (MTX) treatment had no significant change in cell viability and is reportedly non-toxic to non-tumorigenic cell lines [383]. The ethylenediamine-capped and phthalocyanine-capped palladium nanoparticles treatments showed decreased viability relative to ethylenediamine and phthalocyanine control treatments. Despite the amine lone pair of electrons being unavailable, it can further be suggested that the amine functional group is attributed to the notable decrease in cell viability, since other palladium nanoparticles exhibited no significant cell viability changes relative to the control treatments. The folate-ethylenediamine and folate-phthalocyanine capped nanoparticles treatments showed higher cell viability relative to the untreated cell line (control). The small-sized nanoparticles treatment showed a slightly higher cell viability compared to their counterparts, with the exception being the small-sized ethylenediamine capped nanoparticles.

### 4.3 GENERAL DISCUSSION AND CONCLUSION: CYTOTOXICITY STUDIES

Biomolecule conjugation method and capping agent used can have cytotoxicity effects [355–357]. In this study, no significant toxic effect or consistent trend across the four cell lines was observed for the capping agent, because a non-toxic nanoparticle concentration (independent of capping agent and size) was used. Free ethylenediamine (EDA), free phthalocyanine (Pc), folate-ethylenediamines (FA-EDA), and folate-phthalocyanines (FA-Pc), and conjugated nanoparticles (FA-ED<sup>+</sup>-NPs and FA-Pc<sup>-</sup>-NPs) showed similar trends for the large-sized nanoparticles. However, small- and medium-sized phthalocyanine-capped (Pc) indicated that at 10  $\mu$ M palladium content, the used capping agents did not affect cell viability. For the MCF-7, MCF-10A, and MDA-MB-468 cell lines, most of the folate-conjugated nanoparticles showed a significant increase in cell viability relative to the untreated cells, independent of their sizes, except for MDA-MB-231 cell line, which generally showed lower cell viability results compared to the other cell lines. This may be attributed to folate-conjugated nanoparticles being non-cytotoxic at the investigated concentration as previously reported [225, 408, 409].

Except ethylenediamine (EDA) demonstrating a decreased cytotoxic effect on the MDA-MB-468 cells (**Figure 4.2**), the cell viability differences between the free capping agents and their complimentary capped nanoparticles (for instance, Pc and Pc<sup>-</sup>-NPs) was not significant (<20%).

Thus, it can be concluded that the capping agents and palladium nanoparticles were non-cytotoxic at a 10  $\mu$ M concentration palladium content. For small-sized nanoparticles, only ED $\hat{A}$  and P $\hat{c}$  nanoparticles showed a decrease in cell viability of approximately 18% for more than one cell line (MDA-MB-231, MCF-7, and MCF-10A compared to the untreated cells), with the MDA-MB-468 showing an increase in cell viability in comparison to untreated cells for the MCF-7 and MDA-MB-231 cell lines. For the medium-sized nanoparticles, only the MDA-MB-468 cell line showed increased cell viability when treated with ED $\hat{A}$ -NPs. However, the other cell lines showed their lowest cell viability for the ED $\hat{A}$ -NPs. A possible explanation for this observation is that MDA-MB-468 cells were more susceptible to the toxic effects of free EDA than EDA bound to NPs, while ED $\hat{A}$ -NPs are known to decrease mitochondrial mitosis in the other cell line [410], in comparison to the free EDA. Despite having free amine groups, Pc showed low cytotoxicity compared to EDA treated cells, because of Pc structure [260] resulting in the lone pair of electrons being localised within the ring and not readily available, unlike EDA with a readily available lone pair of electrons in comparison to the aromatic amines [411]. EDA also has better chelating abilities in comparison to Pc, and possibly chelate some key metals for mitochondrial mitosis.

For all cell lines, folate conjugates (FA-EDA and FA-Pc) control treatments showed no significant difference in cell viability compared to the folate-conjugated capped NPs. Borohydride capped nanoparticles had a lower cell viability compared to the folate-conjugated nanoparticles as expected which can be attributed due to the corrosive nature and toxicity of borohydride. Folate-conjugated nanoparticles showed increased cell viability to their non-folate counterparts as reported by other researchers [225, 412].

The exhibited cell viability trend across the four cell lines can be attributed to their different proliferative indexes (**Table 1.8**), which corresponded to the observed trends. MDA-MB-231 and MDA-MB-468 showed the lowest and highest cell viability, respectively, across most of the treatments, and MCF-10A and MCF-7 cell lines showed similar cell viability as previously reported [243]. In some cell lines, folate receptor expression is inversely proportional to cell proliferation [413], and no conclusive FRs-cell viability trend was observed. The MDA-MB-468 cell line was expected to have better proliferation, angiogenesis, invasion, and metastasis [414, 415] compared to the other three cell lines because of the high effects of EGFR on cancer cell lines [416]. This was kept at a minimum as the focus was to investigate uptake.

Folic acid (FA) is essential for cell survival due to its association in various biochemical processes including DNA and RNA synthesis and transmethylation reactions. It is possible that



elevated levels of  $\alpha$ -FR induce proliferation, by mediating folate uptake [205]. Physiological concentrations of FA can induce cell type-specific changes in gene regulation consistent with proliferative phenotype. However, a sub-optimal FA content has been demonstrated to suppress tumorigenesis [417]. The difference in FA internalisation between the cell lines is a crucial factor that determines the effect of FA on cancer-related processes [417]. At similar FA concentrations, different breast cancer cell line's unique gene transcript alterations are either up or down-regulated [417]. For example, TAGLN, an associate gene encoding transgelin, is altered by FA in all breast cancer cell lines, for example, TAGLN is down-regulated in MCF-10A and up-regulated in MCF-7 cell line [417]. TAGLN has been associated with suppression of cell proliferation and invasion, promoting apoptosis in colorectal carcinoma [418], this could have been why the FA (13.6 mM) resulted in low cell viability for the MDA-MB-468 (**Figure 4.1**). It can be concluded that the effect of folate in folate-conjugated nanoparticles may have up-regulated pathways associated with tumorigenesis (migration, proliferation, vascularisation), while pathways associated with apoptosis and cell differentiation were down-regulated as previously reported [418, 419] for the MCF-7 and MCF-10A, resulting in the increased cell viability (>100%).

Methotrexate (MTX) is not taken up *via* the folate receptor, and the observed (**Figure 4.2 – Figure 4.5**) cell viability corresponds with available literature [381–383]. The MDA-MB-468 cell line has a high proliferative index and showed increased cell viability since it is not affected by MTX due to the absence of folate-receptors. MDA-MB-231 and MCF-7 cells are resistant to MTX [413], and displayed a similar cell viability to that found in the MCF-10A cells. It can be concluded that the overexpression of FR did not invariably render cells more sensitive to MTX as reported in literature [413].

At low concentrations, phthalocyanines are non-toxic [420, 421] theranostic agents [422]. Positive cell viability was noted for folate-phthalocyanines and other controls (except for EDA on MDA-MB-468 cell line). The capped nanoparticles showed less cytotoxicity, potentially indicating increased dispersibility, bio- and cytocompatibility and better conjugation with other bioactive molecules which has previously been documented in literature [363]. The nanoparticles were designed to be internalised *via* folate-receptor-mediated endocytosis; however, the reported cell viability results were inconclusive in correlating folate-receptor expression and cell viability. Since cytotoxicity can be due to nanoparticle cell-membrane interactions [423] or nanoparticle intracellular interactions [375, 424] and the inverse regulation of FR expression by the extracellular folate concentration further suggest

heterogeneity in underlying mechanisms as reported [413]. Similarly, cell viability was independent of surface coating as expected [96, 353]. The surface charge was kept within the preferred range (-30 mV to +30 mV) for folate-targeted receptor-mediated endocytosis by ensuring that the synthesised nanoparticles' surface charge would be stable in a physiological environment such as cellular media, and with the surface composition containing a similar functional group (amine), no significant difference was expected [425] and corresponds with what was observed. The hydrophilicity of the nanoparticles and conjugates was particularly important to disperse them in biological systems and also increases ease of synthesis and residence time thereby enhancing cell viability [426–428]. The difference in cell viability between 10 and 100  $\mu\text{m}$  palladium nanoparticles suggest that palladium nanoparticles toxicity is dose and concentration-dependent as previously reported [77, 429].

#### 4.4 CELL UPTAKE STUDIES

As previously discussed (**Section 1.3.2**), the nanoparticles were optimised for folate-receptor targeted endocytosis. During folate-receptor targeted endocytosis, the folate-conjugated nanoparticles bind specifically to folate receptor (FR) creating a folate receptor-folate-conjugated nanoparticle complex; then through invagination and budding off, forms intracellular early endosomes, which undergo acidification and subsequent fusion with lysosomes to release the FR and folate-nanoparticle complex [204, 430] into the cytoplasm. The FR is then translocated to the nucleus, where it binds to *cis*-regulatory elements at promoter regions to self-regulate their expression and nuclear localisation, acting directly as transcription factors [431]. The FR undergoes exocytosis as endosomes [432]. Some endosomes evade cytosol release, mature, and get exocytosed [406, 433]. The cell uptake and internalisation were qualitatively investigated using transmission electron microscopy (TEM).

##### 4.4.1 Cell internalisation studies: Transmission electron microscopy (TEM)

TEM is an essential tool to obtain the information on the cellular structure, confirm uptake, and identify the localisation of the nanoparticles. The preparation of cellular material for TEM considered the resolution of cellular ultrastructure while avoiding significant alteration or loss of target nanoparticles [434, 435]. Sample preparation that does not detrimentally alter the cells or NPs, or obscure NP location, work constraints enhancing heavy metal stains and suitable control of the electron influence during imaging are critical. More importantly, spectroscopic analysis such that the particle structure (and ideally the cellular material) remains unaltered under investigation [436] is key. To improve the visibility of NPs in thin cell

sections of TEM, osmication or bulk and post-embedding and staining steps were originally omitted (**Figure 4.6**) [437].

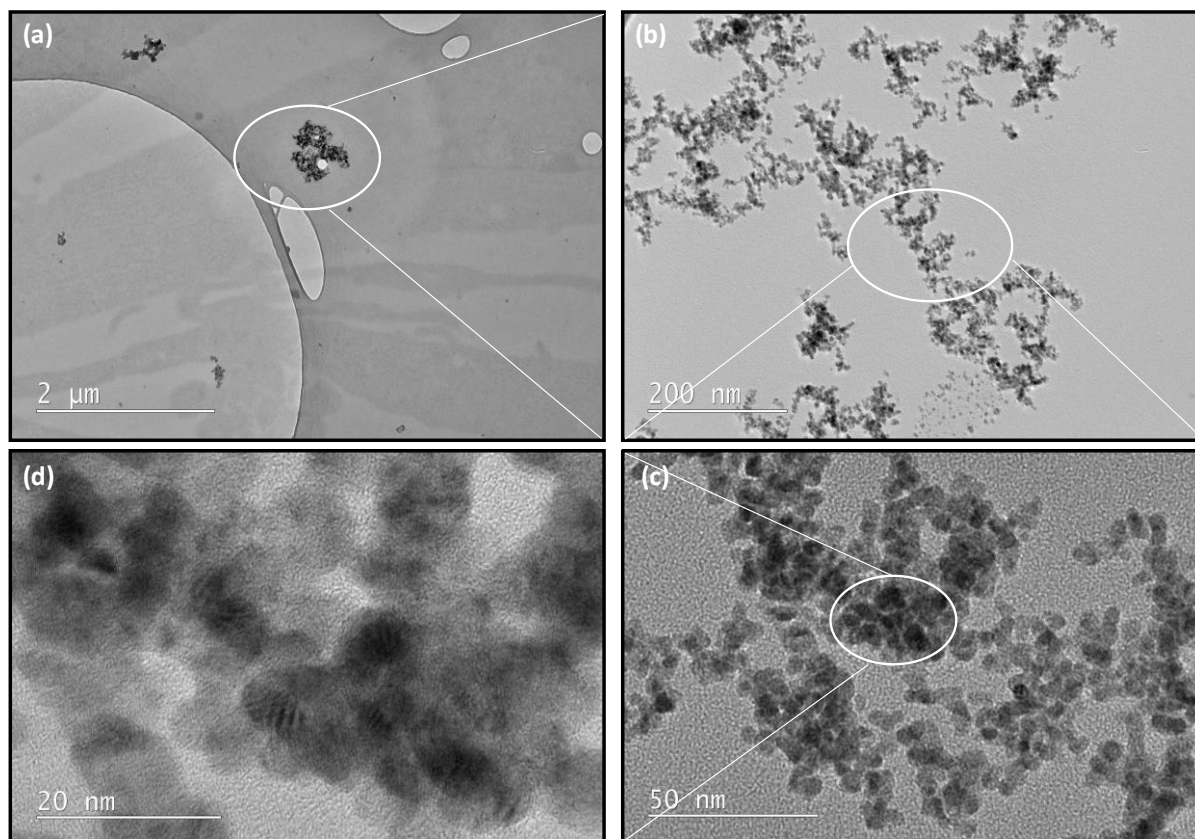


**Figure 4.6:** Bright-field transmission electron microscope (TEM) images of unstained MCF-10A cells after 24 h treatment with 10  $\mu\text{M}$  (palladium content) small-sized folate-ethylenediamine capped palladium(0) nanoparticles (sz-FA-Pc-NPs). Higher magnifications were used, from (a) to (d) to acquire the images, with the encircled regions indicating the area where the following image was acquired. The nanoparticles were clearly visualised with no cell ultrastructure.

The small-sized folate-ethylenediamine capped nanoparticles were easily visualised (**Figure 4.6**) and scanning transmission electron microscopy-energy dispersive X-ray spectroscopy (STEM-EDS) confirmed the composition of the palladium nanoparticles (**Figure 4.7**).

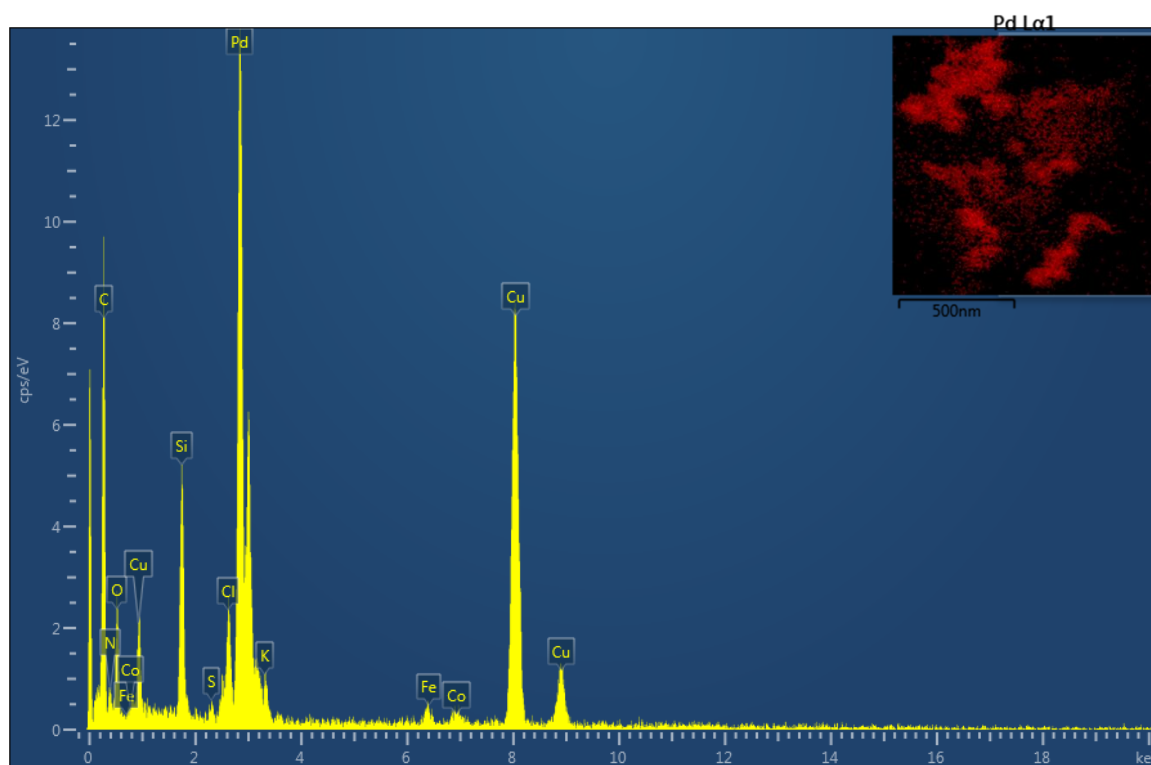


**Figure 4.7:** The STEM-EDS spectrum of the nanoparticles on the unstained sample. Palladium presence was observed. The presence of carbon (C), nitrogen (N), and oxygen (O) can be attributed to the presence of folate-phthalocyanine or cellular organelles. The presence of potassium (K) and chlorine (Cl) can be attributed to incomplete washing of PBSA with the cobalt (Co) and iron (Fe) attributed to system artefacts from the TEM chamber, while the presence of copper is attributed to the use of a copper TEM grid for the sample.

For the unstained specimen, the presence of palladium nanoparticle was confirmed (**Figure 4.7**). However, the absence of stains did not clearly resolve the various cellular ultrastructure, but additional unwanted stain chemical effects were avoided. With localisation being of great interest to our study, an attempt to obtain optimal results without compromising sample preservation and clear visualisation of the structure was attempted as recommended in literature [438]. Unstained specimens' sensitivity to radiation damage is reportedly high [439], and viewing of unstained biological molecules [440, 441] was difficult. The same specimen (**Figure 4.6**) was osmicated and analysed (**Figure 4.8**). Having a stained and unstained sample allowed the identification of artefacts introduced by the osmium stains. The intact cell membranes (**Figure 4.8**) confirmed the expected non-invasive nanoparticle-membrane interactions for the optimised nanoparticles [423, 442–446].



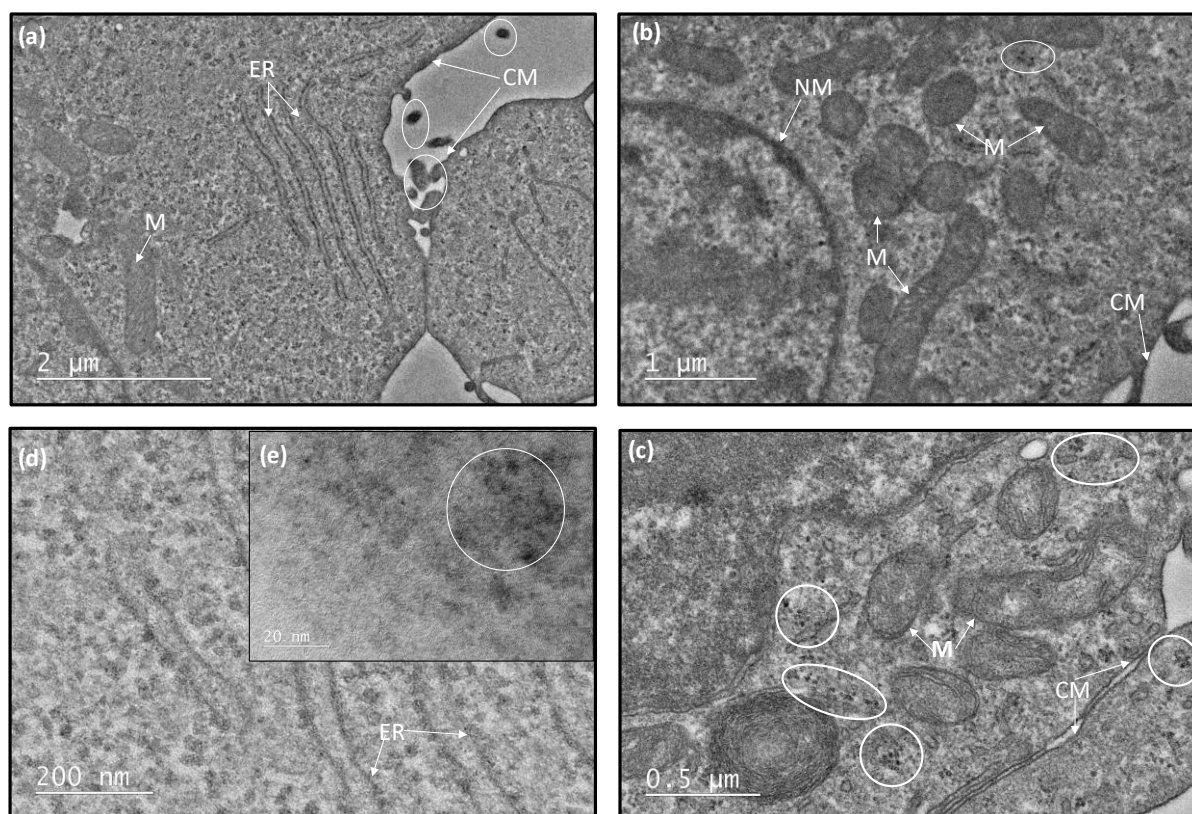


**Figure 4.8:** Bright-field TEM images of osmicated MCF-10A cells (from **Figure 4.6**) after 24 h treatment with small-sized folate-phthalocyanine capped palladium(0) nanoparticles (sz-FA-P $\hat{c}$ -NPs); (a) TEM image showing a well- defined cell ultrastructure; intact cell membranes (CM), protruding cell membranes (encircled CM), mitochondrion (M), endoplasmic reticulum (ER), and possible metal stains, artefacts, or nanoparticles (encircled), (b) A magnified cellular area showing well-defined ultrastructure; nuclear membrane (NM), mitochondrion (M), cell membrane (CM), and unclear possible nanoparticles or metal stains or artefacts (encircled), (c) Clear ultrastructure of magnified specimen area showing intact cell membranes (CM) and possible nanoparticles or metal stains or artefacts (encircled), (d) TEM image displaying the visualised zoomed cytoplasm area with endoplasmic reticulum (ER), and (e) Inset showing a highly magnified section of the cells showing notable metal precipitate or artefacts (encircled).

The crystalline nanoparticles could not be clearly visualised in the prepared samples. This can be attributed to the introduction of artefacts during sample preparation [127, 447], thereby obscuring the nanoparticles. It can also be suggested that palladium nanoparticles can be oxidised to palladium(II) by the staining and post-embedding chemicals, for example, osmium tetroxide is a strong oxidising agent [448–450]. Similarly, staining liver tissues sections with

uranyl acetate and lead citrate to generate image contrast in the TEM oxidised iron in the nanoparticulate core of ferritin molecules [437]. It is also reported that nanoparticles can dissociate or change their oxidation state or ionic state, for example, ZnO nanoparticles are known to dissociate and produce  $Zn^{2+}$  which can cause toxicity [451], and similarly, iron undergoes a redox state change [452]. This poses a challenge as it is difficult to determine the composition of the metal particles once taken up into the cell using microscopy (**Figure 4.8** inset) found on the specimen. This challenge was encountered, and the STEM-EDS could not be done as the specimen was highly unstable under the electronic beam, resulting in the resin disintegrating. Challenges of the beam damaging the specimen and resin [439], unstained specimens sensitivity to radiation damage [441] and viewing of unstained biological molecules have been previously reported [440, 453]. Some nanoparticles are known to be located in mitochondria and nucleus [454]; however, no palladium crystalline nanoparticles were observed in these organelles.

For a different specimen, chemical fixation and staining (with the inclusion of osmium tetroxide) was employed (**Figure 4.9**). It enabled visualisation of some of the main cellular structure because osmium binds to lipid-rich structures such as membranes [455]. This approach did not enable the localisation of NPs within a cell to be clearly visualised, without a contrast from the NPs themselves being obscured by the heavy metal stains as expected [456, 457].

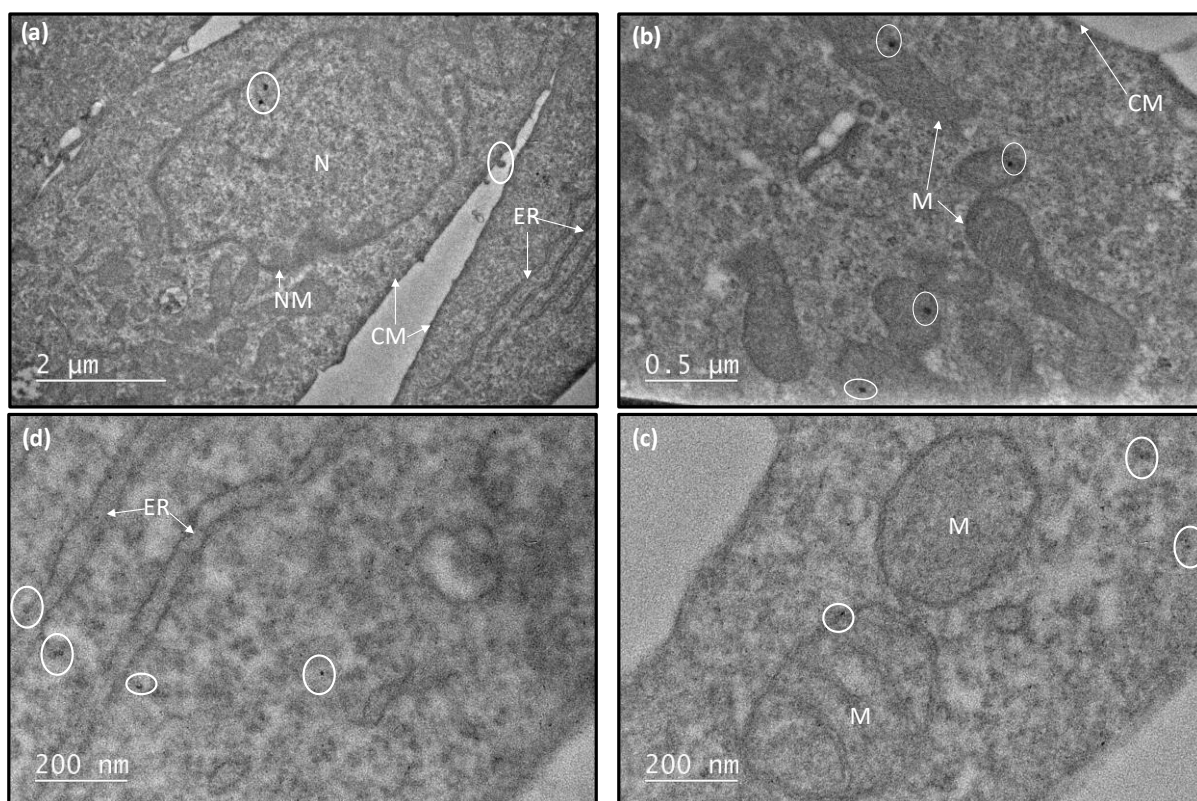


**Figure 4.9:** Bright-field TEM images of osmicated MDA-MB-231 cells after 24 h treatment with large-sized folate-ethylenediamine capped palladium(0) nanoparticles (Iz-FA-EDÂ-NPs); (a) Visible cell membrane (CM), endoplasmic reticulum (ER), nuclear membrane (NM), and nucleus (N) and possible metal nanoparticles or stains (encircled), (b) Visible cell membrane (CM) and mitochondrion (M) with possible nanoparticle or osmium stains (encircled), (c) Zoomed ultrastructure showing mitochondria (M), and possible nanoparticles or osmium stains (encircled), (d) Ultrastructure showing endoplasmic reticulum (ER) and possible nanoparticles or osmium stains (encircled). The ultrastructure was seen, with no confirmed crystalline palladium nanoparticles.

Other specimens were not stained with osmium tetroxide and stained with uranyl nitrate and lead citrate (**Figure 4.10**). The contrast was achieved; however, locating the nanoparticles was not achieved, and this could be due to the possible resin instability under the electron beam, possible oxidation of the nanoparticles or no internalisation having taken place (or preparation technique). However, with inductively coupled plasma-optical emission spectroscopy (ICP-OES) having proved that internalisation or attachment to the cell membrane occurred (**Table 4.3**), it can be suggested that this could be an analytical challenge and this finding was further investigated.



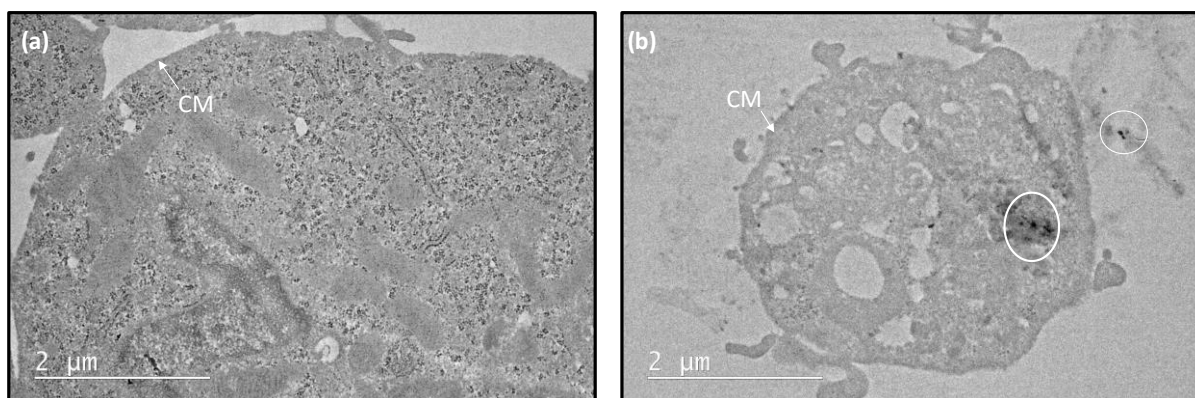


**Figure 4.10:** Bright-field TEM images of non-osmicated, lead citrate and uranyl acetate stained MCF-7 cells treated with medium-sized phthalocyanine capped palladium(0) nanoparticles (mz-Pc-NPs) for 24 h; (a) Cell membrane (CM) is visible and no clear ultrastructure (b) unclear ultrastructure showing possible nanoparticle, artefacts or metal stains (encircled) and cell membrane (CM).

Possible artefacts can be seen (**Figure 4.10**). Additionally, biological systems have the capabilities of converting metal ions into metal NPs [458, 459], effect partial oxidation of nanoparticles [460], and the palladium nanoparticle stability in all cell lines cannot be ruled out [461]. Cells have an unclearly understood ability to change the oxidation state of nanoparticles [462]. Some metal NPs can be oxidised by cells under certain conditions and this could be a possibility for PdNPs [463] in MDA-MB-231 and MCF-7 cell lines. To examine the effects of sample preparation, untreated MCF-7 cells were stained and analysed (**Figure 4.11**).



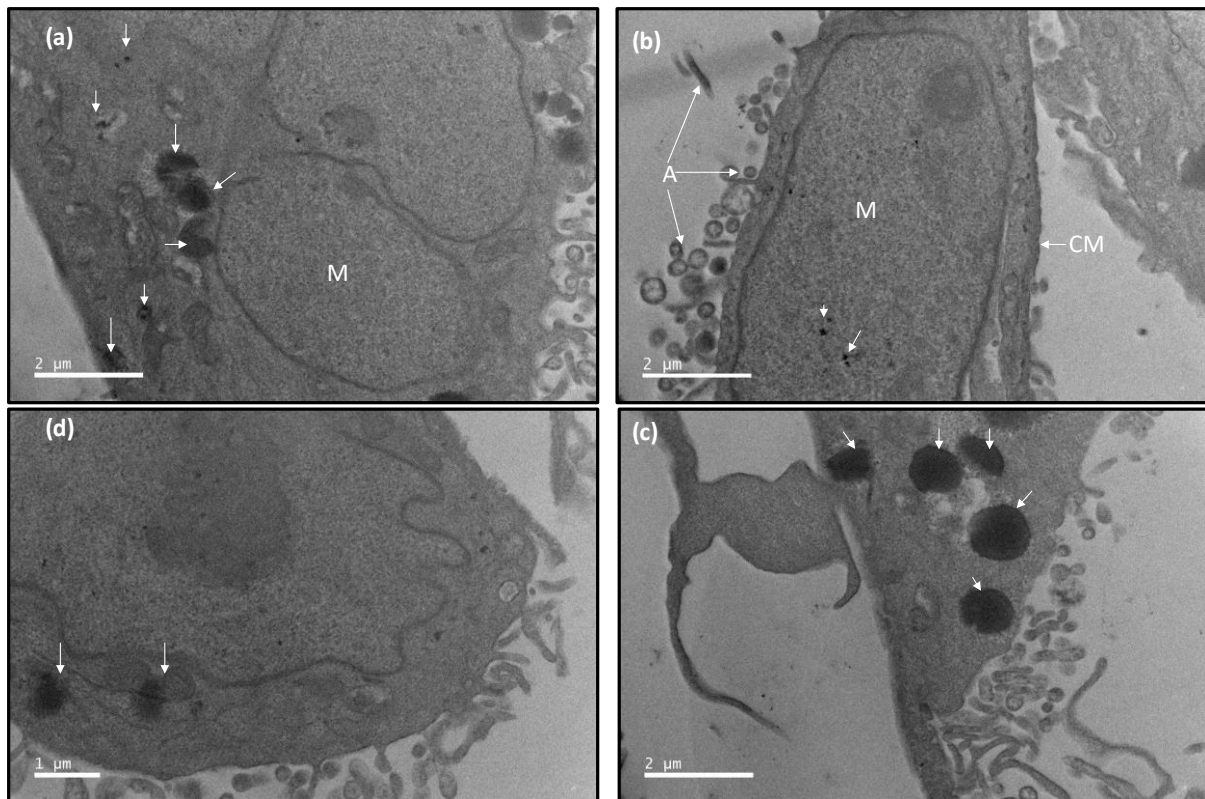


**Figure 4.11:** Bright-field TEM images showing osmicated, lead citrate, and uranyl acetate stained MCF-7 untreated cells (no nanoparticle treatments); (a) Mitochondrion (M) is visible and artefacts are shown by arrows, (b) Cell membrane (CM), mitochondrion (M), and possible artefacts (A) are highlighted, (c) and (d) presents untreated MCF-7 cells showing possible artefacts or unidentifiable organelles.

This proved that possible contamination or presence of artefacts, sample preparation problem, is among the reasons for the unseen or unlocated nanoparticles. No dark spots were expected to be seen. Further analysis was completed (**Figure 4.12**) on the MCF-7 cell line treated with large-sized folate-phthalocyanine capped palladium(0) capped nanoparticles.

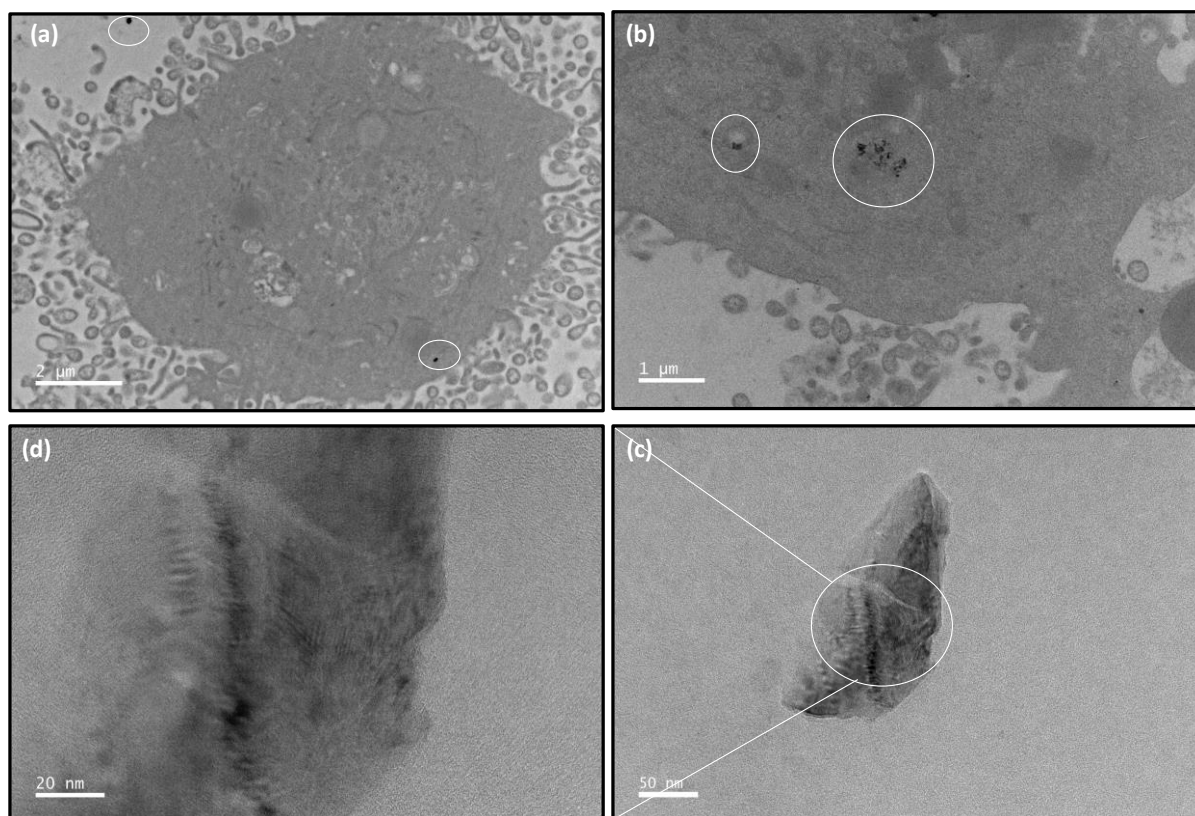


**Figure 4.12:** Bright-field TEM images of osmicated, lead citrate and uranyl acetate stained MCF-7 cells treated with 10  $\mu\text{M}$  large-sized folate-phthalocyanine capped palladium(0) nanoparticles (Iz-FA-Pc-NPs); (a) shows an MCF-7 with an unclear ultrastructure and some dark spots (encircled), (b) a magnified area on the specimen showing possible nanoparticles (encircled) and the dark spot area (arrowed) that gave image (c), (c) a crystalline palladium nanoparticle, and (d) a magnification of the encircled area (on (c)).

Despite inductively coupled plasma-optical emission spectroscopy (ICP-OES) having confirmed the uptake (**Table 4.3**) and or internalisation, very few nanoparticles were visualised and the palladium nanoparticle stability in all cell lines used remained unclear. Nanoparticles stable in cell media can become unstable through chemical modification or loss of surface functionality, or altering charge distribution, thereby affecting their stability in biological systems [90, 464]. STEM-EDS could not be employed to obtain the nanoparticle composition. This was due to the specimen being highly unstable under the electronic beam, resulting in the resin's disintegration. This challenge of the beam damaging the specimen and resin has been previously reported [439].

Considering TEM's limitations [465] and complexity for quantifying uptake, requiring extensive, time-consuming sample preparation, and typically providing qualitative

information, inductively coupled-optical emission spectroscopy (ICP-OES) was employed to quantify the uptake and or the internalisation as a preferred previously recommended method [466].

#### 4.4.2 Cell internalisation studies: Inductively coupled plasma-optical emission spectroscopy (ICP-OES)

ICP-OES is a common technique for absolute quantification of the cellular uptake of NPs. It offers high selectivity for elemental analysis; however, it does not allow for differentiation between single, agglomerates, or ionic species [270]. The quantified cellular uptake were reported (Table 4.3).

**Table 4.2:** The inductively coupled plasma-optical emission spectroscopy (ICP-OES) results obtained for the various treatments from the cell lysate (N=6).

Treatment	[Pd] ppm in media	[Pd] content found in each cell line (ppm)			
		MDA-MB-468	MCF-7	MDA-MB-231	MCF-10A
UT	0.000	0.000	0.000	0.000	0.000
sz-B $\hat{h}$ -NPs	0.870	0.184	0.462	0.463	0.248
lz-B $\hat{h}$ -NPs	0.880	0.251	0.512	0.648	0.190
sz-FA-ED $\hat{A}$ -NPs	0.893	0.294	0.595	0.729	0.297
lz-FA-ED $\hat{A}$ -NPs	0.859	0.299	0.656	0.804	0.279
sz-FA-P $\hat{C}$ -NPs	0.870	0.341	0.417	0.393	0.337
lz-FA-P $\hat{C}$ -NPs	0.873	0.346	0.496	0.720	0.329

The small-sized borohydride capped nanoparticles showed the MDA-MB-468 had the least palladium content (0.184 ppm). MCF-7 (0.462 ppm) and the MDA-MB-468 (0.463 ppm) had relatively similar uptake of the small negatively charged nanoparticles (-2.86 mV), with MCF-10A (0.248 ppm) showing more uptake compared to the breast cancer folate positive cell lines (MCF-7 and MDA-MB-231). With the exception in MCF-10A cell line, large-sized borohydride-capped nanoparticles had a higher nanoparticle uptake compared to their smaller-sized borohydride capped nanoparticles. This was unexpected and is attributed to the tumourigenic cell lines having a higher affinity for borohydride-capped nanoparticles, since the MCF-10A cell line showed a relatively lower palladium uptake. This could also be linked to metabolism

or growth rate since the MCF-10A represents a cell line which is a representative of a “normal cell population” and grow substantially slower.

Small-sized folate-ethylenediamine capped nanoparticles showed a higher palladium content compared to borohydride capped nanoparticles, but lower palladium content compared to the large sized folate-ethylenediamine capped nanoparticles as expected when internalisation is folate receptor-dependent. This can be attributed to their near-neutral charge (-0.05 mV), that favoured the nanoparticle uptake via folate receptor-targeted endocytosis [353]. The large-sized nanoparticles have a larger surface area, therefore, the availability of the capping agents' folate receptor binding moiety is readily available compared to the smaller nanoparticles [427]. The nanoparticles were optimised to minimise other uptake mechanisms [159] and promote folate receptor-mediated endocytosis, it can be concluded that the folate-conjugated and large-sized nanoparticles were internalised *via* folate-receptor mediated endocytosis and not phagocytosis, clathrin-mediated endocytosis, caveolae-dependent endocytosis, micropinocytosis or any other mechanism [467].

The MCF-10A and MDA-MB-231 cells low palladium content can be attributed to folate-conjugated nanoparticle uptake *via* the reduced folate carrier (RFC) or proton coupled-folate transporter (PCFT) [227, 228], since the expression of folate-receptors is very low, almost undetectable in normal cells [468] and absent in the MDA-MB-468 cell line.

The small and large-sized folate-phthalocyanine capped nanoparticles showed a higher palladium uptake for the MDA-MB-468 and MCF-10A cell lines compared to the folate-ethylenediamine and borohydride capped nanoparticles. However, the uptake is about 40% of the available palladium. The MCF-7 cell line also showed reduced palladium nanoparticle uptake for the FA-Pc-NPs compared to the FA-ED-NPs internalisation. In a similar study, MCF-7 cells have been shown to take up folate-functionalised nanoparticles was at around 8 µg/mL from the available 100 µg/mL, and 50 µg/mL when treated with 500 µg/mL concentrations [249]. Folate-conjugated nanoparticles was cell-type specific, time, and concentration dependent until a certain maximum concentration (saturated uptake phenomenon) [101]. There was also a reported increase in cellular uptake of folate within the MCF-7 cell line for preincubation without folic acid [249].

Generally, functionalised nanoparticles have improved uptake and cytotoxicity [250, 469, 470]. However, another possible explanation for folate receptor-targeting nanoparticles not showing much higher palladium uptake compared to non-folate receptor targeting

nanoparticles can be ascribed to the folate receptor-mediated endocytosis mechanism that requires the recycling of the receptor back to the cell surface, a response that has been reported to take between 30 min and 5 h [471–473], highlighting a possible increased uptake if exposure time was increased. There is an optimal size for efficient folate-receptor targeted endocytosis of nanoparticles independent of particle composition [103]. This critical size varies with cell type and surface properties of the nanoparticles [225]. Due to the complexity of biological probes, it was slightly difficult to draw a conclusion of a trend followed by the nanoparticles used. However, from their properties, it can be concluded that the folate-functionalised nanoparticles were taken up *via* the folate-receptor mediated endocytosis.

#### 4.5 GENERAL DISCUSSION AND CONCLUSION: CELL UPTAKE STUDIES

Despite the challenges and limitations for nanomedicine [474], folate receptor-targeted nanoparticles offer great prospects in targeted therapy. Nanoparticle visualisation can be seen (**Figure 4.11**) and the uptake was further confirmed (**Table 4.3**). It can be concluded that it is possible to target cancer cells selectively without damaging healthy tissues. Increased exposure time with reduced concentration can yield higher and selective nanoparticle content in cancer cells. Folate functionalised nanoparticles were internalised in higher amounts in tumorigenic cancer lines compared to non-tumorigenic (**Table 4.3**), corresponding to previously published literature [475].

All the challenges encountered with TEM studies can be circumvented. Instead of using heavy metal stains [465], chemical stains can be used to enhance NP identification, for example, alkaline bismuth has been used to stain iron oxide NPs and biological membranes [476]. Alternative stains have been reported to prevent elemental signals from NPs being obscured, for example, ruthenium tetroxide can be used to replace osmium tetroxide, because osmium irradiated by an electron beam produces X-rays of the same energy as phosphorous, whereas ruthenium does not [477].

Possible artefacts induced by the thin sectioning process itself can be limited when embedding and sectioning [478], for example, by matching the hardness of the epoxy to that of that nanomaterial, limiting the size of the cutting face, and or careful selection of the angle of the cutting knife [479] minimises artefacts. The use of an oscillating knife can further reduce or eliminate section compression [480]. The ultra-microtome sectioning of nanocrystalline materials has also been shown to result in pull out of sample from the embedding resin during cutting [481].



Precise NPs localisation, requiring excellent resolution of cellular ultrastructure, can still be developed further and quantification of NPs alteration or degradation when in cellular environment is possible. Rapid freezing to preserve cellular material closer to its native state can also be explored [434]. The possible change of oxidation state can be investigated by quantifying the oxidation states in and outside the cells, and organelles using correlated scanning transmission spectroscopy [462].

The cytotoxic findings did not corroborate that nanoparticles cellular uptake depends on the particle size distribution, and capping agent [425]. Thus, it can be concluded that at 10  $\mu\text{m}$  palladium content, palladium nanoparticles and the designed nanoradiopharmaceuticals have low or minimal toxicity and are biocompatible. To conclude, this work offers valuable insights into further investigating and understanding the cell uptake and internalisation *in vitro* studies and subsequently paving way for *in vivo* studies. It is possible to use folate-functionalised palladium nanoparticles to target cancer cells selectively, to normal cells.

## CHAPTER FIVE: CONCLUSIONS AND FUTURE WORK

### 5.1 CONCLUSIONS

Despite the challenges and limitations for nanomedicine [474] and the complexity of nanoradiopharmaceutical design, it can be concluded that the study was successful.

- (i) The determination of optimal diamine used as capping agent, optimisation of reducing agent, optimisation of concentrations, stoichiometric ratios and reaction parameters, and the aqueous synthesis of stable (in aqueous solution and cell media) palladium nanoparticles (PdNPs) at room temperature was successfully achieved.
- (ii) The synthesis of tetraaminophthalocyanine (referred to as phthalocyanine, Pc, after its synthesis), and the conjugation of phthalocyanine and ethylenediamine with folate was successfully reported. The nanoparticles capped with the various capping agents were also successfully synthesised.
- (iii) The investigation of a non-cytotoxic concentration for all control and nanoparticle treatments provided an acceptable pre-screening method requiring further confirmatory studies prior to *in vivo* rat model studies and employing the hot ( $^{109}\text{Pd}$ ) isotope. *In vitro*, at 10  $\mu\text{M}$  palladium nanoparticles were found to be non-cytotoxic.
- (iv) The selective uptake of folate functionalised nanoparticles *via* folate receptor-targeted endocytosis was achieved. Folate receptor positive cells (MCF-7 and MDA-MB-231) internalised more palladium nanoparticles than folate receptor negative (MDA-MB-468) or control non-tumourigenic (MCF-7A).

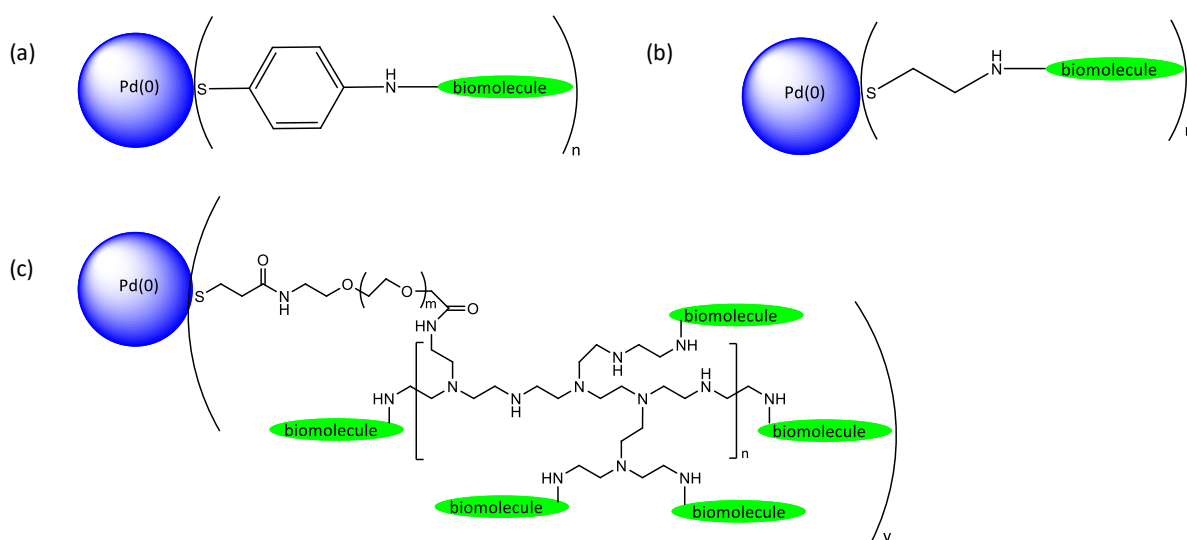
While the *in vitro* experiments may never replace *in vivo* studies [482], the cytotoxic tests and cell internalisation results offered great prospects in the use of palladium nanoparticles in folate receptor-targeted therapy. It can be concluded that folate-functionalised palladium nanoparticles can be employed as theranostic nanoradiopharmaceuticals for selective targeting of cancer cells in the near future. The findings provide a foundation towards an improved experimental design that minimises and circumvents possible shortcomings.

### 5.2 FUTURE WORK

Our future synthesis of palladium nanoparticles (PdNPs) aims to understand and close the knowledge gap in biological NP synthesis, investigating the possible oxidation of NPs to metal ions in biological systems [483], and understanding the retention and clearance of the nanoparticles. In summary, bettering the palladium-based folate receptor-targeted

nanoradiopharmaceutical design reported in this study, addressing all concerns prior to *in vivo* studies.

- (i) Thiol groups are known to stabilise metal nanoparticles better than amine groups [484–487]. Capping agents containing both the amine and thiol groups will be explored (**Scheme 5.1**), from simple molecules [488, 489] to thiol group-containing polymers [490–493], and copolymers conjugated to biomolecules [494–496].



**Scheme 5.1:** The proposed new thiol-amine stabilised palladium(0) nanoparticles; (a) 4-aminophenol-, (b) 2-aminoethanethiol- (cysteamine), and (a) polyethyleneimine (PEI)-capped nanoparticles. For simplicity, one capping agent unit is shown, however,  $m$ ,  $n$ , and  $y$  are unknown.

- (ii) The conjugation and functionalisation of Pcs with poly(ethylene glycol) (PEG) improves the chemical inertness, biocompatibility [449], improved serum life, and tumour accumulation of PEG and PEGylated Pcs [498, 499] and will also be considered.
- (iii) During folate conjugation, the separation of low molecular weight folate conjugates ( $\alpha$ -conjugates, bioconjugates, or unreacted folic acid) by precipitation, and separation of the  $\alpha$  and  $\gamma$  isomers by preparative reverse phase chromatography was not conducted and could also be investigated [258].
- (iv) The investigation of the palladium metal oxidation state in cells could be investigated using correlated scanning transmission spectroscopy to quantify the oxidation states in and outside the cells, and organelles [462, 500], single particle inductively coupled-mass spectroscopy will also be employed to distinguish between ionic Pd(II) and Pd(0) [501, 502] or single cell mass inductively coupled plasma mass spectrometry [503].



- (v) With the reported uptake being receptor recycling-, time- and concentration-dependent, the amount of folate receptors on the cell surface needs investigation. Increased folate receptors levels on the cell surface will be achieved by culturing cells in folate-depleted medium, thereby inducing the overexpression of FRs on the cell-membrane membrane [504]. To fully investigate and understand the effect of folate receptor-mediated endocytosis, cells cultured in media with and without folic acid could be compared [249], and folate receptor expression could also be examined by Western blotting [302]. Surface plasmon resonance (SPR) studies could also provide information on the folate-binding protein in the presence of free folic acid, for instance, despite dietary folate not having been of significant effect in clinical studies, folic acid has been given to the patient in clinical trials to reduce normal tissue uptake of etarfolatide in a clinical trial, suggesting that low concentrations of circulating folate may be helpful for targeting tumour cells *in vivo* [235].
- (vi) Similarly, the cytotoxicity is time- and concentration-dependent, the effects of different concentrations and exposure time will be investigated [482]. Specified time interval imaging after exposure to nanoparticles, will aid in elucidating the underlying mechanisms and possible morphological changes, providing a better understanding and visual confirmation and details of the internalisation routes. The understanding of in-depth effects of nanoparticles is a prerequisite [505–507]. The inability of the cell viability assay to provide possible mechanisms of action prompts the need for additional cell viability assays, for instance, assays to investigate necrosis, DNA synthesis, myology formation, apoptosis (membrane structure) and LIVE-DEAD (esterase activity/membrane integrity) and mechanistic assays to examine DNA damage and oxidative stress, and time- and dose-dependent genotoxicity will also be explored [454]. Qualitative methods could also be considered to and characterise the effects of nanoparticles on cells, and are equally elusive [508].
- (vii) Palladium nanoparticles are known to have anti-microbial effects [83, 252]. A knowledge gap exists on the anti-inflammatory properties of palladium nanoparticles. The *in vivo* effects are key to the success of rat model studies and serum protein opsonisation properties of the nanoparticles could also be investigated prior to the *in vivo* studies and so as the cellular fate of the conjugates and nanoparticles in cells. The imaging of radiolabelled derivatives of folic acid offer greater tissue selectivity [204], and additional visual detection is achieved by attaching a fluorescent probe [509–511] bound to nanoparticles or capping agents, or a colorimetric probe specific for palladium detection

[512], or the use of both radioactive and fluorescent conjugates [513], or radiolabelled folic acid [514], could contribute greatly to the understanding and quantification of the internalisation studies.

- (viii) Computational studies on the interaction of nanoparticles with membranes [515], folate conjugates interaction with the folate binding protein [191], and the investigation of molecular docking and molecular dynamics simulations [510, 516].
- (ix) Evaluating the interaction between the conjugated folate nanoparticles and the folate binding protein using isothermal calorimetry could be considered for an in-depth understanding of the binding studies, and the determination of binding affinity ( $K_D$ ) of the folate conjugates [517, 518].
- (x) The tumour and organ biodistribution studies of the nanoparticles could be completed using micro-SPECT kits and model mice/rat studies (using the “hot” isotopes of  $^{109}\text{Pd}$  in a radiopharmacy laboratory) as published in literature [109]. The effects of the  $^{109}\text{Ag}$  (radioactive product of  $^{109}\text{Pd}$ ) could also be extensively studied.

The success of the above findings would give rise to a new set of palladium theranostic nanoradiopharmaceutical being recommended for clinical trials. Therefore, it can be concluded that palladium nanoparticles and the designed nanoradiopharmaceuticals have great prospects to ensure improved drug delivery: retention, evasion, targeting recognition, and release, by considering various key aspects in drug development [139, 519].

## LIST OF REFERENCES

- [1] B. W. Stewart and P. Kleihues, "World cancer report," IARC Press, Lyon, 2003.
- [2] H. Kitao, M. Imori, Y. Kataoka, T. Wakasa, E. Oki, Y. Maehara, E. Tokunaga, and H. Saeki, "DNA replication stress and cancer chemotherapy," *Cancer Sci.*, vol. 109, no. 2, pp. 264–271, 2017.
- [3] C. J. Sherr, "Cancer cell cycles," *Science.*, vol. 274, no. 5293, pp. 1672–1677, 1996.
- [4] B. S. Reddy, *Diet, nutrition and cancer: A critical evaluation*, 1st ed. Boca Raton: CRC Press, 2018.
- [5] T. Reya, S. J. Morrison, M. F. Clarke, and I. L. Weissman, "Stem cells, cancer, and cancer stem cells," *Nature*, vol. 414, no. 11, pp. 105–111, 2001.
- [6] A. Sudhakar, "History of cancer, ancient and modern treatment methods," *J Cancer Sci Ther.*, vol. 1, no. 2, pp. 1–4, 2010.
- [7] R. L. Siegel, K. D. Miller, and A. Jemal, "Cancer statistics," *CA Cancer J Clin*, vol. 66, no. 1, pp. 7–30, 2016.
- [8] R. Siegel, K. Miller, and A. Jemal, "Cancer statistics," *CA Cancer J Clin*, vol. 68, no. 1, pp. 7–30, 2018.
- [9] A. Wicki, D. Witzigmann, V. Balasubramanian, and J. Huwyler, "Nanomedicine in cancer therapy: Challenges, opportunities, and clinical applications," *J. Control. Release*, vol. 200, no. 1, pp. 138–157, 2015.
- [10] D. Kakde, D. Jain, V. Shrivastava, R. Kakde, and A. T. Patil, "Cancer therapeutics-opportunities, challenges and advances in drug delivery," *J. Appl. Pharm. Sci.*, vol. 1, no. 9, pp. 1–10, 2011.
- [11] L. A. Torre, F. Bray, R. L. Siegel, J. Ferlay, J. Lortet-Tieulent, and A. Jemal, "Global cancer statistics, 2012," *CA A Cancer J. Clinicians*, vol. 65, no. 2, pp. 87–108, 2015.
- [12] F. Bray, J. Ferlay, I. Soerjomataram, R. L. Siegel, L. A. Torre, and A. Jemal, "Global cancer statistics 2018: GLOBOCAN estimates of incidence and mortality worldwide for 36 cancers in 185 countries," *CA. Cancer J. Clin.*, vol. 68, no. 6, pp. 394–424, 2018.
- [13] J. Fang, H. Nakamura, and H. Maeda, "The EPR effect: Unique features of tumor blood

- vessels for drug delivery, factors involved, and limitations and augmentation of the effect," *Adv. Drug Deliv. Rev.*, vol. 63, no. 3, pp. 136–151, 2011.
- [14] P. Gotwals, S. Cameron, D. Cipolletta, V. Cremasco, A. Crystal, B. Hewes, B. Mueller, S. Quarantino, C. Sabatos-Peyton, L. Petruzzelli, J. A. Engelman, and G. Dranoff, "Prospects for combining targeted and conventional cancer therapy with immunotherapy," *Nat. Rev. Cancer*, vol. 17, no. 5, pp. 286–301, 2017.
- [15] J. I. Hare, T. Lammers, M. B. Ashford, S. Puri, G. Storm, and S. T. Barry, "Challenges and strategies in anti-cancer nanomedicine development: An industry perspective," *Adv. Drug Deliv. Rev.*, vol. 108, no. 1, pp. 25–38, 2017.
- [16] Y. Nakamura, A. Mochida, P. L. Choyke, and H. Kobayashi, "Nanodrug delivery: Is the enhanced permeability and retention effect sufficient for curing cancer?," *Bioconjug. Chem.*, vol. 27, no. 10, pp. 2225–2238, 2016.
- [17] R. Malvi, R. Bajpai, and S. Jain, "A review on therapeutic approach of radiopharmaceutical in health care system," *Int. J. Pharm. Biol. Arch.*, vol. 3, no. 3, pp. 487–492, 2012.
- [18] S. D. Steichen, M. Caldorera-Moore, and N. A. Peppas, "A review of current nanoparticle and targeting moieties for the delivery of cancer therapeutics," *Eur. J. Pharm. Sci.*, vol. 48, no. 3, pp. 416–427, 2013.
- [19] H. Maeda, T. Sawa, and T. Konno, "Mechanism of tumor-targeted delivery of macromolecular drugs, including the EPR effect in solid tumor and clinical overview of the prototype polymeric drug SMANCS," *J. Control. Release*, vol. 74, no. 1–3, pp. 47–61, 2001.
- [20] M. Li, F. Zhang, Y. Su, J. Zhou, and W. Wang, "Nanoparticles designed to regulate tumor microenvironment for cancer therapy," *Life Sci.*, vol. 201, no. 5, pp. 37–44, 2018.
- [21] G. L. Zwicke, G. A. Mansoori, and C. J. Jeffery, "Utilizing the folate receptor for active targeting of cancer nanotherapeutics," *Nano Rev.*, vol. 3, no. 1, pp. 1–11, 2012.
- [22] F. Alexis, E. Pridgen, L. K. Molnar, and O. C. Farokhzad, "Factors affecting the clearance and biodistribution of polymeric nanoparticles," *Mol. Pharm.*, vol. 5, no. 4, pp. 505–515, 2008.
- [23] I. Ali, J. Ho, and H. Kuh, "Improving drug delivery to solid tumors : Priming the tumor

- microenvironment,” *J. Control. Release*, vol. 201, pp. 78–89, 2015.
- [24] K. B. Sutradhar and L. Amin, “Nanotechnology in cancer drug delivery and selective targeting,” *ISRN Nanotechnol.*, vol. 2014, no. 1, pp. 1–12, 2014.
- [25] K. L. Farina, J. B. Wyckoff, J. Rivera, H. Lee, J. E. Segall, J. S. Condeelis, and J. G. Jones, “Cell motility of tumor cells visualized in living intact primary tumors using green fluorescent protein,” *Cancer Res.*, vol. 58, no. 12, pp. 2528–2532, 1998.
- [26] A. R. Jalilian, D. Beiki, A. Hassanzadeh-Rad, A. Eftekhari, G. Parham, and M. Eftekhari, “Production and clinical applications of radiopharmaceuticals and medical radioisotopes in Iran,” *Semin. Nucl. Med.*, vol. 46, no. 4, pp. 340–358, 2016.
- [27] A. S. Thakor and S. S. Gambhir, “Nanooncology: The future of cancer diagnosis and therapy,” vol. 63, no. 6, pp. 395–418, 2013.
- [28] J. Thundimadathil, “Cancer treatment using peptides: Current therapies and future prospects,” *J. Amino Acids*, vol. 2012, no. 1, pp. 1–13, 2012.
- [29] J. Liu, Q. Chen, L. Feng, and Z. Liu, “Nanomedicine for tumor microenvironment modulation and cancer treatment enhancement,” *Nano Today*, vol. 21, no. 8, pp. 55–73, 2018.
- [30] X. Xu, W. Ho, X. Zhang, N. Bertrand, and O. Farokhzad, “Cancer nanomedicine: From targeted delivery to combination therapy,” *Trends Mol. Med.*, vol. 21, no. 4, pp. 223–232, 2015.
- [31] S. K. Golombek, J. N. May, B. Theek, L. Appold, N. Drude, F. Kiessling, and T. Lammers, “Tumor targeting *via* EPR: Strategies to enhance patient responses,” *Adv. Drug Deliv. Rev.*, vol. 130, no. 1, pp. 17–38, 2018.
- [32] A. Dupont, M. J. S. Ribeiro, D. Guilloteau, and N. Arlicot, “ $\beta$ -amyloid PET neuroimaging: A review of radiopharmaceutical development,” *Med. Nucl.*, vol. 41, no. 1, pp. 27–35, 2017.
- [33] M. Shokeen and T. J. Wadas, “The development of copper radiopharmaceuticals for imaging and therapy,” *Med. Chem. (Los. Angeles)*, vol. 7, no. 5, pp. 413–429, 2011.
- [34] O. Diou, N. Tsapis, and E. Fattal, “Targeted nanotheranostics for personalized cancer therapy,” pp. 1475–1487, 2012.

- [35] A. Gupta, A. Ahmad, A. I. Dar, and R. Khan, "Synthetic lethality: From research to precision cancer nanomedicine," *Curr. Cancer Drug Targets*, vol. 18, no. 4, pp. 337–346, 2018.
- [36] J. Thom, "Radiopharmaceuticals — an overview of the basic principles," *Pharm. J.*, vol. 4, no. 1, pp. 1–5, 2012.
- [37] C. A. Kluba and T. L. Mindt, "Click-to-chelate: Development of technetium and rhenium-tricarbonyl labeled radiopharmaceuticals," *Molecules*, vol. 18, no. 3, pp. 3206–3226, 2013.
- [38] E. O. Aboagye, S. K. Luthra, F. Brady, K. Poole, H. Anderson, T. Jones, A. Boobis, S. S. Burtles, and P. Price, "Cancer research UK procedures in manufacture and toxicology of radiotracers intended for pre-phase I positron emission tomography studies in cancer patients," *Br. J. Cancer*, vol. 86, no. 7, pp. 1052–1056, 2002.
- [39] P. C. Pieslor, "Barriers to achieving commercial success for diagnostic and therapeutic radiopharmaceutical," *Nucl. Med. Biol.*, vol. 34, no. 1, pp. 729–732, 2007.
- [40] W. Wadsak and M. Mitterhauser, "Basics and principles of radiopharmaceuticals for PET/CT," *Eur. J. Radiol.*, vol. 73, no. 3, pp. 461–469, 2010.
- [41] B. Iqbal, G. Currie, L. Greene, and H. Kiat, "Novel radiopharmaceuticals in cardiovascular medicine: Present and future," *J. Med. Imaging Radiat. Sci.*, vol. 45, no. 4, pp. 423–434, 2014.
- [42] S. Liu and D. S. Edwards, "<sup>99m</sup>Tc-labeled small peptides as diagnostic radiopharmaceuticals," *Chem. Rev.*, vol. 99, no. 9, pp. 2235–2268, 1999.
- [43] R. Santos-Oliveira, S. W. Smith, and A. M. A. Carneiro-Leao, "Radiopharmaceuticals drug interactions: A critical review," *Ann. Brazilian Acad. fof Sci.*, vol. 80, no. 4, pp. 665–675, 2008.
- [44] W. A. Volkert and T. J. Hoffman, "Therapeutic radiopharmaceuticals," *Chem. Rev.*, vol. 99, no. 9, pp. 2269–2292, 1999.
- [45] J. C. Hung, J. A. Ponto, and R. J. Hammes, "Radiopharmaceutical-related pitfalls and artifacts," *Semin. Nucl. Med.*, vol. 26, no. 4, pp. 208–255, 1996.
- [46] R. G. Zimmermann, "Why are investors not interested in my radiotracer? The industrial and regulatory constraints in the development of radiopharmaceuticals," *Nucl. Med.*

- Biol.*, vol. 40, no. 2, pp. 155–166, 2013.
- [47] B. J. Atkinson and S. M. Tu, “Radiopharmaceuticals: Present and future,” *J. Support. Oncol.*, vol. 9, no. 6, pp. 206–207, 2011.
- [48] X. Chen and S. T. C. Wong, *Cancer theranostics: An introduction*, 1st ed. Maryland: Academic Press, 2014.
- [49] D. S. Lee, H. J. Im, and Y. S. Lee, “Radionanomedicine: Widened perspectives of molecular theragnosis,” *Nanomedicine Nanotechnology, Biol. Med.*, vol. 11, no. 4, pp. 795–810, 2015.
- [50] O. Sartor, “Radiopharmaceuticals: A path forward,” *Eur. Urol.*, vol. 70, no. 3, pp. 427–428, 2016.
- [51] M. Neves, A. Kling, and R. M. Lambrecht, “Radionuclide production for therapeutic radiopharmaceuticals,” *Appl. Radiat. Isot.*, vol. 57, no. 5, pp. 657–664, 2002.
- [52] P. Uhl, G. Fricker, U. Haberkorn, and W. Mier, “Radionuclides in drug development,” *Drug Discov. Today*, vol. 20, no. 2, pp. 198–208, 2015.
- [53] J. R. Ballinger, “Pitfalls and limitations of SPECT, PET, and therapeutic radiopharmaceuticals,” *Semin. Nucl. Med.*, vol. 45, no. 5, pp. 470–478, 2015.
- [54] F. Zagni, F. Cesarini, G. Lucconi, G. Cicoria, D. Pancaldi, A. Infantino, S. Vichi, and M. Marengo, “The concept of minimum detectable activity of radionuclide activity meters and their suitability for routine quality control of radiopharmaceuticals. An experimental study,” *Appl. Radiat. Isot.*, vol. 113, no. 1, pp. 22–27, 2016.
- [55] G. Niu and X. Chen, “When radionuclides meet nanoparticles,” *Nat. Nanotechnol.*, vol. 13, no. 5, pp. 359–360, 2018.
- [56] W. H. O. Expert Committee, “Radiopharmaceuticals,” 2008.
- [57] J. R. Zeevart and S. Olsen, “Recent trends in the concept of specific activity: Impact on radiochemical and radiopharmaceutical producers,” *Appl. Radiat. Isot.*, vol. 64, no. 7, pp. 812–814, 2006.
- [58] S. M. Janib, A. S. Moses, and J. A. Mackay, “Imaging and drug delivery using theranostic nanoparticles,” *Adv. Drug Deliv. Rev.*, vol. 62, no. 11, pp. 1052–1063, 2010.
- [59] M. Wang and M. Thanou, “Targeting nanoparticles to cancer,” *Pharmacol. Res.*, vol. 62,



- no. 2, pp. 90–99, 2010.
- [60] G. Sgouros and D. M. Goldenberg, “Radiopharmaceutical therapy in the era of precision medicine,” *Eur. J. Cancer*, vol. 50, no. 13, pp. 2360–2363, 2014.
- [61] M. Marques, “Platinum and palladium polyamine complexes as anticancer agents: the structural factor,” *ISRN Spectrosc.*, vol. 2013, no. 1, pp. 1–29, 2013..
- [62] K. E. Britton, “Current trends in radionuclide therapy,” in *Therapeutic Applications of Radiopharmaceuticals*, 2001, vol. 1, no. 1, pp. 47–49.
- [63] A. C. Albeniz and P. Espinet, “Palladium: Inorganic & coordination chemistry,” in *Encyclopedia of Inorganic Chemistry*, 1st ed., A. C. Albeniz and P. Espinet, Eds. Valladolid: John Wiley & Sons, Ltd, 2006, pp. 1–20..
- [64] J. Kathawa, C. Fry, and M. Thoennessen, “Discovery of palladium, antimony, tellurium, iodine, and xenon isotopes,” *At. Data Nucl. Data Tables*, vol. 99, no. 1, pp. 22–52, 2013.
- [65] J. V. Wittemann, A. Kipke, E. Pippel, S. Senz, A. T. Vogel, J. De Boor, D. S. Kim, T. Hyeon, and V. Schmidt, “Citrate-stabilized palladium nanoparticles as catalysts for sub-20 nm epitaxial silicon nanowires,” *Appl. Phys. Lett.*, vol. 97, no. 2, 2010.
- [66] N. Torapava, L. I. Elding, H. Mandar, K. Roosalu, and I. Persson, “Structures of polynuclear complexes of palladium(II) and platinum(II) formed by slow hydrolysis in acidic aqueous solution,” *Dalton. Trans.*, vol. 42, no. 21, pp. 7755–7760, 2013.
- [67] D. Wheeler, “Precision measurements of the lattice constants of twelve common metals,” *Phys. Rev.*, vol. 25, no. 1, pp. 753–761, 1925.
- [68] S. Grazulis, D. Chateigner, R. T. Downs, A. T. Yokochi, M. Quiros, L. Lutterotti, E. Manakova, J. Butkus, P. Moeck, and A. Le Bail, “Crystallography open database: An open-access collection of crystal structures,” *J. Appl. Crystallogr.*, vol. 42, no. 1, pp. 726–729, 2009.
- [69] G. Hu, T. Sharifi, F. Nitze, H. Reza, C. Tai, and T. Wågberg, “Phase-transfer synthesis of amorphous palladium nanoparticle-functionalized 3D helical carbon nanofibers and its highly catalytic performance towards hydrazine oxidation,” *Chem. Phys. Lett.*, vol. 543, no. 8, pp. 96–100, 2012.
- [70] T. Nagase, R. Yamashita, A. Yabuuchi, and J. Lee, “An amorphous phase formation at palladium/silicon oxide (Pd/SiO<sub>x</sub>) interface through electron irradiation - electronic

- excitation process," *AIP Adv.*, vol. 5, no. 11, pp. 1–7, 2015.
- [71] W. Lu, B. Wang, K. Wang, X. Wang, and J. G. Hou, "Synthesis and characterization of crystalline and amorphous palladium nanoparticles," *Langmuir*, vol. 19, no. 14, pp. 5887–5891, 2003.
- [72] P. Grammatikopoulos, C. Cassidy, V. Singh, and M. Sowwan, "Coalescence-induced crystallisation wave in Pd nanoparticles," *Sci. Rep.*, vol. 4, no. 6, pp. 1–9, 2014.
- [73] R. Divakar and V. S. Raghunathan, "Characterisation of interfaces in nanocrystalline palladium," *Sadhana*, vol. 28, no. 1–2, pp. 47–62, 2003.
- [74] J. B. Omajali, I. P. Mikheenko, J. Wood, and L. E. Macaskie, "Characterization of intracellular palladium nanoparticles synthesized by *Desulfovibrio desulfuricans* and *Bacillus benzeovorans*," *J. Nanopart Res.*, vol. 17, no. 6, pp. 1–17, 2015.
- [75] D. . Narehood, "X-ray diffraction and H-storage in ultra-small palladium particles," *Int. J. Hydrogen Energy*, vol. 34, no. 2, pp. 952–960, 2009.
- [76] S. Pathak, M. T. Greci, R. C. Kwong, K. Mercado, G. K. S. Prakash, G. A. Olah, and M. E. Thompson, "Synthesis and applications of palladium-coated poly(vinylpyridine) nanospheres," *Chem. Mater.*, vol. 12, no. 7, pp. 1985–1989, 2000.
- [77] V. Leso and I. Iavicoli, "Palladium nanoparticles: Toxicological effects and potential implications for occupational risk assessment," *Int. J. Mol. Sci.*, vol. 19, no. 503, pp. 1–19, 2018.
- [78] S. V. Chankeshwara, E. Indrigo, and M. Bradley, "Palladium-mediated chemistry in living cells," *Curr. Opin. Chem. Biol.*, vol. 21, no. 1, pp. 128–135, 2014.
- [79] J. Kielhorn, C. Melber, D. Keller, and I. Mangelsdorf, "Palladium-A review of exposure and effects to human health," *Int. J. Hyg. Environ. Health*, vol. 205, no. 6, pp. 417–32, 2002.
- [80] W. P. Griffith, "Bicentenary of four platinum group metals: Rhodium and palladium - events surrounding their discoveries," *Platin. Met. Rev.*, vol. 47, no. 4, pp. 175–183, 2003
- [81] G. Audi, O. Bersillon, J. Blachot, and A. H. Wapstra, "The NUBASE evaluation of nuclear and decay properties," *Nucl. Phys. A*, vol. 729, no. 1, pp. 3–128, 2003.

- [82] O. Salata, "Applications of nanoparticles in biology and medicine," *J. Nanobiotechnology*, vol. 2, no. 1, pp. 1–6, 2004.
- [83] C. P. Adams, K. A. Walker, S. O. Obare, and K. M. Docherty, "Size-dependent antimicrobial effects of novel palladium nanoparticles," *PLoS One*, vol. 9, no. 1, pp. 1–12, 2014.
- [84] X. Xie, J. Liao, X. Shao, Q. Li, and Y. Lin, "The effect of shape on cellular uptake of gold nanoparticles in the forms of stars, rods, and triangles," *Sci. Rep.*, vol. 7, no. 1, pp. 1–9, 2017.
- [85] T. Lammers, S. Aime, W. E. Hennink, G. Storm, and F. Kiessling, "Theranostic nanomedicines and image-guided drug delivery," *Acc. Chem. Res.*, vol. 44, no. 10, pp. 1029–1038, 2011.
- [86] M. S. Muthu, D. T. Leong, L. Mei, and S.-S. Feng, "Nanotheranostics - Application and further development of nanomedicine strategies for advanced theranostics," *Theranostics*, vol. 4, no. 6, pp. 660–677, 2014.
- [87] D. S. Spencer, A. S. Puranik, and N. A. Peppas, "Intelligent nanoparticles for advanced drug delivery in cancer treatment," *Curr. Opin. Chem. Eng.*, vol. 7, pp. 84–92, 2015.
- [88] L. Y. T. Chou, K. Ming, and W. C. W. Chan, "Strategies for the intracellular delivery of nanoparticles," *Chem. Soc. Rev.*, vol. 40, no. 1, pp. 233–245, 2011.
- [89] H. Bonnemann and R. M. Richards, "Nanoscope metal particles-synthetic methods and potential applications," *Eur. J. Inorg. Chem.*, vol. 2001, no. 10, pp. 2455–2480, 2001.
- [90] N. Pantidos and L. E. Horsfall, "Biological synthesis of metallic nanoparticles by bacteria, fungi and plants," *J. Nanomed. Nanotechnol.*, vol. 5, no. 5, pp. 1–14, 2014.
- [91] A. Kumar, Y. Chisti, and U. Chand, "Synthesis of metallic nanoparticles using plant extracts," *Biotechnol. Adv.*, vol. 31, no. 2, pp. 346–356, 2013.
- [92] A. La Rosa, M. Yan, R. Fernandez, X. Wang, and E. Zegarra, "Top-down and bottom-up approaches to nanotechnology. An overview in the context of developing Proton-fountain Electric-field-assisted Nanolithography (PEN): Fabrication of polymer nanostructures that respond to chemical and electrical stimuli," 2013.
- [93] I. Brigger, C. Dubernet, and P. Couvreur, "Nanoparticles in cancer therapy and diagnosis," *Adv. Drug Deliv. Rev.*, vol. 54, no. 5, pp. 631–651, 2002.

- [94] M. Srinivasarao, C. V. Galliford, and P. S. Low, "Principles in the design of ligand-targeted cancer therapeutics and imaging agents," *Nat. Rev. Drug Discov.*, vol. 14, no. 3, pp. 203–219, 2015.
- [95] L. Brannon-Peppas and J. O. Blanchette, "Nanoparticle and targeted systems for cancer therapy," *Adv. Drug Deliv. Rev.*, vol. 56, no. 1, pp. 1649–1659, 2004.
- [96] J. Jiang, G. Oberdörster, and P. Biswas, "Characterization of size, surface charge, and agglomeration state of nanoparticle dispersions for toxicological studies," *J. Nanopart Res.*, vol. 11, no. 1, pp. 77–89, 2009.
- [97] H. Kettiger, A. Schipanski, P. Wick, and J. Huwyler, "Engineered nanomaterial uptake and tissue distribution: From cell to organism," *Int. J. Nanomedicine*, vol. 8, pp. 3255–3269, 2013.
- [98] B. Haley and E. Frenkel, "Nanoparticles for drug delivery in cancer treatment," *Urol. Oncol. Semin. Orig. Investig.*, vol. 26, no. 1, pp. 57–64, 2008.
- [99] P. Journey, R. Agarwal, V. Singh, D. Choi, K. Roy, S. V. Sreenivasan, and L. Shi, "Unique size and shape-dependent uptake behaviors of non-spherical nanoparticles by endothelial cells due to a shearing flow," *J. Control. Release*, vol. 245, no. 1, pp. 170–176, 2017.
- [100] W. E. N. Jiang, B. Y. S. Kim, J. T. Rutka, and W. C. W. Chan, "Nanoparticle-mediated cellular response is size-dependent," *Nat. Nanotechnol.*, vol. 3, no. 3, pp. 145–150, 2008.
- [101] K. Y. Win and S. Feng, "Effects of particle size and surface coating on cellular uptake of polymeric nanoparticles for oral delivery of anticancer drugs," *Biomaterials*, vol. 26, no. 15, pp. 2713–2722, 2005.
- [102] A. B. Jindal, "The effect of particle shape on cellular interaction and drug delivery applications of micro- and nanoparticles," *Int. J. Pharm.*, vol. 532, no. 1, pp. 450–465, 2017.
- [103] L. Shang, K. Nienhaus, and G. U. Nienhaus, "Engineered nanoparticles interacting with cells: Size matters," *J. Nanobiotechnology*, vol. 12, no. 5, pp. 1–11, 2014.
- [104] C. Von Roemeling, W. Jiang, C. K. Chan, I. L. Weissman, and B. Y. S. Kim, "Breaking down the barriers to precision cancer nanomedicine," *Trends Biotechnol.*, vol. 35, no. 2, pp.

- 159–171, 2017.
- [105] S. Bhattacharjee, “DLS and zeta potential - What they are and what they are not?,” *J. Control. Release*, vol. 235, no. 6, pp. 1–38, 2016.
- [106] R. R. Arvizo, O. R. Miranda, D. F. Moyano, C. A. Walden, K. Giri, R. Bhattacharya, J. D. Robertson, V. M. Rotello, J. M. Reid, and P. Mukherjee, “Modulating pharmacokinetics, tumor uptake and biodistribution by engineered nanoparticles,” *PLoS One*, vol. 6, no. 9, pp. 3–8, 2011.
- [107] M. Mahmoudi, J. Meng, X. Xue, J. X. Liang, M. Rahman, C. Pfeiffer, R. Hartmann, P. Rivera, P. R. Gil, B. Pelaz, W. J. Parak, P. del Pino, S. Carregal-Romero, A. G. Kanaras, and S. T. Selvan, “Interaction of stable colloidal nanoparticles with cellular membranes,” *Biotechnol. Adv.*, vol. 32, no. 4, pp. 679–692, 2014.
- [108] J. Cao, Y. Zhang, Y. Wu, J. Wu, W. Wang, Q. Wu, and Z. Yuan, “The effects of ligand valency and density on the targeting ability of multivalent nanoparticles based on negatively charged chitosan nanoparticles,” *Colloids Surf B Biointerfaces*, vol. 161, no. 1, pp. 508–518, 2018.
- [109] C. Genevois, A. Hocquelet, C. Mazzocco, E. Rustique, F. Couillaud, and N. Grenier, “*In vivo* imaging of prostate cancer tumors and metastasis using non-specific fluorescent nanoparticles in mice,” *Int. J. Mol. Sci.*, vol. 18, no. 12, pp. 1–10, 2017.
- [110] J. D. Byrne, T. Betancourt, and L. Brannon-Peppas, “Active targeting schemes for nanoparticle systems in cancer therapeutics,” *Adv. Drug Deliv. Rev.*, vol. 60, no. 15, pp. 1615–1626, 2008.
- [111] C. He, Y. Hu, L. Yin, C. Tang, and C. Yin, “Effects of particle size and surface charge on cellular uptake and biodistribution of polymeric nanoparticles,” *Biomaterials*, vol. 31, no. 13, pp. 3657–3666, 2010.
- [112] D. W. Pawlak, J. L. Parus, E. Skwarek, and W. Janusz, “A study of selected properties of rhenium sulphide dispersion,” *Physicochem. Probl. Miner. Process.*, vol. 50, no. 1, pp. 387–397, 2013.
- [113] S. Dong, H. J. Cho, Y. W. Lee, M. Roman, V. Tech, and U. States, “Synthesis and cellular uptake of folic acid-conjugated cellulose nanocrystals for cancer targeting,” *Biomacromolecules*, vol. 15, no. 3, pp. 1–8, 2014.

- [114] S. Horikoshi and N. Serpone, "Introduction to nanoparticles," in *Microwaves in Nanoparticle Synthesis: Fundamentals and Applications*, 2013, pp. 1–24..
- [115] C. Kinnear, T. L. Moore, L. Rodriguez-Lorenzo, B. Rothen-Rutishauser, and A. Petri-Fink, "Form follows function: Nanoparticle shape and its implications for nanomedicine," *Chem. Rev.*, vol. 117, no. 17, pp. 11476–11521, 2017.
- [116] N. P. Truong, M. R. Whittaker, C. W. Mak, T. P. Davis, N. P. Truong, M. R. Whittaker, C. W. Mak, and T. P. Davis, "The importance of nanoparticle shape in cancer drug delivery," *Expert Opin. Drug Deliv.*, vol. 12, no. 1, pp. 129–142, 2017.
- [117] H. T. Ta, N. P. Truong, A. K. Whittaker, T. P. Davis, and K. Peter, "The effects of particle size, shape, density and flow characteristics on particle margination to vascular walls in cardiovascular diseases," *Expert Opin. Drug Deliv.*, vol. 15, no. 1, pp. 33–45, 2018.
- [118] Y. Pei and Y. Yeo, "Drug delivery to macrophages: Challenges and opportunities," *J. Control. Release*, vol. 240, no. 1, pp. 202–211, 2016.
- [119] Z. Wang, Z. Wu, J. Liu, and W. Zhang, "Particle morphology: An important factor affecting drug delivery by nanocarriers into solid tumors," *Expert Opin. Drug Deliv.*, vol. 15, no. 4, pp. 379–395, 2018.
- [120] P. Mishra, B. Nayak, and R. K. Dey, "PEGylation in anti-cancer therapy: An overview," *Asian J. Pharm. Sci.*, vol. 11, no. 3, pp. 337–348, 2016.
- [121] B. Kowalczyk, I. Lagzi, and B. A. Grzybowski, "Nanoseparations: Strategies for size and/or shape-selective purification of nanoparticles," *Curr. Opin. Colloid Interface Sci.*, vol. 16, no. 2, pp. 135–148, 2011.
- [122] T. L. Moore, L. Rodriguez-Lorenzo, V. Hirsch, S. Balog, D. Urban, C. Jud, B. Rothen-Rutishauser, M. Lattuada, and A. Petri-Fink, "Nanoparticle colloidal stability in cell culture media and impact on cellular interactions," *Chem. Soc. Rev.*, vol. 44, no. 17, pp. 6287–6305, 2015.
- [123] J. Shi, P. W. Kantoff, R. Wooster, and O. C. Farokhzad, "Cancer nanomedicine: Progress, challenges and opportunities," *Nat. Rev. Cancer*, vol. 17, no. 1, pp. 20–37, 2016.
- [124] L. Tang, X. Yang, Q. Yin, K. Cai, H. Wang, I. Chaudhury, C. Yao, Q. Zhou, M. Kwon, J. A. Hartman, I. T. Dobrucki, L. W. Dobrucki, L. B. Borst, S. Lezmi, W. G. Helferich, A. L. Ferguson, T. M. Fan, and J. Cheng, "Investigating the optimal size of anticancer

- nanomedicine,” *Proc. Natl. Acad. Sci.*, vol. 111, no. 43, pp. 15344–15349, 2014.
- [125] H. Duan, D. Wang, and Y. Li, “Green chemistry for nanoparticle synthesis,” *Chem. Soc. Rev.*, vol. 44, no. 16, pp. 5778–5792, 2015.
- [126] C. Buzea, I. I. P. Blandino, and K. Robbie, “Nanomaterials and nanoparticles: Sources and toxicity,” *Biointerphases*, vol. 2, no. 4, pp. 1–103, 2007.
- [127] B. J. Marquis, S. A. Love, K. L. Braun, and C. L. Haynes, “Analytical methods to assess nanoparticle toxicity,” *Analyst*, vol. 134, no. 3, pp. 425–439, 2009.
- [128] G. Oberdörster, E. Oberdörster, and J. Oberdörster, “Nanotoxicology: An emerging discipline evolving from studies of ultrafine particles,” *Environmental Heal. Perspect.*, vol. 113, no. 7, pp. 823–839, 2005.
- [129] S. J. Tan, N. R. Jana, S. Gao, P. K. Patra, and J. Y. Ying, “Surface-ligand-dependent cellular interaction, subcellular localization, and cytotoxicity of polymer-coated quantum dots,” *Chem. Mater.*, vol. 22, no. 7, pp. 2239–2247, 2010.
- [130] R. Bhattacharya and P. Mukherjee, “Biological properties of ‘naked’ metal nanoparticles,” *Adv. Drug Deliv. Rev.*, vol. 60, no. 11, pp. 1289–1306, 2008.
- [131] W. H. De Jong and P. J. A. Borm, “Drug delivery and nanoparticles: Applications and hazards,” *Int. J. Nanomedicine*, vol. 3, no. 2, pp. 133–149, 2008.
- [132] M. Lelle, S. Kaloyanova, C. Freidel, M. Theodoropoulou, M. Musheev, C. Niehrs, G. Stalla, and K. Peneva, “Octreotide-mediated tumor-targeted drug delivery *via* a cleavable doxorubicin-peptide conjugate,” *Mol. Pharm.*, vol. 12, no. 12, pp. 4290–4300, 2015.
- [133] C. Choulyt, D. Pouliquen, I. Lucet, J. J. Jeune, and P. Jallet, “Development of superparamagnetic nanoparticles for MRI: Effect of particle size, charge and surface nature on biodistribution,” *J. Microencapsul.*, vol. 13, no. 3, pp. 245–255, 1996.
- [134] N. Bertrand, J. Wu, X. Xu, N. Kamaly, and O. C. Farokhzad, “Cancer nanotechnology: The impact of passive and active targeting in the era of modern cancer biology,” *Adv. Drug Deliv. Rev.*, vol. 66, no. 2, pp. 2–25, 2014.
- [135] J. G. Teeguarden, P. M. Hinderliter, G. Orr, B. D. Thrall, and J. G. Pounds, “Particokinetics *in vitro*: Dosimetry considerations for *in vitro* nanoparticle toxicity assessments,” *Toxicol. Sci.*, vol. 95, no. 2, pp. 300–312, 2007.

- [136] C. A. Robertson, D. H. Evans, and H. Abrahamse, "Photodynamic therapy (PDT): A short review on cellular mechanisms and cancer research applications for PDT," *J. Photochem. Photobiol. B Biol.*, vol. 96, no. 1, pp. 1–8, 2009.
- [137] A. C. Anselmo and S. Mitragotri, "Cell-mediated delivery of nanoparticles: Taking advantage of circulatory cells to target nanoparticles," *J. Control. Release*, vol. 190, no. 9, pp. 531–541, 2014.
- [138] B. Stella, S. Arpicco, M. T. Peracchia, D. Desmae, J. Hoebeker, M. Renoir, J. D'Angelo, L. Cattel, and P. Couvreur, "Design of folic acid-conjugated nanoparticles for drug targeting," *J. Pharm. Sci.*, vol. 89, no. 11, pp. 1452–1464, 2000.
- [139] B. Bahrami, M. Hojjat-Farsangi, H. Mohammadi, E. Anvari, G. Ghalamfarsa, M. Yousefi, and Jadidi-Niaragh, "Nanoparticles and targeted drug delivery in cancer therapy," *Immunol. Lett.*, vol. 190, no. 7, pp. 64–83, 2017.
- [140] S. Haller, J. Reber, S. Brandt, P. Bernhardt, R. Schibli, M. Cristina, G. Viola, and S. Roger, "Folate receptor-targeted radionuclide therapy: Preclinical investigation of anti-tumor effects and potential radionephropathy," *Nucl. Med. Biol.*, vol. 42, no. 10, pp. 770–779, 2015.
- [141] T. Haper, "What is nanotechnology?," *Nanotechnology*, vol. 14, no. 1, pp. 1–4, Jan. 2003.
- [142] R. A. Freitas, "What is nanomedicine?," *Nanomed-Nanotechnology.*, vol. 1, no. 1, pp. 2–9, 2005.
- [143] V. P. Chauhan and R. K. Jain, "Strategies for advancing cancer nanomedicine," *Nat. Mater.*, vol. 12, no. 11, pp. 958–962, 2013.
- [144] P. Mélinon, S. Begin-Colin, J. L. Duvail, F. Gauffre, N. H. Boime, G. Ledoux, J. Plain, P. Reiss, F. Silly, and B. Warot-Fonrose, "Engineered inorganic core/shell nanoparticles," *Phys. Rep.*, vol. 543, no. 3, pp. 163–197, 2014.
- [145] D. Rosenblum, N. Joshi, W. Tao, J. M. Karp, and D. Peer, "Progress and challenges towards targeted delivery of cancer therapeutics," *Nat. Commun.*, vol. 9, no. 1, pp. 1410–1422, 2018.
- [146] E. Pérez-Herrero and A. Fernández-Medarde, "Advanced targeted therapies in cancer: Drug nanocarriers, the future of chemotherapy," *Eur. J. Pharm. Biopharm.*, vol. 93, no.



- 1, pp. 52–79, 2015.
- [147] L. Ramzy, M. Nasr, A. A. Metwally, and G. A. S. Awad, “Cancer nanotheranostics: A review of the role of conjugated ligands for overexpressed receptors,” *Eur. J. Pharm. Sci.*, vol. 104, no. 4, pp. 273–292, 2017.
- [148] W. Dai, X. X. Wang, G. Song, T. Liu, B. He, H. Zhang, X. X. Wang, and Q. Zhang, “Combination antitumor therapy with targeted dual-nanomedicines,” *Adv. Drug Deliv. Rev.*, vol. 115, no. 1, pp. 23–45, 2017.
- [149] O. C. Farokhzad and R. Langer, “Impact of nanotechnology on drug delivery,” *ACS Nano*, vol. 3, no. 1, pp. 16–20, 2009.
- [150] J. S. Brenner, D. C. Pan, J. W. Myerson, O. A. Marcos-contreras, C. H. Villa, P. Patel, H. Hekierski, S. Chatterjee, J. Tao, H. Parhiz, K. Bhamidipati, T. G. Uhler, E. D. Hood, R. Y. Kiseleva, V. S. Shuvaev, T. Shuvaeva, M. Khoshnejad, and I. Johnston, “Red blood cell-hitchhiking boosts delivery of nanocarriers to chosen organs by orders of magnitude,” *Nat. Commun.*, vol. 9, no. 1, pp. 1–14, 2018.
- [151] G. Chen, I. Roy, C. Yang, and P. N. Prasad, “Nanochemistry and nanomedicine for nanoparticle-based diagnostics and therapy,” *Chem. Rev.*, vol. 116, no. 1, pp. 2826–2885, 2016.
- [152] V. K. Khanna, “Targeted delivery of nanomedicines,” *ISRN Pharmacol.*, vol. 2012, no. 1, pp. 1–9, 2012.
- [153] A. David, “Peptide ligand-modified nanomedicines for targeting cells at the tumor microenvironment,” *Adv. Drug Deliv. Rev.*, vol. 119, no. 9, pp. 120–142, 2017.
- [154] M. Bjornmalm, K. J. Thurecht, M. Michael, A. M. Scott, and F. Caruso, “Bridging bio-nano science and cancer nanomedicine,” *ACS Nano*, vol. 11, no. 10, pp. 9594–9613, 2017.
- [155] J. Wang, W. Tao, X. Chen, O. C. Farokhzad, and G. Liu, “Emerging advances in nanotheranostics with intelligent bioresponsive systems,” *Theranostics*, vol. 7, no. 16, pp. 3915–3919, 2017.
- [156] X. Yu, I. Trase, M. Ren, K. Duval, X. Guo, and Z. Chen, “Design of nanoparticle-based carriers for targeted drug delivery,” *J. Nanomater.*, vol. 2016, no. 4, pp. 1–15, 2016.
- [157] H. Chen, W. Zhang, G. Zhu, J. Xie, and X. Chen, “Rethinking cancer nanotheranostics,”

- Nat. Rev. Mater.*, vol. 2, no. 5, pp. 1–18, 2017.
- [158] N. P. Praetorius and T. K. Mandal, “Engineered nanoparticles in cancer therapy,” *Recent Pat. Drug Deliv. Formul.*, vol. 1, no. 1, pp. 37–51, 2007.
- [159] G. Sahay, D. Y. Alakhova, and A. V Kabanov, “Endocytosis of nanomedicines,” *J. Control. Release*, vol. 145, no. 3, pp. 182–195, 2010.
- [160] O. C. Farokhzad and R. Langer, “Nanomedicine: Developing smarter therapeutic and diagnostic modalities,” *Adv. Drug Deliv. Rev.*, vol. 58, no. 14, pp. 1456–1459, 2006.
- [161] M. Toporkiewicz, J. Meissner, L. Matuszewicz, A. Czogalla, and A. F. Sikorski, “Toward a magic or imaginary bullet? Ligands for drug targeting to cancer cells: Principles, hopes, and challenges,” *Int. J. Nanomedicine*, vol. 10, no. 1, pp. 1399–1414, 2015.
- [162] M. L. Etheridge, S. A. Campbell, A. G. Erdman, C. L. Haynes, S. M. Wolf, and J. Mccullough, “The big picture on nanomedicine: The state of investigational and approved nanomedicine products,” *Nanomedicine Nanotechnology, Biol. Med.*, vol. 9, no. 1, pp. 1–14, 2013.
- [163] Y. Dekempeneer, M. Keyaerts, A. Krasniqi, J. Puttemans, S. Muyldermans, T. Lahoutte, M. D’huyvetter, and N. Devoogdt, “Targeted alpha therapy using short-lived alpha-particles and the promise of nanobodies as targeting vehicle,” *Expert Opin. Biol. Ther.*, vol. 16, no. 8, pp. 1035–1047, 2016.
- [164] G. A. Mansoori, P. Mohazzabi, P. McCormack, and S. Jabbari, “Nanotechnology in cancer prevention, detection and treatment: bright future lies ahead,” *World Rev. Sci. Technol. Sustain. Dev.*, vol. 4, no. 2, pp. 226–257, 2007.
- [165] J. E. Rosen, S. Yoffe, A. Meerasa, M. Verma, and F. X. Gu, “Nanotechnology and diagnostic imaging: New advances in contrast agent technology,” *J. Nanomed. Nanotechnol.*, vol. 2, no. 5, pp. 1–12, 2011.
- [166] J. Panyam and V. Labhasetwar, “Biodegradable nanoparticles for drug and gene delivery to cells and tissue,” *Adv. Drug Deliv. Rev.*, vol. 55, no. 3, pp. 329–347, 2003.
- [167] E. S. Kawasaki and A. Player, “Nanotechnology, nanomedicine, and the development of new, effective therapies for cancer,” *Nanomedicine Nanotechnology, Biol. Med.*, vol. 1, no. 2, pp. 101–109, 2005.
- [168] A. Babu, A. K. Templeton, A. Munshi, and R. Ramesh, “Nanoparticle-based drug delivery

- for therapy of lung cancer: Progress and challenges," *J. Nanomater.*, vol. 2013, no. 14, pp. 1–11, 2013.
- [169] X. Zeng, R. Morgenstern, and A. M. Nyström, "Nanoparticle-directed sub-cellular localization of doxorubicin and the sensitization breast cancer cells by circumventing GST-Mediated drug resistance," *Biomaterials*, vol. 35, no. 4, pp. 1227–1239, 2014.
- [170] J. Weber, U. Haberkorn, and W. Mier, "Cancer stratification by molecular imaging," *Int. J. Mol. Sci.*, vol. 16, no. 3, pp. 4918–4946, 2015.
- [171] R. Bazak, M. Hourri, S. El Achy, W. Hussein, T. Refaat, S. E. L. Achy, W. Hussein, and T. Refaat, "Passive targeting of nanoparticles to cancer: A comprehensive review of the literature," *Mol. Clin. Oncol.*, vol. 2, no. 6, pp. 904–908, 2014.
- [172] R. R. Wakaskar, "Passive and active targeting in tumor microenvironment," *Int. J. Drug Dev.*, vol. 9, no. 2, pp. 37–41, 2017.
- [173] A. R. Gliga, S. Skoglund, I. O. Wallinder, B. Fadeel, and H. L. Karlsson, "Size-dependent cytotoxicity of silver nanoparticles in human lung cells: The role of cellular uptake, agglomeration and Ag release," *Part. Fibre Toxicol.*, vol. 11, no. 1, p. 11, 2014.
- [174] B. D. Chithrani, A. A. Ghazani, and W. C. W. W. Chan, "Determining the size and shape dependence of gold nanoparticle uptake into mammalian cells," *Nano Lett.*, vol. 6, no. 4, pp. 662–668, 2006.
- [175] B. Yameen, W. Il Choi, C. Vilos, A. Swami, J. Shi, and O. C. Farokhzad, "Insight into nanoparticle cellular uptake and intracellular targeting," *J. Control. Release*, vol. 190, no. 1, pp. 485–499, 2014.
- [176] C. Boyer, M. R. Whittaker, V. Bulmus, J. Liu, and T. P. Davis, "The design and utility of polymer-stabilized iron-oxide nanoparticles for nanomedicine applications," *NPG Asia Mater.*, vol. 2, no. 1, pp. 23–30, 2010.
- [177] E. A. Sykes, J. Chen, G. Zheng, and W. C. W. Chan, "Investigating the impact of nanoparticle size on active and passive tumor targeting efficiency," *ACS Nano*, vol. 8, no. 6, pp. 5696–5706, 2014.
- [178] R. Bazak, M. Hourri, S. El Achy, W. Hussein, and T. Refaat, "Cancer active targeting by nanoparticles: A comprehensive review of literature," *J. Cancer Res. Clin. Oncol.*, vol. 141, no. 5, pp. 769–784, 2014.

- [179] K. Cho, X. Wang, S. Nie, Z. Chen, and D. M. Shin, "Therapeutic nanoparticles for drug delivery in cancer," *Clin. Cancer Res.*, vol. 14, no. 5, pp. 1310–1316, 2008.
- [180] A. Derakhshandeh, Katayoun; Hemmati Azandaryani, "Active-targeted nanotherapy as smart cancer treatment," in *Smart Drug Delivery System*, A. D. Sezer, Ed. IntechOpen, 2015, pp. 91–116.
- [181] C. Muller, "Folate based radiopharmaceuticals for imaging and therapy of cancer and inflammation," *Curr. Pharm. Des.*, vol. 18, no. 8, pp. 1058–1083, 2012.
- [182] A. Kumari and S. K. Yadav, "Cellular interactions of therapeutically delivered nanoparticles," *Expert Opin. Drug Deliv.*, vol. 8, no. 2, pp. 141–151, 2011.
- [183] B. D. Chithrani and W. C. W. Chan, "Elucidating the mechanism of cellular uptake and removal of protein-coated gold nanoparticles of different sizes and shapes," *Nano Lett.*, vol. 7, no. 6, pp. 1542–1550, 2007.
- [184] N. A. Bandara, M. J. Hansen, and P. S. Low, "Effect of receptor occupancy on folate receptor internalization," *Mol. Pharm.*, vol. 11, no. 3, pp. 1007–1013, 2014.
- [185] R. Vacha, F. J. Martinez-Veracoechea, and D. Frenkel, "Receptor-mediated endocytosis of nanoparticles of various shapes," *Nano Lett.*, vol. 11, no. 12, pp. 5391–5395, 2011.
- [186] M. E. Davis, Z. G. Chen, and D. M. Shin, "Nanoparticle therapeutics: An emerging treatment modality for cancer," *Nat. Rev. Drug Discov.*, vol. 7, no. 9, pp. 771–782, 2008.
- [187] S. A. Kulkarni and S.-S. Feng, "Effects of particle size and surface modification on cellular uptake and biodistribution of polymeric nanoparticles for drug delivery," *Pharm. Res.*, vol. 30, no. 10, pp. 2512–22, 2013.
- [188] F. Lu, S.-H. Wu, Y. Hung, and C.-Y. Mou, "Size effect on cell uptake in well-suspended, uniform mesoporous silica nanoparticles," *Small*, vol. 5, no. 12, pp. 1408–1413, 2009.
- [189] B. Kumar, K. Jalodia, P. Kumar, and H. K. Gautam, "Recent advances in nanoparticle-mediated drug delivery," *J. Drug Deliv. Sci. Technol.*, vol. 41, no. 1, pp. 260–268, 2017.
- [190] E. Piktel, K. Niemirowicz, M. Wątek, T. Wollny, P. Deptuła, and R. Bucki, "Recent insights in nanotechnology-based drugs and formulations designed for effective anti-cancer therapy," *J. Nanobiotechnology*, vol. 14, no. 1, pp. 39–62, 2016.
- [191] R. L. Merzel, C. Frey, J. Chen, R. Garn, M. Van Dongen, C. A. Dougherty, A. K. Kandaluru,

- P. S. Low, E. N. G. Marsh, and M. M. Banaszak Holl, "Conjugation dependent interaction of folic acid with folate binding protein," *Bioconjug. Chem.*, vol. 28, no. 9, pp. 2350–2360, 2017.
- [192] C. Müller and R. Schibli, "Prospects in folate receptor-targeted radionuclide therapy," *Front. Oncol.*, vol. 3, no. 249, pp. 1–10, 2013.
- [193] A. S. Wibowo, M. Singh, K. M. Reeder, J. J. Carter, A. R. Kovach, W. Meng, M. Ratnam, F. Zhang, and C. E. Dann, "Structures of human folate receptors reveal biological trafficking states and diversity in folate and antifolate recognition," *Proc. Natl. Acad. Sci. U. S. A.*, vol. 110, no. 38, pp. 15180–15188, 2013.
- [194] A. R. Vortherms, R. P. Doyle, D. Gao, O. Debrah, and P. J. Sinko, "Synthesis, characterization, and *in vitro* assay of folic acid conjugates of 3'-azido-3'-deoxythymidine (AZT): Toward targeted AZT based anticancer therapeutics," *Nucleosides. Nucleotides Nucleic Acids*, vol. 27, no. 2, pp. 173–185, 2008.
- [195] A. R. Hilgenbrink and P. S. Low, "Folate receptor-mediated drug targeting: From therapeutics to diagnostics," *J. Pharm. Sci.*, vol. 94, no. 10, pp. 2135–2146, 2005.
- [196] N. Viola-Villegas, A. Vortherms, and R. P. Doyle, "Targeting gallium to cancer cells through the folate receptor," *Drug Target Insights*, vol. 2008, no. 3, pp. 13–25, 2008.
- [197] R. K. Saini, S. H. Nile, and Y. S. Keum, "Folates: Chemistry, analysis, occurrence, biofortification and bioavailability," *Food Res. Int.*, vol. 89, no. 1, pp. 1–13, 2016.
- [198] A. R. Hashemian and G. A. Mansoori, "Cancer nanodiagnostics and nanotherapeutics through the folate-conjugated nanoparticles," *J. Bioanal. Biomed.*, vol. 5, no. 3, pp. 61–64, 2015.
- [199] C. Chen, J. Ke, E. X. Zhou, W. Yi, J. S. Brunzelle, J. Li, E.-L. Yong, H. E. Xu, and K. Melcher, "Structural basis for molecular recognition of folic acid by folate receptors," *Nature*, vol. 500, no. 7463, pp. 486–489, 2013.
- [200] C. Muller, M. Bruhlmeier, P. A. Schubinger, and R. Schibli, "Effects of antifolate drugs on the cellular uptake of radiofolates *in vitro* and *in vivo*," *J. Nucl. Med.*, vol. 47, no. 12, pp. 2057–2064, 2006.
- [201] S. Della-Longa and A. Arcovito, "Intermediate states in the binding process of folic acid to folate receptor  $\alpha$ : Insights by molecular dynamics and metadynamics," *J. Comput.*

- Aided. Mol. Des.*, vol. 29, no. 1, pp. 23–35, 2015.
- [202] N. Gonen and Y. G. Assaraf, “Antifolates in cancer therapy: Structure, activity and mechanisms of drug resistance,” *Drug Resist. Updates.*, vol. 15, no. 4, pp. 183–210, 2012.
- [203] P. T. Wong and S. K. Choi, “Mechanisms and implications of dual-acting methotrexate in folate-targeted nanotherapeutic delivery,” *Int. J. Mol. Sci.*, vol. 16, no. 1, pp. 1772–1790, 2015.
- [204] A. Cheung, H. J. Bax, D. H. Josephs, K. M. Ilieva, G. Pellizzari, J. Opzoomer, J. Bloomfield, M. Fittall, A. Grigoriadis, M. Figini, S. Canevari, J. F. Spicer, A. N. Tutt, and S. N. Karagiannis, “Targeting folate receptor alpha for cancer treatment,” *Oncotarget*, vol. 7, no. 32, pp. 52553–52574, 2016.
- [205] M. S. Jhaveri, A. S. Rait, K.-N. Chung, J. B. Trepel, and E. H. Chang, “Antisense oligonucleotides targeted to the human  $\alpha$  folate receptor inhibit breast cancer cell growth and sensitize the cells to doxorubicin treatment,” *Mol. Cancer Ther.*, vol. 3, no. 12, pp. 1505–1512, 2004.
- [206] V. Sanna, N. Pala, and M. Sechi, “Targeted therapy using nanotechnology: Focus on cancer,” *Int. J. Nanomedicine*, vol. 9, no. 1, pp. 467–483, 2014.
- [207] A. Shakeri-Zadeh, G. A. Mansoori, A. R. Hashemian, H. Eshghi, A. Sazgarnia, and A. R. Montazerabadi, “Cancerous cells targeting and destruction using folate conjugated gold nanoparticles,” *Dyn. Biochem. Process Biotechnol. Mol. Biol.*, vol. 4, no. 1, pp. 6–12, 2010.
- [208] Y. Tian, G. Wu, J.-C. Xing, J. Tang, Y. Zhang, Z. Huang, Z. Jia, R. Zhao, Z.-Q. Tian, S.-F. Wang, X.-L. Chen, L. Wang, Y.-Z. Wu, and B. Ni, “A novel splice variant of folate receptor 4 predominantly expressed in regulatory T cells,” *BMC Immunol.*, vol. 13, no. 30, pp. 1–8, 2012.
- [209] A. Puig-Kröger, E. Sierra-Filardi, A. Domínguez-Soto, R. Samaniego, M. T. Corcuera, F. Gómez-Aguado, M. Ratnam, P. Sánchez-Mateos, and A. L. Corbí, “Folate receptor  $\beta$  is expressed by tumor-associated macrophages and constitutes a marker for M2 anti-inflammatory/regulatory macrophages,” *Cancer Res.*, vol. 69, no. 24, pp. 9395–9403, 2009.

- [210] X. Zhao, H. Li, and R. J. Lee, "Targeted drug delivery *via* folate receptors," *Expert Opin. Drug Deliv.*, vol. 5, no. 3, pp. 309–319, 2017.
- [211] Y. G. Assaraf, C. P. Leamon, and J. A. Reddy, "The folate receptor as a rational therapeutic target for personalized cancer treatment," *Drug Resist. Updates.*, vol. 17, no. 4, pp. 89–95, 2014.
- [212] J. Sudimack and R. J. Lee, "Targeted drug delivery *via* the folate receptor," *Adv. Drug Deliv. Rev.*, vol. 41, no. 2, pp. 147–162, 2000.
- [213] H. Kurahara, S. Takao, T. Kuwahata, T. Nagai, Q. Ding, K. Maeda, H. Shinci, Y. Mataka, K. Maemura, T. Matsuyama, and S. Natsugoe, "Clinical significance of folate receptor  $\beta$ -expressing tumor-associated macrophages in pancreatic cancer," *Ann. Surg. Oncol.*, vol. 19, no. 7, pp. 2264–2271, 2012.
- [214] C. Müller, P. A. Schubiger, and R. Schibli, "*In vitro* and *in vivo* targeting of different folate receptor-positive cancer cell lines with a novel  $^{99m}\text{Tc}$ -radiofolate tracer," *Eur. J. Nucl. Med. Mol. Imaging*, vol. 33, no. 10, pp. 1162–1170, 2006.
- [215] L. Teng, J. Xie, L. Teng, and R. J. Lee, "Clinical translation of folate receptor-targeted therapeutics," *Expert Opin. Drug Deliv.*, vol. 9, no. 8, pp. 901–908, 2012.
- [216] P. S. Low, W. A. Henne, and D. D. Doorneweerd, "Discovery and development of folic acid-based receptor targeting for imaging and therapy of cancer and inflammatory diseases," *Acc. Chem. Res.*, vol. 41, no. 1, pp. 120–129, 2008.
- [217] F. M. Sirotnak and B. Tolner, "Carrier-mediated membrane transport of folates in mammalian cells," *Annu. Rev. Nutr.*, vol. 19, no. 1, pp. 91–122, 1999.
- [218] R. Schneider, F. Schmitt, C. Frochot, Y. Fort, N. Lourette, F. Guillemin, J. F. Müller, and M. Barberi-Heyob, "Design, synthesis, and biological evaluation of folic acid targeted tetraphenylporphyrin as novel photosensitizers for selective photodynamic therapy," *Bioorganic Med. Chem.*, vol. 13, no. 8, pp. 2799–2808, 2005.
- [219] I. Vergote and C. P. Leamon, "Vintafolide: A novel targeted therapy for the treatment of folate receptor expressing tumors," *Ther. Adv. Med. Oncol.*, vol. 7, no. 4, pp. 206–218, 2015.
- [220] H. Jing, Z. Guo, W. Guo, W. Yang, P. Xu, and X. Zhang, "Synthesis and characterization of folic acid modified water-soluble chitosan derivatives for folate receptor-mediated

- targeting," *Bioorg. Med. Chem. Lett.*, vol. 22, no. 10, pp. 3418–3424, 2012.
- [221] J. E. Nutt, A. R. A. Razak, K. O'Toole, F. Black, A. E. Quinn, A. H. Calvert, E. R. Plummer, and J. Lunec, "The role of folate receptor alpha (FR $\alpha$ ) in the response of malignant pleural mesothelioma to pemetrexed-containing chemotherapy," *Br. J. Cancer*, vol. 102, no. 3, pp. 553–60, 2010.
- [222] S. F. Atkinson, T. Bettinger, L. W. Seymour, J.-P. Behr, and C. M. Ward, "Conjugation of folate *via* gelonin carbohydrate residues retains ribosomal-inactivating properties of the toxin and permits targeting to folate receptor positive cells," *J. Biol. Chem.*, vol. 276, no. 30, pp. 27930–27935, 2001.
- [223] L. H. Matherly and I. D. Goldman, "Membrane transport of folates," *Vitam. Horm.*, vol. 66, no. 1, pp. 403–456, 2003.
- [224] M. V. B. Dias, J. C. Santos, G. A. Libreros-Zuniga, J. Ribeiro, and S. M. Chavez-Pacheco, "Folate biosynthesis pathway: Mechanisms and insights into drug design for infectious diseases," *Future Med. Chem.*, vol. 10, no. 8, pp. 935–959, 2018.
- [225] G. Ak, H. Yilmaz, A. Güneş, and S. H. Sanlier, "*In vitro* and *in vivo* evaluation of folate receptor-targeted a novel magnetic drug delivery system for ovarian cancer therapy," *Artif. Cells, Nanomedicine, Biotechnol.*, vol. 46, no. 1, pp. 926–937, 2018.
- [226] Y. Lu and P. S. Low, "Folate-mediated delivery of macromolecular anticancer therapeutic agents," *Adv. Drug Deliv. Rev.*, vol. 64, no. 1, pp. 342–352, 2012.
- [227] I. B. Vergote, C. Marth, and R. L. Coleman, "Role of the folate receptor in ovarian cancer treatment: Evidence, mechanism, and clinical implications," *Cancer Metastasis Rev.*, vol. 34, no. 1, pp. 41–52, 2015.
- [228] R. Zhao, N. Diop-Bove, M. Visentin, and I. D. Goldman, "Mechanisms of membrane transport of folates into cells and across epithelia," *Annu. Rev. Nutr.*, vol. 31, no. 8, pp. 177–201, 2011.
- [229] K. R. Kalli, A. L. Oberg, G. L. Keeney, T. J. H. Christianson, P. S. Low, K. L. Knutson, and L. C. Hartmann, "Folate receptor alpha as a tumor target in epithelial ovarian cancer," *Gynecol. Oncol.*, vol. 108, no. 3, pp. 619–626, 2008.
- [230] M. J. Spinella, K. E. Brigle, E. E. Sierra, and D. I. Goldman, "Distinguishing between folate receptor- $\alpha$ -mediated transport and reduced folate carrier-mediated transport in L1210



- leukemia cells," *J. Biol. Chem.*, vol. 270, no. 14, pp. 7842–7849, 1994.
- [231] A. Brzezińska, P. Wińska, and M. Balińska, "Cellular aspects of folate and antifolate membrane transport," *Acta Biochim. Pol.*, vol. 47, no. 3, pp. 735–749, 2000.
- [232] N. Hagner and M. Joerger, "Cancer chemotherapy: Targeting folic acid synthesis," *Cancer Manag. Res.*, vol. 2, no. 1, pp. 293–301, 2010.
- [233] N. Movagharneshad and P. N. Moghadam, "Folate-decorated carboxymethyl cellulose for controlled doxorubicin delivery," *Colloid Polym. Sci.*, vol. 294, no. 1, pp. 199–206, 2016.
- [234] L. Xu, Q. Bai, X. Zhang, and H. Yang, "Folate-mediated chemotherapy and diagnostics: An updated review and outlook," *J. Control. Release*, vol. 252, no. 1, pp. 73–82, 2017.
- [235] A. H. Maurer, P. Elsinga, S. Fanti, B. Nguyen, W. J. G. Oyen, and W. A. Weber, "Imaging the folate receptor on cancer cells with  $^{99m}\text{Tc}$ -etarfolatide: Properties, clinical use, and future potential of folate receptor imaging," *J. Nucl. Med.*, vol. 55, no. 5, pp. 701–704, 2014.
- [236] C. Decristoforo and S. J. Mather, "Technetium-99m somatostatin analogues: Effect of labelling methods and peptide sequence," *Eur. J. Nucl. Med.*, vol. 26, no. 8, pp. 869–876, 1999.
- [237] S. Lu, W. Zhang, R. Zhang, P. Liu, Q. Wang, Y. Shang, M. Wu, K. Donaldson, and Q. Wang, "Comparison of cellular toxicity caused by ambient ultrafine particles and engineered metal oxide nanoparticles," *Part. Fibre Toxicol.*, vol. 12, no. 5, pp. 1–12, 2015.
- [238] D. Holliday and V. Speirs, "Choosing the right cell line for breast cancer research," *Breast Cancer Res.*, vol. 13, no. 4, pp. 215–222, 2011.
- [239] S. E. Burdall, A. M. Hanby, M. R. J. Lansdown, and V. Speirs, "Breast cancer cell lines: Friend or foe?," *Breast Cancer Res.*, vol. 5, no. 2, pp. 89–95, 2003.
- [240] M. Lacroix and G. Leclercq, "Relevance of breast cancer cell lines as models for breast tumours: An update," *Breast Cancer Res. Treat.*, vol. 83, no. 3, pp. 249–289, 2004.
- [241] M. Panjehpour, M. Castro, and K.-N. Klotz, "Human breast cancer cell line MDA-MB-231 expresses endogenous  $A_{2B}$  adenosine receptors mediating a  $\text{Ca}^{2+}$  signal," *Br. J. Pharmacol.*, vol. 145, no. 2, pp. 211–218, 2005.

- [242] R. M. Neve, K. Chin, J. Fridlyand, J. Yeh, F. L. Baehner, T. Fevr, L. Clark, N. Bayani, J.-P. Coppe, F. Tong, T. Speed, P. T. Spellman, S. Devries, A. Lapuk, N. J. Wang, F. McCormick, R. B. Dickson, and J. W. Gray, "A collection of breast cancer cell lines for the study of functionally distinct cancer subtypes," *Cancer Cell*, vol. 10, no. 6, pp. 515–527, 2006.
- [243] P. A. Kenny, G. Y. Lee, C. A. Myers, R. M. Neve, J. R. Semeiks, P. T. Spellman, K. Lorenz, E. H. Lee, M. H. Barcellos-hoff, O. W. Petersen, J. W. Gray, and M. J. Bissell, "The morphologies of breast cancer cell lines in three-dimensional assays correlate with their profiles of gene expression," *Mol. Oncol.*, vol. 1, no. 1, pp. 84–96, 2007.
- [244] R. Meier, T. D. Henning, S. Boddington, G. Piontek, M. Rudelius, C. Corot, and H. E. Daldrop-Link, "Breast Cancers: MR imaging of folate-receptor expression with the folate-specific nanoparticle P1133," *Radiology*, vol. 255, no. 2, pp. 527–535, 2010.
- [245] N. M. Jackson, "The regulation and mechanisms of EGFR-mediated apoptosis in MDA-MB-468 cells," University of Louisville, 2015.
- [246] R. B. Dickson, S. E. Bates, M. E. McManaway, and M. E. Lippman, "Characterization of estrogen responsive transforming activity in human breast cancer cell lines," *Cancer Res.*, vol. 46, no. 4, pp. 1707–1713, 1986.
- [247] R. T. Morris, R. N. Joyrich, R. W. Naumann, N. P. Shah, A. H. Maurer, H. W. Strauss, J. M. Uszler, J. T. Symanowski, P. R. Ellis, and W. A. Harb, "Phase II study of treatment of advanced ovarian cancer with folate receptor-targeted therapeutic (vintafolide) and companion SPECT-based imaging agent ( $^{99m}\text{Tc}$ -etarfolatide)," *Ann. Oncol.*, vol. 25, no. 4, pp. 852–858, 2014.
- [248] H. D. Soule, T. M. Maloney, S. R. Wolman, E. C. Line, W. D. Peterson, R. Brenz, C. M. Mcgrath, J. Russo, R. J. Pauley, R. F. Jones, and S. C. Brooks, "Isolation and characterization of a spontaneously immortalized human breast epithelial cell line, MCF-10," *Cancer Res.*, vol. 50, no. 18, pp. 6075–6086, 1990.
- [249] J. Chen, S. Li, and Q. Shen, "Folic acid and cell-penetrating peptide conjugated PLGA-PEG bifunctional nanoparticles for vincristine sulfate delivery," *Eur. J. Pharm. Sci.*, vol. 47, no. 2, pp. 430–443, 2012.
- [250] D. Bobo, K. J. Robinson, J. Islam, K. J. Thurecht, and S. R. Corrie, "Nanoparticle-based medicines: A review of FDA-approved materials and clinical trials to date," *Pharm. Res.*, vol. 33, no. 10, pp. 2373–2387, 2016.

- [251] A. C. Anselmo and S. Mitragotri, "Nanoparticles in the clinic," *Bioeng. Transl. Med.*, vol. 1, no. 1, pp. 10–29, 2016.
- [252] A. Dumas and P. Couvreur, "Palladium: A future key player in the nanomedical field?," *Chem. Sci.*, vol. 6, no. 4, pp. 2153–2157, 2015.
- [253] L. Tavakoli, Y. Yamini, H. Ebrahimzadeh, and A. Nezhadali, "Development of cloud point extraction for simultaneous extraction and determination of gold and palladium using ICP-OES," *J. Hazard. Mater.*, vol. 152, no. 1, pp. 737–743, 2008.
- [254] J. Fang, L.-W. Liu, and X.-P. Yan, "Minimization of mass interferences in quadrupole inductively coupled plasma mass spectrometric (ICP-MS) determination of palladium using a flow injection on-line displacement solid-phase extraction protocol," *Spectrochim. Acta Part B*, vol. 61, no. 7, pp. 864–869, 2006.
- [255] T. W. May and R. H. Wiedmeyer, "A table of polyatomic interferences in ICP-MS," *At. Spectroscopy*, vol. 19, no. 5, pp. 150–155, 1998.
- [256] S. Hann, E. Rudolph, G. Köllensperger, and C. Reiter, "Analysis of palladium by high resolution ICP-MS," in *Palladium emissions in the environment*, F. Zereini and F. Alt, Eds. Springer Berlin Heidelberg, 2004, pp. 73–82.
- [257] K. Simitchiev, V. Stefanova, V. Kmetov, G. Andreev, A. Sanchez, and A. Canals, "Investigation of ICP-MS spectral interferences in the determination of Rh, Pd and Pt in road dust: Assessment of correction algorithms *via* uncertainty budget analysis and interference alleviation by preliminary acid leaching," *Talanta*, vol. 77, no. 2, pp. 889–896, 2008.
- [258] A. F. Trindade, R. F. M. Frade, E. M. S. Macoas, C. Graça, C. A. B. Rodrigues, J. M. G. Martinho, and C. A. M. Afonso, "'Click and go': Simple and fast folic acid conjugation," *Org. Biomol. Chem.*, vol. 12, no. 20, pp. 3181–3190, 2014.
- [259] D. W. Lee, H. Ha, and W. K. Lee, "Selective mono-Boc protection of diamines," *Synth. Commun.*, vol. 37, no. 5, pp. 737–742, 2007.
- [260] J. Alzeer, P. J. C. Roth, and N. W. Luedtke, "An efficient two-step synthesis of metal-free phthalocyanines using a Zn(II) template," *Chem. Commun.*, vol. 15, no. 1, pp. 1970–1971, 2009.
- [261] N. Viola-Villegas, A. E. Rabideau, J. Cesnavicius, J. Zubieta, and R. P. Doyle, "Targeting

- the folate receptor (FR): Imaging and cytotoxicity of Rel conjugates in FR-overexpressing cancer cells," *ChemMedChem*, vol. 3, no. 9, pp. 1387–1394, 2008.
- [262] R. O. Ogbodu, E. Antunes, and T. Nyokong, "Physicochemical properties of zinc monoamino phthalocyanine conjugated to folic acid and single walled carbon nanotubes," *Polyhedron*, vol. 60, no. 1, pp. 59–67, 2013.
- [263] T. H. Tran, C. T. Nguyen, D.-P. Kim, Y.-K. Lee, and K. M. Huh, "Microfluidic approach for highly efficient synthesis of heparin-based bioconjugates for drug delivery," *Lab Chip*, vol. 12, no. 3, pp. 589–584, 2011.
- [264] V. L. Nguyen, D. C. Nguyen, H. Hirata, M. Ohtaki, T. Hayakawa, and M. Nogami, "Chemical synthesis and characterization of palladium nanoparticles," *Adv. Nat. Sci. Nanosci. Nanotechnol.*, vol. 1, no. 3, p. 035012, 2010.
- [265] N. V. Long, T. Hayakawa, T. Matsubara, N. D. Chien, M. Ohtaki, and M. Nogami, "Controlled synthesis and properties of palladium nanoparticles," *J. Exp. Nanosci.*, vol. 7, no. 4, pp. 426–439, 2012.
- [266] D. Berger, G. A. Trăistaru, B. S. Vasile, I. Jitaru, and C. Matei, "Palladium nanoparticles synthesis with controlled morphology obtained by polyol method," *UPB Sci. Bull. Ser. B Chem. Mater. Sci.*, vol. 72, no. 1, pp. 113–120, 2010.
- [267] S. Ferrone, M. Hardy, and P. O. Alderson, "Potential of palladium-109-labeled antimelanoma monoclonal antibody for tumor therapy," *J. Nucl. Med.*, vol. 25, no. 7, pp. 796–799, 1984.
- [268] Y. Pan, S. Neuss, A. Leifert, M. Fischler, F. Wen, U. Simon, G. Schmid, W. Brandau, and W. Jahnen-Dechent, "Size-dependent cytotoxicity of gold nanoparticles," *Small*, vol. 3, no. 11, pp. 1941–1949, 2007.
- [269] A. E. Egger, C. Rappel, M. A. Jakupec, C. G. Hartinger, P. Heffeter, and B. K. Keppler, "Development of an experimental protocol for uptake studies of metal compounds in adherent tumor cells," *J. Anal. At. Spectrom.*, vol. 24, no. 1, pp. 51–61, 2009.
- [270] I. L. Hsiao, F. S. Bierkandt, P. Reichardt, A. Luch, Y. J. Huang, N. Jakubowski, J. Tentschert, and A. Haase, "Quantification and visualization of cellular uptake of TiO<sub>2</sub> and Ag nanoparticles: Comparison of different ICP-MS techniques," *J. Nanobiotechnology*, vol. 14, no. 1, pp. 1–13, 2016.

- [271] N. Bhandare and A. Narayana, "Applications of nanotechnology in cancer: A literature review of imaging and treatment," *J. Nucl. Med. Radiat. Ther.*, vol. 5, no. 4, pp. 125–133, 2014.
- [272] X. Yi, Y. Wu, G. Tan, P. Yu, L. Zhou, Z. Zhou, J. Chen, Z. Wang, J. Pang, and C. Ning, "Palladium nanoparticles entrapped in a self-supporting nanoporous gold wire as sensitive dopamine biosensor," *Sci. Rep.*, vol. 7, no. 1, pp. 1–9, 2017.
- [273] J. G. Rebelein and T. R. Ward, "In vivo catalyzed new-to-nature reactions," *Curr. Opin. Biotechnol.*, vol. 53, no. 2, pp. 106–114, 2018.
- [274] H. Chen, Y. He, L. D. Pfefferle, W. Pu, Y. Wu, and S. Qi, "Phenol catalytic hydrogenation over palladium nanoparticles supported on metal-organic frameworks in the aqueous phase," *ChemCatChem*, vol. 10, no. 12, p. 2508, 2018.
- [275] D. I. Gittins and F. Caruso, "Spontaneous phase transfer of nanoparticulate metals from organic to aqueous media," *Angew. Chemie Int. Ed.*, vol. 40, no. 16, pp. 3001–3005, 2001.
- [276] K. Riehemann, S. W. Schneider, T. A. Luger, B. Godin, M. Ferrari, and H. Fuchs, "Nanomedicine - Challenge and perspectives," *Angew. Chemie Int. Ed.*, vol. 48, no. 5, pp. 872–897, 2009.
- [277] W. H. Gmeiner and S. Ghosh, "Nanotechnology for cancer treatment," *Nanotechnol. Rev.*, vol. 3, no. 2, pp. 111–122, 2015.
- [278] K. B. Sutradhar and M. L. Amin, "Nanotechnology in cancer drug delivery and selective targeting," *ISRN Nanotechnol.*, vol. 2014, no. 1, pp. 1–12, 2014.
- [279] M. Hamzeh and G. I. Sunahara, "In vitro cytotoxicity and genotoxicity studies of titanium dioxide (TiO<sub>2</sub>) nanoparticles in Chinese hamster lung fibroblast cells," *Toxicol. Vitro.*, vol. 27, no. 2, pp. 864–873, 2013.
- [280] A. Gniewek, J. J. Ziółkowski, A. M. Trzeciak, and L. Kepiński, "Influence of palladium colloid synthesis procedures on catalytic activity in methoxycarbonylation reaction," *J. Catal.*, vol. 239, no. 2, pp. 272–281, 2006.
- [281] R. Redon, S. Rendon-Lara, A. L. Fernandez-Osorio, and V. M. Ugalde-Saldivar, "Aerobic synthesis of palladium nanoparticles," *Rev. Adv. Mater. Sci.*, vol. 27, no. 1, pp. 31–42, 2011.

- [282] N. Rout, 2013. *Synthesis, characterization, and catalytic activity of monometallic Pd and AgPd bimetallic nanoparticles in different solvent media*. MSc Thesis. National Institute of Technology.
- [283] M. N. Nadagouda and R. S. Varma, "Green synthesis of silver and palladium nanoparticles at room temperature using coffee and tea extract," *Green Chem.*, vol. 10, no. 8, pp. 859–862, 2008.
- [284] K. Mallikarjuns, N. J. Sushma, G. Narasimha, K. V. Rao, L. Manoj, and B. D. P. Raju, "Synthesis and spectroscopic characterization of palladium nanoparticles by using broth of edible mushroom extract," in *International Conference on Nanoscience, Engineering and Technology*, 2011, pp. 612–615.
- [285] A. Kalaiselvi, S. M. Roopan, G. Madhumitha, C. Ramalingam, and G. Elango, "Synthesis and characterization of palladium nanoparticles using *Catharanthus roseus* leaf extract and its application in the photo-catalytic degradation," *Spectrochim. Acta A.*, vol. 135, no. 1, pp. 116–119, 2015.
- [286] A. J. Kora and L. Rastogi, "Green synthesis of palladium nanoparticles using gum ghatti (*Anogeissus latifolia*) and its application as an antioxidant and catalyst," *Arab. J. Chem.*, vol. 11, no. 7, pp. 1097–1106, 2018.
- [287] X. Yang, Q. Li, H. Wang, J. Huang, L. Lin, W. Wang, D. Sun, Y. Su, J. B. Opiyo, L. Hong, Y. Wang, N. He, and L. Jia, "Green synthesis of palladium nanoparticles using broth of *Cinnamomum camphora* leaf," *J. Nanoparticle Res.*, vol. 12, no. 5, pp. 1589–1598, 2010.
- [288] S. Gundy, W. Van Der Putten, A. Shearer, D. Buckton, A. G. Ryder, and M. Ball, "The use of chloroaluminium phthalocyanine tetrasulfonate (ALPcTS ) for time-delayed fluorescence imaging," *Phys. Med. Biol.*, vol. 49, no. 3, pp. 359–369, 2004.
- [289] K. Svanberg, I. Wang, S. Colleen, I. Idvall, C. Ingvar, R. Rydell, D. Jocham, J. Diddens, S. Bown, G. Gregory, S. Montán, S. Andersson-Engels, and S. Svanberg, "Clinical multi-colour fluorescence imaging of malignant tumours - initial experience," *Acta radiol.*, vol. 39, no. 1, pp. 2–9, 1998.
- [290] M. Ethirajan, Y. Chen, P. Joshi, and R. K. Pandey, "The role of porphyrin chemistry in tumor imaging and photodynamic therapy," *Chem. Soc. Rev.*, vol. 40, no. 1, pp. 340–362, 2011.

- [291] N. Masilela, P. Kleyi, Z. Tshentu, G. Priniotakis, P. Westbroek, and T. Nyokong, "Photodynamic inactivation of *Staphylococcus aureus* using low symmetrically substituted phthalocyanines supported on a polystyrene polymer fiber," *Dye. Pigment.*, vol. 96, no. 2, pp. 500–508, 2013.
- [292] K. S. Lokesh and A. Adriaens, "Synthesis and characterization of tetra-substituted palladium phthalocyanine complexes," *Dye. Pigment.*, vol. 96, no. 1, pp. 269–277, 2013.
- [293] M. O. Calculations and R. R. Systems, "Spectra of Porphyrins," 1965.
- [294] A. M. Schaffer, M. Gouterman, and E. R. Davidson, "Porphyrins XXVIII. Extended Huckel calculations on metal phthalocyanines and tetrazaporphins," *Theor. Chim. Acta*, vol. 30, no. 1, pp. 9–30, 1973.
- [295] A. J. McHugh, M. Gouterman, and C. Weiss, "Porphyrins XXIV. Energy, oscillator strength, and Zeeman splitting calculations (SCMO-CI) for phthalocyanine, porphyrins, and related ring systems," *Theor. Chim. Acta*, vol. 24, no. 4, pp. 346–370, 1972.
- [296] S. Wang, J. Wang, and J. Chen, "Conjugates of folic acids with zinc aminophthalocyanine for cancer cell targeting and photodynamic therapy by one-photon and two-photon excitations," *J. Mater. Chem. B*, vol. 2, no. 1, pp. 1594–1602, 2014.
- [297] V. Çakir, M. Durmus, M. Goksel, and Z. Biyiklioglu, "Synthesis and photophysical properties of novel water soluble phthalocyanines," *Dye. Pigment.*, vol. 125, no. 12, pp. 414–425, 2016.
- [298] E. Dube, D. O. Oluwole, N. Nwaji, and T. Nyokong, "Glycosylated zinc phthalocyanine-gold nanoparticle conjugates for photodynamic therapy: Effect of nanoparticle shape," *Spectrochim. Acta A*, vol. 203, no. 5, pp. 85–95, 2018.
- [299] N. Mills, "ChemDraw Ultra 10.0," *J. Am. Soc.*, vol. 128, no. 41, pp. 13649–13650, 2006.
- [300] L. Yu, L. Zhou, M. Ding, J. Li, H. Tan, Q. Fu, and X. He, "Synthesis and characterization of novel biodegradable folate conjugated polyurethanes," *J. Colloid Interface Sci.*, vol. 358, no. 2, pp. 376–383, 2011.
- [301] P. Chan, M. Kurisawa, J. E. Chung, and Y. Y. Yang, "Synthesis and characterization of chitosan-g-poly(ethylene glycol)-folate as a non-viral carrier for tumor-targeted gene delivery," *Biomaterials*, vol. 28, no. 3, pp. 540–549, 2007.

- [302] S. Yang, F. Lin, K. Tsai, M. Wei, H. Tsai, and J. Wong, "Folic acid-conjugated chitosan nanoparticles enhanced protoporphyrin IX accumulation in colorectal cancer cells," *Bioconjug. Chem.*, vol. 21, no. 4, pp. 679–689, 2010.
- [303] A. Magadla, D. O. Oluwole, J. Britton, and T. Nyokong, "Effect of nature of nanoparticles on the photophysicochemical properties of asymmetrically substituted Zn phthalocyanines," *Inorganica Chim. Acta*, vol. 482, no. 1, pp. 438–446, 2018.
- [304] G. Gold, D. O. Oluwole, E. Prinsloo, and T. Nyokong, "Photodynamic therapy activity of zinc phthalocyanine linked to folic acid and magnetic nanoparticles," *J. Photochem. Photobiol. B Biol.*, vol. 186, no. 1, pp. 216–224, 2018.
- [305] E. Ramirez, S. Jansat, K. Philippot, P. Lecante, M. Gomez, A. M. Masdeu-Bulto, and B. Chaudret, "Influence of organic ligands on the stabilization of palladium nanoparticles," *J. Organomet. Chem.*, vol. 689, no. 24, pp. 4601–4610, 2004.
- [306] A. Dani, V. Crocella, L. Maddalena, C. Barolo, S. Bordiga, and E. Groppo, "Spectroscopic study on the surface properties and catalytic performances of palladium nanoparticles in poly(ionic liquid)s," *J. Phys. Chem. C*, vol. 120, no. 3, pp. 1683–1692, 2016.
- [307] P. A. Namini, a a Babaluo, and B. Bayati, "Palladium nanoparticles synthesis using polymeric matrix: poly(ethyleneglycol) molecular weight and palladium concentration effects," *Int. J. Nanosci. Nanotechnol.*, vol. 3, no. 1, pp. 37–43, 2007.
- [308] C. Zhu, J. Zeng, P. Lu, J. Liu, Z. Gu, and Y. Xia, "Aqueous-phase synthesis of single-crystal Pd seeds 3 nm in diameter and their use for the growth of Pd nanocrystals with different shapes," *Chem. A Eur. J.*, vol. 19, no. 16, pp. 5127–5133, 2013.
- [309] Y. Hu, Y. Wang, J. Jiang, B. Han, S. Zhang, K. Li, S. Ge, and Y. Liu, "Preparation and characterization of novel perfluorooctyl bromide nanoparticle as ultrasound contrast agent *via* layer-by-layer self-assembly for folate-receptor-mediated tumor imaging," *Biomed Res. Int.*, vol. 2016, no. 1, pp. 1–14, 2016.
- [310] M. Chen, J. Falkner, W.-H. Guo, J.-Y. Zhang, and C. Sayes, "Synthesis and self-organization of soluble monodisperse palladium nanoclusters," *J. Colloid Interface Sci.*, vol. 287, no. 1, pp. 146–151, 2005.
- [311] N. C. Bigall, M. Reitzig, W. Naumann, P. Simon, K.-H. Van Pee, and A. Eychmüller, "Fungal templates for noble-metal nanoparticles and their application in catalysis,"



- Angew. Chemie Int. Ed.*, vol. 47, no. 41, pp. 7876–7879, 2008.
- [312] K. Naka, M. Sato, and Y. Chujo, “Stabilized spherical aggregate of palladium nanoparticles prepared by reduction of palladium acetate in octa(3-aminopropyl)octasilsesquioxane as a rigid template,” *Langmuir*, vol. 24, no. 20, pp. 2719–2726, 2008.
- [313] A. Kumar and D. A. Buttry, “Size-dependent anodic dissolution of water-soluble palladium nanoparticles,” *J. Phys. Chem. C*, vol. 117, no. 50, pp. 26783–26789, 2013.
- [314] L. Zhang, L. Wang, Z. Jiang, and Z. Xie, “Synthesis of size-controlled monodisperse Pd nanoparticles *via* a non-aqueous seed-mediated growth,” *Nanoscale Res. Lett.*, vol. 7, no. 312, pp. 1–6, 2012.
- [315] A. Kumar and D. A. Buttry, “Size-dependent underpotential deposition of copper on palladium nanoparticles,” *J. Phys. Chem. C*, vol. 119, no. 29, pp. 16927–16933, 2015.
- [316] L. Schiavo, L. Aversa, R. Tatti, R. Verucchi, and G. Carotenuto, “Structural characterizations of palladium clusters prepared by polyol reduction of  $[PdCl_4]^{2-}$  ions,” *J. Anal. Methods Chem.*, vol. 2016, no. 1, pp. 1–7, 2016.
- [317] J. C. Ferreira, R. V. Cavallari, V. S. Bergamaschi, R. M. Antoniassi, Â. A. Teixeira-Neto, M. Linardi, and J. C. M. Silva, “Palladium nanoparticles supported on mesoporous biocarbon from coconut shell for ethanol electro-oxidation in alkaline media,” *Mater. Renew. Sustain. Energy*, vol. 7, no. 4, pp. 1–9, 2018.
- [318] Y. Zhang, Y. Xiong, J. Ge, R. Lin, C. Chen, Q. Peng, D. Wang, and Y. Li, “Porous organic cage stabilised palladium nanoparticles: Efficient heterogeneous catalysts for carbonylation reaction of aryl halides,” *Chem. Commun.*, vol. 54, no. 22, pp. 2796–2799, 2018.
- [319] J. J. Yin, S. Sharma, S. P. Shumyak, Z. X. Wang, Z. W. Zhou, Y. Zhang, P. Guo, C. Z. Li, J. R. Kanwar, T. Yang, S. S. Mohapatra, W. Liu, W. Duan, J. C. Wang, X. Zhang, J. Tan, L. Jia, and S. F. Zhou, “Synthesis and biological evaluation of novel folic acid receptor-targeted,  $\beta$ -cyclodextrin-based drug complexes for cancer treatment,” *PLoS One*, vol. 8, no. 5, pp. 1–20, 2013.
- [320] M. Chen, Y. Feng, L. Wang, L. Zhang, and J.-Y. Zhang, “Study of palladium nanoparticles prepared from water-in-oil microemulsion,” *Colloids Surfaces A Physicochem. Eng.*

- Asp.*, vol. 281, no. 1, pp. 119–124, 2006.
- [321] Y. Sekiguchi, Y. Hayashi, and H. Takizawa, "Synthesis of palladium nanoparticles and palladium/spherical carbon composite particles in the solid–liquid system of palladium oxide-alcohol by microwave Irradiation," *Mater. Trans.*, vol. 52, no. 5, pp. 1048–1052, 2011.
- [322] A. A. Athawale, S. V Bhagwat, and P. P. Katre, "Nanocomposite of Pd-polyaniline as a selective methanol sensor," *Sensors Actuators B*, vol. 114, no. 1, pp. 263–267, 2006.
- [323] C. R. K. Rao, V. Lakshminarayanan, and D. C. Trivedi, "Synthesis and characterization of lower size, laurylamine protected palladium nanoparticles," *Mater. Lett.*, vol. 60, no. 25, pp. 3165–3169, 2006.
- [324] A. A. Athawale, S. V Bhagwat, P. P. Katre, A. J. Chandwadkar, and P. Karandikar, "Aniline as a stabilizer for metal nanoparticles," *Mater. Lett.*, vol. 57, no. 24, pp. 3889–3894, 2003.
- [325] T. Yonezawa, K. Imamura, and N. Kimizuka, "Direct preparation and size control of palladium nanoparticle hydrosols by water-soluble isocyanide ligands," *Langmuir*, vol. 17, no. 16, pp. 4701–4703, 2001.
- [326] M. Martis, K. Mori, K. Fujiwara, W.-S. Ahn, and H. Yamashita, "Amine-functionalized MIL-125 with imbedded palladium nanoparticles as an efficient catalyst for dehydrogenation of formic acid at ambient temperature," *J. Phys. Chem. C*, vol. 117, no. 44, pp. 22805–22810, 2013.
- [327] B. P. Burke, J. Seemann, and S. J. Archibald, *Advanced chelator design for metal complexes in imaging applications: Radiopharmaceuticals, protein targeting, and conjugation*, 1st ed., vol. 68. Hull: Elsevier Inc., 2016.
- [328] W. Dong, Y. Dong, Y. Wang, S. Zhou, X. Ge, L. Sui, and J. Wang, "Labeling of human hepatocellular carcinoma cells by hexamethylene diamine modified fluorescent carbon dots," *Spectrochim. Acta A*, vol. 116, no. 1, pp. 209–213, 2013.
- [329] H. Kim, M. Lee, Y. Kim, J. Huh, H. Kim, M. Kim, T. Kim, V. N. Phan, Y.-B. Lee, G.-R. Yi, S. Haam, and K. Lee, "Quantitative assessment of nanoparticle single crystallinity: Palladium-catalyzed splitting of polycrystalline metal oxide," *Angew. Chemie*, vol. 48, no. 28, pp. 5129–5133, 2009.

- [330] K. T. Chow, D. C. T. Tan, and R. Gokhale, "Small is big: Is nanoamorphous better than amorphous solid dispersion and nanocrystalline in pharma?," *J. Pharm. Nanotechnol.*, vol. 4, no. 3, pp. 11–14, 2016.
- [331] L. Lindfors, P. Skantze, U. Skantze, J. Westergren, and U. Olsson, "Amorphous drug nanosuspensions. 3 . Particle dissolution and crystal growth," *Langmuir*, vol. 23, no. 16, pp. 9866–9874, 2007.
- [332] J. M. Rosenholm, R. M. Korpi, E. Lammentausta, S. Lehtonen, P. Lehenkari, R. Niemi, W. Xiao, J. Zhang, D. Lindberg, H. Gu, C. Sahlgren, and R. B. Sequeiros, "Novel, fast-processed crystalline and amorphous manganese oxide nanoparticles for stem labeling," *Inorg. Chem. Front.*, vol. 2, no. 7, pp. 640–648, 2015.
- [333] R. Jog and D. J. Burgess, "Pharmaceutical amorphous nanoparticles," *J. Pharm. Sci.*, vol. 106, no. 1, pp. 39–65, 2017.
- [334] V. Van Hoang and D. Ganguli, "Amorphous nanoparticles — Experiments and computer simulations," *Phys. Rep.*, vol. 518, no. 3, pp. 81–140, 2012.
- [335] N. J. Babu and A. Nangia, "Solubility advantage of amorphous drugs and pharmaceutical cocrystals," *Cryst. Growth Des.*, vol. 11, no. 7, pp. 2662–2679, 2011.
- [336] J. Chen, J. Zhang, Z. Shen, J. Zhong, and J. Yun, "Preparation and characterization of amorphous cefuroxime axetil drug nanoparticles with novel technology: High-gravity antisolvent precipitation," *Ind. Eng. Res.*, vol. 45, no. 25, pp. 8723–8727, 2006.
- [337] W. J. H. Borghols, D. Lützenkirchen-hecht, U. Haake, W. Chan, U. Lafont, E. M. Kelder, E. R. H. Van Eck, A. P. M. Kentgens, F. M. Mulder, and M. Wagemaker, "Lithium storage in amorphous TiO<sub>2</sub> nanoparticles," *J. Electrochem. Soc.*, vol. 157, no. 5, pp. 582–588, 2010.
- [338] H. Tuyusuz and C. K. Chan, "Preparation of amorphous and nanocrystalline sodium tantalum oxide photocatalysts with porous matrix structure for overall water splitting," *Nano Energy*, vol. 2, no. 1, pp. 116–123, 2012.
- [339] D. B. Do, N. D. Phu, N. Van Hung, L. H. Hoang, T. M. Oanh, D. M. Thanh, and N. Van Minh, "Amorphous CoFe<sub>2</sub>O<sub>4</sub> nanoparticles: Synthesis, crystallization process, and magnetic properties," *IEEE Trans. Magentics*, vol. 50, no. 6, pp. 25–28, 2014.
- [340] L. M. Moreau, D. Ha, H. Zhang, R. Hovden, D. A. Muller, and R. D. Robinson, "Defining

- crystalline/amorphous phases of nanoparticles through X-ray absorption spectroscopy and X-ray diffraction: The case of nickel phosphide," *Chem. Mater.*, vol. 25, no. 12, pp. 2394–2403, 2013.
- [341] B. Fleury, M.-A. Neouze, J.-M. Guigner, N. Menguy, O. Spalla, T. Gacoin, and D. Carriere, "Amorphous to crystal conversion as a mechanism governing the structure of luminescent YVO<sub>4</sub>: Eu nanoparticles," *ACS Nano*, vol. 8, no. 3, pp. 2602–2608, 2014.
- [342] M. José-Yacamán, M. Marín-Almazo, and J. . Ascencio, "High resolution TEM studies on palladium nanoparticles," *J. Mol. Catal. A Chem.*, vol. 173, no. 1–2, pp. 61–74, 2001.
- [343] A. Patterson, "The Scherrer formula for X-ray particle size determination," *Phys. Rev.*, vol. 56, no. 10, pp. 978–982, 1939.
- [344] P. A. Stadelmann, "EMS - A software package for electron diffraction analysis and HREM image simulation in material science," *Ultramicroscopy*, vol. 21, no. 2, pp. 131–146, 1987.
- [345] P. A. Stadelmann, *JEMS: Java Electron Microscopy Software*. 2008.
- [346] I. E. Espino-López, M. Romero-Romo, M. G. M. de Oca-Yemha, P. Morales-Gil, M. T. Ramírez-Silva, J. Mostany, and M. Palomar-Pardavé, "Palladium nanoparticles electrodeposition onto glassy carbon from a deep eutectic solvent at 298 K and their catalytic performance toward formic acid oxidation," *J. Electrochem. Soc.*, vol. 166, no. 1, pp. 3205–3211, 2019.
- [347] H. Choo, B. He, K. Y. Liew, H. Liu, and J. Li, "Morphology and control of Pd nanoparticles," *J. Mol. Catal. A Chem.*, vol. 244, no. 1, pp. 217–228, 2006.
- [348] Y. Xiong, J. M. McLellan, J. Chen, Y. Yin, Z. Y. Li, and Y. Xia, "Kinetically controlled synthesis of triangular and hexagonal nanoplates of palladium and their SPR/SERS properties," *J. Am. Chem. Soc.*, vol. 127, no. 48, pp. 17118–17127, 2005.
- [349] I. Favier, E. Teuma, and M. Gomez, "Palladium and ruthenium nanoparticles: Reactivity and coordination at the metallic surface," *Comptes Rendus - Chim.*, vol. 12, no. 5, pp. 533–545, 2009.
- [350] M. S. Bakshi, "1D Flower-like morphologies of palladium nanoparticles using strongly hydrophobic surfactants," *J. Phys. Chem. C*, vol. 113, no. 25, pp. 10921–10928, 2009.
- [351] C. Jayaseelan, P. R. Gandhi, S. Ravindranath, R. Rajasree, T. Y. Suman, and R. R. Mary,

- “Toxicity studies of nanofabricated palladium against filariasis and malaria vectors,” *Environ. Sci. Pollut. Res.*, vol. 25, no. 1, pp. 324–332, 2018.
- [352] J. Turkevich, P. C. Stevenson, and J. Hillier, “A study of the nucleation and growth process in the synthesis of colloidal gold,” *Discuss. Faraday Soc.*, vol. 55, no. 1, pp. 55–75, 1951.
- [353] S. M. A. Sadat, S. T. Jahan, and A. Haddadi, “Effects of size and surface charge of polymeric nanoparticles on *in vitro* and *in vivo* applications,” *J. Biomater. Nanobiotechnol.*, vol. 7, no. 2, pp. 91–108, 2016.
- [354] R. C. Murdock, L. Braydich-Stolle, A. M. Schrand, J. J. Schlager, and S. M. Hussain, “Characterization of nanomaterial dispersion in solution prior to *in vitro* exposure using dynamic light scattering technique,” *Toxicol. Sci.*, vol. 101, no. 2, pp. 239–253, 2008.
- [355] S. Zhang, H. Gao, and G. Bao, “Physical principles of nanoparticle cellular endocytosis,” *ACS Nano*, vol. 9, no. 9, pp. 8655–8671, 2015.
- [356] D. S. Sidhaye, T. Bala, S. Srinath, H. Srikanth, P. Poddar, M. Sastry, and B. L. V Prasad, “Preparation of nearly monodisperse nickel nanoparticles by a facile solution based methodology and their ordered assemblies,” *J. Phys. Chem. C*, vol. 113, no. 9, pp. 3426–3429, 2009.
- [357] E. Sabbioni, S. Fortaner, M. Farina, R. Del Torchio, C. Petrarca, G. Bernardini, R. Mariani-costantini, S. Perconti, L. Di Giampaolo, R. Gornati, and M. Di Gioacchino, “Interaction with culture medium components, cellular uptake and intracellular distribution of cobalt nanoparticles, microparticles and ions in Balb/3T3 mouse fibroblasts,” *Nanotoxicology*, vol. 8, no. 1, pp. 88–99, 2014.
- [358] A. M. Gazzali, M. Lobry, L. Colombeau, S. Acherar, H. Azaïs, S. Mordon, P. Arnoux, F. Baros, R. Vanderesse, and C. Frochot, “Stability of folic acid under several parameters,” *Eur. J. Pharm. Sci.*, vol. 93, no. 10, pp. 419–430, 2016.
- [359] R. Agarwal, P. Journey, M. Raythatha, V. Singh, S. V Sreenivasan, L. Shi, and K. Roy, “Effect of shape, size, and aspect ratio on nanoparticle penetration and distribution inside solid tissues using 3D spheroid models,” *Adv. Healthc. Mater.*, vol. 4, no. 15, pp. 2269–2280, 2015.
- [360] N. Nalajala, W. F. G. Saleha, B. Ladewig, and M. Neergat, “Sodium borohydride

- treatment: A simple and effective process for the removal of stabilizer and capping agents from shape-controlled palladium nanoparticles," *Chem. Commun.*, vol. 50, no. 66, pp. 9365–9368, 2014.
- [361] B. Zewde, A. Ambaye, J. S. Iii, and D. Raghavan, "A review of stabilized silver nanoparticles—synthesis, biological properties, characterization, and potential areas of applications," *JSM Nanotechnol. Nanomedicine*, vol. 4, no. 2, pp. 1043–1057, 2016.
- [362] R. Mathaes, G. Winter, A. Besheer, and J. Engert, "Non-spherical micro- and nanoparticles: Fabrication, characterization and drug delivery applications," *Expert Opin. Drug Deliv.*, vol. 12, no. 3, pp. 481–492, 2015.
- [363] K. Chatterjee, S. Sarkar, K. Jagajjanani Rao, and S. Paria, "Core/shell nanoparticles in biomedical applications," *Adv. Colloid Interface Sci.*, vol. 209, no. 1, pp. 8–39, 2014.
- [364] B. Desoize, "Metals and metal compounds in cancer treatment," *Anticancer Res.*, vol. 24, no. 3, pp. 1529–1544, 2004.
- [365] U. Ndagi, N. Mhlongo, and M. E. Soliman, "Metal complexes in cancer therapy – an update from drug design perspective," *Drug Des. Devel. Ther.*, vol. 11, no. 1, pp. 599–616, 2017.
- [366] Z. Guo and P. J. Sadler, "Metals in medicine," *Angew. Chemie Int. Ed.*, vol. 38, no. 11, pp. 1512–1531, 1999.
- [367] J. Conde, G. Doria, and P. Baptista, "Noble metal nanoparticles applications in cancer," *J. Drug Deliv.*, vol. 2012, no. 1, pp. 1–12, 2012.
- [368] A. Nel, T. Xia, L. Madler, and N. Li, "Toxic potential of materials at the nanolevel," *Science*, vol. 311, no. 5761, pp. 622–627, 2006.
- [369] L. C. Hartmann, G. L. Keeney, W. L. Lingle, T. J. H. H. Christianson, B. Varghese, D. Hillman, A. L. Oberg, and P. S. Low, "Folate receptor overexpression is associated with poor outcome in breast cancer," *Int. J. Cancer*, vol. 121, no. 5, pp. 938–942, 2007.
- [370] M. Fernandez, F. Javaid, and V. Chudasama, "Advances in targeting the folate receptor in the treatment/imaging of cancers," *Chem. Sci.*, vol. 9, no. 4, pp. 790–810, 2018.
- [371] G. Bystrzejewska-Piotrowska, J. Golimowski, and P. L. Urban, "Nanoparticles: Their potential toxicity, waste and environmental management," *Waste Manag.*, vol. 29, no. 9, pp. 2587–2595, 2009.

- [372] T. Z. Liu, S. D. Lee, and R. S. Bhatnagar, "Toxicity of palladium," *Toxicol. Lett.*, vol. 4, no. 1, pp. 469–473, 1979.
- [373] J. Hostynek, R. S. Hinz, C. R. Lorence, M. Price, and R. H. Guy, "Metals and the skin," *Crit. Rev. Toxicol.*, vol. 23, no. 2, pp. 171–235, 1993.
- [374] C. E. Garrett and K. Prasad, "The art of meeting palladium specifications in active pharmaceutical ingredients produced by Pd-catalyzed reactions," *Adv. Synth. Catal.*, vol. 346, no. 8, pp. 889–900, 2004.
- [375] K. Kinska, J. Jiménez-Lamana, J. Kowalska, B. Krasnodedska-Ostrega, and J. Szpunar, "Study of the uptake and bioaccumulation of palladium nanoparticles by *Sinapis alba* using single particle ICP-MS," *Sci. Total Environ.*, vol. 615, no. 1, pp. 1078–1085, 2018.
- [376] J. D. Spikes and C. F. Hodgson, "Enzyme inhibition by palladium chloride," *Biochem. Biophys. Res. Commun.*, vol. 35, no. 3, pp. 420–422, 1969.
- [377] S. Mitragotri and J. Lahann, "Physical approaches to biomaterial design," *Nat. Mater.*, vol. 8, no. 1, pp. 15–23, 2009.
- [378] M.-J. Hosseini, I. Jafarian, S. Farahani, R. Khodadi, S. . Tagavi, P. Naserzadeh, A. Mohammadi-Bardbori, and N. Arghavanifard, "New mechanistic approach of inorganic palladium toxicity: impairment in mitochondrial electron transfer," *Metallomics*, vol. 8, no. 2, pp. 252–259, 2015.
- [379] M. U. Gürbüz, K. Öztürk, A. S. Ertürk, D. Y. Ermis, G. Esendagli, S. Çalış, and M. Tülü, "Cytotoxicity and biodistribution studies on PEGylated EDA and PEG cored PAMAM dendrimers," *J. Biomater. Sci. Polym. Ed.*, vol. 27, no. 16, pp. 1645–58, 2016.
- [380] C. E. Butterworth and T. Tamura, "Folic acid safety and toxicity: A brief review," *Am. J. Clin. Nutr.*, vol. 50, no. 2, pp. 353–358, 1989.
- [381] C. H. Takimoto, "New antifolates: Pharmacology and clinical applications," *Oncologist*, vol. 1, no. 1, pp. 68–81, 1996.
- [382] I. Fabre, G. Fabre, and I. D. Goldman, "Polyglutamylolation, an important element in methotrexate cytotoxicity and selectivity in tumor versus murine granulocytic progenitor cells *in vitro*," *Cancer Res.*, vol. 44, no. 8, pp. 3190–3195, 1984.
- [383] C. Chittasupho, M. Jaturanpinyo, and S. Mangmool, "Pectin nanoparticle enhances cytotoxicity of methotrexate against hepG2 cells," *Drug Deliv.*, vol. 20, no. 1, pp. 1–9,

- 2013.
- [384] R. S. H. Yang, R. H. Garman, R. R. Maronpot, J. A. McKelvey, C. S. Weil, and M. D. Woodside, "Acute and subchronic toxicity of ethylenediamine in laboratory animals," *Fundam. Appl. Toxicol.*, vol. 3, no. 1, pp. 512–520, 1983.
- [385] H. Mansouri-Torshizi, M. Saeidifar, G. R. Rezaei-Behbehani, A. Divsalar, and A. A. Saboury, "DNA binding studies and cytotoxicity of ethylenediamine 8-Hydroxyquinolino palladium(II) chloride," *J. Chinese Chem. Soc.*, vol. 57, no. 6, pp. 1299–1308, 2010.
- [386] G. Zhao, H. Lin, P. Yu, H. Sun, S. Zhu, X. Su, and Y. Chen, "Ethylenediamine-palladium(II) complexes with pyridine and its derivatives: Synthesis, molecular structure and initial antitumor studies," *J. Inorg. Biochem.*, vol. 73, no. 3, pp. 145–149, 1999.
- [387] E. Stoykova, R. Alexandrova, K. Nedkova, K. Zdravkov, O. Sabotinov, G. Minchev, and R. Ion, "In vitro cytotoxicity assessment of phthalocyanines on virus-transformed animal cells," *Proc. SPIE-Int. Soc. Opt. Eng.*, vol. 5830, no. 1, pp. 404–408, 2005.
- [388] J. D. Spikles, "Phthalocyanines as photosensitizers in biological systems and for the photodynamic therapy of tumors," *Photochem. Photobiol.*, vol. 43, no. 6, pp. 691–699, 1986.
- [389] R. O. Ogbodu, I. Ndhundhuma, A. Karsten, and T. Nyokong, "Photodynamic therapy effect of zinc monoamino phthalocyanine-folic acid conjugate adsorbed on single walled carbon nanotubes on melanoma cells," *Spectrochim. Acta A.*, vol. 137, no. 9, pp. 1120–1125, 2015.
- [390] G. Gold, N. Kobayashi, M. Kimura, and T. Nyokong, "Physicochemical properties of water soluble unsymmetrical phthalocyanine-folic acid conjugates," *Dye. Pigment.*, vol. 149, no. 1, pp. 393–398, 2018.
- [391] E. Stoykova, R. Alexandrova, K. Nedkova, K. Zdravkov, O. Sabotinov, G. Minchev, and R. Ion, "In vitro cytotoxicity assessment of phthalocyanines on human tumour cells," *Proc. SPIE-Int. Soc. Opt. Eng.*, vol. 1, no. 1, pp. 1–5, 2011.
- [392] C. Petrarca, E. Clemente, L. Di Giampaolo, R. Mariani-Costantini, K. Leopold, R. Schindl, L. V. Lotti, R. Mangifesta, E. Sabbioni, Q. Niu, G. Bernardini, and M. Di Gioacchino, "Palladium nanoparticles induce disturbances in cell cycle entry and progression of



- peripheral blood mononuclear cells: Paramount role of ions,” *J. Immunol. Res.*, vol. 2014, no. 1, pp. 1–9, 2014.
- [393] L. Migliore, G. Frenzilli, C. Nesti, S. Fortaner, and E. Sabbioni, “Cytogenetic and oxidative damage induced in human lymphocytes by platinum, rhodium and palladium compounds,” *Mutagenesis*, vol. 17, no. 5, pp. 411–417, 2002.
- [394] M. A. Musa, V. L. D. Badisa, and L. M. Latinwo, “Cytotoxic activity of N,N’-bis(2-hydroxybenzyl) ethylenediamine derivatives in human cancer cell lines,” *Anticancer Res.*, vol. 34, no. 4, pp. 1601–1607, 2014.
- [395] M. Chen, Y.-G. Feng, X. Wang, T.-C. Li, J.-Y. Zhang, and D.-J. Qian, “Silver nanoparticles capped by oleylamine: Formation, growth, and self-organization,” *Langmuir*, vol. 10, no. 22, pp. 5296–5304, 2007.
- [396] T. M. Walker, P. C. Rhodes, and C. Westmoreland, “The differential cytotoxicity of methotrexate in rat hepatocyte monolayer and spheroid cultures,” *Toxicol. Vitr.*, vol. 14, no. 5, pp. 475–485, 2000.
- [397] N. Kohler, C. Sun, J. Wang, and M. Zhang, “Methotrexate-modified superparamagnetic nanoparticles and their intracellular uptake into human cancer cells,” *Langmuir*, vol. 21, no. 19, pp. 8858–8864, 2005.
- [398] S. M. A. Pinto, V. A. Tomé, M. J. F. Calvete, M. M. Pereira, H. D. Burrows, A. M. S. Cardoso, A. Pallier, M. M. C. A. Castro, É. Tóth, and C. F. G. C. Geraldés, “The quest for biocompatible phthalocyanines for molecular imaging: Photophysics, relaxometry and cytotoxicity studies,” *J. Inorg. Biochem.*, vol. 154, no. 1, pp. 50–59, 2016.
- [399] T. Nyokong and I. Gledhill, “The use of phthalocyanines in cancer therapy,” in *AIP Conference Proceedings 1517*, 2013, vol. 49, no. 2013, pp. 49–52.
- [400] C. De Oliveira, S. L. Büttenbender, W. A. Prado, A. Beckenkamp, A. C. Asbahr, A. Buffon, S. S. Guterres, and A. R. Pohlmann, “Enhanced and selective antiproliferative activity of methotrexate-functionalized-nanocapsules to human breast cancer cells (MCF-7),” *Nanomaterials*, vol. 8, no. 24, pp. 1–19, 2018.
- [401] S. Yoon, J. R. Choi, J.-O. Kim, J.-Y. Shin, X. Zhang, and J.-H. Kang, “Influence of reduced folate carrier and dihydrofolate reductase genes on methotrexate-induced cytotoxicity,” *Cancer Res. Treat.*, vol. 42, no. 3, pp. 163–171, 2010.

- [402] M. Haber, J. Madafiglio, and M. D. Norris, "Methotrexate cytotoxicity determination using the MTT assay following enzymatic depletion of thymidine and hypoxanthine," *J. Cancer Res. Clin. Oncol.*, vol. 119, no. 1, pp. 315–317, 1993.
- [403] R. O. Ogbodu and T. Nyokong, "The effect of ascorbic acid on the photophysical properties and photodynamic therapy activities of zinc phthalocyanine-single walled carbon nanotube conjugate on MCF-7 cancer cells," *Spectrochim. Acta A.*, vol. 151, no. 6, pp. 174–183, 2015.
- [404] S. L. Moses, V. M. Edwards, and E. Brantley, "Cytotoxicity in MCF-7 and MDA-MB-231 breast cancer cells, without harming MCF-10A healthy cells," *J. Nanomed. Nanotechnol.*, vol. 7, no. 2, pp. 1–11, 2016.
- [405] Z. Teng, Y. Luo, T. Wang, B. Zhang, and Q. Wang, "Development and application of nanoparticles synthesized with folic acid-conjugated soy protein," *J. Agric. Food Chem.*, vol. 61, no. 10, pp. 2556–2564, 2013.
- [406] M. Ahamed, M. Karns, M. Goodson, J. Rowe, S. M. Hussain, J. J. Schlager, and Y. Hong, "DNA damage response to different surface chemistry of silver nanoparticles in mammalian cells," *Toxicol. Appl. Pharmacol.*, vol. 233, no. 3, pp. 404–410, 2008.
- [407] T. Keswani, S. Chowdhury, S. Mukherjee, A. Bhattacharyya, S. Chowdhury, and S. Mukherjee, "Palladium(II) complex induces apoptosis through ROS-mediated mitochondrial pathway in human lung adenocarcinoma cell line (A549)," *Curr. Sci.*, vol. 107, no. 10, pp. 1711–1719, 2014.
- [408] A. J. Cortez, P. Tudrej, K. A. Kujawa, and K. M. Lisowska, "Advances in ovarian cancer therapy," *Cancer Chemother. Pharmacol.*, vol. 81, no. 1, pp. 17–38, 2018.
- [409] K. Li, Y. Liu, S. Zhang, Y. Xu, J. Jiang, F. Yin, Y. U. E. Hu, B. Han, S. Ge, L. I. Zhang, and Y. Wang, "Folate receptor-targeted ultrasonic PFOB nanoparticles: Synthesis, characterization and application in tumor-targeted imaging," *Int. J. Mol. Med.*, vol. 39, no. 6, pp. 1505–1515, 2017.
- [410] R. T. Dean, W. Jessup, and C. R. Roberts, "Effects of exogenous amines on mammalian cells, with particular reference to membrane flow," *Biochem. J.*, vol. 217, no. 1, pp. 27–40, 1984.
- [411] J. L. Radomski, "The primary aromatic amines: Their biological properties and

- structure-activity relationships," *Annu. Rev. Pharmacol. Toxicol.*, vol. 19, no. 4, pp. 129–157, 1979.
- [412] F. Akbarzadeh, K. Khoshgard, L. Hosseinzadeh, E. Arkan, and D. Rezazadeh, "Investigating the cytotoxicity of folate-conjugated bismuth oxide nanoparticles on KB and A549 cell lines," *Adv. Pharm. Bull.*, vol. 8, no. 4, pp. 627–635, 2018.
- [413] A. C. Antony, "Folate receptors," *Annu. Rev. Nutr.*, vol. 16, no. 1, pp. 501–521, 1996.
- [414] M. Scaltriti and J. Baselga, "The epidermal growth factor receptor pathway: A model for targeted therapy," *Clin. Cancer Res.*, vol. 12, no. 18, pp. 5268–5273, 2006.
- [415] S. Acharya, F. Dilnawaz, and S. K. Sahoo, "Biomaterials targeted epidermal growth factor receptor nanoparticle bioconjugates for breast cancer therapy," *Biomaterials*, vol. 30, no. 29, pp. 5737–5750, 2009.
- [416] H. Xu, Y. Yu, D. Marciniak, A. Rishi, S. H. Fazlul, O. Kucuk, and A. P. N. Majumdar, "Epidermal growth factor receptor (EGFR)-related protein inhibits multiple members of the EGFR family in colon and breast cancer cells," *Mol. Cancer Ther.*, vol. 4, no. 3, pp. 435–442, 2005.
- [417] J. R. Price, K. A. Lillycrop, and G. C. Burdge, "Folic acid induces cell type-specific changes in the transcriptome of breast cancer cell lines: a proof-of-concept study," *J. Nutr. Sci.*, vol. 5, no. 1, pp. 1–8, 2016.
- [418] Q. Li, R. Shi, Y. Wang, and X. Niu, "TAGLN suppresses proliferation and invasion, and induces apoptosis of colorectal carcinoma cells," *Tumor Biol.*, vol. 34, no. 1, pp. 505–513, 2013.
- [419] R. Hunter, J. Barnes, H. F. Oakeley, and D. M. Matthews, "Toxicity of folic acid given in pharmacological doses to healthy volunteers," *Lancet*, vol. 295, no. 7637, pp. 61–63, 1970.
- [420] Ł. Lamch, M. Tsirigotis-Maniecka, J. Kulbacka, and K. A. Wilk, "Synthesis of new zinc(II) phthalocyanine conjugates with block copolymers for cancer therapy," *Ark. Online J. Chem.*, vol. 2017, no. 2, pp. 433–445, 2017.
- [421] C. Uslan, N. I. Durmus, Y. Ozturk, B. T. Yildiz, Z. P. Cakar, M. Goksel, M. Durmus, Y. H. Gursel, and B. S. Sesalan, "A novel of PEG-conjugated phthalocyanine and evaluation of its photocytotoxicity and antibacterial properties for photodynamic therapy," *J.*

- Porphy. Phthalocyanines*, vol. 21, no. 1, pp. 2–15, 2017.
- [422] J. F. Lovell and P.-C. Lo, “Porphyrins and phthalocyanines for theranostics,” *Theranostics*, vol. 2, no. 9, pp. 815–816, 2012.
- [423] C. Contini, M. Schneemilch, S. Gaisford, and N. Quirke, “Nanoparticle-membrane interactions,” *J. Exp. Nanosci.*, vol. 13, no. 1, pp. 62–81, 2018.
- [424] S. Arayachukiat, J. Seemork, P. Pan-in, K. Amornwachirabodee, N. Sangphech, T. Sansureerungsikul, K. Sathornsantikun, C. Vilaivan, K. Shigyou, P. Pienpinijtham, T. Vilaivan, T. Palaga, W. Banlunara, T. Hamada, and S. Wanichwecharungruang, “Bringing macromolecules into cells and evading endosomes by oxidized carbon nanoparticles,” *Nano Lett.*, vol. 15, no. 5, pp. 3370–3376, 2015.
- [425] J. D. Unciti-Broceta, V. Cano-Cortés, P. Altea-Manzano, S. Pernagallo, J. J. Díaz-Mochón, and R. M. Sánchez-Martín, “Number of nanoparticles per cell through a spectrophotometric method - A key parameter to assess nanoparticle-based cellular assays,” *Sci. Rep.*, vol. 5, no. 10091, pp. 1–10, 2015.
- [426] L. C. Cheng, X. Jiang, J. Wang, C. Chen, and R. S. Liu, “Nano-bio effects: Interaction of nanomaterials with cells,” *Nanoscale*, vol. 5, no. 9, pp. 3547–3569, 2013.
- [427] Q. Feng, Y. Liu, J. Huang, K. Chen, J. Huang, and K. Xiao, “Uptake, distribution, clearance, and toxicity of iron oxide nanoparticles with different sizes and coatings,” *Sci. Rep.*, vol. 8, no. 1, pp. 1–13, 2018.
- [428] I. Z. Vass, Z. Deák, K. Paul, S. Kovács, and I. Vass, “Interaction of nanoparticles with biological systems,” *Acta Biol. Szeged.*, vol. 59, no. 2, pp. 225–245, 2015.
- [429] S. S. Rokade, K. A. Joshi, K. Mahajan, S. Patil, G. Tomar, D. S. Dubal, V. S. Parihar, R. Kitture, J. R. Bellare, and S. Ghosh, “*Gloriosa superba* mediated synthesis of platinum and palladium nanoparticles for induction of apoptosis in breast cancer,” *Bioinorg. Chem. Appl.*, vol. 2018, no. 1, pp. 1–9, 2018.
- [430] W. Xia and P. S. Low, “Folate-targeted therapies for cancer,” *J. Med. Chem.*, vol. 53, no. 19, pp. 6811–6824, 2010.
- [431] V. Boshnjaku, K.-W. Shim, T. Tsurubuchi, S. Ichi, E. V Szany, G. Xi, B. Mania-Farnell, D. G. Mclone, T. Tomita, and C. S. Mayanil, “Nuclear localization of folate receptor alpha: A new role as a transcription factor,” *Sci. Rep.*, vol. 2, no. 980, pp. 1–7, 2012.

- [432] V. Mohanty, M. R. Siddiqui, T. Tomita, C. Shekhar, and C. S. Mayanil, "Folate receptor alpha is more than just a folate transporter," *Neurogenesis*, vol. 4, no. 1, pp. 2–6, 2017.
- [433] Z. Chu, S. Zhang, B. Zhang, C. Zhang, C. Y. Fang, I. Rehor, P. Cigler, H.-C. Chang, G. Lin, R. Liu, and Q. Li, "Unambiguous observation of shape effects on cellular fate of nanoparticles," *Sci. Rep.*, vol. 4, no. 1, pp. 1–9, 2014.
- [434] A. Brown and N. Hondow, *Electron microscopy of nanoparticles in cells*, 1st ed., vol. 5. Elsevier Ltd., 2013.
- [435] K. W. Powers, S. C. Brown, V. B. Krishna, S. C. Wasdo, B. M. Moudgil, and S. M. Roberts, "Research strategies for safety evaluation of nanomaterials. Part VI. Characterization of nanoscale particles for toxicological evaluation," *Toxicol. Sci.*, vol. 90, no. 2, pp. 296–303, 2006.
- [436] K. W. Powers, M. Palazuelos, B. M. Moudgil, and S. M. Roberts, "Characterization of the size, shape, and state of dispersion of nanoparticles for toxicological studies," *Nanotoxicology*, vol. 1, no. 1, pp. 42–51, 2007.
- [437] J. Brown, A., Brydson, R., Calvert, C., Warley, A., Bomford, A., Li, A., Powell, "Analytical electron microscope investigation of iron within human liver biopsies," in *Institute of Physics Conference Series no. 179*, 2003, pp. 83–86.
- [438] P. B. Bell and B. Safiejko-Mroczka, "Preparing whole mounts of biological specimens for imaging macromolecular structures by light and electron microscopy," *Int. J. Imaging Syst. Technol.*, vol. 8, no. 3, pp. 225–239, 1997.
- [439] R. M. Glaeser and K. A. Taylor, "Radiation damage relative to transmission electron microscopy of biological specimens at low temperature: A review," *J. Microsc.*, vol. 112, no. 1, pp. 127–138, 1978.
- [440] R. Henderson, "The potential and limitations of neutrons, electrons and X-rays for atomic resolution microscopy of unstained biological molecules," *Q. Rev. Biophys.*, vol. 2, no. 1, pp. 171–193, 1995.
- [441] P. N. T. Unwin and R. Henderson, "Molecular structure determination by electron microscopy of unstained crystalline specimens," *J. Mol. Biol.*, vol. 94, no. 3, pp. 425–440, 1975.
- [442] S. A. Nowak and T. Chou, "Membrane lipid segregation in endocytosis," *Phys. Rev. E*,

- vol. 78, no. 2, pp. 1–13, 2008.
- [443] P. Decuzzi and M. Ferrari, “The receptor-mediated endocytosis of nonspherical particles,” *Biophys. J.*, vol. 94, no. 10, pp. 3790–3797, 2008.
- [444] C. Huang, Y. Zhang, H. Yuan, H. Gao, and S. Zhang, “Role of nanoparticle geometry in endocytosis: Laying down to stand up,” *Nano Lett.*, vol. 19, no. 9, pp. 4546–4550, 2013.
- [445] X. Yi, X. Shi, and H. Gao, “A universal law for cell uptake of one-dimensional nanomaterials,” *Nano Lett.*, vol. 14, no. 2, pp. 1049–1055, 2014.
- [446] A. H. Bahrami, M. Raatz, J. Agudo-Canalejo, R. Michel, E. M. Curtis, C. K. Hall, M. Gradzielski, R. Lipowsky, and T. R. Weikl, “Wrapping of nanoparticles by membranes,” *Adv. Colloid Interface Sci.*, vol. 208, no. 1, pp. 214–224, 2014.
- [447] A. M. Kashi, K. Tahermanesh, S. Chaichian, M. T. Joghataei, F. Moradi, S. M. Tavangar, A. S. M. Najafabadi, N. Lotfibakhshaiesh, S. P. Beyranvand, A. F. Anvari-Yazdi, and S. M. Abed, “How to prepare biological samples and live tissues for scanning electron microscopy (SEM),” *Galen Med. J.*, vol. 3, no. 2, pp. 63–80, 2014.
- [448] K. R. Porter and F. Kallman, “The properties and effects of osmium tetroxide as a tissue fixative with special reference to its use for electron microscopy,” *Exp. Cell Res.*, vol. 4, no. 1, pp. 127–141, 1953.
- [449] T. A. Foglia, P. A. Barr, A. J. Malloy, and M. J. Costanzo, “Oxidation of unsaturated fatty acids with ruthenium and osmium tetroxide,” *J. Am. Oil Chem. Soc.*, vol. 54, no. 11, pp. 870–872, 1977.
- [450] Ľ. Švorc, P. Tomčík, J. Durdiak, M. Rievaj, and D. Bustin, “Analytical methods for the detection of osmium tetroxide: A review,” *Polish J. Environ. Stud.*, vol. 21, no. 1, pp. 7–13, 2012.
- [451] Q. Mu, C. A. David, J. Galceran, C. Rey-Castro, L. Krzeminski, R. Wallace, F. Bamiduro, S. J. Milne, N. S. Hondow, R. Brydson, G. Vizcay-Barrena, M. N. Routledge, L. J. C. Jeuken, and A. P. Brown, “Systematic investigation of the physicochemical factors that contribute to the toxicity of ZnO nanoparticles,” *Chem. Res. Toxicol.*, vol. 27, no. 2, pp. 558–567, 2014.
- [452] N. Singh, G. J. S. Jenkins, B. C. Nelson, B. J. Marquis, T. G. G. Maffei, A. P. Brown, P. M. Williams, C. J. Wright, and S. H. Doak, “The role of iron redox state in the genotoxicity

- of ultrafine superparamagnetic iron oxide nanoparticles," *Biomaterials*, vol. 33, no. 1, pp. 163–170, 2012.
- [453] X. Ke, C. Bittencourt, and G. Van Tendeloo, "Possibilities and limitations of advanced transmission electron microscopy for carbon-based nanomaterials," *J. Nanotechnol.*, vol. 6, no. 1, pp. 1541–1557, 2015.
- [454] P. V Asharani, K. L. G. Mun, M. P. Hande, and S. Valiyaveetil, "Cytotoxicity and genotoxicity of silver in human cells," *ACS Nano*, vol. 3, no. 2, pp. 279–290, 2009.
- [455] Y. Pan, K. Sader, J. J. Powell, A. Bleloch, M. Gass, J. Trinick, A. Warley, A. Li, R. Brydson, and A. Brown, "3D morphology of the human hepatic ferritin mineral core: New evidence for a subunit structure revealed by single particle analysis of HAADF-STEM images," *J. Struct. Biol.*, vol. 166, no. 12, pp. 22–31, 2009.
- [456] Q. Mu, N. S. Hondow, Ł. Krzemi, A. P. Brown, L. J. C. Jeuken, and M. N. Routledge, "Mechanism of cellular uptake of genotoxic silica nanoparticles," *Part. Fibre Toxicol.*, vol. 9, no. 29, pp. 1–11, 2012.
- [457] N. Hondow, J. Harrington, R. I. K. Brydson, S. H. Doak, N. Singh, B. Manshian, and A. Brown, "STEM mode in the SEM: A practical tool for nanotoxicology," *Nanotoxicology*, vol. 5, no. 2, pp. 215–227, 2011.
- [458] S. H. Anwar, "A brief review on nanoparticles: Types of platforms, biological synthesis and applications," *J. Mater. Sci.*, vol. 6, no. 2, pp. 109–116, 2018.
- [459] X. Li, H. Xu, Z. Chen, and G. Chen, "Biosynthesis of nanoparticles by microorganisms and their applications," *J. Nanomater.*, vol. 2011, no. 1, pp. 1–16, 2011.
- [460] C.-N. Lok, C.-M. Ho, R. Chen, Q.-Y. He, W.-Y. Yu, H. Sun, P. K.-H. Tam, J.-F. Chiu, and C.-M. Che, "Silver nanoparticles: Partial oxidation and antibacterial activities," *J. Biol. Inorg. Chem.*, vol. 12, no. 1, pp. 257–534, 2007.
- [461] M. Rai, A. P. Ingle, I. R. Gupta, S. S. Birla, A. P. Yadav, and A. Kamel, "Potential role of biological systems in formation of nanoparticles: mechanism of synthesis and biomedical applications," *Curr. Nanosci.*, vol. 9, no. 5, pp. 576–587, 2013.
- [462] C. J. Szymanski, P. Munusamy, C. Mihai, Y. Xie, D. Hu, M. K. Gilles, T. Tyliczszak, S. Thevuthasan, D. R. Baer, and G. Orr, "Shifts in oxidation states of cerium oxide nanoparticles detected inside intact hydrated cells and organelles," *Biomaterials*, vol.

- 62, no. 1, pp. 147–154, 2015.
- [463] N. Jardón-Maximino, M. Pérez-Alvarez, R. Sierra-Avila, C. A. Ávila-Orta, E. Jiménez-Regalado, A. M. Bello, P. González-Morones, and G. Cadenas-Pliego, “Oxidation of copper nanoparticles protected with different coatings and stored under ambient conditions,” *J. Nanomater.*, vol. 2018, no. 1, pp. 1–8, 2018.
- [464] T. J. Brunner, P. Wick, P. Manser, P. Spohn, N. Grass, L. K. Limbach, A. Bruinink, and W. J. Stark, “*In vitro* cytotoxicity of oxide nanoparticles: Comparison to asbestos, silica, and the effect of particle solubility,” *Environ. Sci. Technol.*, vol. 40, no. 14, pp. 4374–4381, 2006.
- [465] A. M. Schrand, J. J. Schlager, L. Dai, and S. M. Hussain, “Preparation of cells for assessing ultrastructural localization of nanoparticles with transmission electron microscopy,” *Nat. Protoc.*, vol. 5, no. 4, pp. 744–757, 2010.
- [466] B. Drasler, D. Vanhecke, L. Rodriguez-Lorenzo, A. Petri-Fink, and B. Rothen-Rutishauser, “Quantifying nanoparticle cellular uptake: Which method is best?,” *Nanomedicine*, vol. 12, no. 10, pp. 1095–1099, 2017.
- [467] S. Behzadi, V. Serpooshan, W. Tao, M. A. Hamaly, M. Y. Alkawareek, E. C. Dreaden, D. Brown, A. M. Alkilany, O. C. Farokhzad, and M. Mahmoudi, “Cellular uptake of nanoparticles: Journey inside the cell,” *Chem. Soc. Rev.*, vol. 46, no. 14, pp. 4218–4244, 2017.
- [468] Y.-S. Yi, “Folate receptor-targeted diagnostics and therapeutics for inflammatory diseases,” *Immune Netw.*, vol. 16, no. 6, pp. 337–343, 2016.
- [469] J. D. Robertson, L. Rizzello, M. Avila-Olias, J. Gaitzsch, C. Contini, M. Magori, S. A. Renshaw, and G. Battaglia, “Purification of nanoparticles by size and shape,” *Sci. Rep.*, vol. 6, no. 1, pp. 1–9, 2016.
- [470] M. Mendes, J. J. Sousa, A. Pais, and C. Vitorino, “Targeted theranostic nanoparticles for brain tumor treatment,” *Pharmaceutics*, vol. 10, no. 4, pp. 1–47, 2018.
- [471] D. S. Theti and A. L. Jackman, “The role of alpha folate receptor-mediated transport in the antitumor activity of antifolate drugs,” *Clin. Cancer Res.*, vol. 10, no. 3, pp. 1080–1089, 2004.
- [472] S. A. A. Rizvi and A. M. Saleh, “Applications of nanoparticle systems in drug delivery



- technology," *Saudi Pharm. J.*, vol. 26, no. 1, pp. 64–70, 2018.
- [473] S. Chatterjee, E. R. Smith, K. Hanada, V. L. Stevens, and S. Mayor, "GPI anchoring leads to sphingolipid-dependent retention of endocytosed proteins in the recycling endosomal compartment," *EMBO J.*, vol. 20, no. 7, pp. 1583–1592, 2001.
- [474] T. J. Anchordoquy, Y. Barenholz, D. Boraschi, M. Chorny, P. Decuzzi, M. A. Dobrovolskaia, Z. S. Farhangrazi, D. Farrell, A. Gabizon, H. Ghandehari, B. Godin, N. M. La-Beck, J. Ljubimova, S. M. Moghimi, L. Pagliaro, E. Ruoslahti, N. J. Serkova, and D. Simberg, "Mechanisms and barriers in cancer nanomedicine: Addressing challenges, looking for solutions," *ACS Nano*, vol. 11, no. 1, pp. 12–18, 2017.
- [475] C. P. Leamon, J. A. Reddy, M. Vetzal, R. Dorton, E. Westrick, N. Parker, Y. Wang, and I. Vlahov, "Folate targeting enables durable and specific antitumor responses from a therapeutically null tubulysin B analogue," *Cancer Res.*, vol. 68, no. 23, pp. 9839–9845, 2008.
- [476] K. Mu, J. N. Skepper, M. Posfai, R. Trivedi, S. Howarth, C. Corot, E. Lancelot, P. W. Thompson, A. P. Brown, and J. H. Gillard, "Effect of ultrasmall superparamagnetic iron oxide nanoparticles (Ferumoxtran-10) on human monocyte-macrophages *in vitro*," *Biomaterials*, vol. 28, no. 9, pp. 1629–1642, 2007.
- [477] W. J. Landis, M. C. Paine, and M. J. Glimchbr, "Use of acrolein vapors for the anhydrous preparation of bone tissue for electron microscopy," *J. Ultrastruct. Res.*, vol. 70, no. 2, pp. 171–180, 1980.
- [478] J. R. McIntosh, "Methods in cell biology," in *Cellular electron microscopy*, 2007, vol. 79.
- [479] N. Reid, "Ultramicrotomy," in *Ultramicrotomy*, 1975.
- [480] K. Sader, M. Reedy, D. Popp, C. Lucaveche, and J. Trinick, "Measuring the resolution of uncompressed plastic sections cut using an oscillating knife ultramicrotome," *J. Struct. Biol.*, vol. 159, no. 1, pp. 29–35, 2007.
- [481] G. McMahon and T. Malis, "Ultramicrotomy of nanocrystalline materials," *Microsc. Res. Tech.*, vol. 31, no. 4, pp. 267–274, 1995.
- [482] J. Domey, L. Haslauer, I. Grau, C. Strobel, M. Kettering, and I. Hilger, "Probing the cytotoxicity of nanoparticles: Experimental pitfalls and artifacts," in *Measuring Biological Impacts of Nanomaterials*, vol. 5, J. Wegener, Ed. Springer, Cham, 2014, pp.

- 31–44.
- [483] X. Zhang, X. Xu, N. Bertrand, E. Pridgen, A. Swami, and O. C. Farokhzad, “Interactions of nanomaterials and biological systems: Implications to personalized nanomedicine,” *Adv. Drug Deliv. Rev.*, vol. 64, no. 13, pp. 1363–1384, 2012.
- [484] G. Corthey, A. A. Rubert, A. L. Picone, G. Casillas, L. J. Giovanetti, J. M. Ramallo-Lopez, E. Zelaya, G. A. Benitez, F. G. Requejo, M. Jose-Yacaman, R. C. Salvarezza, and M. H. Fonticelli, “New insights into the chemistry of thiolate-protected palladium nanoparticles,” *J. Phys. Chem. C*, vol. 116, no. 17, pp. 9830–9837, 2012.
- [485] S. M. Rogers, N. Dimitratos, W. Jones, M. Bowker, A. G. Kanaras, P. P. Wells, C. R. A. Catlow, and S. F. Parker, “The adsorbed state of a thiol on palladium nanoparticles,” *Phys. Chem. Chem. Phys.*, vol. 18, no. 26, pp. 17265–17271, 2016.
- [486] K. San and Y.-S. Shon, “Synthesis of alkanethiolate-capped metal nanoparticles using alkyl thiosulfate ligand precursors: A method to generate promising reagents for selective catalysis,” *Nanomaterials*, vol. 8, no. 5, pp. 346–357, 2018.
- [487] G. Corthey, J. A. Olmos-Asar, G. Casillas, M. M. Mariscal, S. Mejía-Rosales, J. C. Azcárate, E. Larios, M. José-Yacamán, R. C. Salvarezza, and M. H. Fonticelli, “Influence of capping on the atomistic arrangement in palladium nanoparticles at room temperature,” *J. Phys. Chem. C*, vol. 118, no. 42, pp. 24641–24647, 2014.
- [488] S. Ghiamkazemi, A. Amanzadeh, R. Dinarvand, M. Rafiee-Tehrani, and M. Amini, “Synthesis, and characterization, and evaluation of cellular effects of the FOL-PEG-g-PEI-GAL nanoparticles as a potential non-viral vector for gene delivery,” *J. Nanomater.*, vol. 2010, no. 1, pp. 1–10, 2010.
- [489] M. Besouw, R. Masereeuw, L. Van Den Heuvel, and E. Levchenko, “Cysteamine: An old drug with new potential,” *Drug Discov. Today*, vol. 18, no. 15, pp. 785–792, 2013.
- [490] Y. Chen, M. Wang, L. Zhang, Y. Liu, and J. Han, “Poly(o-aminothiophenol)-stabilized Pd nanoparticles as efficient heterogenous catalysts for Suzuki cross-coupling reactions,” *RSC Adv.*, vol. 7, no. 1, pp. 47104–47110, 2017.
- [491] C. Y. Chen, G. Y. Li, L. Zhang, X. H. Huang, D. Cheng, S. C. Wu, C. Z. Xu, J. H. Zhou, and L. Xun, “MicroRNA delivery mediated by PEGylated polyethyleneimine for prostate cancer therapy,” *Open Chem.*, vol. 16, no. 1, pp. 1257–1267, 2018.

- [492] X. Shuai, T. Merdan, F. Unger, M. Wittmar, and T. Kissel, "Novel biodegradable ternary copolymers hy-PEI-g-PCL-b-PEG: Synthesis, characterization, and potential as efficient nonviral gene delivery vectors," *Macromolecules*, vol. 36, no. 15, pp. 5751–5759, 2003.
- [493] H. Petersen, P. M. Fechner, A. L. Martin, K. Kunath, S. Stolnik, C. J. Roberts, D. Fischer, M. C. Davies, and T. Kissel, "Polyethylenimine-graft-poly(ethylene glycol) copolymers: Influence of copolymer block structure on DNA complexation and biological activities as gene delivery system," *Bioconjug. Chem.*, vol. 13, no. 4, pp. 845–854, 2002.
- [494] S. R. Sirsi, R. C. Schray, X. Guan, N. M. Lykens, J. H. Williams, M. L. Erney, and G. J. Lutz, "Functionalized PEG–PEI copolymers complexed to exon-skipping oligonucleotides improve dystrophin expression in mdx mice," *Hum. Gene Ther.*, vol. 19, no. 8, pp. 795–806, 2008.
- [495] G. J. Lutz, S. R. Sirsi, and J. H. Williams, "PEG-PEI copolymers for oligonucleotide delivery to cells and tissues," in *Gene Therapy Protocols: Production and In Vivo Applications of Gene Transfer Vectors*, Totowa, NJ: Humana Press, 2008, pp. 141–150.
- [496] N. Kim, D. Jiang, A. Jacobi, K. Lennox, S. Rose, M. A. Behlke, and A. K. Salem, "Synthesis and characterization of mannosylated pegylated polyethylenimine as a carrier for siRNA," *Int. J. Pharm.*, vol. 427, no. 1, pp. 123–133, 2013.
- [497] G. A. Mansoori, K. S. Brandenburg, and A. Shakeri-Zadeh, "A comparative study of two folate-conjugated gold nanoparticles for cancer nanotechnology applications," *Cancers (Basel)*, vol. 2, no. 4, pp. 1911–1928, 2010.
- [498] H. Dincer, H. Mert, E. Caliskan, G. Y. Atmaca, and A. Erdogmus, "Synthesis and photophysicochemical studies of poly(ethylene glycol) conjugated symmetrical and asymmetrical zinc phthalocyanines," *J. Mol. Struct.*, vol. 1102, no. 12, pp. 190–196, 2015.
- [499] H. Li, F. R. Fronczek, and M. G. H. Vicente, "Pegylated phthalocyanines: Synthesis and spectroscopic properties," *Tetrahedron Lett.*, vol. 52, no. 50, pp. 6675–6678, 2011.
- [500] N. Hondow, R. M. Brown, T. Starborg, A. G. Monteiths, R. Brydson, H. D. Summers, P. Rees, and A. Brown, "Quantifying the cellular uptake of semiconductor quantum dot nanoparticles by analytical electron microscopy," *J. Microsc.*, vol. 261, no. 2, pp. 167–176, 2015.

- [501] R. Aznar, F. Barahon, O. Geiss, J. Ponti, and J. T. Luis, "Quantification and size characterisation of silver nanoparticles in environmental aqueous samples and consumer products by single particle-ICPMS," *Talanta*, vol. 175, no. 4, pp. 200–208, 2017.
- [502] F. Laborda, E. Bolea, and J. Jimenez-Lamana, "Single particle inductively coupled plasma mass spectrometry: A powerful tool for nanoanalysis," *Anal. Chem.*, vol. 86, no. 1, pp. 2270–2278, 2014.
- [503] S. Meyer, A. López-Serrano, H. Mitze, N. Jakubowski, and T. Schwerdtle, "Single-cell analysis by ICP-MS/MS as a fast tool for cellular bioavailability studies of arsenite," *Metallomics*, vol. 10, no. 1, pp. 73–76, 2018.
- [504] S. Nayak, H. Lee, J. Chmielewski, and L. A. Lyon, "Folate-mediated cell targeting and cytotoxicity using thermoresponsive microgels," *J. Am. Chem. Soc.*, vol. 126, no. 33, pp. 10258–10259, 2004.
- [505] G. A. Van Norman, "Drugs, devices, and the FDA: Part 1: An overview of approval processes for drugs," *JACC Basic to Transl. Sci.*, vol. 1, no. 3, pp. 170–179, 2016.
- [506] G. A. Van Norman, "Drugs, devices, and the FDA: Part 2: An overview of approval processes: FDA approval of medical devices," *JACC Basic to Transl. Sci.*, vol. 1, no. 4, pp. 277–287, 2016.
- [507] M. E. B. Holbein, "Understanding FDA regulatory requirements for investigational new drug applications for sponsor-investigators," *J. Investig. Med.*, vol. 57, no. 6, pp. 688–694, 2015.
- [508] K. Groves, B. Bao, J. Zhang, G. Cuneo, W. Yared, and J. D. Peterson, "Quantitative assessment of folate receptor expression by FMT imaging with a NIR fluorescent folate agent," no. 800, p. 4602, 2012.
- [509] J. Zhang, X. Zhao, M. Xian, C. Dong, and S. Shuang, "Folic acid-conjugated green luminescent carbon dots as a nanoprobe for identifying folate receptor-positive cancer cells," *Talanta*, vol. 183, no. 1, pp. 39–47, 2018.
- [510] L. Xing, Y. Xu, K. Sun, H. Wang, F. Zhang, and Z. Zhou, "Identification of a peptide for folate receptor alpha by phage display and its tumor targeting activity in ovary cancer xenograft," *Sci. Rep.*, vol. 8, no. 1, pp. 1–13, 2018.

- [511] J. Qian, F. Quan, F. Zhao, C. Wu, Z. Wang, and L. Zhou, "Aconitic acid derived carbon dots: Conjugated interaction for the detection of folic acid and fluorescence targeted imaging of folate receptor overexpressed cancer cells," *Sens. Actuators B. Chem.*, vol. 262, no. 1, pp. 444–451, 2018.
- [512] H. Li, J. Fan, J. Du, K. Guo, S. Sun, X. Liu, and X. Peng, "A fluorescent and colorimetric probe specific for palladium detection," *Chem. Commun.*, vol. 46, no. 1, pp. 1079–1081, 2010.
- [513] M. D. Kennedy, K. N. Jallad, J. Lu, P. S. Low, and D. Ben Amotz, "Evaluation of folate conjugate uptake and transport by the choroid plexus of mice," *Pharm. Res.*, vol. 20, no. 5, pp. 714–719, 2003.
- [514] F. Sonvico, S. Mornet, S. Vasseur, C. Dubernet, D. Jaillard, J. Degrouard, J. Hoebeke, E. Duguet, P. Colombo, and P. Couvreur, "Folate-conjugated iron oxide nanoparticles for solid tumor targeting as potential specific magnetic hyperthermia mediators: Synthesis, physicochemical characterization, and *in vitro* experiments," *Bioconjug. Chem.*, vol. 16, no. 5, pp. 1181–1188, 2005.
- [515] Y. Li, X. Chen, and N. Gu, "Computational investigation of interaction between nanoparticles and membranes: Hydrophobic/hydrophilic effect," *J. Phys. Chem. B*, vol. 112, no. 1, pp. 16647–16653, 2008.
- [516] P. Chanphai, V. Konka, and H. A. Tajmir-Riahi, "Folic acid – chitosan conjugation : A new drug delivery tool," *J. Mol. Liq.*, vol. 238, pp. 155–159, 2017.
- [517] C. Contini, M. Schneemilch, S. Gaisford, and N. Quirke, "Nanoparticle–membrane interactions," *J. Exp. Nanosci.*, vol. 13, no. 1, pp. 62–81, 2017.
- [518] F. Bou-Abdallah and T. R. Terpstra, "The thermodynamic and binding properties of the transferrins as studied by isothermal titration calorimetry," *Biochim. Biophys. Acta - Gen. Subj.*, vol. 1820, no. 3, pp. 318–325, 2012.
- [519] P. V Danenberg, B. Gustavsson, P. Johnston, P. Lindberg, R. Moser, E. Odin, G. J. Peters, and N. Petrelli, "Folates as adjuvants to anticancer agents: Chemical rationale and mechanism of action," *Crit. Rev. Oncol. Hematol.*, vol. 106, no. 1, pp. 118–131, 2016.